Sound Propagation around Underwater Seamounts

by

Joseph J. Sikora III

B.S., Rensselaer Polytechnic Institute (2003)
M.S., Massachusetts Institute of Technology (2005)

Submitted in partial fulfillment of the
requirements of the degree of

Doctor of Philosophy

at the

MASSACHUSETTS INSTITUTE OF TECHNOLOGY

and the

WOODS HOLE OCEANOGRAPHIC INSTITUTION

February 2009

Signature of Author .....
MIT Department of Electrical Engineering and Computer Science
MIT/WHOI Joint Program in Applied Ocean Physics and Engineering
January 30, 2009

Certified by .....
Arthur B. Baggeroer, Thesis Supervisor
Ford Professor of Engineering
Secretary of the Navy/Chief of Naval Operations Chair for Ocean Sciences
Massachusetts Institute of Technology

Accepted by .....
Terry P. Orlando
Chairman, EECS Departmental Committee on Graduate Students
Massachusetts Institute of Technology

Accepted by .....
James C. Preisig
Chairman, Joint Committee for Applied Ocean Science and Engineering
Massachusetts Institute of Technology/Woods Hole Oceanographic Institution

Sound Propagation around Underwater Seamounts

by

Joseph J. Sikora III

Submitted to the Department of Electrical Engineering and Computer Science
on January 30, 2009, in partial fulfillment of the
requirements for the degree of
Doctor of Philosophy in Electrical Engineering and Computer Science

Abstract

In the ocean, low frequency acoustic waves propagate with low attenuation and cylindrical spreading loss over long-ranges, making them an effective tool for underwater source localization, tomography, and communications. Underwater mountains, or *seamounts*, are ubiquitous throughout the world's oceans and can absorb and scatter acoustic energy, offering many interesting acoustic modeling challenges. The goal of the research performed in support of this thesis is to measure the acoustic scattered field of a large, conical seamount at long-range, and reconcile observations with 2-D range-dependent acoustic models, for the purpose of understanding the effects of highly range-dependent bathymetry.

The Basin Acoustic Seamount Scattering Experiment (BASSEX) was conducted to measure the scattered fields of the two seamounts which form the Kermit-Roosevelt Seamount Complex in the Northeast Pacific Ocean during September and October of 2004. The experiment used fixed and ship-deployed acoustic sources transmitting m-sequence signals at 68.2 and 250 Hz carrier frequencies, with 35 and 83 Hz bandwidth, respectively. The receiver was a towed hydrophone array with 3 m sensor spacing, cut for 250 Hz. BASSEX is the first experiment to measure acoustic arrival patterns in the scattered field of a seamount at many locations at sound path ranges of order 500 km, utilizing a rich bathymetry and sound velocity database.

Convergence zones in the forward-scattered field of seamounts at long-range are observed, created by higher order mode coupling and blockage. Acoustic ray arrival angles, travel times, and amplitudes show good agreement with parabolic equation (PE) acoustic modeling results inside the forward-scattered fields; in particular, simulated results are fairly accurate for weak surface-reflected-bottom-reflected acoustic rays. The width of the forward-scattered field is shown to span the projected width of a seamount. Temporal coherence of ray amplitude inside a seamount scattered field could not be determined due to array movement issues, and should be the focus of future research to determine the stability of scattered acoustic rays for applications such as acoustic tomography.

Robust adaptive beamforming methods are used to process hydrophone array data gathered in the BASSEX experiment. Non-stationarity in the observed noise field caused by array fluctuations and data acquisition system malfunctions motivate the use of a time-varying Capon adaptive beamformer, and strong acoustic harmonics from ship operations motivate the use of a frequency and steering angle dependent white noise gain constraint. In an effort to process snap-shot deficient data sets, the novel physically constrained maximum likelihood (PCML) beamformer was further developed and applied. By using orthonormal trigonometric eigenvector bases to determine the maximum likelihood spectral covariance matrix, the PCML beamformer computational efficiency is significantly increased.

Thesis Supervisor: Arthur B. Baggeroer

Title: Ford Professor of Engineering
Secretary of the Navy/Chief of Naval Operations Chair for Ocean Sciences

David H. Staelin
Title: Professor of Electrical Engineering
Massachusetts Institute of Technology

Henrik Schmidt
Title: Professor of Ocean Engineering
Massachusetts Institute of Technology

James F. Lynch
Title: Senior Scientist/Department Chair of Applied Ocean Physics and Engineering
Massachusetts Institute of Technology/Woods Hole Oceanographic Institution

Acknowledgments

First and foremost, I would like to thank my advisor, Professor Arthur Baggeroer, for his support of my thesis research, and my other academic pursuits, during the past five-and-a-half years. In working with Art, a giant in the fields of Ocean Sciences and Signal Processing, I have gained first-hand oceanographic research knowledge, and also learned, in particular, to be introspective and thorough in my work.

I gratefully acknowledge the assistance of my doctoral committee members: Dr. James Lynch, Professor David Staelin and Professor Henrik Schmidt. Jim has been very encouraging and has taught me much about physical oceanography. Dave's amazing curiosity has led me to better understand the data supporting this thesis, and has improved the way I present results. Henrik was one of my first-year professors at MIT; he taught me the fundamentals of acoustic modeling, the foundation upon which this thesis is largely based. I also thank Dr. Mark Grosenbaugh for chairing my dissertation defense.

The work of Edward Scheer, Keith Von der Hydt and Kevin Heaney were critical elements of the experiment and data analyses supporting my thesis. In particular, I have worked closely with Edward over the years and came to appreciate his talents as both researcher and musician, as well as his unique sense of humor. I am very appreciative of the acoustic modeling results provided by Hyun Joe Kim, without which this thesis would be incomplete, and of Jon Paul Kitchens, who helped inspire the beamforming method developed in this thesis.

The Digital Signal Processing Group (DSPG), led by Professor Alan Oppenheim, has provided me a wonderful environment in which to work and interact with other skilled and knowledgeable electrical engineers. Al is clearly concerned with improving the learning process as well as with the development of innovative research. Our newly renovated office space promotes interaction among students and faculty, and our weekly group meetings take advantage of our scientific diversity to solve problems across many different fields of research.

I wish to express my gratitude to my close friends for their support during my graduate years; in particular Chris E., Erin B., Seb N., Andrew R., Joanna G., Vedran S., Dave F. and George M.. Thanks also to the members of the DSPG who have helped create a great work environment, including Eric Strattman, Dennis Wei, Tom Baran, Zahi Karam, and

Melanie Rudoy.

I would like to thank my parents, and all the rest of my family, for their support and encouragement which has led me to this milestone. Finally, I would like to give special thanks to my father, who throughout my academic career has pushed me to always take on the most challenging work, and to pursue my doctorate; not in the least, he has always been a willing and able grammar coach.

The research supporting this thesis was made possible because of work performed by the North Pacific Acoustic Laboratory (NPAL) group. I am grateful for the financial support provided by the Office of Naval Research (ONR), under Grant N00014-04-1-0124.

Contents

List of Figures

List of Tables

Chapter 1

Introduction

Basin-scale acoustic propagation in the ocean has been utilized by tomography and telemetry systems to measure ocean properties and to monitor natural and man-made acoustic activity. Environmental variability in the ocean – *e.g.*, caused by internal waves[1] – has been shown [4],[5] to affect the acoustic multipath structure of transmitted signals. This thesis investigates the effects of bathymetric range-dependence and environmental variability on low frequency acoustic propagation in long-range waveguides.

Acoustic propagation in range-dependent ocean waveguides has been studied in several contexts. The Heard Island Feasibility Test [6] demonstrated that phase-coherent acoustic transmission is possible over multiple ocean basins. The Acoustic Thermometry of Ocean Climate (ATOC) experiment [7],[8],[9] investigated acoustic mode amplitude temporal coherence and arrival pattern variability due to natural phenomena for acoustic transmissions across an ocean basin. Acoustic scattering by the Dickins Seamount was investigated [10],[11], and demonstrated acoustic shadowing by a seamount for a short-range waveguide. Despite this work, and due to the complexity of the problem, acoustic propagation around seamounts is still not well understood for long-range ocean waveguides.

1.1 Hypotheses

This thesis validates three important hypotheses. First, that 2-D acoustic models can predict acoustic ray travel time, arrival angle, and amplitude in the forward-scattered field of a seamount at long-range; model accuracy will be investigated and acoustic paths will be

[1] Internal waves cause variability in the sound velocity profile.

identified where possible. Second, that convergence zones [12] exist in the forward-scattered field of a seamount at long-range behind the seamount. Third, that the computational efficiency of the physically constrained maximum likelihood (PCML) beamformer [13] is increased using orthonormal basis functions to model the array spectral covariance matrix, and that this method can be applied to the data supporting this thesis to improve array resolution to interpret the forward-scattered field.

To prove these hypotheses the forward-scattered fields of ocean seamounts are investigated at long-range using experimental and theoretical data. The performance of the PCML beamformer is evaluated using simulated and real hydrophone array data from the BASSEX experiment, and to measure the seamount acoustic scattered field, the PCML beamformer is applied to data records with non-stationary noise environments and/or are corrupted by data acquisition system malfunction.

1.2 Experiment

The data supporting this thesis comes from the Basin Acoustic Seamount Scattering Experiment (BASSEX) of 2004, which was designed to study the scattered field of the Kermit-Roosevelt Seamounts in the Northeast Pacific Ocean. Acoustic arrival patterns were measured in the scattered fields of the seamounts on a 400-800 km range scale inside the seamount forward-scattered fields to investigate acoustic multipath structure. Bathymetry measurements were obtained using a swath echosounder and sound velocity measurements were obtained using expendable bathythermometers (XBT). The Five Octave Research Array (FORA) [14], provided and operated by Pennsylvania State University, is a towed hydrophone array with 64 sensors cut for 250 Hz (3 m spacing), which was used to measure acoustic arrival patterns. Moored and ship deployed acoustic sources transmitted pseudo-random sequences (m-sequences) on 68.2 and 250 Hz carrier frequencies, with 35 and 83 Hz bandwidth, respectively. Random timing errors in the data acquisition system precluded accurate travel time measurement. BASSEX is the first experiment to measure broadband acoustic modal coupling[2] at many locations inside the forward-scattered field of a seamount at ranges of order 500 km.

[2]Modal coupling is a transfer of acoustic energy between modes.

1.3 Thesis Contributions

The overall goal of this thesis is to investigate modal coupling in the forward-scattered field of a seamount and determine the accuracy of acoustic modeling codes to understand the impact of environmental variability and bathymetric range-dependence on long-range acoustic propagation. The specific objectives supporting the overall goal of this thesis are described in Sections 1.3.1-1.3.3.

1.3.1 Convergence Zones

The effects of environmental variability and ray chaos [15] on acoustic propagation – *e.g.*, modal coupling and arrival pattern broadening – increase with range. Natural convergence zones widen and dissipate in range, spreading acoustic energy fairly evenly throughout the water column at long-range [16]. The Dickins Seamount experiment [10],[11] examined acoustic shadowing at short-range where narrow, well defined convergence zones exist. This thesis demonstrates the formation of refracted and reflected convergence zones, by mode blockage and coupling, inside the forward-scattered fields for two isolated, conical seamounts at long-range.

1.3.2 Range-Dependent Acoustic Modeling

Range-dependent acoustic modeling codes are qualified for the long-range ocean environments investigated in this thesis by reconciling simulated results with measured acoustic ray arrival angle, travel time, and amplitude gathered inside the seamount forward-scattered fields. The complex bathymetry of a seamount is particularly challenging to model accurately due to strong range-dependence, 3-D diffraction/scattering, geoacoustic inhomogeneity, and environmental variability.

Ray trace model results generated with range-dependent Ocean Acoustical Ray-Tracing Software (RAY) [17] are used to identify and reconcile measured acoustic ray travel times and arrival angles. The inherent high frequency eigenray approximation to the acoustic field made by ray trace algorithms results in arrival patterns which are very sensitive to environmental inhomogeneity and variability. Parabolic equation (PE) approximation model simulated results, generated using the Range-dependent Acoustic Modeler (RAM) [18],[19], are used to reconcile measured acoustic ray amplitudes, travel times, and arrival angles.

The PE method models 2-D diffraction around a seamount and is not as sensitive to environmental uncertainty, compared with the ray tracing method. RAM uses the Padé approximation [20] method, which reduces phase error inherent to the PE model for high angle acoustic propagation.

1.3.3 Adaptive Beamforming

Strong, spatially dependent acoustic interference in the ocean lowers the signal-to-noise ratio (SNR) of acoustic transmissions and the probability for detection of acoustic rays. Time-varying, adaptive Capon and PCML beamformers are developed to increase array spatial resolution and SNR to detect and estimate the parameters of acoustic rays in the presence of strong interference. The PCML beamforming algorithm is applied to improve array spatial resolution in non-stationary noise environments. Some BASSEX data sets show significant array orientation changes over time and data drop-outs; these issues increase Capon beamformer sensitivity and bias the wavenumber-power estimate. With real and simulated data, the PCML beamformer provides robustness to snap-shot deficiency, and higher resolution compared with the Bartlett beamformer.

1.4 Thesis Organization

Chapter 2 provides an overview of previous work, basic sound propagation principles of the open-ocean and around seamounts, a detailed description of the BASSEX experiment, and a review of the numeric acoustic modeling techniques used to support this thesis. This chapter also establishes the nomenclature and provides the relevant background material necessary to interpret the processed data presented later.

Chapter 3 describes the observational methods used to process the available BASSEX data and presents the transmitted signal characteristics, source position, and source clock timing data.

Chapter 4 reviews discrete-time array processing methods and develops the Capon beamforming algorithm used to process the available BASSEX data. This chapter establishes a data processing algorithm which yields accurate travel time estimation and noise suppression for acoustic rays using a hydrophone array.

Chapter 5 presents the PCML beamformer and develops an efficient implementation,

which is then applied to the available BASSEX data. Simulated data are used to measure the array gain, sensitivity, and beampattern characteristics of the PCML beamformer. BASSEX data are used to verify that the PCML beamformer performs with real array data and to compare its performance with the Bartlett and Capon beamforming methods.

Chapter 6 investigates the scattered field of the Kermit-Roosevelt Seamounts using the available BASSEX data. The ambient noise field is carefully examined, and measured multipath arrival patterns are reconciled with ray trace and PE acoustic model simulated results. Horizontally scattered acoustic energy is also presented; however, numeric models which can efficiently handle 3-D range-dependent environments at 250 Hz are currently unavailable, and ray path reconciliation is not attempted.

Chapter 7 provides conclusions and discusses future work.

Chapter 2

Background

Seamounts are a ubiquitous bathymetric feature in the world's oceans. The effects of seamounts on acoustic propagation are of interest in applications such as tomography and telemetry systems because they scatter acoustic energy and can affect transmission between a source and receiver. Physical experiments to date have focused on acoustic transmission loss in the forward-scattered field of seamounts at long-range [21],[22],[10],[11], and do not provide sufficient analysis of acoustic multipath structure to demonstrate strong modal coupling by seamounts, or to qualify range-dependent acoustic modeling codes.

This chapter provides a review of previous work relating to the topics discussed in this thesis, to motivate the current research and to provide context. Relevant background information regarding underwater acoustic propagation in the ocean and the effects of range-dependence are presented to establish the nomenclature and interpret experimental results. Section 2.1 will explore the previous physical and theoretical experimental results relating to this thesis. Section 2.2 discusses known methods by which sound propagates in the ocean and around seamounts to lay the groundwork for understanding experimental results. Section 2.3 provides a description of the BASSEX experiment. Section 2.4 reviews the numerical modeling techniques supporting this thesis. Section 2.5 discusses the approach used to reconcile experimental data with simulated results.

2.1 Previous Work

2.1.1 Experimental Approach

One of the first experiments which studied sound propagation around seamounts was reported by Northrop [21] in 1970. This study measured propagation loss in the 5 to 180 Hz band using underwater explosions on and above the sound channel axis, and hydrophones located at SOFAR depth on the Wake and Midway Islands. The results showed that, except for several bathymetric windows with sill depths near 4 km, the Hawaiian Arch and Midway Island completely shadowed acoustic signals. Acoustic shadowing inside bathymetric windows was measured up to 35 dB, and shown to be frequency independent.

Nutile and Guthrie [22] reported an experiment conducted near Midway Island in 1979 designed to study acoustic shadowing by seamounts; acoustic path lengths were $O(1600$ km). The study reconciled acoustic data from explosive charges, in the 8 to 300 Hz range, and from a continuous wave (CW) source at 14.65 Hz, with ray trace modelers. The CW source allowed for the continuous measurement of transmission loss over latitude, while the explosive charges allowed for discrete travel time and arrival pattern measurements. The results showed individual ray path blockage by seamounts. Missing from their study was information on sound velocity structure and bathymetry of the area.

In 1982 Ebbeson and Turner [10] used experimental results and ray tracing to measure the scattered field of the Dickins Seamount in the Northeast Pacific Ocean; maximum sound path lengths were about 130 km. The experiment used a fixed vertical hydrophone array between 323 and 633 m depth, and a 230 Hz CW ship deployed source towed at 18 and 184 m depths. They showed that the acoustic energy inside the shadow zone can drop as much as 15 dB, compared with that of the field outside the shadow zone, and that the shape of the shadow zone corresponds roughly to the projected width of the seamount. When the source was 3 to 5 km from the peak, back-reflected signals were observed, and when the source was less than 3 km from the peak, enhancement was observed. When the source was deployed at 18 m, the seamount blocked deep refracting acoustic energy and only surface-reflected-bottom-reflected acoustic energy with a low number of reflections were observed in the forward-scattered field. When the source was deployed at 184 m, most of the sound energy was confined closely to the sound channel axis and propagated over the seamount peak. The BASSEX experiment measured acoustic scattering by seamounts for sound paths

of much longer range where strong modal blockage and coupling occur.

Chapman and Ebbeson [11] gave results from a short-range experiment that measured the scattered field of the Dickens Seamount. This study used explosive charges at 24 and 196 m depths and a fixed vertical hydrophone array between 323 and 633 m depth to measure acoustic shadowing. Measured data was compared to the Medwin-Spaulding model [23] of seamount shadowing and laboratory experiments with a scale model of the Dickens Seamount. Acoustic shadowing of 10-15 dB was shown for the shallow source depth. Examination of the data revealed that diffracted waves which passed over the seamount through rough-surface forward scattering and diffraction were the dominant pulse in the seamount shadow zone.

The Heard Island Feasibility Test (HIFT), reported by Munk *et al.* [6], showed that phase-coherent acoustic transmission could be achieved between a ship deployed source array southeast of Heard Island in the Indian Ocean, and bottom-mounted vertical line receiver arrays in every ocean except the Arctic. This experiment was a prerequisite to the ATOC experiment. Noted issues in the experiment include the identification and stability of individual features in acoustic arrival patterns. Munk suggests stable acoustic multipaths caused by tomographic features, such as seamounts, could be used to provide temperature information along additional paths; this has not been realized to date.

Wage [8] analyzed data from the ATOC experiment, where a source moored on the Pioneer Seamount transmitted a signal to vertical line arrays in Hawaii and Kiritimati at ranges of 3515 and 5171 km, respectively. She showed that the Pioneer Seamount was responsible for weak, late arrival signals in the receptions, and that modes 1-10 have temporal mode peak amplitude coherence of about 5.5 min. Wage also investigated the effect of a downsloping bathymetry on mode propagation from a source near the bottom, and showed that a slope greater than 4 deg caused variability in lower order modes and arrival patterns at a range of approximately 50 km. Temporal mode amplitude coherence could not be investigated in this thesis because the required signal duration and sensor positioning were not available.

2.1.2 Theoretical Approach

Seamount scattering over long-ranges has been studied theoretically using a variety of methods. Generally, a complex waveguide is broken into finite regions, inside which the Helmholtz

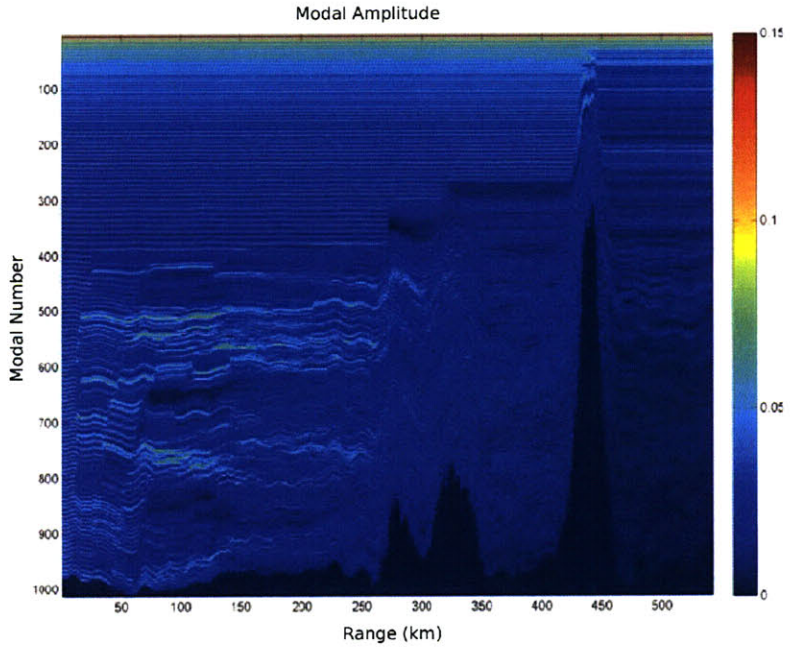

Figure 2-1: Amplitude of the first 1000 modes using a cylindrically symmetric waveguide containing Kermit-Roosevelt Seamount bathymetry and sound velocity data gathered during the BASSEX experiment (figure is from Hyun Joe Kim, MIT, PhD Thesis).

equation can be solved numerically. The size of these regions and the size of the waveguide affect accuracy and computation time. Methods which model the acoustic field in range-dependent waveguides include wavenumber integration, ray tracing, normal mode, and parabolic equation approximation. Ray tracing and the parabolic equation methods will be discussed in further detail in Section 2.4.

Pierce [24] introduced the adiabatic approximation to the coupled normal mode approach. The adiabatic approximation requires that no energy be transferred between higher and lower order modes from one range step to the next. Pierce showed that when the range-dependence in the waveguide is sufficiently weak, the adiabatic approximation provides accurate results.

Evans [25] used the stepwise coupled mode procedure to investigate how seamounts scatter low frequency ambient noise. A cylindrically symmetric seamount model was used, which had the general characteristics of the Dickens Seamount. It was shown that the seamount served to remove energy from steep angles through bottom interaction, but not necessarily through mode coupling.

Figure 2-1 shows the amplitude of the first 1000 vertical modes at 250 Hz, generated

with a PE code, in a typical 2-D waveguide transecting one of the seamounts investigated in this thesis. The seamount is located at 440 km in range. Modal cutoff and transfer of energy to lower order modes is evident on the left hand side of the seamount, and a repopulation of higher order acoustic modes is evident on the right hand side.

Larsson and Abrahamsson [20] applied Helmholtz and parabolic equation modelers to a benchmark 2-D shallow water seamount problem. A wide-angle Claerbout parabolic equation modeler was used, supporting propagation angles less than 36 deg. For the soft bottom case, results showed that the two methods agree. Energy propagates nearly adiabatically since sound impinging upon the seamount is absorbed. As the bottom becomes stiffer, modes couple, rays become steeper, and the parabolic approximation method breaks down. Larsson and Abrahamsson concluded that high-angle parabolic equation codes, such as those which employ the Padé approximation, would solve this problem; the RAM model supporting this thesis uses the Padé approximation.

Harrison [26], [27] provides analytical methods for determining horizontal propagation paths and shadow zone boundaries around conical seamounts. Munk and Zachariasen [2] showed the two mechanisms for coastal scatter to be specular reflection from steep cliffs and Bragg scatter from a rough sea floor. They also showed that seamounts horizontally repel acoustic energy from deep water. Horizontal diffraction effects of a seamount were not separable in the available data supporting this thesis due to array conical ambiguity.

Taroudakis [28] modeled a seamount as a set of superimposed rings, where each of the rings is a range-independent waveguide; this method yields numerically unstable results. Inspired by Taroudakis, Eskenazi [29] modeled a seamount with cylinders, of decreasing diameter, stacked one on top of another. He used a Direct Global Matrix approach, developed by Schmidt [30], for numerically modeling the size of the acoustic perturbation zone around a seamount, for a point source. His method offered better numerical stability than Taroudakis' approach. The results from Eskenazi's work show that a perturbation zone appears behind seamounts and fans out with boundaries on each side tangent to the seamount and passing through the source. The perturbation zone can contain regions of higher or lower acoustic energy than the region outside of the zone equidistant from the source. Eskenazi also showed that the perturbation zone "heals" itself at a far enough distance behind the seamount. The scale of the BASSEX experiment is too large to implement Eskenazi's approach effectively.

Recently, Luo [31] presented a normal mode acoustic modeler which was fundamentally identical to Taroudakis' method, without high-frequency modeling, waveguide size, seabed composition, and seamount geometry limitations. He showed that the N×2D method is a poor approximation for modeling the 3-D effects of a seamount. Unlike parabolic equation methods which usually only model in one direction, his method can be used to treat problems with significant backscatter. The method presented by Luo is computationally intensive, especially at 250 Hz, and is not used to reconcile data supporting this thesis; the computation time is even worse for broadband acoustic modeling.

2.2 Underwater Acoustic Propagation Principles

This section will briefly present some of the current understanding of sound propagation in the ocean to interpret the available data supporting this thesis. Section 2.2.1 discusses basic acoustic propagation principles in the open-ocean and describes the characteristic arrival pattern observed in the BASSEX results. Section 2.2.2 presents an understanding of the scatter field of a seamount using canonical environmental models.

2.2.1 Open-Ocean Acoustic Propagation

Sound waves travel for great distances in the ocean because they tend to travel along the Sound Frequency And Ranging (SOFAR) channel, or minimum sound speed axis, only incurring cylindrical spreading loss. The SOFAR channel axis is formed from temperature and pressure differences in the ocean. Sound velocity in water is primarily affected by temperature, salinity, and hydrostatic pressure. Typically, sound velocity is higher in deep water, and deep diving acoustic rays, with longer path length, tend to have shorter travel times than shallow acoustic rays.

Snell's law governs wavefront propagation, and is given by

$$\frac{\cos\theta}{c} = p \text{ (slowness)}, \tag{2.1}$$

where c is the medium velocity, θ is the horizontal angle of the wavefront, and slowness, p, is the reciprocal of the horizontal phase speed of an acoustic wavefront through the medium. As a plane wave passes into a medium of slower sound speed, its angle of attack increases

to match phase velocity with the plane wave in the faster medium to satisfy the normal displacement boundary condition.

The acoustic field in the ocean can be represented as a sum of orthogonal normal modes which meet the pressure-release boundary condition at the sea surface, and stress/displacement boundary conditions at the sea floor. The acoustic field can also be represented as a sum of acoustic rays which are governed by the eikonal and first order transport equations; this is a high-frequency approximation method. These methods will be discussed futher in Section 2.4.

A typical flat-bottom, open-ocean propagation arrival pattern contains ray groups, the number of which increases with range from the source. Ray groups, for a temperate climate, consist of four rays. The first and third rays arrive from below, and the second and fourth rays arrive from above. The first ray is the steepest, fastest ray, and leaves the source traveling downward. The second ray is shallower and travels an additional half cycle relative to the first ray, and also leaves the source traveling downward. The third ray travels only slightly shallower than the first ray, and leaves the source traveling upward. The fourth ray is only slightly shallower than the second ray, and leaves the source traveling upward. It is noted that the towed hydrophone array used in the BASSEX experiment has conical ambiguity, and therefore cannot differentiate between upward and downward traveling rays.

Figure 2-2 shows a time front generated using the RAM model to simulate BASSEX data recording *jd264093326Spice*[1] for a range-independent ocean waveguide. The sound velocity profile was an average of XBT casts between the source and receiver and the receiver range was 574 km. The direct path travel time is subtracted from the observed travel time to determine reduced travel time.[2] The fronts are everywhere normal to the rays and identify where and when a pulse can be detected in depth. The upward traveling rays travel normal to fronts with positive slope, and the downward going rays travel normal to fronts with negative slope. The rays which travel the deepest, in the fastest water, arrive first. This figure shows the typical accordion pattern seen in open-ocean time fronts caused by rays becoming progressively shallower in time. The time beyond 4 sec is referred to as the finale region.

[1]Data file labels in the BASSEX data set start with the Julian day, hour, minute, and second the data was recorded (*e.g.* day 264, hour 09, minute 33, second 26), followed by the words "Spice," "Kauai," and "L1000," which indicate which acoustic source transmissions were measured.

[2]Reduced time = travel time - range/sound speed.

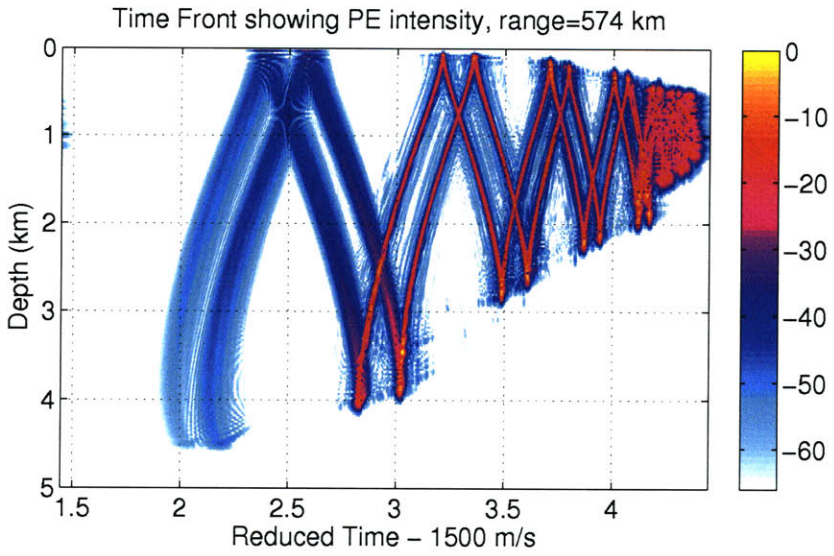

Figure 2-2: Time front generated using the Range-dependent Acoustic Modeler parabolic equation approximation code for BASSEX data recording *jd264093326Spice*. The sound velocity profile was an average of XBT casts between the source and receiver and the receiver range was 574 km. Normalized transmission loss is given in dB.

2.2.2 Seamount Scattering Theory

Seamount bathymetry greatly affects sound propagation through reflection, diffraction, and absorption. A simplified view of seamounts is to treat them as cylindrical objects in the ocean. A plane wave traveling through the ocean is blocked by the seamount, but propagates undisturbed everywhere else. Christian Huygens (1629-1695), the Dutch physicist-astronomer, hypothesized that every point on an advancing wavefront can be treated as a spherically spreading point source in an isotropic medium [32]. In the far-field (radius^2/wavelength), or Fraunhofer Region, beyond the Fresnel distance [33], the perturbation in the acoustic field from the seamount will be small compared with that of the original plane wave.

Figure 2-3 shows the shadow zone of a sphere which, as a gross simplification, has some of the expected features of a seamount shadow zone. Under this assumption, the Poisson Cone begins at 589 km; shown in Fig. 2-3, the Poisson Cone is the region between the deep shadow zone to the Fraunhofer Region. The deep shadow region directly behind the sphere is a region of high transmission loss, the Fresnel/penumbra region is partially shadowed by

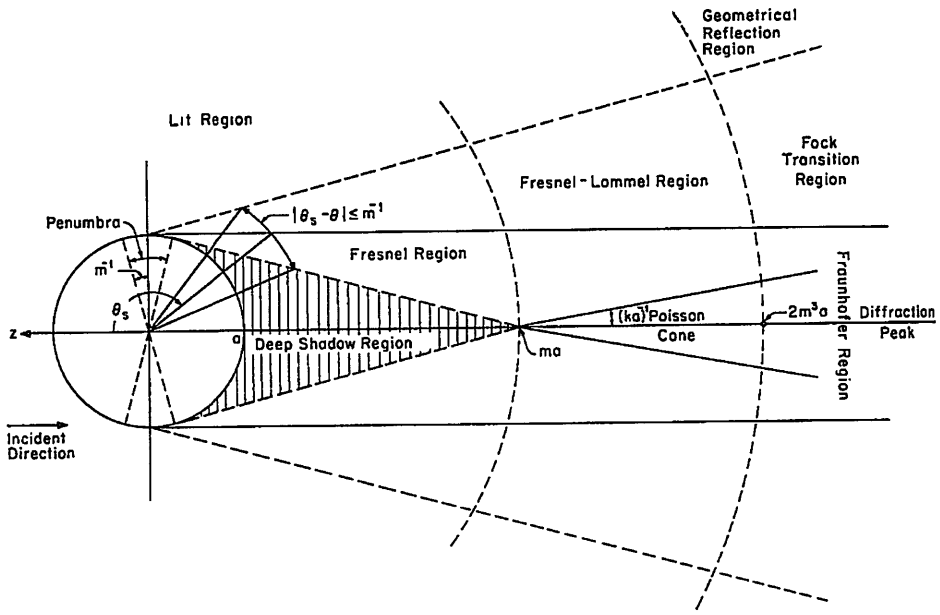

Figure 2-3: Geometrical shadow zone regions for a spherical scatterer, where $ka \gg 1$ and $m = (\frac{1}{2}ka)^{\frac{1}{3}}$, from Sengupta *et al.* [1].

the sphere, and the lit region contains strong direct, open-ocean propagation energy.[3] The deep shadow and penumbra region will be used to define the forward-scattered field of the Kermit-Roosevelt Seamounts in Chapter 6.

Clearly defined convergence zones[4] form due to varying sound velocity. Over long-ranges, convergence zones tend to widen in range, because of differing modal group velocities, and transmission loss becomes fairly uniform with depth; this increases seamount ensonification and thus the scattering effect. At long-range, a subset of higher order modes will "skip" over the seamount undistorted, forming strong refracted convergence zones, and bottom-bounce reflected acoustic energy will create strong reflected convergence zones in the forward-scattered field of a seamount.

Figures 2-4(a) and 2-4(b) show RAM acoustic pressure level results using a canonical model of the measured sound velocity and bathymetry of the Kermit-Roosevelt Seamount, where the source transmits a 250 Hz signal at a depth of 750 m. Figure 2-4(a) shows the acoustic pressure for an absorptive bottom to demonstrate the formation of refracted convergence zones in the forward-scattered field. Figure 2-4(b) shows the difference between

[3]The other regions are not relevant to this thesis, considering the range scale of the BASSEX experiment; the reader is referred to Sengupta *et al.* [1] for a complete description of this figure.

[4]Convergence zones, first reported by Hale [12], are areas of high sound intensity formed by deep diving sound paths, and typically occur every 50 km in the deep ocean.

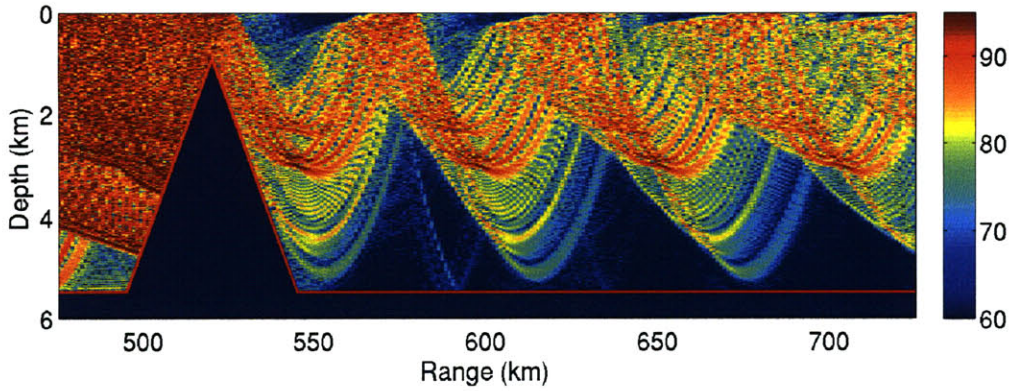

(a) Refracted forward-scattered field.

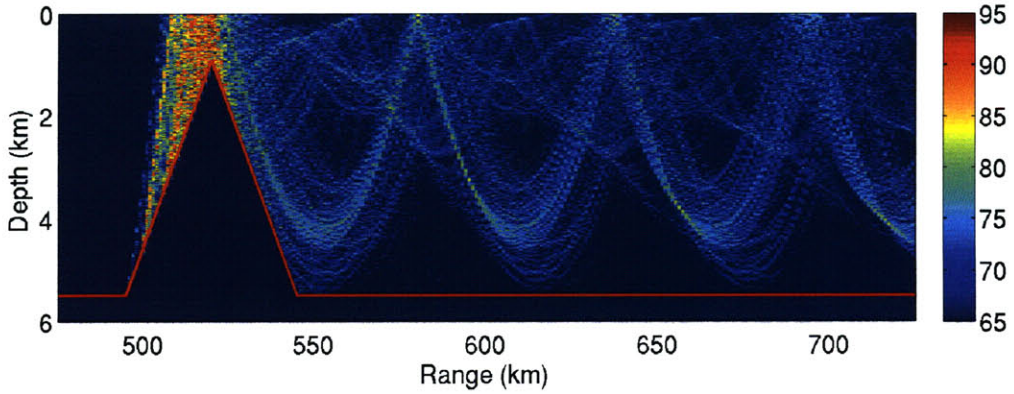

(b) Reflected forward-scattered field.

Figure 2-4: Pressure level, given in dB re 1μPa, inside the forward-scattered field of the Kermit-Roosevelt Seamount. Results are generated using the RAM acoustic code, for a canonical bathymetry and sound velocity models derived from measured data, at 250 Hz. The top plot is generated using an absorptive bottom. The bottom plot is generated by taking the difference of the complex pressure between absorptive bottom and reflective seamount results.

the pressure field for a waveguide with an absorptive bottom and for a waveguide where the right hand side of the seamount is reflective. This figure shows acoustic energy reflected off the left hand side of the seamount inside the forward-scattered field, and demonstrates the formation of significant reflected convergence zones.

Seamount Side Scatter

Munk and Zachariasen [2], in an effort to advance acoustic tomography research, investigated the refraction around islands and seamounts, with an emphasis on the dispersion of sound waves in shallow water. From this paper, and drawing upon equations presented in

Harrison [26], Munk [34] provides the graph in Fig. 2-5 showing horizontal ray paths and phase speed around islands and seamounts. The refractive effects of the seamount decrease with its shoal depth Z_o, but increase with propagation angle, or mode number. The figure shows some horizontal diffraction suggesting acoustic energy will eventually fill-in the shadow zone behind the seamount at long-range. During the BASSEX experiment the conical ambiguity of the hydrophone array made it difficult to separate horizontal diffracted acoustic rays from axial acoustic rays in the forward-scattered field.

2.3 North Pacific Acoustic Laboratory Experiment

The North Pacific Acoustic Laboratory Experiment (NPAL) is an ongoing experiment, funded by ONR, to study sound transmission behavior over long distances in the ocean. After the ATOC demonstration, ONR began sponsorship of NPAL; ATOC showed that a small number of acoustic transmitters and receivers could adequately characterize temperature changes across an entire ocean-basin at ranges of O(5000 km). In 2004, NPAL was funded to conduct the SPICEX, LOAPEX, and BASSEX experiments. All three experiments were coincident upon each other and ran between September and October of 2004.

Two acoustic transceivers were moored prior to the experiments, south of the Kermit-Roosevelt Seamount Complex in the central Pacific Ocean; the Kauai Island, Hawaii acoustic source, moored earlier in support of previously performed experiments, was also utilized. Two automated vertical line arrays (VLA's) were also moored before the experiments. The VLA's were designed to listen to the moored sources and to ship-deployed sources. Tables 2.1-2.3 [5] describe each of the sources used during the experiments [35].

Two ships were used during the experiments, the *R/V Roger Revelle* and the *R/V Melville*. The *R/V Melville* carried an acoustic transceiver; this transceiver was deployed at stations across the Pacific Ocean and transmitted m-sequences, specified in Table 2.2. The *R/V Roger Revelle* towed the FORA hydrophone array, cut for 250 Hz (3 m sensor spacing), and discussed in Section 2.3.6.

[5] Phase modulation angle is chosen such that the processed signal has no self-clutter in the time domain; *i.e.*, $\tan^2\theta_0 = L$, where θ_0 is the phase angle and L is the length of the sequence.

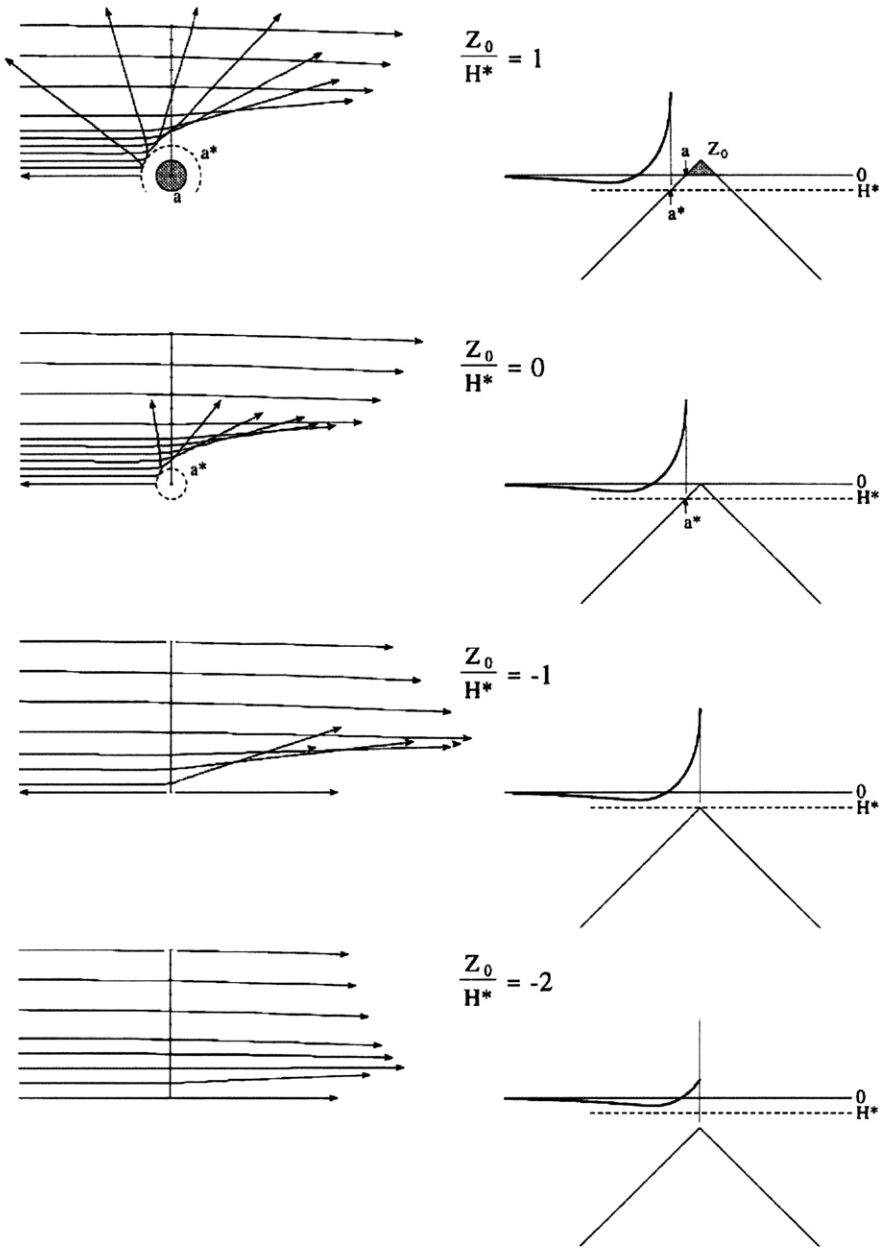

Figure 2-5: Acoustic ray paths (left) by islands and seamounts, and phase speed (right), taken from Ocean Acoustic Tomography, Munk *et al.* [2].

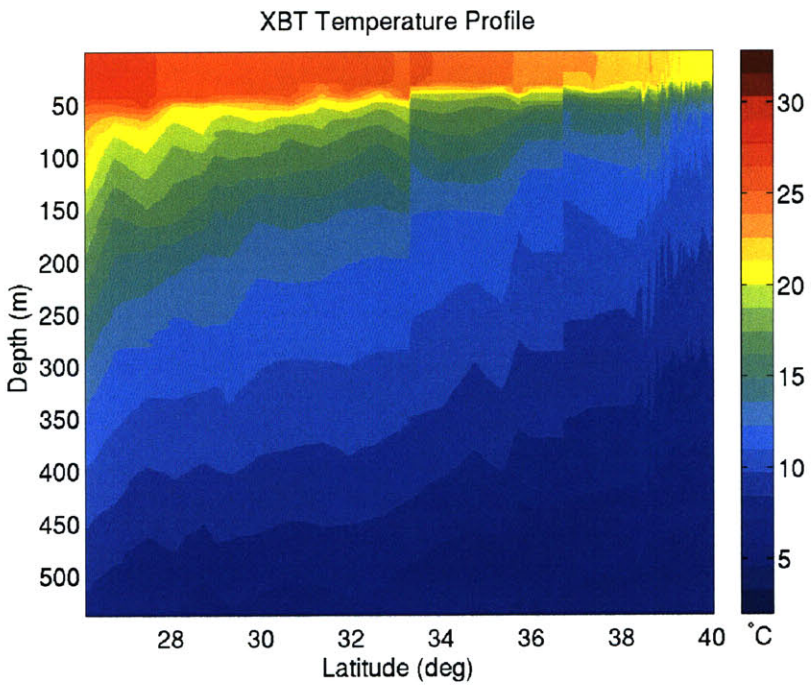

Figure 2-6: Temperature profiles from XBT casts during the BASSEX experiment plotted versus latitude.

2.3.1 SPICE04

The SPICE04 (SPICEX) experiment was designed to measure ocean "spicyness," a term referring to salinity and temperature fluctuations which mimic ocean internal waves; these fluctuations add randomness to the sound velocity profile of the ocean, altering sound paths. SPICEX measured ocean spicyness between the moored sources and VLA's. Figure 2-6 shows an example temperature profile of the Pacific Ocean from data gathered during the NPAL experiment to help understand ocean spicyness.

2.3.2 Long-range Ocean Acoustic Propagation Experiment

The Long-range Ocean Acoustic Propagation Experiment (LOAPEX) was designed to study the evolution of the acoustic arrival pattern with range, understand acoustic energy transmission below critical depth, and observe the effects of bottom interaction on sound propagation. The experiment used the source deployed by the *R/V Melville*, which moved to each station, shown in Fig. 2-7, and transmitted m-sequence signals. VLA's deployed for the SPICEX experiment were also used during the LOAPEX experiment to listen to the signals arriving from the *R/V Melville* and to the source off-shore of Kauai Island.

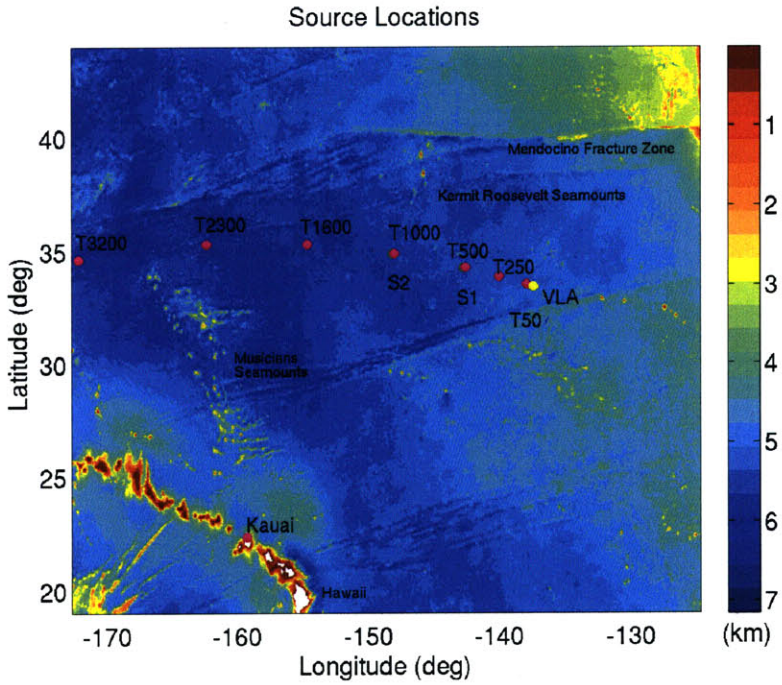

Figure 2-7: Location of sources used in the BASSEX experiment: [S] SPICEX moored source, [T] LOAPEX stations.

Table 2.1: Kauai Source

ATOC/NPAL Kauai Source		
center frequency	75	Hz
cycles/digit	2	
digit length	26.6667	msec
sequence length	1023	digits (degree 10)
sequence period	27.2800	sec
sequence law	3471_8	
artifact location	474	
sequence initialization	1000_8	
phase modulation angle	89.209215°	
sequence repetitions transmitted	44	
transmission duration	1200.3200	sec
source level	195	dB re 1 μPa at 1 m
latitude	22°20.949360'	N
longitude	159°34.195440'	W
depth	811	m
distance to Kermit-Roosevelt Seamount	2,253	km

Table 2.2: LOAPEX Sources

center frequency	68.2	75	Hz
law [octal]	2033	2033	
cycles/digit	2	2	
sequence period	30.0882	27.2800	sec
digits	1023	1023	
phase modulation angle	89.209215°	89.209215°	
source level	194-195	195	dB re 1 μPa at 1 m
depth	350-500	800	m

Transponder	Latitude N	Longitude W	Depth (m)
T50	33°30.8154'N	138°12.5010'W	5176
T250	33°52.1868'N	140°19.3794'W	
T500	34°14.9304'N	142°52.9500'W	5366
T1000	34°51.8502'N	148°16.8078'W	5286
T1600	35°17.1366'N	154°56.9982'W	
T2300	35°18.7638'N	162°38.8782'W	5868
T3200	34°38.9092'N	172°28.3722'W	

Table 2.3: SPICEX Sources

HLF-5 Acoustic Sources		
center frequency	250	Hz
cycles/digit	2	
digit length	12.0000	msec
sequence length	1023	digits (degree 10)
sequence period	12.2760	sec
sequence initialization	1000_8	
phase modulation angle	89.209215°	
sequence repetitions transmitted	11	
transmission duration	135.0360	sec
source level	192	dB re 1 μPa at 1 m
distance to Kermit-Roosevelt Seamount (S1)	616.8	km
distance to Kermit-Roosevelt Seamount (S2)	503.9	km

Source	Sequence Law	Artifact Location	Latitude	Longitude	Depth
S1	2033_8	531	34°16.03'N	143°1.02'W	774 m
S2	3471_8	474	34°53.35'N	148°24.48'W	738 m

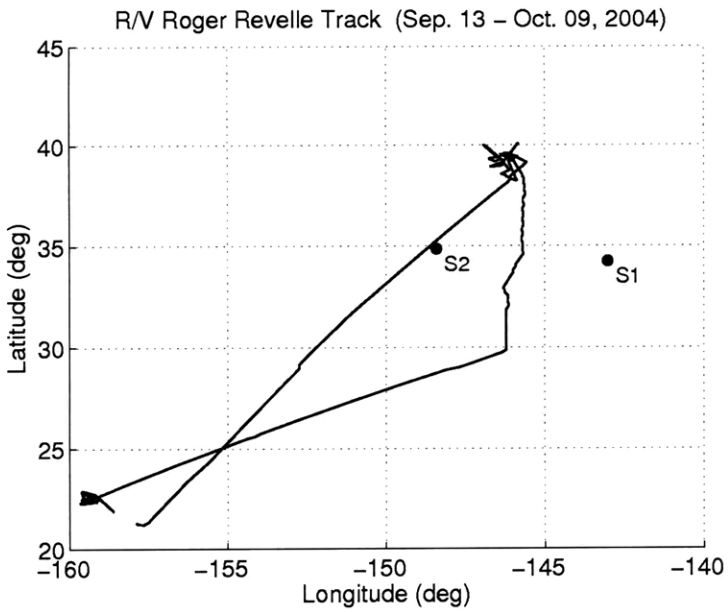

Figure 2-8: Ship track of the *R/V Roger Revelle* during the BASSEX experiment.

2.3.3 BASSEX

Data recorded during the BASSEX experiment included array hydrophone acoustic pressure, multibeam echo sounder bathymetry, and XBT temperature profiles. The array was towed along geodesics which transected the seamounts and the desired sources to measure the length of the perturbation zone behind the seamount. The array was also towed perpendicular to these paths to measure the width of the perturbation zone behind the seamount. Forward scattering was measured by towing the array behind and directly over the seamounts, relative to the source.

Figure 2-8 shows the ship track of the *R/V Roger Revelle* during the BASSEX experiment. Notice the ship traveled along a path which follows the sound path of acoustic waves from source S2 to the Kermit-Seamount Complex at 39 N, 146 W. It will be shown in Chapter 6 that measured acoustic arrival patterns from source S2 are more reconcileable with models than are those from source S1; this is because sound velocity measurements were not gathered near the sound path connecting to source S1.

2.3.4 Bathymetry Data

Bathymetry measurements of a seamount are necessary to facilitate accurate numerical modeling. Current bathymetric databases were reviewed before and during BASSEX, including

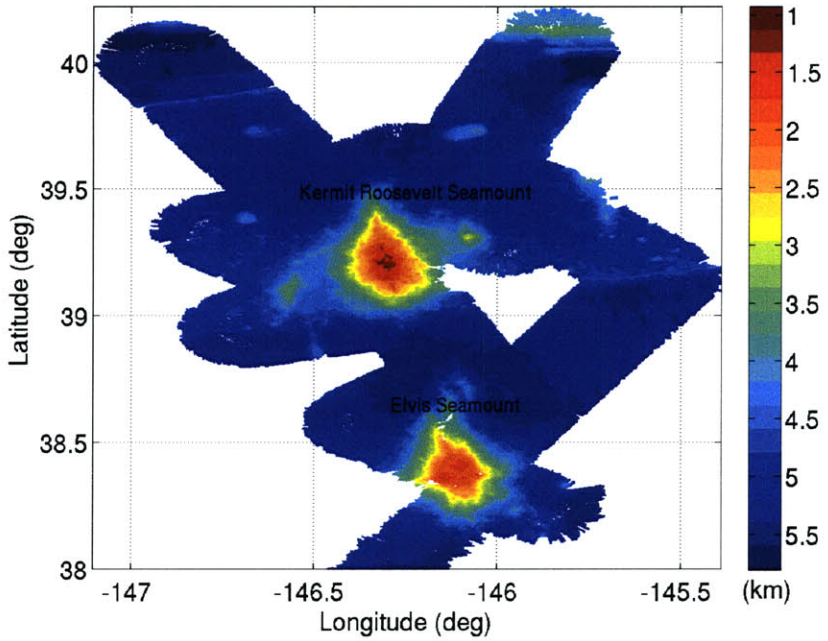

Figure 2-9: A top-down view of raw multibeam bathymetry of the Kermit-Roosevelt Seamount from the sea surface.

the Smith-Sandwell bathymetry database [36], version 8.2, and the General Bathymetry Chart of the Ocean (GEBCO) [37]. Databases were useful as a guide for positioning the array, but the ship's echo sounder revealed significant error in seamount height measurements, justifying bathymetry data collection.

Bathymetry measurements taken during the experiment were made using the *R/V Roger Revelle*'s EM120 Multibeam Swathbathymetry Echo Sounder. The EM120 operates at 12-kHz, uses 191 beams covering up to 150 deg, and has a swath width of about 30 km for a 5 km water depth. An echo sounder works by transmitting a signal and measuring the time it takes to detect an echo. The EM120 uses a flat hydrophone array to measure signals at different angles to obtain a swath bathymetry measurement. Figure 2-9 shows the raw multibeam bathymetry gathered around the Kermit-Roosevelt Seamount Complex, and Fig. 2-10 gives an isometric view.

2.3.5 Expendable Bathythermometers

Temperature, pressure, and salinity affect sound velocity in the water. In the Pacific Ocean during the summer, warm temperatures near the sea surface increase the sound velocity and create a minimum sound speed axis about 700 m deep. Below about 1000 m, temperature

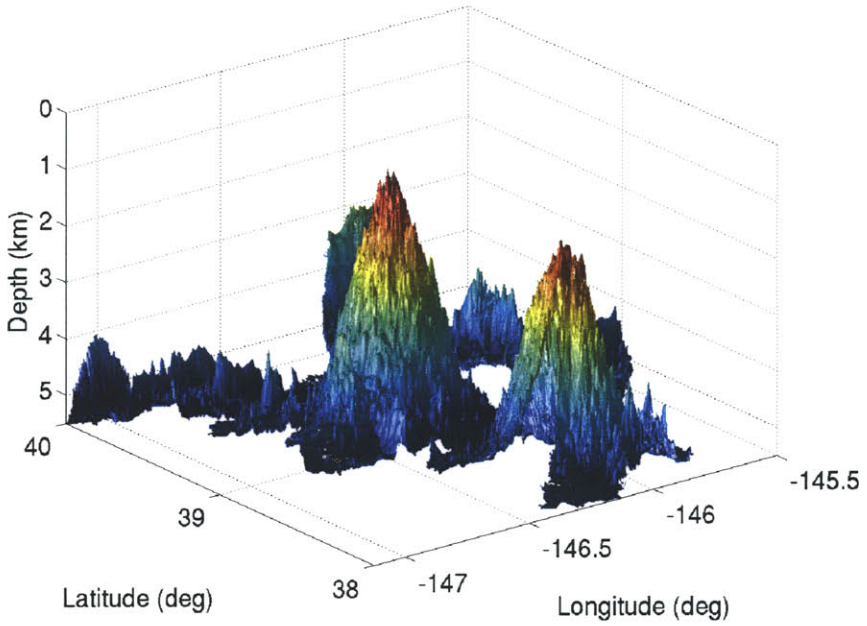

Figure 2-10: An isometric view of multibeam bathymetry of the Kermit-Roosevelt Seamount.

is relatively constant and hydrostatic pressure increases sound velocity linearly with depth. Accurate sound velocity information is necessary over the entire sound path to reconcile experimental results with simulated results.

XBT's are torpedo shaped weights, with a temperature sensor and spool of data transmission wire, which are dropped into water to measure the temperature profile. An XBT was cast every four hours during the BASSEX experiment. Data from XBT casts, as well as salinity data, are used to determine ocean spicyness and the sound velocity profile of the ocean. The relationship between temperature, depth, salinity and sound speed is given by [38]

$$\begin{aligned} c = 1449.2 + 4.6T - 0.055T^2 + 0.00029T^3 \\ +(1.34 - 0.01T)(S - 35) + 0.016z. \end{aligned} \tag{2.2}$$

Sippican T-5 XBT's, capable of $\pm 0.1°C$ and 65 cm accuracy, were used throughout most of the BASSEX experiment to gather temperature data. Figure 2-11(a) shows an example temperature file from a typical XBT cast, and Fig. 2-11(b) shows the sound velocity profile derived from the temperature data.

The Munk sound velocity profile is typically used to model the actual profile of the ocean during the summer. The canonical Munk summer sound velocity profile is given

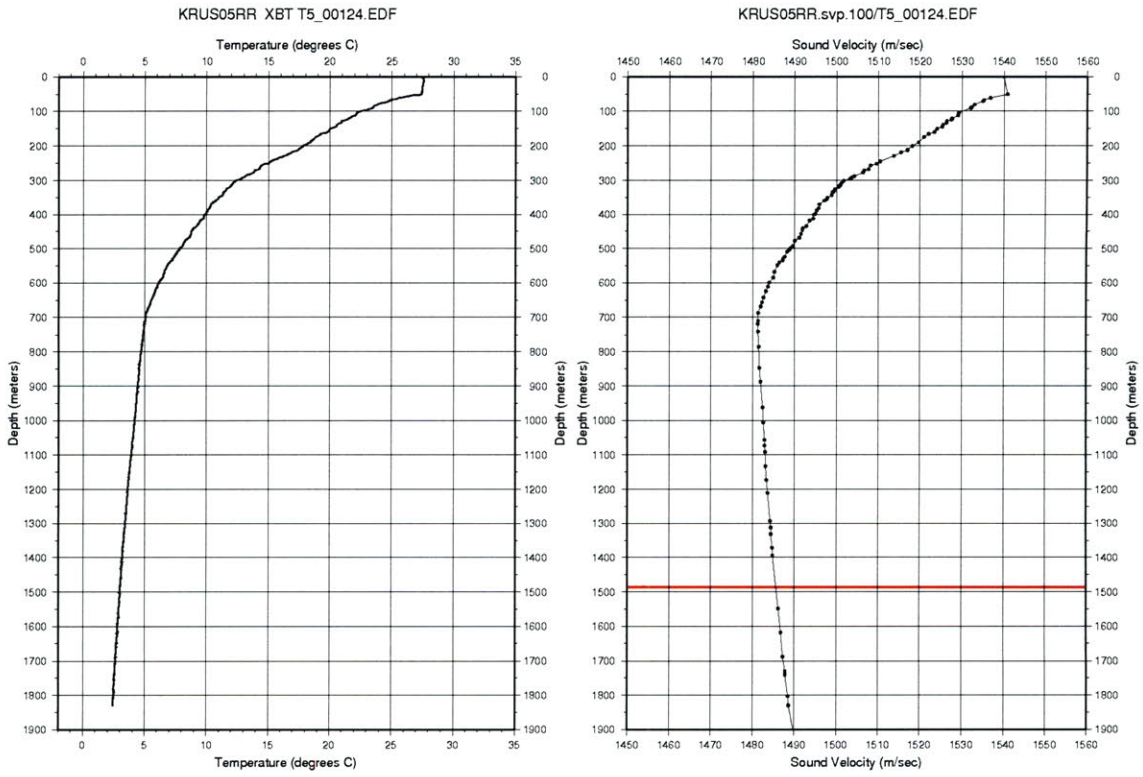

(a) Measured temperature profile.

(b) Sound velocity profile, calculated using the measured temperature profile.

Figure 2-11: Data from XBT cast T5_00124.

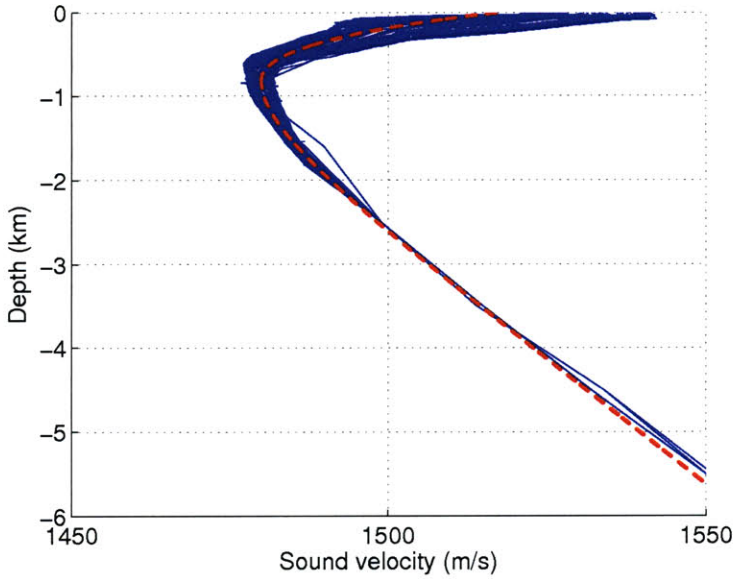

Figure 2-12: BASSEX sound velocity profiles (solid), and Munk summer sound velocity profile (dashed).

by [39]

$$c(z) = c_{min}\left[1 + \epsilon(\eta + e^{-\eta} - 1)\right], \tag{2.3}$$

where

$$\eta = 2(z - c_{axis})/B, \tag{2.4}$$

and B=1.3 km, $\epsilon = 7.4 \times 10^{-3}$ is a perturbation coefficient, c_{min} is the minimum sound speed, and c_{axis} is the sound channel axis depth. Figure 2-12 shows the BASSEX XBT cast sound velocity profiles, and a fitted canonical sound velocity profile derived from Eq. 2.3. Sound velocity above c_{axis} is modeled with $\epsilon = 21.1 \times 10^{-3}$; higher ϵ in the main thermocline indicates a higher temperature gradient than expected.

2.3.6 Five Octave Research Array

The FORA array is a towed 162 element nested hydrophone array developed by Pennsylvania State University and the Chesapeake Science Corporation. Hydrophones are non-linearly spaced to create sub-apertures designated by ultra-low, low, mid, and high frequency bands, corresponding to cut frequencies of 250, 500, 1000, and 2000 Hz respectively. The FORA array has an array gain of approximately 18 dB at 250 Hz and 13 dB at 75 Hz, and

is 32 wavelengths long at 250 Hz. The sampling rate of the array is 6.25 kHz. Non-acoustic sensors (NAS) inside the array measure heading, pitch, roll, depth, and temperature for orientation and positioning. The tow speed of the array was 3-4 knots at a target depth of 300 m throughout the experiment. The tow cable is a 950 m long armored cable containing optical and copper wire for information and power transfer. A drogue was used for drag to ensure proper interelement spacing. Figure 2-13 shows the FORA hydrophone array sensor spacing. The array was operated by a team from Pennsylvania State University, led by Kyle Becker. Becker [14] reported buoyancy issues with the fluid-filled array which were presumed to be addressed before the experiment.

A number of issues have been discovered with the hydrophone array system. An error in the data acquisition system source code introduced a random, uniformly distributed 0-0.25 sec delay, and there was no timestamp available to determine the amount of delay. The data acquisition system suffered from short data drop-outs, due primarily to CPU overusage. A small number of sensors did not function. The array did not appear to be neutrally buoyant, and consistently changed orientation and shape during data recording.

The missing timestamp at the start of each data recording made acoustic ray identification difficult because observed data could not be directly correlated in time with numeric simulations. Data drop-outs associated with CPU overusage increased the sensitivity of the Capon beamformer used to process array data, and was addressed by increasing robustness parameters; the PCML beamformer was applied for recordings with significant data drop-outs. Non-functioning sensors reduced the size of the ultra-low section of the towed array to 63 sensors, which were uniformly spaced; this did not appear to have a significant impact on array performance. Array movement fluctuations resulted in spatial smearing, and beamformer mismatch was addressed by implementing time-varying adaptive filtering algorithms. Processed data were rotated in angle to adjust for the measured pitch and orientation of the array.

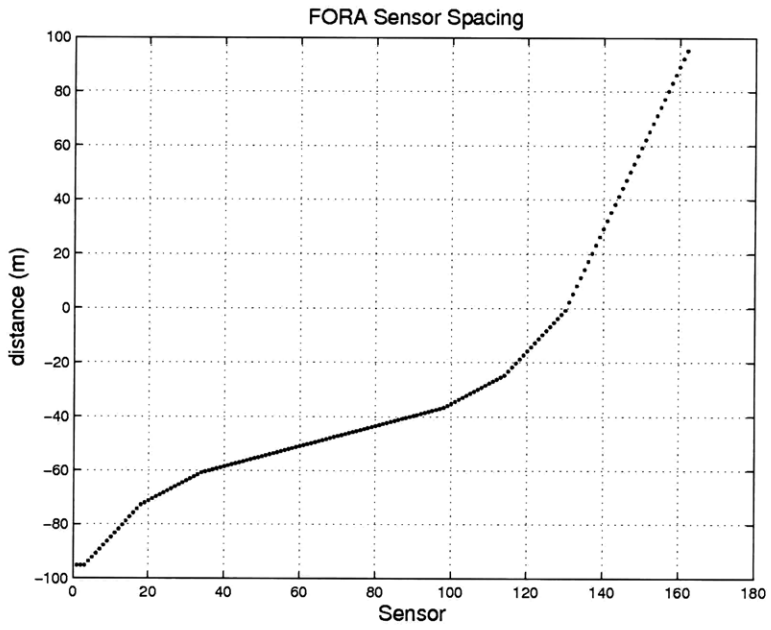

Figure 2-13: Five Octave Research Array hydrophone sensor positions.

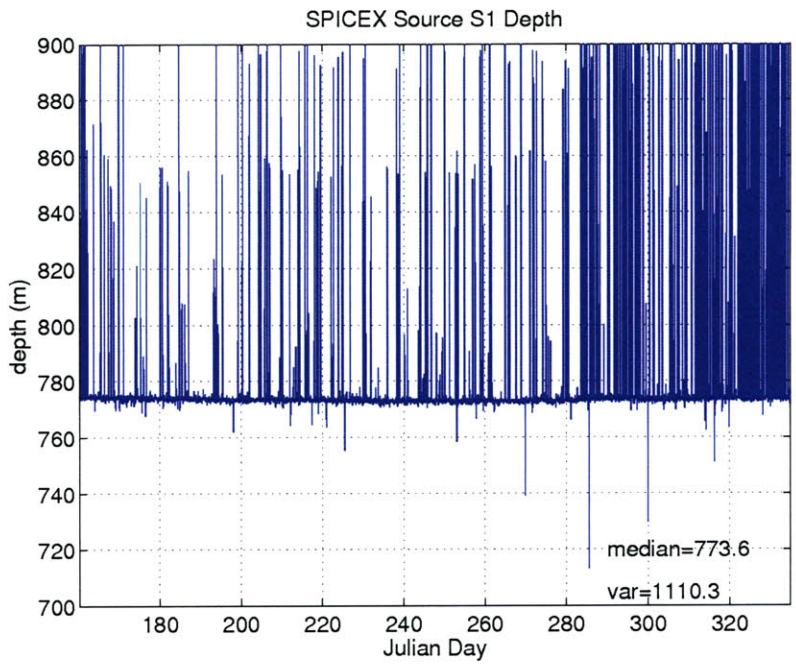

Figure 2-14: SPICEX source depth for source S1.

2.3.7 SPICEX Source Position

The SPICEX sources were tethered to the sea floor throughout the experiment. The sources experienced drift due to ocean current, and acoustic transducers were placed on the sea floor around the sources to measure their position. The difference between the reported and actual source location is accounted for when processing the BASSEX data in order to achieve accurate travel time calculations.

Figures 2-14 and 2-15 show the measured source depth of SPICEX source S1 and S2, respectively. The median source depth for source S1 was 773.6 m, and the median source depth for source S2 was 737.9 m; spikes in depth data are attributed to transducers temporarily losing lock on the source. Variations in source position are attributed to tidal cycles and changing water current in the ocean.

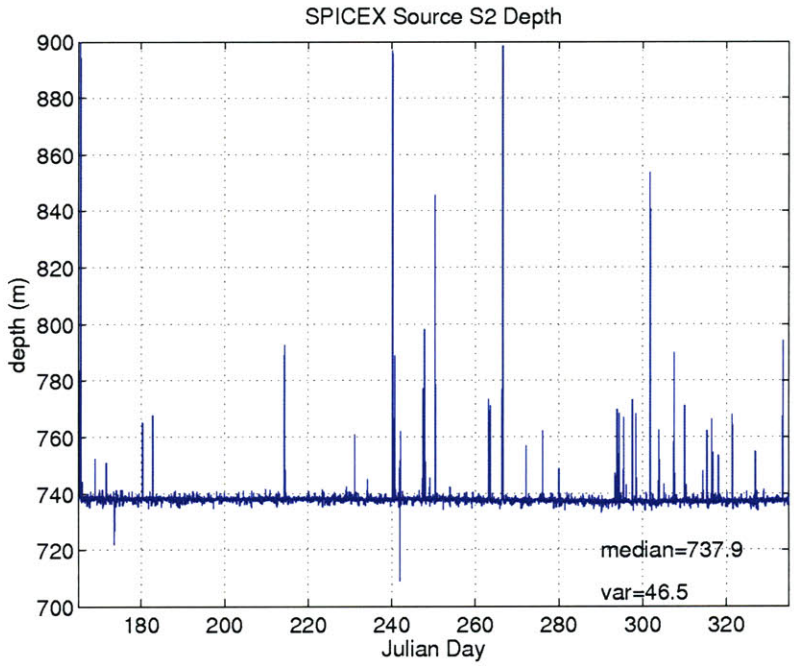

Figure 2-15: SPICEX source depth for source S2.

2.4 Numerical Modeling

Acoustic modeling is a useful tool used to predict how sound propagates in ocean waveguides without the need for costly, time consuming experimentation. Some waveguides have simple solutions and match real world experimental results. Take, for example, a point source in an infinite half space. The solution to the acoustic field can be solved using the Helmholtz equation and the result is exact. Treating complicated range-dependent waveguides has only recently become possible through the use of high performance computer technology.

2.4.1 The Helmholtz Equation

The wave equation, derived from the equations for conservation of mass, Newton's 2^{nd} Law, and the adiabatic equation of state, is the basis for many acoustic models, and is given by

$$\frac{1}{c^2}\frac{\partial^2 p(t,x)}{\partial t^2} = \nabla^2 p(t,x), \tag{2.5}$$

where $p(t,x)$ is pressure in time and space, c is the wave speed of the medium, and ∇^2 is the Laplacian operator. Applying the Fourier transform to the wave equation in the time domain leads to the Helmholtz equation, given by

$$[\nabla^2 + k^2(\mathbf{r})]\psi(r,\omega) = p(\mathbf{r},\omega), \tag{2.6}$$

where $\psi(r,\omega)$ is the displacement potential in range and radial frequency, and $k(\mathbf{r}) = \frac{\omega}{c(\mathbf{r})}$ is the wavenumber. This transformation allows for efficient modeling of narrow-band signals, and is the basis for the wavenumber integration, normal mode, and parabolic equation acoustic modeling techniques. In a homogeneous medium, the solution to the Helmholtz equation is given by

$$\psi(\mathbf{r},\omega) = \begin{cases} (A/r)e^{\jmath \mathbf{kr}} \\ (B/r)e^{\jmath \mathbf{kr}} \end{cases}, \tag{2.7}$$

and is an example of a Green's function consisting of an incoming and outgoing plane wave.

Generating a solution to the Helmholtz equation becomes very difficult as the spatial dimension of the problem increases. Having a depth-dependent sound speed and a changing bathymetry add two dimensions to the problem, and makes finding an exact, analytic solution nearly impossible for most cases. One approach used to work around this problem

is to divide a continuously varying waveguide into finite regions, inside which the exact, or an approximate, solution to the acoustic field can be generated. The solution in each region is then coupled with the solutions in adjacent regions and propagated throughout the waveguide. This is typically referred to as the finite element approach.

2.4.2 Ray Tracing

Ray tracing is a modeling technique which assumes the solution to the acoustic field is the sum of an infinite number of ray paths, along which sound travels, which vary in amplitude and phase. This technique is fast and can provide great insight into long-range acoustic propagation problems. There is some debate over the ability of ray tracers to handle bottom interaction accurately, which this thesis will help resolve.

Ray tracers seek a solution to the Helmholtz equation for a point source at location $\mathbf{x}_s$, given by

$$\nabla^2 p + \frac{\omega^2}{c^2(\mathbf{x})} p = -\delta(\mathbf{x} - \mathbf{x}_s), \tag{2.8}$$

in ray series form, given by

$$p(\mathbf{x}) = e^{i\omega\tau(\mathbf{x})} \sum_{n=0}^{\infty} \frac{A_n(\mathbf{x})}{(i\omega)^n}, \tag{2.9}$$

where $\tau(\mathbf{x})$ is the travel time along a wavefront at position $\mathbf{x}$. When Eq. 2.9 is applied, the first term in Eq. 2.8 can be expressed as

$$\nabla^2 p = e^{\imath\omega\tau} \left\{ [-\omega^2 |\nabla^2 \tau|^2 + i\omega \nabla^2 \tau] \sum_{n=0}^{\infty} \frac{A_n}{(i\omega)^n} + 2i\omega \nabla\tau \cdot \sum_{n=0}^{\infty} \frac{\nabla A_n}{(i\omega)^n} + \sum_{n=0}^{\infty} \frac{\nabla^2 A_n}{(i\omega)^n} \right\}. \tag{2.10}$$

Equations 2.9 and 2.10 can be substituted back into the Helmholtz equation. Separating terms of the same order ω gives the following eikonal equation, of $O(\omega^2)$, and lower order transport equations:

$$\begin{aligned} O(\omega^2) \quad &: \quad |\nabla\tau|^2 = c^{-2}(\mathbf{x}), \\ O(\omega) \quad &: \quad 2\nabla\tau \cdot \nabla A_0 + (\nabla^2\tau) A_0 = 0, \\ O(\omega^{1-n}) \quad &: \quad 2\nabla\tau \cdot \nabla A_n + (\nabla^2\tau) A_0 = -\nabla^2 A_{n-1}, \quad n = 1, 2, \ldots \end{aligned} \tag{2.11}$$

Ray trajectories can be computed by solving the eikonal equation, and ray amplitude can be computed with the first transport equation.[6] Figure 2-16 shows the ray paths generated

[6] Chapter 3 of Jensen *et al.* [16] discusses and solves the transport equations.

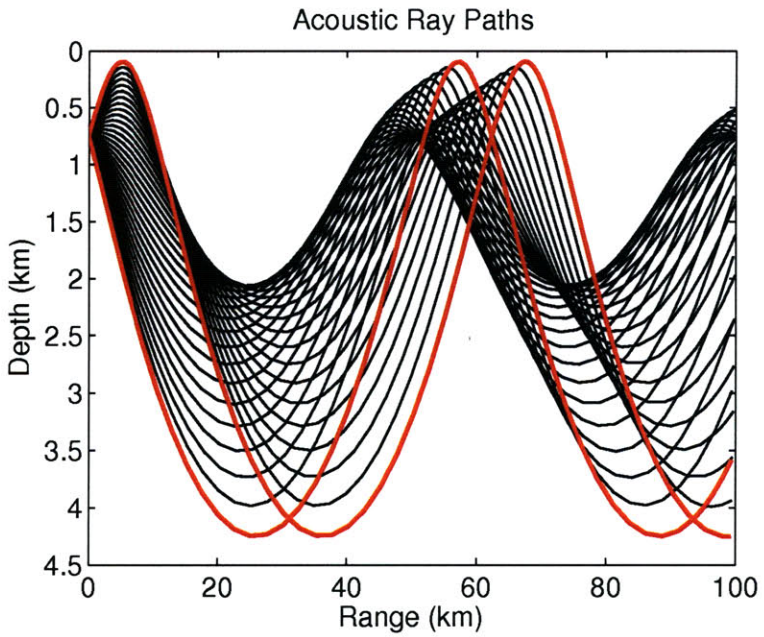

Figure 2-16: Ray paths radiating from a point source at 750 m below sea level with a sound channel axis at 1000 m. The red paths show the upward and downward 12 deg ray path.

with this method for a point source 750 m below sea level with a sound channel axis at 1000 m.[7] Only rays leaving the source at an absolute angle less than 12 deg are plotted. Note the convergence and shadow zones that form as a result of the non-uniform sound velocity profile of the ocean. In this example, the limiting rays are defined as the rays which form the boundary between the convergence and shadow zones. Eigenrays are rays which connect a source and receiver.

The Ocean Acoustical Ray-Tracing Software, or RAY, program, written in 1992 by James Bowlin *et al.* [17] for the Woods Hole Oceanographic Institution, is used to reconcile data from the BASSEX experiment. The RAY program is a ray tracer code that can handle range-varying sound velocity profiles and bathymetry. Most notably, the RAY code smooths sound velocity and bathymetry data between samples to eliminate false turning point caustics.

2.4.3 The Parabolic Equation Approximation

Parabolic equation methods use an approximation to the Helmholtz equation to dramatically improve computational efficiency. There are a variety of approximation techniques

[7]The ray trace code used to generate this figure was the version used in Jensen *et al.* [16].

available, including the Clarbout and Padé approximation, which affect the accuracy of the parabolic equation acoustic modelers.

The parabolic equation approximation method starts with the Helmholtz equation for an isotropic-density medium, in cylindrical coordinates, given by

$$\frac{\partial^2 p(r,z)}{\partial r^2} + \frac{1}{r}\frac{\partial p(r,z)}{\partial r} + \frac{\partial^2 p(r,z)}{\partial z^2} + k_0^2 n^2 p(r,z) = 0, \tag{2.12}$$

where $k_0 = \omega/c_0$ is the wavenumber and $n(r,z) = c_0/c(r,z)$ is the index of refraction. Assuming the solution is of the form

$$p(r,z) = \psi(r,z) H_0^{(1)}(k_0 r), \tag{2.13}$$

and applying the asymptotic approximation for $k_0 r \gg 1$, given by

$$H_0^{(1)}(k_0 r) \simeq \sqrt{\frac{2}{\pi k_0 r}} e^{i(k_0 r - \frac{\pi}{4})}, \tag{2.14}$$

and applying the paraxial approximation, the standard parabolic equation is given by

$$2ik_0\frac{\partial \psi}{\partial r} + \frac{\partial^2 \psi}{\partial z^2} + k_0^2(n^2 - 1)\psi = 0, \tag{2.15}$$

which can be reduced to

$$\frac{\partial \psi}{\partial r} = ik_0\left(\sqrt{n^2 + \frac{1}{k_0^2}\frac{\partial^2}{\partial z^2}} - 1\right)\psi. \tag{2.16}$$

Equation 2.16 is exact within the limits of the far-field approximation, and is the basis for many of the parabolic approximation methods available.

The current research supporting this thesis uses the Range-dependent Acoustic Modeler, or RAM, written by Michael Collins, of the Office of Naval Research (ONR), for use by the Navy. RAM uses the split-step Padé approximation; Collins *et al.* [18], [19] presents a split-step Padé method which gives high numerical accuracy and efficiency in range-dependent waveguides as compared with other parabolic approximation methods, addressing the issues presented by McDaniel [40]. The split-step Padé approximation solves Eq. 2.16 in range-

dependent waveguides using the update equation

$$p(r+\Delta r, z) = \exp(ik_0\Delta r)\left(1+\sum_{j=1}^{n}\frac{\gamma_{j,n}X}{1+\beta_{j,n}X}\right)p(r,z), \tag{2.17}$$

where X is related to the term under the square-root in Eq. 2.16; the scalar terms $\alpha_{j,n}$ and $\gamma_{j,n}$ can be solved using parallel processors to improve computational efficiency.

2.5 Summary

This chapter provided a brief review of previous work regarding seamount scattering, provided known underwater acoustic propagation theory, explained the BASSEX experiment, and explained computational acoustic modeling techniques used in this thesis. The next chapter will discuss the methods utilized to process data from the BASSEX experiment.

Chapter 3

Observational Methods

Both hydrophone array data and non-acoustic sensor data are utilized to measure direction-of-arrival (DOA), signal strength, and travel time of acoustic rays. The challenges of obtaining high SNR results include removing the effects of Doppler shift, array motion, noise, and data acquisition errors. This chapter develops the methods used to analyze and process data from the BASSEX experiment.

Munk *et al.* [34] motivates the use of broadband signals to measure the impulse response of the ocean over long-range. Data processing and analysis concepts presented in this chapter include the sonar equation, transmission loss, pulse compression, travel time, Doppler shift, positioning, and timekeeping. Section 3.1 presents equations for determining the expected signal pressure levels. Section 3.2 motivates the use of matched filtering to separate signals in time and space. Section 3.3 reviews the ambiguity function of the m-sequence signals used in the BASSEX experiment. Section 3.4 discusses the effect of Doppler shift, and a method to remove it. Section 3.5 presents the methods used to determine and correct for the position and orientation of the hydrophone array. Section 3.6 discusses timekeeping and provides the clock drift corrections and the position time corrections for the SPICEX sources used in the BASSEX experiment.

3.1 The Sonar Equation

During the BASSEX experiment, SPICEX sources were located in the Pacific Ocean between 400-800 km from the receiver. M-sequence signals were transmitted which had 83.3 Hz bandwidth and 11 periods of 1023 bit length. This section will determine the expected

SNR and signal strength at the receiver using this information; these parameters are useful for verifying measured data.

The sonar (sound navigation and ranging) equation is used to determine the SNR between a source and receiver. Units are generally given in decibels (dB). The sonar equation, which accounts for most of the mechanisms which affect SNR in the open-ocean, is given by

$$SNR = SL - TL - (NL - AG) \quad \text{dB}, \tag{3.1}$$

where SL is the source level, TL is transmission loss, NL is noise level, and AG is array gain[1]. The SPICEX sources have a signal root-mean-square (rms) pressure strength of SL = 192 dB re 1μPa at 1 m.[2]

3.1.1 Attenuation

Transmission loss in the ocean is generally separated into attenuation and geometric spreading terms. The attenuation term accounts for energy loss in the form of thermal energy, mostly due to boric acid and magnesium sulfate relaxation. The attenuation, for frequencies below 8 kHz at the sound-channel axis depth, is given by

$$\alpha(f) = 0.79A\frac{f^2}{(0.8)^2 + f^2} + \frac{36f^2}{5000 + f^2} \quad \text{dB/km}. \tag{3.2}$$

Attenuation increases monotonically with frequency; this is one of the motivating factors for using signals bandlimited below 300 Hz in the BASSEX experiment.

3.1.2 Geometrical Spreading

The geometrical spreading term accounts for transmission loss incurred by the expansion of the surface of the acoustic wavefront as it travels through the ocean. At short-ranges, spherical spreading can be used to model loss. The transmission loss from spherical spreading is given by

$$TL_s = 10\log_{10}[I(r_0)/I(r)] = 20\log_{10}(r/r_0) \quad \text{dB}, \tag{3.3}$$

where $I(r)$ is acoustic intensity, r is range, and r_0 is the initial range. Given the ducted nature of the ocean, cylindrical spreading is more commonly used to model transmission

[1] Array gain will be discussed in Chapter 4.

[2] It is important to always provide the pressure reference to avoid miscommunication.

loss. For long-range problems, the geometric spreading loss term is either neglected or cut-off at some distance r_1 away from the source (this thesis uses 5 km). Cylindrical spreading loss is given by

$$TL_c = 10\log_{10}(r/r_1), \tag{3.4}$$

and the combined spherical and cylindrical spreading transmission loss is given by

$$TL_g = 20\log_{10}(r_1/r_0) + 10\log_{10}(r/r_1) \text{ dB}. \tag{3.5}$$

3.1.3 Noise Level

Noise sources which contribute to the ocean's ambient acoustic noise field include shipping traffic, breaking waves, cavitation, and surface waves, drawing upon work presented by Wenz [3]. Figure 3-1 offers a summary of the different source contributions to the ambient noise field in the ocean. Throughout the BASSEX experiment acoustic noise from the tow ship, especially propeller and engine noise, was audible around 70 dB re 1μPa. Discrete and spatially spread interferences can degrade matched filter performance significantly when SNR is low, especially in seamount shadow zones. The presence of strong noise in the data, including interfering m-sequence signals, motivates the use of adaptive beamforming algorithms prior to pulse compression.

In reference to the sonar equation, the NL term is generally given in terms of dB re $1\mu\text{Pa}/\sqrt{\text{Hz}}$; $\sqrt{\text{Hz}}$ is used because spectral noise is given in terms of $(\mu\text{Pa})^2/\text{Hz}$. The NL term can be derived from tables and graphs found in many references, including Urick [41].

3.2 Pulse Compression

Acoustic time series are matched filtered to measure signal amplitude and travel time. The matched filter maximizes the SNR under the assumptions that the ocean is a linear time-invariant system, ray paths are linear and non-dispersive, and noise is Gaussian; see Appendix B.

The sources in the BASSEX experiment transmitted 11 period binary m-sequences, each of sample length 1023; binary sequences consist of ± 1 amplitude square waves. Assuming phase coherence, the processing gain for each period is $10\log_{10} 1023 = 30.1$ dB. For a moving receiver, phase coherence can be achieved between periods using Doppler shift correction.

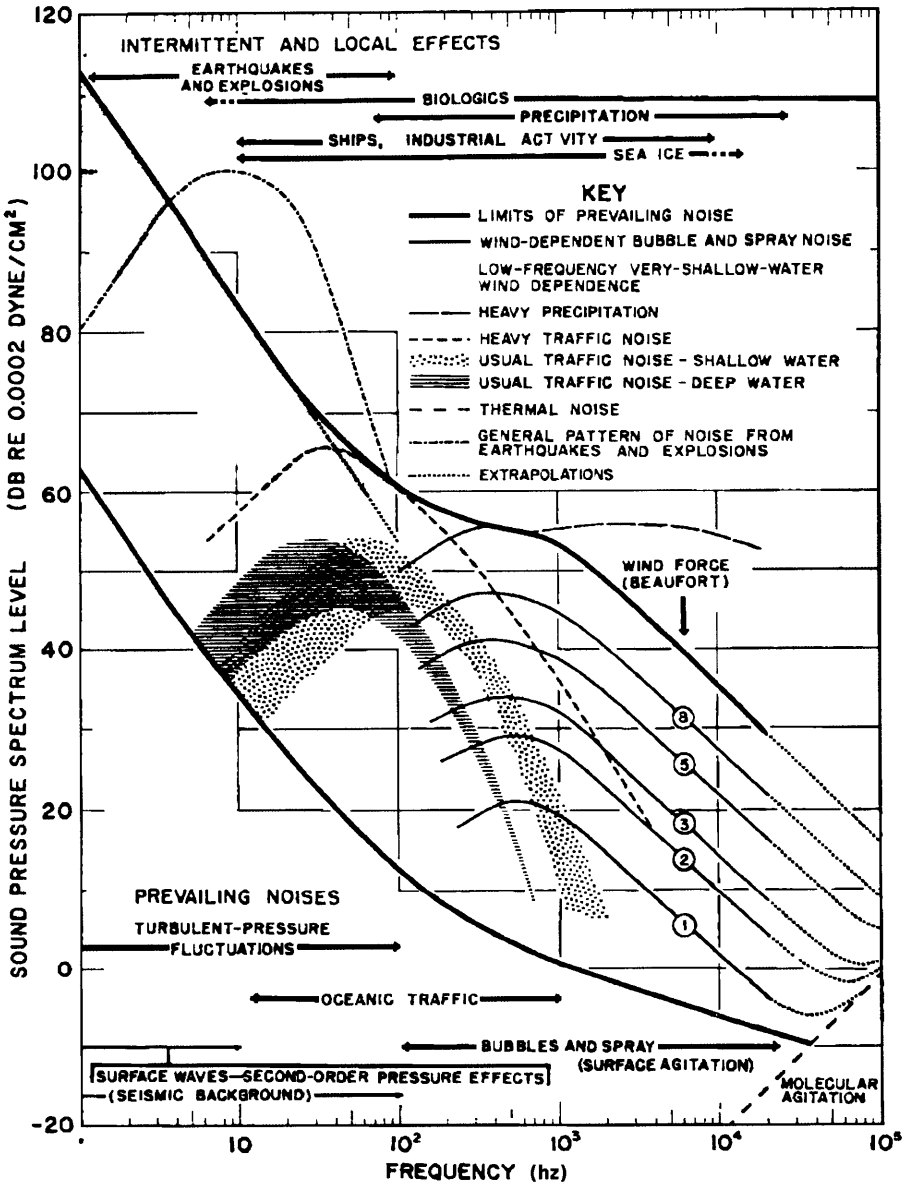

Figure 3-1: Summary of the ambient noise field in the open ocean, taken from Wenz [3].

Table 3.1: Transmission Loss and SNR at 250 Hz in the Pacific Ocean

	500 km	1000 km	
Source level (rms)	192	192	dB re 1μPa at 1m
Spreading Loss (cylindrical)	-94	-97	dB
Volume attenuation (0.00432 dB/km)	-2.16	-4.32	dB
Received signal level	98	95	dB
Noise (1 Hz band)	68	68	dB re 1μPa/$\sqrt{Hz}$
Bandwidth (83.3 Hz)	19.21	19.21	dB re 1 Hz
Total noise level	87.2	87.2	dB re 1μPa
Broadband SNR (before processing)	10.8	7.8	dB
Pulse compression gain (1023)	30.1	30.1	dB
Total signal processing gain	30.1	30.1	dB
Single hydrophone SNR	40.9	37.8	dB

Unfortunately, phase coherence was not observed in the BASSEX data between periods; therefore, incoherent period averaging was used to increase SNR.

3.2.1 Transmission Loss

Table 3.1 provides the estimated hydrophone SNR at both 500 km and 1 Mm, given typical Pacific Ocean characteristics and spreading loss. Ideally, the SNR should be at least 20 dB for good signal detection, and this is indeed the case for open-ocean propagation at these ranges. These results will be helpful in Chapter 6 to verify acoustic data pressure and SNR levels in the BASSEX data set.

3.3 Ambiguity Function

The ambiguity function is a commonly used tool in sonar and radar system signal design to determine travel time and Doppler resolution. For the transmitted signal $s(t)$, the ambiguity function is given by

$$\phi(\Delta_T, \Delta_{f_d}) = \int_{-\infty}^{\infty} s(t)s^*(t-\Delta_T)e^{-\jmath 2\pi \Delta_{f_d} t}dt, \tag{3.6}$$

where Δ_T is the change in travel time and Δ_{f_d} is Doppler shift. Using the convolution identity property of the Fourier Transform, Eq. 3.6 can be expressed in the frequency

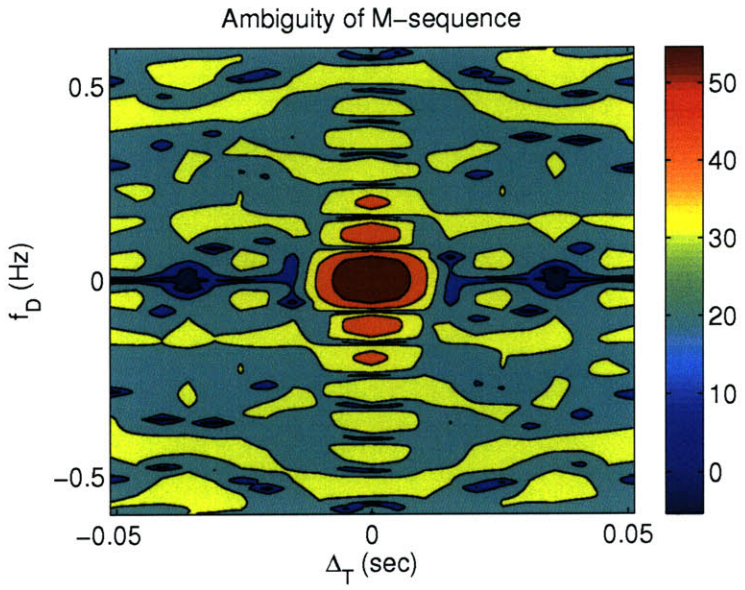

Figure 3-2: Ambiguity of m-sequence signals used in the BASSEX experiment.

domain as

$$\phi(\Delta_T, \Delta_{f_d}) = S(f)S^*(f + \Delta_{f_d})e^{-j2\pi f \Delta_T}. \tag{3.7}$$

Figure 3-2 shows the ambiguity function of the m-sequences used in the BASSEX experiment. The figure shows that the signal has approximately $O(0.01$ sec) time resolution and $O(0.1$ Hz) Doppler resolution. The signal has significant sidelobes in the Doppler direction approximately 13 dB below the peak level; fortunately in the BASSEX experiment, Doppler resolution is less important that temporal resolution.

3.4 Doppler Shift

Doppler shift is a phenomenon by which a relative velocity between a transmitter and receiver causes a signal's apparent frequency to shift. The amount of Doppler shift is given by

$$\Delta f = f\frac{v}{c}, \tag{3.8}$$

where v is relative speed, and c is the wave speed of the medium. For moving towed hydrophone array time series, the Doppler shift must be removed to achieve the highest processing gain.

The Doppler shift of the BASSEX hydrophone data is determined from the acoustic

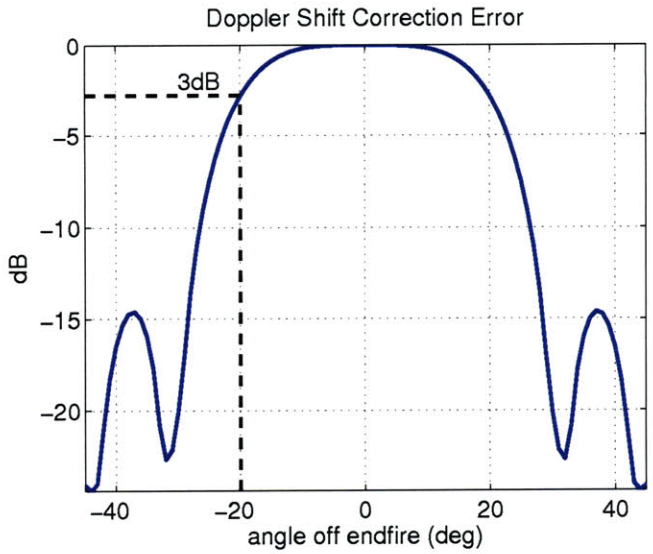

Figure 3-3: Attenuation caused by Doppler shift mismatch.

pressure time series. The signals are matched filtered with time dilated reference signals[3], to determine the most likely Doppler shift.

The relative speed of the array is not only affected by the speed of the tow ship, but by the orientation of the array relative to the source; signals which arrive near endfire have the highest Doppler shift, and signals which arrive near broadside have the lowest. Figure 3-3 shows the correlation of an m-sequence signal at endfire with signals arriving off-endfire, where the array is traveling at 3.5 m/s. The figure shows that signals below 20 deg are attenuated by less than 3 dB; therefore, only a single Doppler shift correction is necessary as most acoustic rays arrive below 20 deg for endfire SPICEX receptions.

3.5 Array Position and Orientation

The exact position and orientation of the hydrophone array is required to accurately measure travel time and arrival angle of acoustic rays in the BASSEX data. The FORA array is equipped with three NAS sensors which take measurements including magnetic heading, pitch, and depth. One NAS sensor is located at the bow of the array and another is located at 108.5 m, towards the middle of the array.[4] The tow distance of the array behind the ship

[3]The time dilated signals are created by interpolating the reference signal onto either an expanded or compressed time axis.

[4]The third NAS sensor was not used in the analysis presented in this thesis, because it is part of a cardioid section of the FORA array which was not utilized in the BASSEX experiment.

was approximately 981 m. GPS data gathered at the stern of the ship is used to determine the coordinates of the array and make clock corrections.

3.5.1 Angle Rotation

The heading and pitch of the FORA array used in the BASSEX experiment were often off target. To adequately reconcile pulse compressed data with simulated results, a geometrical rotation is applied to correct for the array orientation. Appendix C presents the mathematical approach used to determine the angle correction for each beam.

The direction of the array towards the source and the pitch of the array are used to correct the measured arrival angles of acoustic rays. The heading toward the source is determined using the GPS location of the ship and source and the WGS 1984 ellipsoid model of the Earth. The array heading is averaged between the two NAS magnetic sensors inside the array; magnetic declination was 15.3° E (National Geophysical Data Center [42]). Array pitch is determined using the difference in depth measurements taken with the NAS sensor units, assuming the array depth is linear between the sensors.

3.6 Timekeeping

Timekeeping involves removing the timing errors caused by clock and mooring drift.

3.6.1 Clock Drift

All clocks experience drift over time, so it is important to keep source and receiver clocks synchronized. On-board GPS receivers are used to correct shipboard data acquisition system clocks to $O(1\ \mu\text{sec})$ accuracy. SPICEX sources were equipped with rubidium frequency clocks which have $O(1\ \text{msec})$ accuracy; these sources were moored underwater, and could not receive GPS clock corrections.[5] Clock drift was determined after the sources were retrieved using the measured error and assuming a linear drift over time. Figures 3-4 and 3-5 show the clock drift throughout the experiment. The clock drift is relatively constant for both SPICEX sources, and in both cases must be removed to accurately compute travel time to $O(0.01\ \text{sec})$.

[5]The SPICEX sources transmitted signals at pre-programmed times.

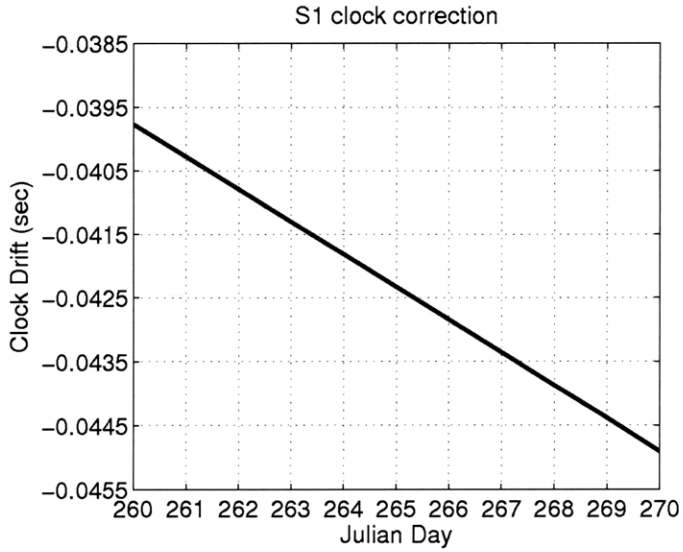

Figure 3-4: SPICEX source S1 clock drift during the BASSEX experiment.

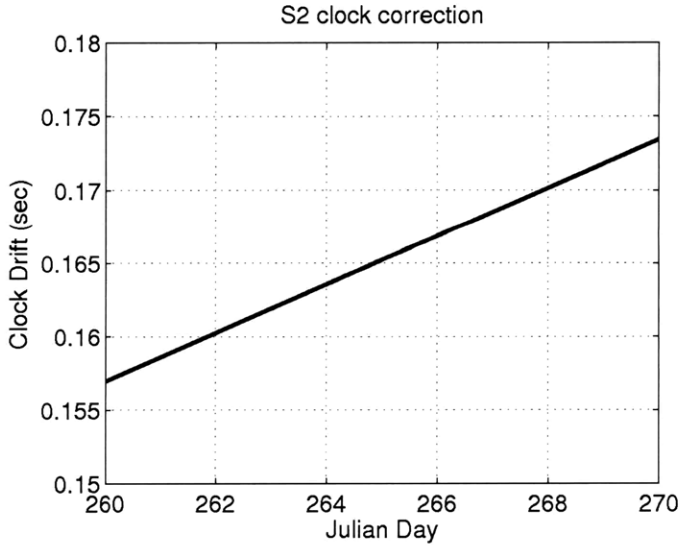

Figure 3-5: SPICEX source S2 clock drift during the BASSEX experiment.

3.6.2 Mooring Correction

Measuring acoustic signal travel time requires an accurate knowledge of source and receiver location. In water, which has an approximate sound speed of 1500 m/s, this implies that these locations must be known to better that 15 m to ensure $O(0.01$ sec) travel time measurement accuracy.

During the BASSEX experiment, ship location was determined using GPS data which, because of receiver motion due to waves and lack of WAAS information, has a position error of $O(10$ m). The LOAPEX source used in the BASSEX experiment was a ship deployed source which also used GPS data to position the array. Acoustic transducers placed around the sources were used to determine the location of the source during the experiment.

Figure 3-6 shows the difference in path length to the Kermit Roosevelt Seamount between that of the nominal source locations and that of the source locations perturbed by changing water currents, and also shows the power spectrum of the source positions over the duration of the experiment generated using the periodogram averaging method described in Welch [43], with a 60-length Hamming window, where position is sampled 24 times per day. The path length difference is computed by taking the cosine of the angle between the geodesic to the receiver from the reported source location and the measured position of the source, and multiplying that by the magnitude of the measured source position relative to the reported position. The effect of mooring motion is usually less than 50 m, resulting in travel time errors of 0-0.03 sec. Fluctuations in the source position correction appear strongly correlated with the tidal cycle, and spikes are clearly visible in the horizontal position power spectra for both sources at the diurnal tidal frequency, which is 1.93 cycles/day.

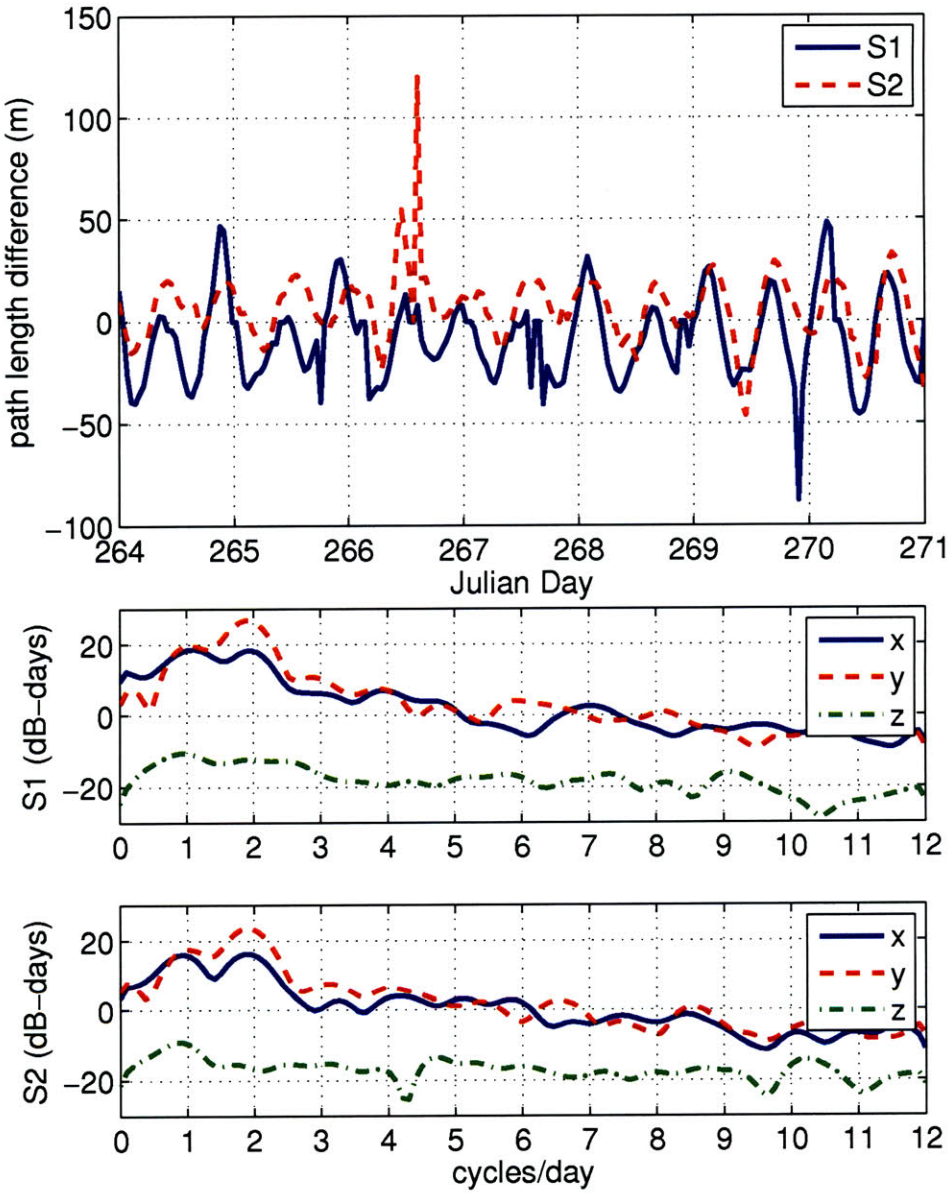

Figure 3-6: SPICEX source position (top) path length difference and the power spectrum of source (middle) S1 and (bottom) S2 in x-y (north-south) and z (depth) coordinates.

3.7 Summary

This chapter discussed the characteristics of the BASSEX experiment relating to measured amplitude and travel time accuracy. The expected SNR, after data processing, is determined to be about 40.9 dB for flat-bottom acoustic transmission for a distance of 500 km; this range is on the order of the sound paths investigated later in this thesis. The expected travel time accuracy, after data processing, is determined to be $O(0.02$ sec); however, there is also data acquisition system (DAQ) random start time error, which introduces timing errors of $O(0.25$ sec).

Ambient noise sources and interfering m-sequence signals decrease the SNR of received hydrophone array time series. The next chapter will discuss array processing methods with which to suppress plane wave interference and measure the DOA of acoustic rays.

Chapter 4

Array Processing Methods

Measurement of acoustic ray angle-of-arrival is necessary to investigate the effects of modal coupling in the scattered field of a seamount. Array processing techniques are applied to the FORA array time series to measure angle-of-arrival. Adaptive array processing techniques are used to improve array resolution and increase SNR to improve signal detection and estimation.

This chapter will briefly discuss some of the beamforming techniques which were applied to the data supporting this thesis. Section 4.1 will discuss the conventional beamformer and provide metrics used to characterize beamformer performance. Section 4.2 presents the Capon minimum variance and minimum power distortionless response beamformers. Section 4.3 motivates the use of time-varying adaptive filters. Section 4.4 introduces the correlation matrix distance metric as a means of choosing an adequate filter update period and training time. Section 4.5 describes the data processing algorithm used to process the data from the BASSEX experiment, including beamformer parameters.

4.1 Frequency Domain Array Steering

Array steering, or beamforming, is the process of weighting sensor outputs with gain and phase such that the sum of their outputs add constructively for a plane wave arriving at some desired direction. This section will present the nomenclature needed to understand the implementation and performance of the conventional beamformer and adaptive beamformers presented later on. For simplicity, only linear hydrophone arrays will be considered in this chapter.

4.1.1 Conventional Beamforming

Consider the narrow-band plane wave signal of interest $f(\omega t - \mathbf{k}^T\mathbf{x})$ traveling at some speed c and impinging upon an array at some angle θ. The travel time of the wave from the origin of the array to the sensor at position p_n is given by

$$\tau_n = \frac{p_n \cos\theta}{c}. \tag{4.1}$$

In the $\omega - frequency$ domain, the N-dimensional column-vector sensor output is given by

$$\mathbf{x}(\omega) = F(\omega)\mathbf{v}_\theta(\omega) \in \mathbb{C}^N, \tag{4.2}$$

where the array manifold is given by

$$\mathbf{v}_\theta(\omega) = \begin{bmatrix} e^{-\jmath\omega\tau_1} \\ e^{-\jmath\omega\tau_2} \\ \vdots \\ e^{-j\omega\tau_N} \end{bmatrix}. \tag{4.3}$$

The array manifold can also be expressed as a function of wavenumber k, where

$$\omega\tau_n = \mathrm{k}p_n.^1 \tag{4.4}$$

Often it is simpler to work in wavenumber $k - space$ because of the uniform array response. Sensor outputs are time shifted in the frequency domain by applying sensor weights given by

$$\mathbf{w}_\theta^H(\omega) = \frac{1}{N}\mathbf{v}_\theta^H(\omega),^2 \tag{4.5}$$

and is commonly referred to as the conventional, or Bartlett beamformer weighting. Other non-adaptive weighting schemes used to control beamformer performance are thoroughly discussed in Harris [44]. The spectral covariance matrix, $\mathbf{S}_x(\omega)$, gives the covariance between each sensor in the frequency domain. The conventional beamformer estimated wavenumber

[1]The magnitude of k is constrained by the wave equation to be $|\mathrm{k}| = \sqrt{k_x^2 + k_y^2 + k_z^2} \leq \frac{\omega}{c}$.

[2]The superscript H indicates the conjugate transpose.

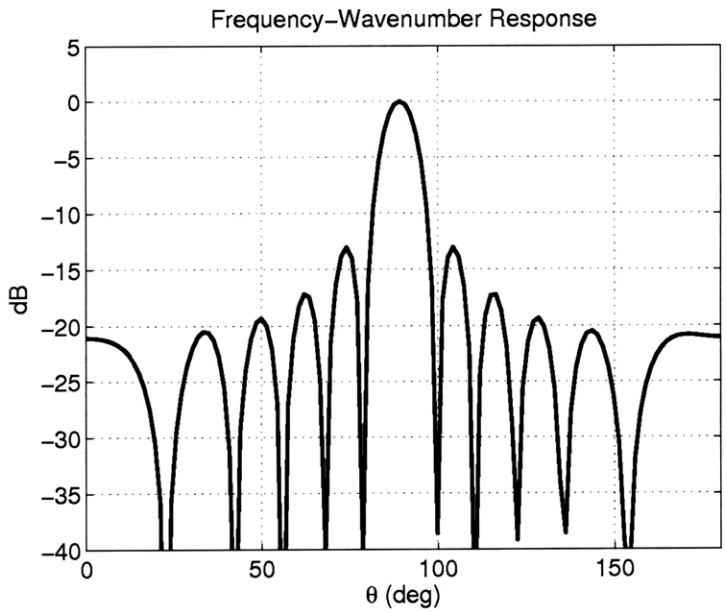

Figure 4-1: Broadside frequency-wavenumber response for a linear hydrophone array with half-wavelength sensor spacing and N=11.

power in terms of the spectral covariance matrix is given by

$$P(\omega,\theta) = \frac{1}{N^2}\mathbf{v}_\theta^H(\omega)\mathbf{S}_x(\omega)\mathbf{v}_\theta(\omega). \tag{4.6}$$

The performance of the beamformer can be determined by calculating the frequency-wavenumber response, or beampattern, at some steering direction θ_s. In vector notation the frequency-wavenumber response is given by

$$\Upsilon_{\theta_s}(\omega,\theta) = 10\log_{10}\left|\mathbf{w}_{\theta_s}^H(\omega)\mathbf{v}_\theta(\omega)\right|^2. \tag{4.7}$$

Figure 4-1 shows the broadside beampattern for a linear eleven sensor array with half-wavelength sensor spacing. The beampattern shows the signal attenuation of the array as a function of arrival angle. Other performance characteristics can be gleaned from the beampattern, including array gain, white noise gain, sensitivity, and resolution.

4.1.2 Array Resolution

The resolution, or half power beam width (HPBW), of the array is determined by measuring the width 3 dB down from the mainlobe peak.[3] An approximation to the HPBW at broadside for a standard array is given by

$$\theta_H = 0.891\frac{\lambda}{Nd}, \tag{4.8}$$

and the resolution at endfire is given by

$$\theta_H = 2\sqrt{0.890\frac{\lambda}{Nd}}, \tag{4.9}$$

where λ is the wavenumber of the plane wave and d is the sensor spacing. The FORA array used in the BASSEX experiment was a 32λ array corresponding to a resolution of 1.8 deg at broadside and 19.1 deg at endfire.

4.1.3 Array Gain

Array gain is the measure of an array's ability to remove unwanted interference and noise. For the case of a spatially white noise field, where the noise spectra at each sensor is $S_n(\omega)$, the output SNR is

$$SNR_o(\omega) = \frac{1}{\sum_{n=1}^{N}|w_n|^2}\frac{S_f(\omega)}{S_n(\omega)}, \tag{4.10}$$

and the white noise array gain (WNG) is therefore given by

$$A_w = \frac{SNR_o(\omega)}{SNR_{in}(\omega)} = \frac{1}{\sum_{n=1}^{N}|w_n|^2} = \| \mathbf{w} \|^{-2}. \tag{4.11}$$

The WNG is a commonly used sensitivity constraint for adaptive beamformers, and is employed in the beamformers used to process the data supporting this thesis. A good rule of thumb is to choose sensor weights $\mathbf{w}_o$ such that

$$\| \mathbf{w}_o \|^2 < \frac{3}{N}. \tag{4.12}$$

The spectral noise covariance matrix of the array is used to determine array gain in

[3] Chapter 2 of Van Trees [45] gives tables of approximations for the resolution of a line array.

more complicated noise fields. The spectral covariance matrix gives the correlation between sensors. For the input noise covariance $\mathbf{S}_n(\omega)$, the array gain is given by

$$A_o(\omega, k_s) = \frac{SNR_o(\omega, k_s)}{SNR_{in}(\omega)} = \frac{\mathbf{S}_f(\omega, k_s)}{\mathbf{w}^H(\omega, k_s)\mathbf{S}_n(\omega)\mathbf{w}(\omega, k_s)} \frac{\mathbf{S}_n(\omega)}{\mathbf{S}_f(\omega, k_s)}. \tag{4.13}$$

Using the normalized covariance matrix $\rho_n(\omega)$, and the relation $\mathbf{S}_n(\omega) = S_n(\omega)\rho_n(\omega)$, the array gain is given by

$$A_o(\omega, k_s) = \frac{1}{\mathbf{w}^H(\omega, k_s)\rho_n(\omega)\mathbf{w}(\omega, k_s)}. \tag{4.14}$$

4.2 Adaptive Beamformers

Adaptive beamforming methods can improve SNR by utilizing information about the signal environment and *a priori* information to optimally shape the beampattern. These methods have the potential to greatly improve array resolution and array gain, but can be difficult to implement and highly sensitive to sensor position perturbations and electronic malfunctions. This section will review the Minimum Variance Distortionless Response (MVDR) and the Minimum Power Distortionless Response (MPDR) beamforming methods.

4.2.1 Minimum Variance Distortionless Response Beamformer

Assuming the noise covariance is a product of circular complex Gaussian random variables, the MVDR beamformer method seeks a weighting that minimizes the variance in the array output given by

$$E[|Y_n|^2] = \mathbf{w}^H(\omega : k_s)\mathbf{S}_n(\omega)\mathbf{w}(\omega : k_s), \tag{4.15}$$

subject to the constraint that the output be distortionless, given by

$$\mathbf{w}^H(\omega, k_s)\mathbf{v}(\omega, k_s) = 1. \tag{4.16}$$

Applying the complex Lagrange multiplier and complex gradient operations, the optimum weighting is given by

$$\mathbf{w}_o^H(\omega, k_s) = \frac{\mathbf{v}^H(\omega, k_s)\mathbf{S}_n^{-1}(\omega)}{\mathbf{v}^H(\omega, k_s)\mathbf{S}_n^{-1}(\omega)\mathbf{v}(\omega, k_s)}, \tag{4.17}$$

and the MVDR power is therefore given by

$$\hat{P}_{MVDR}(\omega, k) = \frac{1}{\mathbf{v}_\theta^H(\omega : k)\hat{\mathbf{S}}_x^{-1}(\omega)\mathbf{v}_\theta(\omega : k)}. \tag{4.18}$$

The MVDR output is also the maximum likelihood estimate only when the signal wavenumber is known. The MVDR array gain is given by

$$A_o(\omega : k_s) = \mathbf{v}^H(\omega : k_s)\rho_n^{-1}(\omega)\mathbf{v}(\omega : k_s). \tag{4.19}$$

4.2.2 Minimum Power Distortionless Response Beamformer

The minimum power distortionless response (MPDR) beamformer is designed to minimize the power in the array output, where the spectral covariance matrix contains the target signal. The equation for the MPDR weights is similar to the equation for the MVDR weights, and is given by

$$\mathbf{w}_o^H(\omega : k_s) = \frac{\mathbf{v}^H(\omega : k_s)\mathbf{S}_x^{-1}(\omega)}{\mathbf{v}^H(\omega : k_s)\mathbf{S}_x^{-1}(\omega)\mathbf{v}(\omega : k_s)}, \tag{4.20}$$

where

$$\mathbf{S}_x(\omega) = \mathbf{S}_f(\omega) + \mathbf{S}_n(\omega). \tag{4.21}$$

MPDR beamforming is primarily used when the signal SNR is low, or where beamformer weights need to be determined using data where the signal is present.

A time-varying MPDR beamformer is used to process BASSEX data for the following two reasons. First, the SPICEX sources transmitted at the same time, and the spatially separated m-sequence signals arrived at the towed array at approximately the same time; the interfering m-sequence signal was usually quite strong and necessary to remove. Second, array flexing and changes in array orientation affected snap-shot statistics over time.

4.2.3 Robustness

The true spectral covariance matrix is often unavailable in real world data processing; an estimate is made using frequency domain snapshots of the array output. Assuming the

noise field is stationary over the sample period, the covariance estimate is given by

$$\hat{\mathbf{S}}_n(\omega) = \frac{1}{L}\sum_{l=1}^{L} \mathbf{X}_l(\omega)\mathbf{X}_l^H(\omega), \quad [4] \tag{4.22}$$

where L is the number of frequency domain snapshots. A good rule of thumb is to choose $L \geq 2N$. Capon and Goodman [46] showed that the power estimate $\hat{P}_{MVDR}(\omega, k)$ has a chi-squared distribution and bias and variance given by

$$\frac{E[\hat{P}_{MVDR}(\omega, k)]}{P_{MVDR}(\omega, k)} = \frac{L - N + 1}{L} \tag{4.23}$$

$$\frac{E[\sigma_{\hat{P}_{MVDR}}(\omega, k)]}{P_{MVDR}(\omega, k)} = \frac{\sqrt{L - N + 1}}{L}. \tag{4.24}$$

Nadakuditi [47] presents a method for estimating the bias of the MVDR estimate in the sidelobe region, using infinite matrix theory, when diagonal loading is applied to the spectral covariance matrix estimate.

When the noise field is non-stationary, it is necessary to condition the covariance matrix estimate to reduce sensitivity. The simplest way to improve beamformer robustness is to add a diagonal loading to the covariance matrix, such that

$$\hat{\mathbf{S}}_n(\omega) \rightarrow \hat{\mathbf{S}}_n(\omega) + dl \cdot \mathbf{I}; \tag{4.25}$$

see Carlson [48] for a discussion of the benefits of diagonal loading. A good rule of thumb is to choose the diagonal loading to be

$$dl \geq 1 \cdot 10^{-2} \left(\frac{1}{N} \mathrm{Tr}[\hat{\mathbf{S}}_n(\omega)] \right). \tag{4.26}$$

Adding a diagonal loading term whitens the covariance matrix and reduces the adaptivity of the array. In the limit as the diagonal loading term goes to infinity, the MVDR estimate becomes equal to the Bartlett beamformer estimate.

The white noise gain constraint (WNGC), given by Eq. 4.12, is another method used to improve robustness, described in detail by Cox [49]. The WNGC is applied by first checking the sensitivity of the MVDR weights. If necessary, the diagonal loading to the covariance

[4] A hat over a variable indicates it is an estimate.

matrix is increased until the WNGC is achieved.

.

4.3 Discrete Time Fourier Transform Filtering

Changing array orientation causes measured array snap-shots to become non-stationary in time. The data supporting this thesis is processed with MPDR and PCML beamformers using time-varying filters which implement the overlap-add technique, discussed in Oppenheim [50].

The Fast Fourier Transform (FFT) is used to transform the array output into the frequency domain.[5] The FFT transformed array data are used to generate sensor weights at each frequency. Baggeroer and Cox [51] showed that to avoid phase errors, the FFT length must be chosen such that the frequency spacing is

$$\Delta f \leq \frac{c}{8L_{array}}, \tag{4.27}$$

where L is the length of the array. Sensor weights at each frequency are combined to create filters for each channel using the inverse Fast Fourier Transform. The filtered time series are summed and the results are time shifted to remove any digital filter lag.

4.4 Correlation Matrix Distance

MPDR beamformers require a stationary noise field to optimally weight the sensor output. Like the name implies, the correlation matrix distance (CMD) metric, presented in Herdin [52], gives a measure of the distance between two correlation matrices, and is given by

$$d_{corr}(t_1, t_2) = 1 - \frac{\mathrm{Tr}\{\mathbf{S}(t_1)\mathbf{S}(t_2)\}}{||\mathbf{S}(t_1)||_f ||\mathbf{S}(t_2)||_f} \in [0, 1].^{6} \tag{4.28}$$

For the BASSEX experiment this equation is modified to be used with spectral covariance matrices. Assuming zero-mean Gaussian random data, the CMD, applied to the BASSEX

[5] Using Matlab, the function *specgram* can be used to efficiently compute the power spectrum for each sensor.

[6] The $||\cdot||_f$ is the Frobenius norm.

data, becomes

$$d_{corr}(\omega, t) = 1 - \frac{\mathrm{Tr}\{\mathbf{S}(\omega, t_o)\ \mathbf{S}\ (\omega, t)\}}{||\mathbf{S}(\omega, t_o)||_f ||\mathbf{S}(\omega, t)||_f} \in [0, 1], \tag{4.29}$$

where

$$\hat{\mathbf{S}}(\omega, t_o) = \frac{1}{L} \sum_{l=1}^{L} \mathbf{X}_l(\omega)\ \mathbf{X}\ {}_l^H(\omega), \tag{4.30}$$

where $\mathbf{X}$ is a vector of Fourier transformed array data, l is the snap-shot, t_o is a reference time, ω is the frequency bin, and L is the number of snap-shots to be used in the correlation estimation. Herdin [52] shows that a CMD of 0.5 indicates half the arriving power changes spatially; this is a natural CMD threshold limit, and the training time over which the spectral covariance matrices are estimated is chosen such that the CMD between estimated covariance matrices is less than 0.5.

Figure 4-2 shows the CMD of a BASSEX hydrophone array data set containing two m-sequence signals with different arrival times and bearings. When the m-sequence signals arrive, there is a clear increase in the CMD in the 200-300 Hz frequency band. Certain frequency bands appear to have a very low CMD throughout the entire reception; these frequencies are dominated by strong, stationary tow ship noise harmonics. In this example, the CMD is below 0.3 for $\pm$15 sec, and below 0.4 for $\pm$40 sec, about the sample point at 50 sec. These results show that the signal space is highly stationary over 30 sec; however, to achieve adequate snapshot support, 80 sec of data are used to estimate the spectral covariance matrix, and beamformer robustness mitigates the small degree of non-stationarity. Based on this example, the spectral covariance matrix estimates used to create beamformer weights to process BASSEX data are determined using approximately 83 sec of data, or 80 snap-shots, which is greater than the number of sensors available.

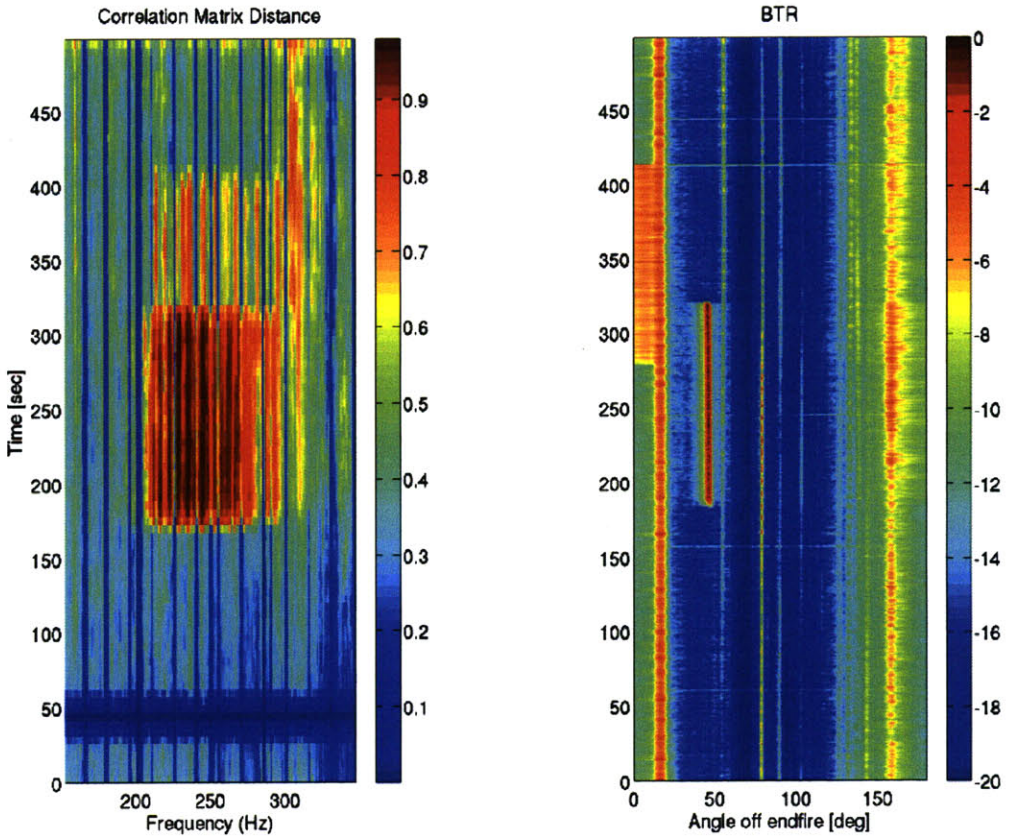

Figure 4-2: Correlation matrix distance (left) for BASSEX data with two m-sequences arriving at 45 deg and 10 deg, seen in the normalized bearing time response (right), given in dB.

4.5 Processing BASSEX Data

The noise environment in the Pacific Ocean and acoustic measurement techniques during the BASSEX experiment presented many signal detection issues. The ambient noise field in the ocean contributed many discrete and spatially spread noise sources to the array data at levels between 60-70 dB re 1μPa; this is stronger than the observed target signal in the seamount shadow zones. Noise from the tow ship was present in the range 13-18 deg off endfire, which is where the target signal often appeared. Array flexing and changes in orientation over time, caused by array movement through the water, affected the stationarity of the noise field.

It was stated in Section 4.2.2 that a time varying MPDR beamformer could address the non-stationarity issues and provide the best resolution and noise suppression for the SPICEX sources. An adaptive WNGC was applied to reduce the sensitivity of the beamformer, which was greatly affected by tow ship noise harmonics. Table 4.1 gives the MPDR beamformer design parameters; this is the beamformer used to process the SPICEX signals in the BASSEX data set.

Observational methods discussed in Chapter 3, and the beamforming methods discussed in this chapter, are used to convert received hydrophone data into acoustic ray arrival patterns. Computing technical details are offered in Appendix A. Figure 4-3 diagrams the different stages for processing hydrophone data from the BASSEX experiment. The following is a walkthrough of the processing steps:

1. Acoustic pressure time series from the ultra-low section of the FORA array are selected from sensors uniformly spaced 3 meter apart.

2. The raw data, with 781.25-Hz sample frequency, are quadrature demodulated to base-band and decimated by four to improve computational efficiency.

3. Frequency bin size is chosen to minimize phase distortion across the array.

4. Frequency domain snap-shots of the data are calculated using the FFT algorithm. The Hanning window is applied to reduce sidelobes in the frequency domain, and snap-shots are 50% overlapped in time.

5. The spectral covariance matrix is estimated from the available snap-shots.

6. The amount of diagonal loading is adjusted to meet the WNGC, which is set to 2.75/N.

7. Capon beamformer weights are determined from the estimated, diagonally loaded spectral covariance matrix.

8. Time domain filters are generated using the inverse FFT; the time domain filters are updated over time to account for changing signal field statistics.

9. The Doppler shift is determined from the raw data and transmitted signal.

10. Matched filtering is applied to each beam to determine acoustic ray arrival time and amplitude.

11. Angle correction is applied using non-acoustic sensor data. Array and source positioning, along with clock corrections, are included in this step as well.

Table 4.1: Specifications for the MPDR time-varying beamformer, which is applied to BASSEX data containing SPICEX source transmissions.

L_{array}	=	190.5 m
c	=	$c_{measured} \approx 1500$ m/s
f_{samp}	=	195.3 Hz
nfft	=	$256 \geq \frac{c}{8L_{array}} f_{samp}$
filter update every	=	21 sec
covariance matrix sample	=	83 sec
number of snapshots	=	80
diagonal loading	$\geq$	$1 \cdot 10^{-2} \left(\frac{1}{N} \mathrm{Tr}[\hat{\mathbf{S}}_n(\omega)] \right)$
WNGC	$\rightarrow$	$\| \mathbf{w}_o \|^2 < \frac{2.75}{N}$

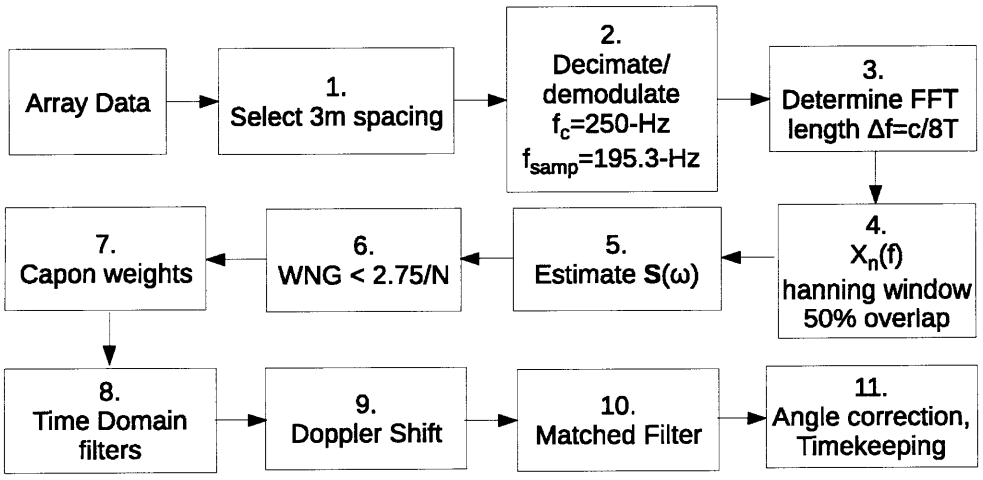

Figure 4-3: Signal processing block diagram for processing BASSEX data.

4.6 Summary

The MPDR adaptive beamforming algorithm developed in this chapter is necessary to detect and resolve acoustic rays in the scattered field of a seamount with the highest resolution possible. Array movement and interference from other sources and target multipath structure motivated the use of a time-varying algorithm. The amount of training time was based on the measured correlation matrix distance metric. An example BASSEX data record filtered with the MPDR algorithm developed in this chapter will be presented in Chapter 5, and its performance will be measured using a broadband m-sequence signal and compared with the Bartlett and PCML beamformer.

The next chapter develops the PCML beamformer to improve signal detection and estimation for data records which contain significant signal degradation caused by data acquisition system data drop-outs.

Chapter 5

Physically Constrained Maximum Likelihood Method

Accurate acoustic ray amplitude and angle-of-arrival estimation are important for understanding the seamount scattered field and reconciling experimental and simulated data. The MPDR beamformer developed in Chapter 4 used a sampled spectral covariance matrix, which assumes that array snap-shots are stationary in time. Data gathered during the BASSEX experiment show significant array flexing and orientation changes which affect snap-shot statistics. A new, computationally efficient PCML method is developed in this chapter to improve array resolution and suppress interference when snap-shot support is low.

Without physical constraints, the maximum-likelihood spectral covariance matrix of an array is given by [53]

$$\hat{\mathbf{S}}_{DATA}(\omega) = \frac{1}{L}\sum_{l=1}^{L}\mathbf{X}_l(\omega)\mathbf{X}_l^H(\omega), \tag{5.1}$$

where $\mathbf{X}_l(\omega)$ are stationary, independent and identically distributed (iid) zero-mean complex Gaussian random vectors of sensor output at frequency ω, and L is the number of snap-shots. The Physically Constrained Maximum Likelihood (PCML) Method, developed by Kraay [13], determines the maximum-likelihood spectral covariance matrix when physical constraints are applied, which are based on array geometry, to reduce the required snap-shot support. In this chapter, the PCML method will be reviewed, and an efficient method for modeling the spectral covariance matrix using trigonometric bases will be presented. The

approach developed in this chapter is applied to snap-shot deficient BASSEX data records to investigate the scattered field of the Kermit-Roosevelt Seamount in Chapter 6.

5.1 Maximum Likelihood Estimator

Acoustic signals in the ocean are typically modeled as real iid zero-mean Gaussian random noise, and array snapshots $\mathbf{X}_1, \mathbf{X}_2, \ldots, \mathbf{X}_L$[1] can be shown to have circular complex Gaussian distributions [45]. The joint probability density function (pdf) of the snap-shots is

$$p(\mathbf{X}_1, \ldots, \mathbf{X}_L) = p(\mathbf{X}_1)p(\mathbf{X}_2)\cdots p(\mathbf{X}_L) = \prod_{l=1}^{L} \frac{1}{\pi^N |\mathbf{S}|} e^{-\mathbf{X}_l^H \mathbf{S} \mathbf{X}_l}, \tag{5.2}$$

where $|\cdot|$ is the determinant operator and $\mathbf{S}$ is the covariance matrix. The maximum-likelihood estimate of the covariance matrix is therefore given by

$$\hat{\mathbf{S}}_{ML} = \underset{\mathbf{S}\subseteq\mathcal{R}}{\operatorname{argmax}}\, p(\mathbf{X}_1, \ldots, \mathbf{X}_L) = \underset{\mathbf{S}\subseteq\mathcal{R}}{\operatorname{argmax}} \prod_{l=1}^{L} \frac{1}{\pi^N |\mathbf{S}|} e^{-\mathbf{X}_l^H \mathbf{S} \mathbf{X}_l}, \tag{5.3}$$

where $\mathcal{R}$ is the covariance constraint set. By taking the log of Eq. 5.3, and manipulating the result, it can be shown that

$$\hat{\mathbf{S}}_{ML} = \underset{\mathbf{S}\subseteq\mathcal{R}}{\operatorname{argmax}} \left\{ -\log|\mathbf{S}| - \operatorname{Tr}\left(\frac{1}{L} \sum_{l=1}^{L} \mathbf{S}^{-1} \mathbf{X}_l \mathbf{X}_l^H \right) \right\} \tag{5.4}$$

$$\hat{\mathbf{S}}_{ML} = \underset{\mathbf{S}\subseteq\mathcal{R}}{\operatorname{argmax}} \left\{ -\log|\mathbf{S}| - \operatorname{Tr}\left(\mathbf{S}^{-1} \hat{\mathbf{S}}_{DATA} \right) \right\} \tag{5.5}$$

$$\hat{\mathbf{S}}_{ML} = \underset{\mathbf{S}\subseteq\mathcal{R}}{\operatorname{argmax}}\, L(\mathbf{S}, \hat{\mathbf{S}}_{DATA}), \tag{5.6}$$

where $L(\mathbf{S}, \hat{\mathbf{S}}_{DATA})$ is the likelihood function for the maximum-likelihood spectral covariance matrix estimate. Under some parameterized model for the covariance matrix, for which $\mathbf{S} \subseteq \mathcal{R}$, iterative estimation can be applied to determine $\hat{\mathbf{S}}_{ML}$.

Previous work by Miller [54], Burg [55], and Barton [56] impose the Toeplitz matrix constraint on the spectral covariance matrix for linearly spaced arrays. The PCML method separates propagating and non-propagating power components of the spectral covariance matrix, constrains the propagating power spectrum to the visible space of the array and, unlike previous methods, is applicable to any array geometry.

[1] For notational simplicity, the "(ω)" will be omitted.

5.1.1 PCML Algorithm

An iterative procedure is used to converge on the most likely spectral covariance matrix. In each iteration, the power spectrum is estimated and $\hat{\mathbf{S}}_{ML}$ is updated using the relationship given by

$$[\mathbf{S}]_{i,j} = \sigma^2 \delta_{i,j} + \frac{1}{(2\pi)^3} \int_{\Omega(\mathbf{k})} P(\mathbf{k}) [\mathrm{v}_{\mathbf{k}}(\mathbf{k})]_i [\mathrm{v}_{\mathbf{k}}^H(\mathbf{k})]_j d\mathbf{k}, \tag{5.7}$$

where $\Omega(\mathbf{k})$ is the three dimensional space spanning all visible wavenumbers for a given frequency, $P(\mathbf{k})$ is the propagating power spectrum, and σ^2 is the non-propagating power. The propagating and non-propagating power are separated in Eq. 5.7 to ensure the spectral covariance matrix is positive semi-definite, and to desensitize the PCML beamformer to superdirectivity. The integral in Eq. 5.7 is performed in Cartesian space, where the norm of $\mathbf{k}$ is constrained by

$$||\mathbf{k}|| = \sqrt{k_x^2 + k_y^2 + k_z^2} \leq \frac{2\pi}{\lambda}. \tag{5.8}$$

The first and second order derivatives of the likelihood function, with respect to the propagating and non-propagating power spectra, are used to determine global peaks in the likelihood function. The process described in Kraay [13] first initializes the covariance matrix and power spectrum, then applies physical constraints and updates the power spectrum repeatedly until convergence is reached for $P(\mathbf{k})$ and σ^2.

The covariance matrix update is determined by applying the relationship given by Eq. 5.7 to the previous power spectrum estimate. For discretely sampled wavenumbers, this relationship is given by

$$[\mathbf{S}_m]_{i,j} = \sigma_{m-1}^2 \delta_{i,j} + \left(\sum_n P_{m-1}(\mathbf{k}_n) e^{-j\mathbf{k}_n^T(\mathrm{p}_i - \mathrm{p}_j)} \right) \cdot W_{i,j}, \tag{5.9}$$

where $W_{i,j}$ is the inverse Fourier transform of the taper used to approximate the spectrum around each wavenumber-power sample. A uniform window taper, for wavenumber resolution Δu and sensor position p_x, is given by

$$W_{i,j} = \Delta u \cdot \mathrm{sinc}\left(\frac{2\pi}{\lambda} \cdot \frac{\Delta u}{2} (\mathrm{p}_i - \mathrm{p}_j) \right). \tag{5.10}$$

5.2 The Orthonormal Basis PCML Method

The method presented by Kraay relies on a computationally intensive iterative estimation technique to determine the maximum-likelihood spectral covariance matrix. This section presents an orthonormal trigonometric basis approach for determining the maximum-likelihood spectral covariance matrix of a linear array which improves computational efficiency over Kraay's method.

The spectral covariance matrix is assumed to be of the form

$$\hat{\mathbf{S}} = \sigma^2 \mathbf{I}_{N\times N} + \sum_{n=1}^{N} p_n \phi_n \phi_n^H = \sum_{n=1}^{N} (p_n + \sigma^2)\phi_n \phi_n^H, \tag{5.11}$$

where the non-propagating power is given by

$$\sigma^2 \in \left[\varepsilon, \frac{1}{N}\mathrm{Tr}\{\hat{\mathbf{S}}_{DATA}\}\right], \tag{5.12}$$

for $0 < \varepsilon \ll \frac{1}{N}\mathrm{Tr}\{\hat{\mathbf{S}}_{DATA}\}$, the propagating wavenumber-power along basis vector ϕ_n is given by

$$p_n \in \mathbb{R}^+ = \{x : x \in \mathbb{R}, x \geq 0\}, \tag{5.13}$$

and the orthonormal column-vector set defined by ϕ_n represents plane wave array output which together span visible wavenumber space. The constraints on the power terms ensure a positive definite spectral covariance matrix, and ε can be chosen to ensure a well conditioned and invertible matrix. The wavenumber-power projected onto the ϕ_n basis vector is given by

$$\xi_n = \phi_n^H \hat{\mathbf{S}}_{DATA} \phi_n. \tag{5.14}$$

The covariance matrix given by Eq. 5.11 can be substituted into the log-likelihood formula, given by Eq. 5.5; *i.e.*,

$$L(\hat{\mathbf{S}}, \hat{\mathbf{S}}_{DATA}) = -\log|\hat{\mathbf{S}}| - \mathrm{Tr}(\hat{\mathbf{S}}^{-1}\mathbf{S}_{DATA}), \tag{5.15}$$

$$L(\hat{\mathbf{S}}, \hat{\mathbf{S}}_{DATA}) = -\log\left|\sum_{n=1}^{N}(p_n + \sigma^2)\phi_n\phi_n^H\right| - \mathrm{Tr}\left(\sum_{n=1}^{N}\frac{\xi_n}{(p_n+\sigma^2)}\phi_n\phi_n^H\right), \tag{5.16}$$

$$L(\hat{\mathbf{S}}, \hat{\mathbf{S}}_{DATA}) = -\log\left(\prod_{n=1}^{N}(p_n + \sigma^2)\right) - \sum_{n=1}^{N}\frac{\xi_n}{(p_n + \sigma^2)}. \tag{5.17}$$

The value of p_n which maximizes the likelihood is determined by setting the derivative with respect to p_n of Eq. 5.17 equal to zero; *i.e.*,

$$\frac{\partial L(\hat{\mathbf{S}}, \hat{\mathbf{S}}_{DATA})}{\partial p_n} = -\frac{1}{p_n + \sigma^2} + \frac{\xi_n}{(p_n + \sigma^2)^2} = 0. \tag{5.18}$$

The maximum-likelihood value of p_n is given by

$$p_n = \xi_n - \sigma^2. \tag{5.19}$$

From Kraay [13] the derivative of the log-likelihood function with respect to p_n is given by

$$\frac{\partial L(\hat{\mathbf{S}}, \hat{\mathbf{S}}_{DATA})}{\partial p_n} = -\mathbf{v}_k^H(\mathbf{k}_n)\hat{\mathbf{S}}^{-1}\mathbf{v}_k(\mathbf{k}_n) + \mathbf{v}_k^H(\mathbf{k}_n)\hat{\mathbf{S}}^{-1}\hat{\mathbf{S}}_{DATA}\hat{\mathbf{S}}^{-1}\mathbf{v}_k(\mathbf{k}_n); \tag{5.20}$$

Equation 5.20 can be manipulated to

$$\frac{\partial L(\hat{\mathbf{S}}, \hat{\mathbf{S}}_{DATA})}{\partial p_n} = p_n^{-1} \times \left(\frac{\frac{1}{L}\sum_{l=1}^{L}|\mathbf{w}_{n,MVDR}^H\mathbf{X}_l|^2}{p_n} - 1\right), \tag{5.21}$$

which is useful for showing the stationarity of the covariance matrix estimate. The power estimated from $\hat{\mathbf{S}}$ using the conventional beamformer will equal the power estimated from $\hat{\mathbf{S}}_{DATA}$ using the PCML beamformer when a stationary point is reached; *i.e.*, a local-maximun on the likelihood function. Since $p_n = \xi_n - \sigma^2$ satisfies Eq. 5.18, it therefore must satisfy the stationarity condition $\frac{1}{L}\sum_{l=1}^{L}|\mathbf{w}_{n,MVDR}^H\mathbf{X}_l|^2 = p_n$; thus it is a global maximum-likelihood solution since it is the only feasible point where $\partial L/\partial p_n = 0$.

The global maximum-likelihood value of p_n is determined by searching for the value of σ^2 which maximizes the log-likelihood function while preserving physical constraints given in Eq. 5.12 and 5.13. The log-likelihood function with respect to σ^2 is generally a multimodal, non-linear function which motivates techniques such as brute force, bisection, and simulated annealing to find the maximum-likelihood value of σ^2.

5.2.1 Non-propagating Power Estimation

The following root-finding method was explored as a possible technique for finding the maximum-likelihood value of σ^2. This method assumes some initial estimate of σ^2 to determine p_n; *e.g.*,

$$\sigma_0^2 = 1 \times 10^{-2} \cdot \frac{1}{N} \mathrm{Tr}\{\hat{\mathbf{S}}_{DATA}\}. \tag{5.22}$$

From Kraay, the derivative of the likelihood function with respect to σ^2 is given by

$$\frac{\partial L(\hat{\mathbf{S}})}{\partial \sigma^2} = \mathrm{Tr}\left[(\hat{\mathbf{S}}^{-1}\mathbf{S}_{DATA} - \mathbf{I})\hat{\mathbf{S}}^{-1}\right] = 0. \tag{5.23}$$

The covariance matrix given by Eq. 5.11 can be substituted into Eq. 5.23; *i.e.*,

$$\frac{\partial L(\hat{\mathbf{S}})}{\partial \sigma^2} = \mathrm{Tr}\left[\left(\sum_{m=1}^{M} \frac{\xi_n}{p_n + \sigma^2}\phi_n\phi_n^H - \sum_{m=1}^{M} \phi_n\phi_n^H\right)\sum_{m=1}^{M} \frac{1}{p_n + \sigma^2}\phi_n\phi_n^H\right] = 0, \tag{5.24}$$

$$\sum_{m=1}^{M} \frac{(\xi_n - p_n) + \sigma^2}{p_n^2 + 2p_n\sigma^2 + \sigma^4} \prod_{n=1}^{M}(p_n^2 + 2p_n\sigma^2 + \sigma^4) = 0. \tag{5.25}$$

The roots of this $(M+2)^{th}$ order polynomial expression contain the maximum likelihood value of σ^2 for a given set p_n, but are difficult to determine analytically, especially for high values of M. The Fast-Fourier transform (FFT) algorithm can be applied to efficiently determine the roots by taking advantage of the convolution property of polynomial multiplication. The following Matlab code is presented to determine the roots of the polynomial given by Eq. 5.25.

```
M                                   %the number of roots
w                                   %the vector that holds the sum, initialized to zero
q = M + 2                           %additional convolution tail length is 3 - 1 = 2
Ξ = [ξ0 ξ1 ··· ξM−1 ]
P = [p0 p1 ··· pM−1 ]
B = [Ξ − P; −1_{1×M}; 0_{1×M}]_{3×M}   %numerator polynomial
A = [P^2; 2P; 1_{1×M}]_{3×M}           %denominator polynomial

for m=1:M                           %compute m^th term in summation
    W=prod(fft([A(:,[1:m-1 m+1:end]) B(:,m)],q),2);
    w=w+ifft(W,q);
end
r=roots(w);                         %find roots
```

Only the likelihood of the roots which are real and greater than zero must be checked in order to determine the physically possible root that maximizes the log-likelihood function. To improve parameter accuracy, the root finding method can be repeated until convergence is reached in p_n and σ^2. Unfortunately, this method tends to converge on local maxima which lie off the real axis, and is therefore not reliable for estimating σ^2_{ML} for the PCML covariance matrix.

5.3 The Array Manifold Trigonometric Basis

One physically realizable orthonormal basis set is the array manifold trigonometric vectors which span visible wavenumber space, given by

$$\phi_n = \frac{1}{\sqrt{N}} \begin{bmatrix} e^{-\jmath \frac{2\pi}{\lambda}(0)du_n} \\ e^{-\jmath \frac{2\pi}{\lambda}(1)du_n} \\ \vdots \\ e^{-\jmath \frac{2\pi}{\lambda}(N-1)du_n} \end{bmatrix}_{N\times 1}, \tag{5.26}$$

which are uniformly sampled at wavenumbers given by $u_n = \cos(\theta_n)$, where $n \in \{1, 2, \ldots, N\}$. Equation 5.26 represents the normalized array response to a plane wave arriving with wavenumber u_n, such that $\phi_n^H \phi_n = 1$. The set of wavenumbers for which ϕ_n form an orthonormal basis is given by

$$u_n = \frac{\lambda}{\lambda_{cut}}(-1 + n\Delta), \tag{5.27}$$

where $\lambda_{cut} = 2d$ and $\Delta = 2/N$. The visible wavenumber space constraint is maintained by forcing $p_n = 0$ for $u_n \notin [-1, 1]$.

Plane waves coincident upon the basis vectors will be perfectly represented by the spectral covariance matrix, and plane waves not coincident upon the basis will experience non-zero projections across the entire basis; this is a phenomenon known as spectral leakage, which is discussed in Harris [44]. The power of a plane wave with power σ_i^2 at wavenumber u_i, projected onto the trigonometric basis vector u_n, is given by

$$\vartheta_n(u_i) = \sigma_i^2 \cdot |\Upsilon(u_i, u_n)|^2, \tag{5.28}$$

where

$$|\Upsilon(u_i, u_n)|^2 = \frac{1}{N^2} \left| \frac{\sin\left(\frac{N}{2}\frac{2\pi}{\lambda}(u_i - u_n) \cdot d\right)}{\sin\left(\frac{1}{2}\frac{2\pi}{\lambda}(u_i - u_n) \cdot d\right)} \right|^2. \tag{5.29}$$

It can be shown that the wavenumber-power estimate determined from the covariance matrix $\sum_{n=1}^{N} \vartheta_n(u_i)\phi_n\phi_n^H$ is not uniform for all possible angles of incidence; *i.e.*,

$$\begin{array}{rcll} \sum_{n=1}^{N} \vartheta_n(u_i)|\Upsilon(u_n, u_i)|^2 & < & \sigma_i^2, & u_i \neq u_n \forall n \\ & = & \sigma_i^2, & u_i = u_n \forall n \end{array}. \tag{5.30}$$

Figure 5-1 shows the estimated power spectrum for a plane wave arriving off-basis at $u = 0.02$ with strength of 0 dB, for a 32 sensor standard line array, using the ensemble spectral covariance matrix and the covariance matrix generated using the PCML trigonometric basis approach (T-PCML). The figure demonstrates that the trigonometric basis modeling method does not produce a wavenumber-power estimate which peaks in the direction of off-basis plane wave interference.

It is important that on- and off-basis plane wave interference be weighted equally in the formation of the PCML covariance matrix to ensure accurate null placement. Section 5.3.1 introduces covariance matrix tapering, a technique which smooths the wavenumber power

spectrum and skews the power spectrum towards the direction of interference. Section 5.3.2 discusses a technique which can be applied to the PCML spectral covariance matrix estimation procedure such that plane waves are equally weighted in the generation of $\hat{\mathbf{S}}_{ML}$, regardless of incidence angle.

5.3.1 Covariance Matrix Tapering

Covariance matrix tapers are weight matrices applied to the spectral covariance matrix which are designed to improve the robustness of adaptive beamformers by mimicking some type of natural phenomenon, such as phase dither. Guerci [57] reported on the theory and effects of covariance matrix tapers, and in particular studied the taper

$$[\mathbf{T}]_{mn} = \frac{\sin((m-n)\Delta)}{(m-n)\Delta} \triangleq \text{sinc}\,((m-n)\Delta/\pi), \tag{5.31}$$

which is the covariance matrix of spatially bandlimited isotropic noise. When designing a taper, it is important that the matrix be positive semi-definite to ensure the tapered covariance matrix is positive definite.

Figure 5-1 shows the effect of the covariance matrix taper given by Eq. D.11 on the wavenumber-power estimate for the spectral covariance matrix generated using the trigonometric basis approach, where $\Delta = 2/N$. Tapering the covariance matrix spreads power in wavenumber space and moves the "center-of-mass" of the wavenumber-power towards the actual plane wave arrival direction. Unfortunately, tapering tends to skew the main lobe center-of-mass of an incident plane wave toward the nearest basis vector wavenumber.

5.3.2 Phase-shifted Basis PCML Approach

Assuming the true continuous propagating wavenumber-power $\sigma_p^2(\psi)$ is available in ψ-space,[2] the spectral covariance matrix for a standard linear array can be expressed as [56]

$$\mathbf{S}(\omega) = \frac{1}{2\pi}\int_{-\pi}^{\pi} \sigma_p^2(\psi)\mathbf{v}_\psi(\psi)\mathbf{v}_\psi^H(\psi)d\psi, \tag{5.32}$$

where $\mathbf{v}_\psi(\psi)$ are array manifold column-vectors. Unfortunately, $\sigma_p^2(\psi)$ is rarely available in practice, and the wavenumber-power must be estimated at different wavenumbers to

[2] $\psi = \frac{2\pi}{\lambda}\cos(\theta)\cdot d$.

approximate the true covariance matrix. Using array manifold vectors to form the PCML covariance matrix, the question becomes how fine the wavenumber sample spacing must be such that all possible visible propagating plane waves incident upon the array are equally weighted in the creation of $\hat{\mathbf{S}}_{ML}$.

The spectral covariance matrix for a uniform line array is Hermitian Toeplitz, in the limit as L goes to infinity, and the first row is the right-hand side of the unbiased autocorrelation sequence of the snap-shots. The correct wavenumber sample spacing can be determined using power spectrum estimation theory from time series analysis (see Oppenheim [50]), in the sense that the estimated wavenumber-power spectrum perfectly represents the autocorrelation sequence; undersampling the wavenumber-power spectrum leads to an aliasing of the autocorrelation sequence.

The stationary iid array snap-shots are re-written as windowed sequences; *i.e.*,

$$x_l[m] = \mathbf{X}_l[m] \cdot w[m], \tag{5.33}$$

where $m = 0, 1, \ldots, N-1$ and $w[m]$ is the window function of the array. The autocorrelation of $x_l[m]$ is given by

$$c_{xx}[m] = x_l[m] * x_l^*[-m]. \tag{5.34}$$

The wavenumber-power function can be determined by taking the discrete-Fourier transform of the autocorrelation of the snap-shot sequence; *i.e.*,

$$|\Upsilon(\psi)|^2 = \sum_{m=0}^{2N-1} c_{xx}[m] e^{jm\psi}, \tag{5.35}$$

which is periodic with 2π, for any N. The length of the autocorrelation is $2N$, and therefore, at least $2N$ samples of the wavenumber-power spectrum are required to perfectly reconstruct the autocorrelation sequence.[3] The requisite wavenumber-power samples chosen to represent the autocorrelation sequence are taken at

$$\psi_k = \tfrac{2\pi d}{\lambda_{cut}} \cdot \tfrac{k}{N}, \quad k = \{-N, -N+1, \ldots, N-1\}. \tag{5.36}$$

The expected value of the narrowband wavenumber-power function is shown by Capon [58]

[3]Including additional wavenumber-power samples is equivalent to zero-padding the autocorrelation function, which will not affect the formation of beamformer weights.

to be

$$E[|\Upsilon(\psi)|^2] = \sigma_p^2(\psi) * |W(\psi)|^2, \tag{5.37}$$

where the wavenumber-power spectrum of the Bartlett window is given by

$$|W(\psi)|^2 = \frac{1}{N^2}\left|\frac{\sin\left(N\frac{\psi}{2}\right)}{\sin\left(\frac{\psi}{2}\right)}\right|^2; \tag{5.38}$$

the wavenumber-power is asymptotically unbiased, where $|W(\psi)|^2$ approaches a delta function as N approaches infinity. The variance of the wavenumber-power estimate is shown by Capon [58] to be

$$\begin{aligned} \text{var}\left[|\Upsilon(\psi)|^2\right] &\cong \tfrac{1}{L}(E[|\Upsilon(\psi)|^2])^2, \quad \psi \neq 0 \\ &= \tfrac{2}{L}(E[|\Upsilon(\psi)|^2])^2, \quad \psi = 0 \end{aligned}, \tag{5.39}$$

which is consistent; *i.e.*, the variance approaches zero in the limit as L approaches infinity.

The spectral covariance matrix formed from $2N$ wavenumber-power samples taken at ψ_k can be generated using length $2N$ orthogonal array manifold vectors, *i.e.*,

$$\hat{\mathbf{S}}(\omega) = \sum_{k=-N}^{N-1} |\Upsilon(\psi_k)|^2 \mathbf{v}_\psi(\psi_k)\mathbf{v}_\psi^H(\psi_k); \tag{5.40}$$

this matrix is $2N \times 2N$ and perfectly represents the wavenumber-power samples obtained from the available snap-shots. The first $N \times N$ elements of the covariance matrix can be used to generate Capon beamformer weights for an N sensor array; however, truncating the matrix smooths the wavenumber-power spectrum by Eq. 5.38.[4] Appendix D gives a much more thorough investigation of this approach and the relationship between the sampled and PCML covariance matrices.

PCML Covariance Matrix Estimation using 2N Wavenumber Samples

The orthonormal basis set used to determine the PCML covariance matrix should contain $2N$ array manifold vectors which uniformly sample wavenumber space to ensure on- and

[4]Truncating the matrix leads to self-convolution which increases the final wavenumber-power estimate. The effects of self-convolution can be removed using a scale factor computed *a priori* based on location of the wavenumber samples; however, the physical constraints can affect the size of the scale factor and may lead to significant error in certain cases.

off-basis plane wave interference is equally weighted. Unfortunately, implementing the orthonormal basis maximum-likelihood PCML approach with $2N$ wavenumber-power samples requires a $2N \times 2N$ sampled spectral covariance matrix. One way to work around this issue is to zero-pad the sampled covariance matrix to create a $2N \times 2N$ covariance matrix. In fact, it can be easily shown that the covariance matrix given by Eq. 5.40 is equal to the maximum-likelihood covariance matrix for the zero-padded sampled covariance matrix, multiplied by 4,[5] in the case where $\lambda \leq \lambda_{cut}$.[6]

Using $2N$-length array manifold column-vectors to form the PCML covariance matrix, the maximum-likelihood estimate is determined by maximizing the log-likelihood function given by

$$L(\hat{\mathbf{S}}) = -\log|\hat{\mathbf{S}}| - \mathrm{Tr}\left(\hat{\mathbf{S}}^{-1}\begin{bmatrix} 4\cdot\hat{\mathbf{S}}_{DATA} & \mathbf{0} \\ \mathbf{0} & \mathbf{0} \end{bmatrix}\right), \tag{5.42}$$

while preserving the physical constraints given in Eq. 5.12 and 5.13; the resulting $2N \times 2N$ maximum-likelihood covariance matrix is that of the sampled covariance matrix smoothed in the wavenumber-power spectrum by Eq. 5.38 due to the zero-padding. The zero-padding method will henceforth be referred to as the phase-shifted PCML (PS-PCML) approach since the covariance matrix is formed from two orthogonal basis sets which are shifted in phase by half a resolution cell. The zero-padding approach is good in the sense that the smoothing function is symmetric, non-negative, and the first and second moments of the wavenumber-power estimates are known for Gaussian distributed snap-shots.

Figure 5-1 shows the estimated power spectrum for a plane wave arriving at $u = 0.02$ with strength of 0 dB for a 32 sensor linear array using the Capon beamformer and the ensemble, T-PCML, tapered, and PS-PCML covariance matrices. This figure shows that the PS-PCML wavenumber-power estimate peaks exactly in the direction of incidence, and is smoothed in wavenumber-space compared with the estimate from the ensemble covariance matrix.

[5]The wavenumber-power estimated from the truncated spectral covariance matrix given by $\mathbf{v}\mathbf{v}^H$ is a factor of 4 smaller than the true covariance matrix; *i.e.*,

$$\begin{aligned} \tfrac{1}{(2N)^2}\mathbf{v}^H\left[\ \mathbf{v}\mathbf{v}^H\ \right]\mathbf{v} &= \tfrac{4}{(2N)^2}\cdot\mathbf{v}^H\left(\left[\ \mathbf{v}\mathbf{v}^H\ \right]\odot\begin{bmatrix} \mathbf{1}_{N\times N} & \mathbf{0} \\ \mathbf{0} & \mathbf{0} \end{bmatrix}\right)\mathbf{v} \\ \tfrac{1}{(2N)^2}\mathbf{v}^H\mathbf{v}\cdot\mathbf{v}^H\mathbf{v} &= \tfrac{4}{(2N)^2}\cdot\tfrac{\mathbf{v}^H\mathbf{v}}{2}\cdot\tfrac{\mathbf{v}^H\mathbf{v}}{2} \end{aligned}. \tag{5.41}$$

[6]Another approach is to create a $2N \times 2N$ banded-Toeplitz matrix, with bandwidth N, from the available snap-shots; however, the resulting covariance matrix wavenumber-power estimates have a higher variance and the associated wavenumber smoothing function has negative values.

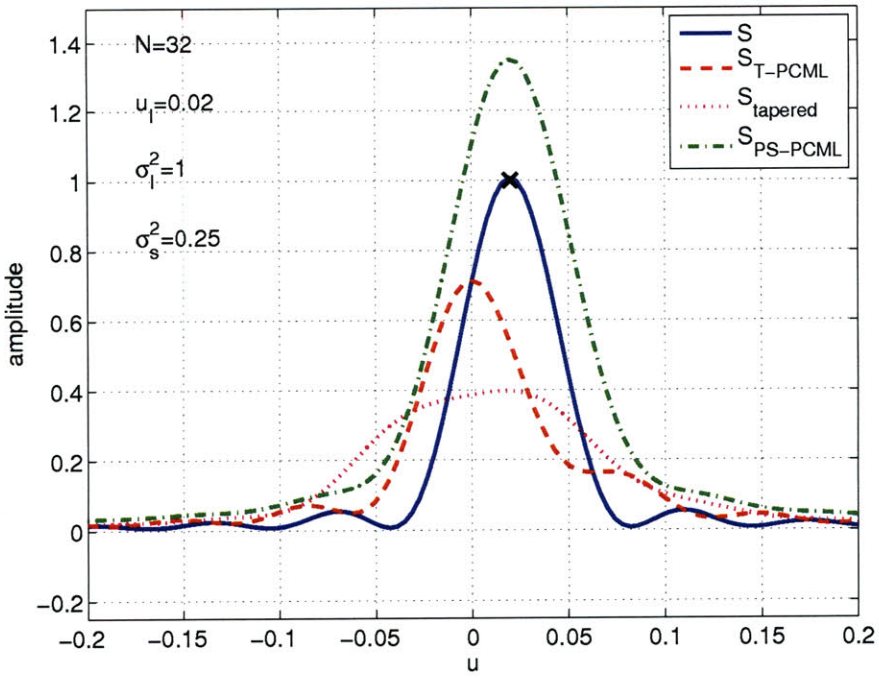

Figure 5-1: Estimated wavenumber-power using the Capon beamformer and the ensemble, T-PCML, tapered, and PS-PCML covariance matrices. The black × indicates the direction and amplitude of the plane wave interference.

Broadband Beamforming using PS-PCML

The orthogonal trigonometric basis vectors ϕ_n are not a function of frequency, and therefore the wavenumber samples always span 2π of wavenumber space for all λ. For $\lambda < \lambda_{cut}$, the space spanned by the wavenumber samples is inside the visible wavenumber space; propagating plane waves incident outside the sample space are aliased into the sample space. For $\lambda > \lambda_{cut}$, the wavenumber sample space is larger than the visible wavenumber space; wavenumber-power estimates for array manifold vectors outside of visible space are simply set to zero when determining the maximum-likelihood spectral covariance matrix.

Figure 5-2 shows the absolute value of the frequency-wavenumber function for an 11 sensor linear array for the cases where $\lambda = \lambda_{cut}$, $\lambda = 0.75\lambda_{cut}$, and $\lambda = 1.5\lambda_{cut}$. The blue lines indicate the wavenumber sample locations used to implement the PS-PCML beamformer. The magenta lines are time shifted frequency-wavenumber functions which indicate the 2π periodicity over the sample region. For $\lambda > \lambda_{cut}$, some wavenumber-power samples exist outside of visible space and must be set to zero when determining the PS-PCML covariance matrix.

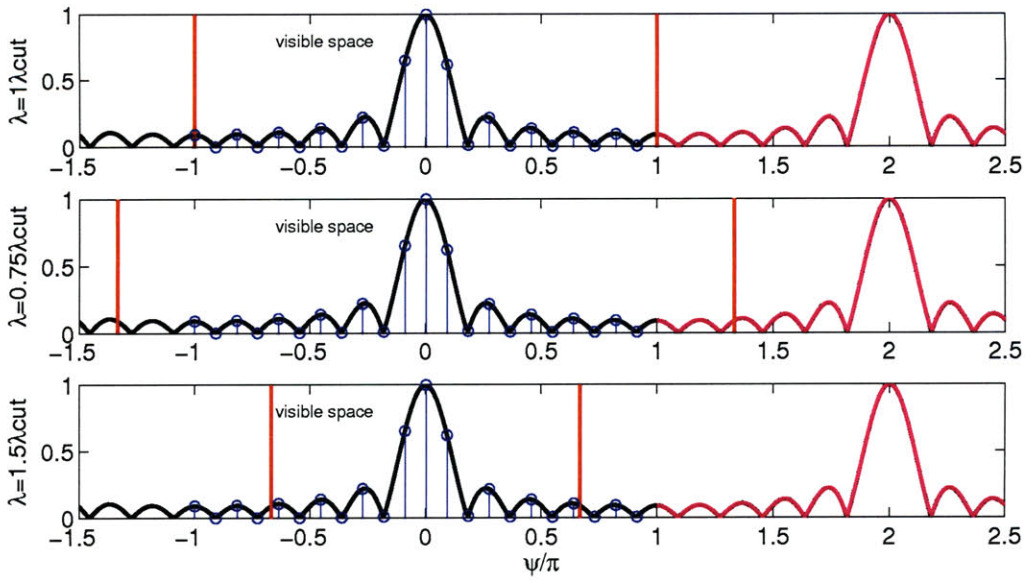

Figure 5-2: Absolute value frequency-wavenumber functions and wavenumber-sample locations for an 11 sensor linear array for the cases where $\lambda = \lambda_{cut}$, $\lambda = 0.75\lambda_{cut}$, and $\lambda = 1.5\lambda_{cut}$. Blue lines indicate wavenumber-power samples, magenta lines are time-shifted frequency-wavenumber functions which indicate 2π periodicity, and red lines indicate the boundary of visible wavenumber space.

PS-PCML Covariance Matrix Estimation Steps

The following steps provide the approach towards estimating the PS-PCML covariance matrix using the techniques discussed in this chapter.

- Step 1: Form the zero-padded $2N \times 2N$ sampled spectral covariance matrix from available snap-shots.
- Step 2: Form the $2N$-length orthonormal array manifold vectors ϕ_n which span the visible wavenumber space.
- Step 3: Determine ξ_n from the zero-padded covariance matrix for each orthonormal array manifold basis vector ϕ_n.
- Step 4: Form the spectral covariance matrix $\hat{\mathbf{S}}_{2N} = \sigma^2\mathbf{I} + \sum_{n=1}^{2N}(\xi_n - \sigma^2)\phi_n\phi_n^H$ and determine the log-likelihood. Search for the value of σ^2 which maximizes the likelihood in the range $[\varepsilon, \frac{1}{N}\mathrm{Tr}\{\hat{\mathbf{S}}_{DATA}\}]$. Enforce the physical constraints, which are that $(\xi_n - \sigma^2) \geq 0$ and ϕ_n lie in visible wavenumber space, by setting propagating power terms to zero.

- Step 5: Truncate $\hat{\mathbf{S}}_{2N}$ to create the $N \times N$ PS-PCML covariance matrix; use this matrix to form Capon beamformer weights for the N sensor array.

5.3.3 PS-PCML Performance with Simulated Data

SNR Performance

The expected SNR of the Capon beamformer using the sampled spectral covariance matrix is the function of L snap-shots and N sensors given by [59]

$$E(SNR) = \frac{L+2-N}{L+1}, \tag{5.43}$$

which is about 3 dB below the SNR using the ensemble covariance matrix for $L = 2N-3 \cong 2N$. The PS-PCML beamformer should achieve a higher SNR than the Capon beamformer when snap-shot support is low due to the physical constraints.

Figure 5-3 shows the array gain of the PS-PCML, Bartlett, and MPDR (Capon) beamformer outputs at 200 Hz for a 20 sensor linear array cut for 250 Hz, with a 10 dB interference plane wave at $u = 0.5$ and 5 dB sensor noise. The array is steered to $u = 0.4$, and results are averaged over 5 trials. Figure 5-3 shows that the PS-PCML beamforming approach has a much higher output SNR for $L < 2N$ compared with the Bartlett and Capon beamformers. As the number of snap-shots increases, the Capon beamformer output SNR will converge on the SNR level achieved using the ensemble covariance matrix; the PS-PCML output SNR will never reach this SNR level because it uses the maximum-likelihood covariance matrix for the smoothed wavenumber-power spectrum.

Figure 5-4 shows the array gain for the Bartlett, MPDR, and PS-PCML beamformers using the simulated spectral covariance matrix of a standard 20 sensor linear array for a 20 dB discrete plane wave interference, 0 dB sensor noise, and 0 dB isotropic noise. The array gain is computed for interference plane wave wavenumbers between 0 to 2 null-to-null beamwidths (BW_{NN}) from the steering angle. The figure shows the PS-PCML beamformer has higher gain than the Bartlett beamformer in the main lobe region, and has smoother sidelobes, but less gain at $0.5/BW_{NN}$; this is expected because the PS-PCML approach smooths power in the wavenumber domain. The first sidelobe in the PS-PCML array gain is located at $0.4/BW_{NN}$ and is 15.9 dB higher than the array gain at u_I=0.

Figure 5-5 shows the array gain for the Bartlett, MPDR, and PS-PCML beamformers

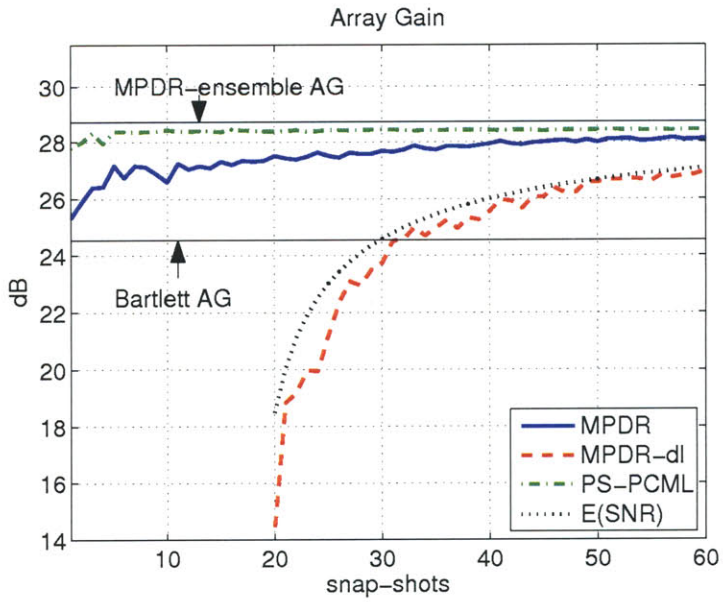

Figure 5-3: Array gain for the (blue) MPDR without diagonal loading, (red) MPDR with 1% diagonal loading, and PCML beamformers at 250 Hz. The results are averaged over 20 trials for a 20 sensor array steered at $u = 0.4$, $u_I = 0.5$ at 10 dB, and 5 dB sensor noise.

using the sampled covariance matrix, generated with two snap-shots, of a standard 20 sensor linear array for a 20 dB discrete plane wave interference, 0 dB sensor noise, and 0 dB isotropic noise; results are averaged over 50 trials. In the sidelobe region, the PS-PCML beamformer has over 2 dB more gain than the MPDR beamformer, and at $u_I = 0$ the PS-PCML beamformer has higher array gain than the MPDR beamformer.

Sensor Position Sensitivity

Figure 5-6 shows the wavenumber-power estimate for the Bartlett, MPDR, and PS-PCML beamformers using the simulated spectral covariance matrix of a standard 20 sensor linear array for a 20 dB discrete plane wave interference at $u_I = 0.1$, 0 dB sensor noise, and 0 dB isotropic noise. Sensor positions are varied using a unit-variance Gaussian random variable to measure the effect of sensor position perturbation on estimated wavenumber-power. The figure shows that the PS-PCML response at $u = 0.1$ is about the same as that of the unbiased Bartlett beamformer; the MPDR response is noticeably lower. Measured over 100 trials, the variances of the wavenumber-power estimate at $u = 0.1$ for the Bartlett, PS-PCML, and MPDR beamformers are -15.1, 7.8, and 34.5 dB, respectively, and the mean values are 40.0, 39.9, and 32.9 dB, respectively. This example shows that the PS-PCML

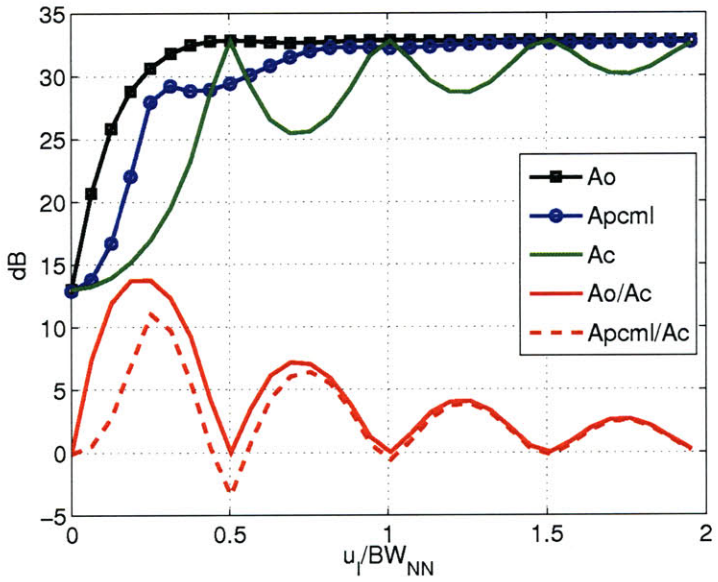

Figure 5-4: Array gain with the actual covariance matrix: (black) MPDR, (blue) PS-PCML, and (green) Bartlett beamformers.

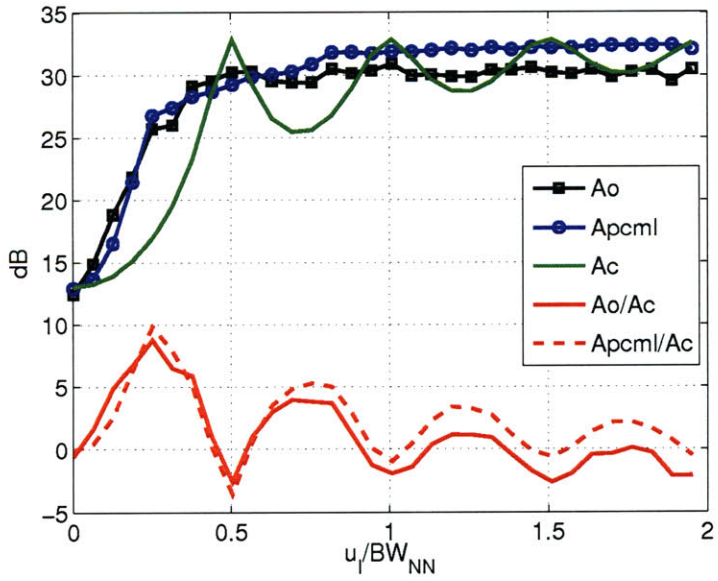

Figure 5-5: Array gain with the sampled covariance matrix: (black) MPDR, (blue) averaged covariance PS-PCML, and (green) Bartlett beamformers.

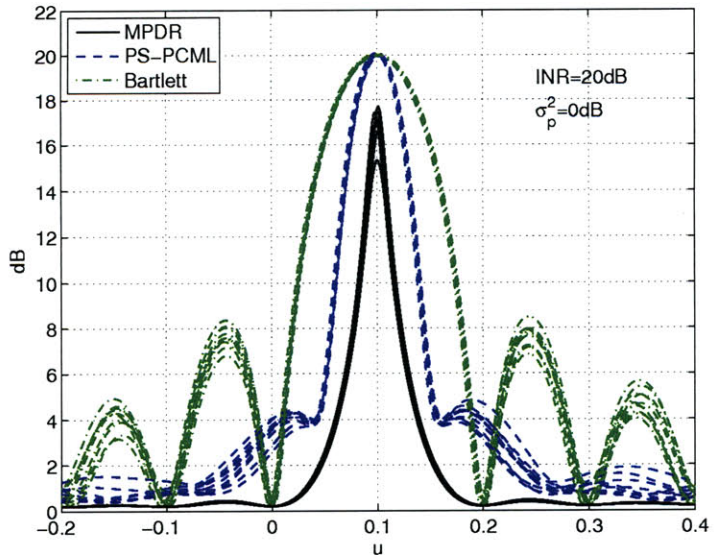

Figure 5-6: Wavenumber power estimate of a 20 dB interference using the MPDR, PCML, and Bartlett beamformers, with a unit-variance Gaussian sensor position perturbation added; results are plotted for 10 trials.

beamformer wavenumber-power estimate is less biased and has less variance compared with the Capon beamformer when sensor positions are randomly perturbed. In practice, array sensor positions are often not known with any high degree of precision – e.g., for towed hydrophone arrays – and the PS-PCML beamformer is clearly a good compromise between high SNR gain and low wavenumber-estimate bias/variance.

Beampattern Characteristics

Figure 5-7 shows the beampatterns for the Bartlett, MPDR, and PS-PCML beamformers using the simulated spectral covariance matrix of a standard 20 sensor linear array for a 20 dB discrete plane wave interference at $u = 0.175$, 0 dB sensor noise, and 0 dB isotropic noise. The figure shows that the PS-PCML beampattern has a wider null at $u = 0.175$ and stronger attenuation in the surrounding region than the MPDR beampattern; this is an effect of the PS-PCML's inherent wavenumber-power smoothing which limits the theoretical maximum SNR gain below that of the Capon beamformer, for a stationary environment with a large number of snap-shots. One advantage of wide-nulls is that small changes in array orientation or interference direction will have a less deleterious effect on the output SNR of the PS-PCML beamformer than the Capon beamformer.

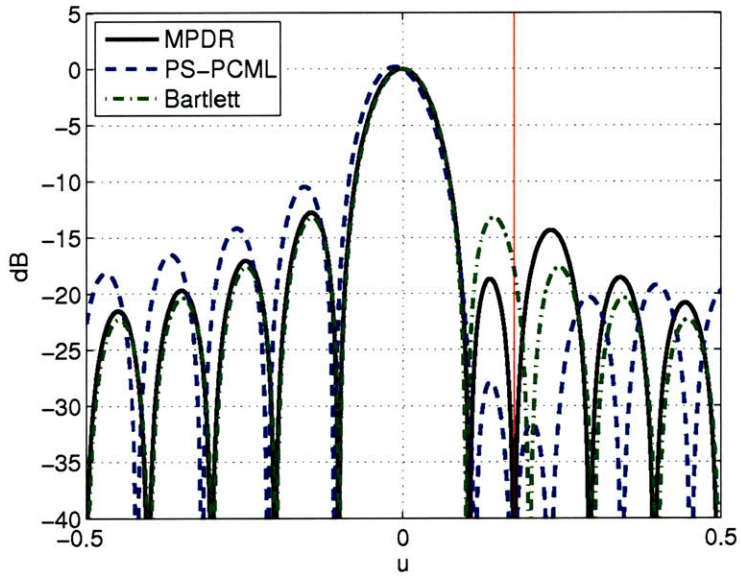

Figure 5-7: Beampatterns for the PCML, Bartlett, and MPDR beamformers for a 20 sensor standard array, with a 20 dB interference at u=0.175.

5.4 PS-PCML Performance with Real Data

This section investigates the performance of the PS-PCML beamformer with BASSEX data record *jd266025147L1000*, gathered with the FORA hydrophone array in the Kermit-Roosevelt Seamount scattered field. The record contains 1300 sec LOAPEX transmissions, transmitted on a 68.2 Hz carrier, and the acoustic pressure time series from 62 hydrophones spaced 3 m apart. The data shows array orientation changes over the duration of the transmission and significant background noise. The PS-PCML beamformer sidelobe control, sensitivity, and bias will be compared with that of the Bartlett and MPDR beamformer performances. Table 5.1 provides the specifications of the PS-PCML and MPDR beamformers used.

Figure 5-8 shows the Bartlett beamformer bearing-time response (BTR) [7] for data record *jd266025147L1000*. The LOAPEX m-sequence signal arrives at about 100 deg and spans 1300 sec. Strong engine and distant shipping traffic noise are present in the BTR between 0 and 50 deg. Signal arrival angle variations are visible in time, and high sidelobes are present at angles above and below the m-sequence DOA.

Figure 5-10 shows the PS-PCML beamformer BTR for data record *jd266025147L1000*. The PS-PCML beamform appears to have lower sidelobes and higher resolution compared with the Bartlett BTR. Figure 5-9 shows the MPDR beamformer BTR for data record *jd266025147L1000*. The MPDR has higher resolution than the PS-PCML beamformer.

Figure 5-11 shows the measured broadband half-power beamwidth (HPBW) at each time step for the Bartlett, MPDR, and PS-PCML beamformers. The HPBW of the Bartlett, MPDR, and PS-PCML beamformers are approximately 6.8, 1.7, 3.2 deg.[8] The MPDR beamformer has the highest resolution; however, the PS-PCML beamformer resolution is a significant improvement over the Bartlett beamformer.

Figure 5-12 shows the estimated power response at each time step for the Bartlett, MPDR, and PS-PCML beamformers. The PS-PCML is relatively unbiased throughout the reception, compared with the Bartlett beamformer, whereas the MPDR is biased by about 1 dB.[9]

[7] BTR's show spatial-spectral power over time and angle off-endfire.

[8] The FORA array has a 8.7λ aperture at 68.2 Hz, which gives approximately 6.6 deg spatial resolution at broadside.

[9] The addition of diagonal loading from the WNGC makes it difficult to determine exactly how much bias is to be expected.

Table 5.1: Specifications for the PS-PCML and MPDR time-varying beamformers, which are applied to BASSEX data containing LOAPEX source transmissions.

L_{array}	=	190.5 m
c	=	$c_{measured} \approx 1500$ m/s
f_{samp}	=	195.3 Hz
nfft	=	$256 \geq \frac{c}{8L_{array}} f_{samp}$
filter update every	=	21 sec
covariance matrix sample	=	83 sec
number of snapshots	=	128
diagonal loading	$\geq$	$1 \cdot 10^{-2} \left(\frac{1}{N} \mathrm{Tr}[\hat{\mathbf{S}}_n(\omega)] \right)$
WNGC	$\rightarrow$	$\| \mathbf{w}_o \|^2 < \frac{3}{N}$

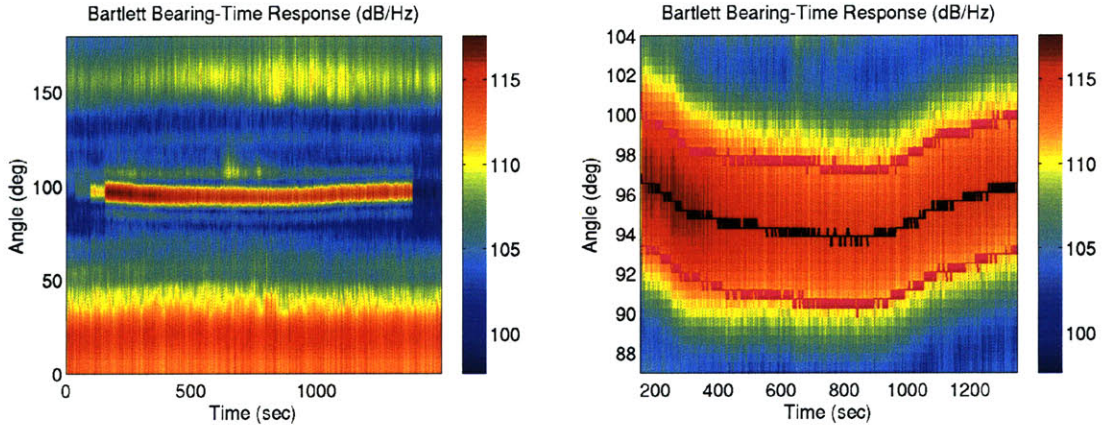

Figure 5-8: Bearing-time response for Bartlett beamformer, BASSEX data set *jd266025147L1000*; peak response (black), 3 dB boundary (magenta), angle is off-endfire.

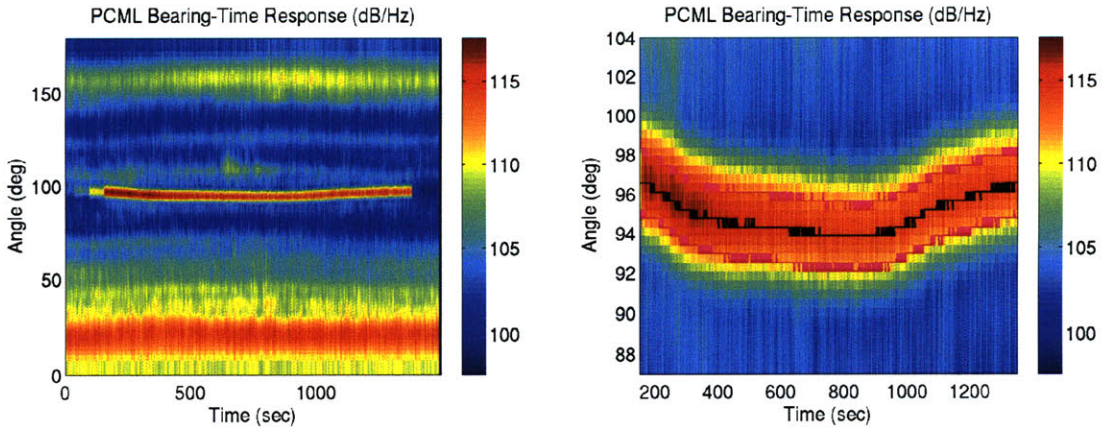

Figure 5-9: Bearing-time response for PCML beamformer, BASSEX data set *jd266025147L1000*; peak response (black), 3 dB boundary (magenta), angle is off-endfire.

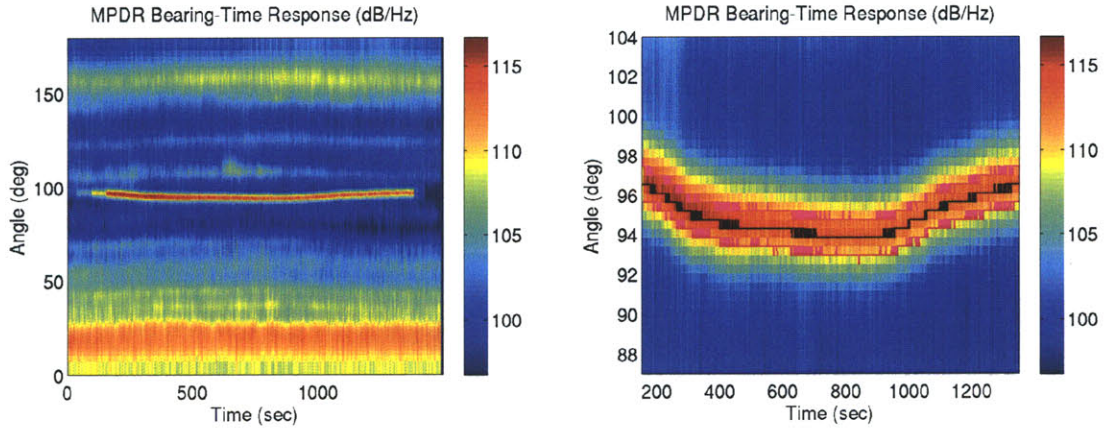

Figure 5-10: Bearing-time response for MPDR beamformer, BASSEX data set *jd266025147L1000*; peak response (black), 3 dB boundary (magenta), angle is off-endfire.

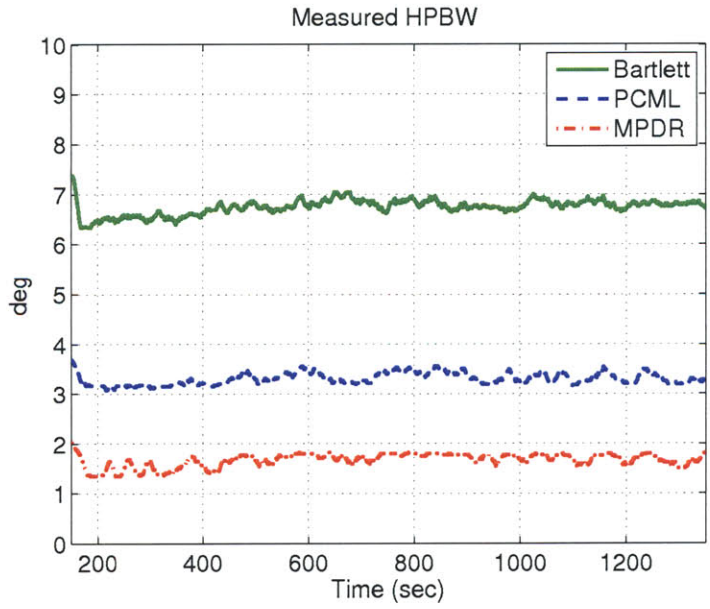

Figure 5-11: Measured broadband HPBW for BASSEX data set *jd266025147L1000*.

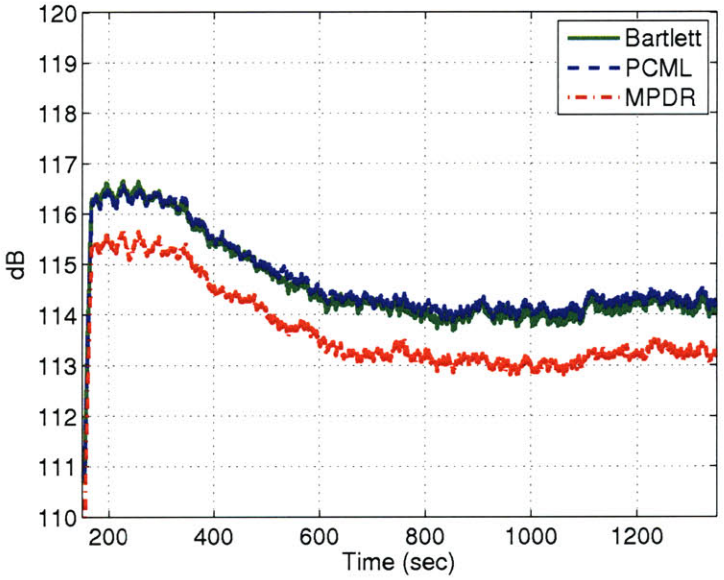

Figure 5-12: Estimated signal level for BASSEX data set *jd266025147L1000*.

5.5 Conclusion

This chapter reviewed the PCML beamfomer and offered the new PS-PCML method to improve computational efficiency and to improve SNR when snap-shot support is low. The PS-PCML method estimates the maximum-likelihood spectral covariance matrix for a uniform line array by modeling the covariance matrix as the sum of propagating and sensor noise covariance matricies; propagating energy is modeled using a set of trigonometric basis functions which represent plane waves that span visible wavenumber space, and sensor noise is modeled with a weighted identity matrix. It was determined that the maximum-likelihood estimates of the propagating energy are only a function of the known power terms ξ_n and unknown sensor noise; therefore, only the maximum-likelihood value of sensor noise must be determined, improving computational efficiency over previous methods. Physical constraints are presented to ensure a positive definite, well conditioned spectral covariance matrix estimate for broadband beamforming with reduced superdirectivity. A zero-padding approach is offered which gives equal weighting to both on- and off-basis propagating energy in the creation of the PS-PCML covariance matrix, ensuring proper null placement.

The PS-PCML method is shown to be robust to sensor position perturbation, snap-shot deficiency, has higher array resolution than the conventional beamformer, and has low wavenumber-power estimate bias. The PS-PCML method was applied to seamount side-scattered data from the BASSEX data set to measure beamformer performance with real-world data. Results show that the PS-PCML wavenumber-power estimate has very low bias, and higher resolution and lower sidelobes compared with the Bartlett beamformer.

The PS-PCML method is applied to BASSEX data in Chapter 6 to investigate the Kermit-Roosevelt side-scattered acoustic field. Records containing side-scattered acoustic pressure measurements are corrupted by data drop-outs and show significant array orientation changes which reduce snap-shot support, both of which affect the bias and sensitivity of the MPDR beamformer.

Chapter 6

Analysis of the BASSEX Data Set

This thesis has discussed the underwater principles and data analysis techniques necessary to investigate the forward-scattered acoustic fields of the Kermit-Roosevelt Seamounts using data from the BASSEX experiment. In Chapter 2, previous work relating to the topics in this thesis were summarized, underwater acoustic propagation principles were presented, details of the BASSEX experiment were given, and the RAY and RAM acoustic modeling codes were discussed. In Chapter 3, observational methods were presented which are used to interpret BASSEX data. In Chapter 4, adaptive beamforming was discussed, and a complete description of the data processing algorithm used to process much of the BASSEX data was given. In Chapter 5, a computationally efficient method for implementing the PCML beamformer was developed to improve the SNR and resolution of hydrophone array output data which is corrupted and/or non-stationary in time. This chapter investigates the forward-scattered fields of the Kermit-Roosevelt Seamounts using BASSEX data. Measured and simulated acoustic arrival patterns are presented to demonstrate the formation of convergence zones and to identify acoustic rays in the forward-scattered fields of the Kermit-Roosevelt Seamount, and to verify the accuracy of acoustic modeling codes in range-dependent ocean environments. Effects caused by environmental uncertainty and natural variability on acoustic arrival patterns are identified in the experimental data.

Section 6.1 discusses the quality of the BASSEX data set in regards to measured ambient and ship generated acoustic noise. Section 6.2 presents Fresnel tube and ray chaos theory to explain unexpected refracted acoustic energy measured inside shadow zones. Section 6.3 presents data used to measure the size and shape of acoustic shadow zones in the scattered

fields of the Kermit-Roosevelt Seamounts. Section 6.4 presents data used to measure the forward-scattered field of the Elvis[1] Seamount in the Kermit-Roosevelt Seamount Complex. Sections 6.5 and 6.6 present data used to measure the forward-scattered field of the Kermit-Roosevelt Seamounts. Section 6.7 presents data used to measure the side-scattered field of the Kermit-Roosevelt Seamount.

6.1 BASSEX Noise Field Analysis

Investigating the measured acoustic noise in a typical data record is useful for designing robust data processing algorithms which maximize signal detection and estimation, and is useful for interpreting processed data. This section characterizes the ambient and ship generated acoustic noise measured inside the Kermit-Roosevelt Seamount Complex, and investigates anomalies in the measured data. The ambient noise in the ocean is dominated by shipping, surface waves, biologics, and cavitation, as was shown by Wenz [3]. In the BASSEX experiment, noise generated by operations aboard the *R/V Roger Revelle* tow ship also contributed to the measured noise field; for example, motor and compressor rotation and propeller blade rate.

Figure 6-1 shows the frequency-power spectrum of the acoustic pressure time series from hydrophone 33 in data record *jd268083141Spice*, estimated using the periodogram averaging method described in Welch [43]. The measured acoustic pressure is strongest at low frequencies, and contains noise from wind, surface waves, earthquakes and explosions. Shipping noise and industrial activity constitutes much of the noise in the 10-300 Hz band. The contribution of an m-sequence signal to the frequency-power spectrum is shown in the 200-300 Hz band; it has a "Gaussian" shaped distribution centered about the 250 Hz carrier frequency. Strong harmonics in the power spectrum are caused by propeller blade rate, motor and compressor rotation, and electric power generation.

Fans, motors, and compressors can create a 30 Hz mechanical hum at 1800-rpm and 60 Hz at 3600-rpm (*i.e.*, at once times shaft rotation frequency). Transformers and motors which use 60 Hz electrical power can generate vibrations at 120 Hz due to *magnetostriction*, a process caused by magnetic forces acting on the core and back iron magnetic domains, and the square relationship between mechanical force and magnetic field which doubles fre-

[1]Edward Scheer named the southern seamount in the Kermit-Roosevelt Seamount Complex the Elvis Seamount during the BASSEX experiment, in honor of Elvis Presley.

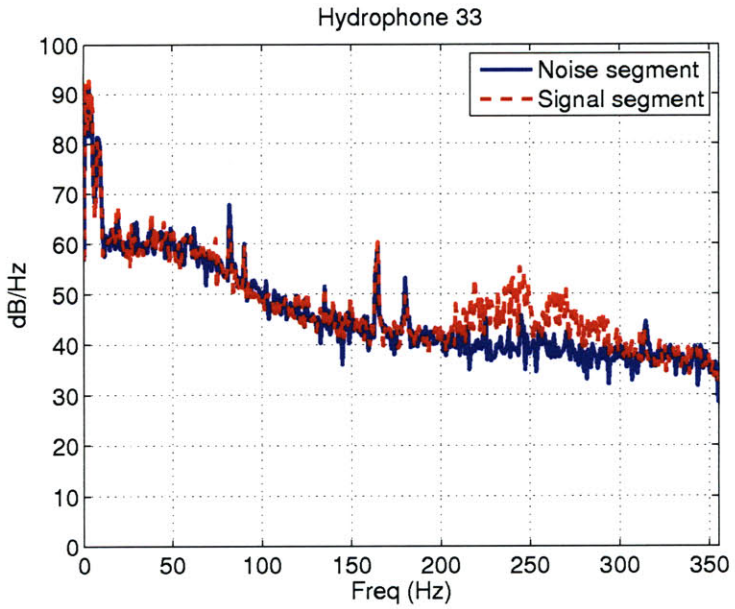

Figure 6-1: Estimated noise spectra for hydrophone 33. The blue line was computed using a section of data without the m-sequence signals present; the red line was computed using data with the m-sequence signals present.

quency, described in Wowk [60]. Other harmonics can be attributed to motor characteristics and misalignment/tolerances.

6.1.1 Horizontal Directionality using Wavenumber-Frequency Diagrams

A wavenumber-frequency $(k-\omega)$ diagram shows the spatial dependence of acoustic power in the frequency domain, and is commonly used with towed hydrophone arrays to identify noise sources. The $k-\omega$ diagram is generated by plotting the power at different frequencies and visible wavenumbers, given by

$$P(k,\omega) = \frac{\omega}{2\pi} \frac{1}{\mathbf{v}_k^H(\omega)\hat{\mathbf{S}}_{DATA}^{-1}\mathbf{v}_k(\omega)}; \tag{6.1}$$

this is the equation for the Capon beamformer wavenumber-power estimator, linearly weighted by frequency.

Figure 6-2 shows the $k-\omega$ diagram for data record *jd268083141Spice*. Red lines are drawn along constant phase speed at ± 1.48 km/s - endfire, ± 3.0 km/s - 60°, and ∞ km/s - broadside. Two m-sequence signals appear in the 200-300 Hz band at forward endfire and 62 deg. The engine and propeller noise appears near forward endfire, spanning the

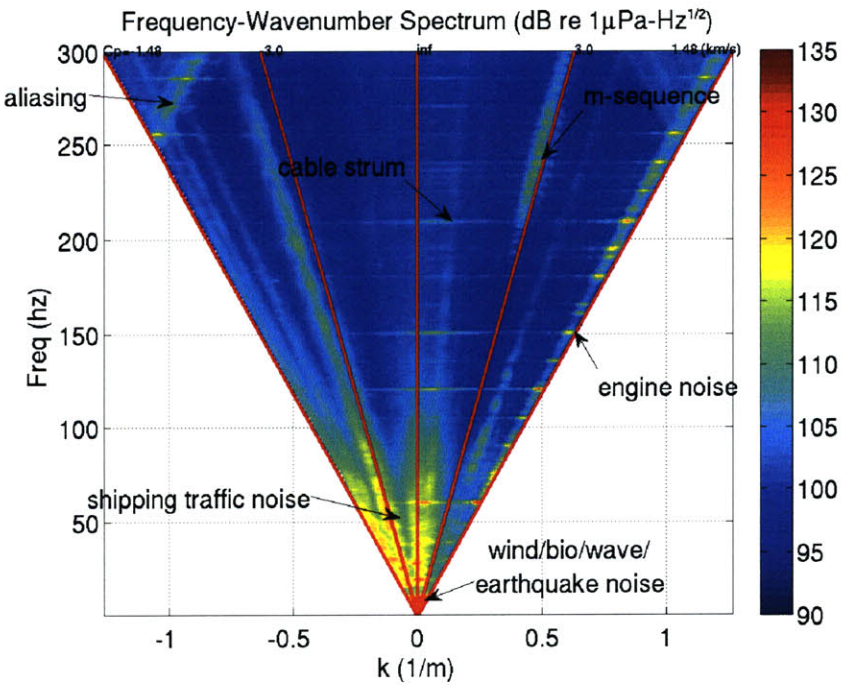

Figure 6-2: Estimated frequency-wavenumber spectrum of noise data in BASSEX record *jd268083141Spice*.

frequency spectrum, and contains harmonics associated with electric power generation. Shipping noise appears in the negative phase speed directions, spanning the frequency spectrum; oscillations in the frequency spectrum are attributed to the constructive and destructive interference. The noise labeled as "cable strum" is not necessarily caused by vortex shedding, and is more probably caused by mechanical vibrations from the tow ship traveling down the tow cable, due to its strong correlation with the observed "engine noise."

Figure 6-3 shows a zoomed view of Fig. 6-2, with a different dynamic range to emphasize low frequency noise. Signals below 10 Hz are difficult to resolve because of array aperture constraints. At frequencies above 10 Hz, the diagram shows structure in the shipping traffic, and vibrational noise near broadside at 60 Hz. Harmonics in the shipping traffic noise are attributed to engine noise and propeller blade rate, and offer a potential means of ship identification; this is beyond the scope of this thesis.

Figure 6-4 shows the frequency-power spectra along four beams using data record *jd268083141Spice* to show changes in noise statistics over time. The upper-left figure shows the power spectrum along the 7.2 deg beam. This figure shows shifting engine noise har-

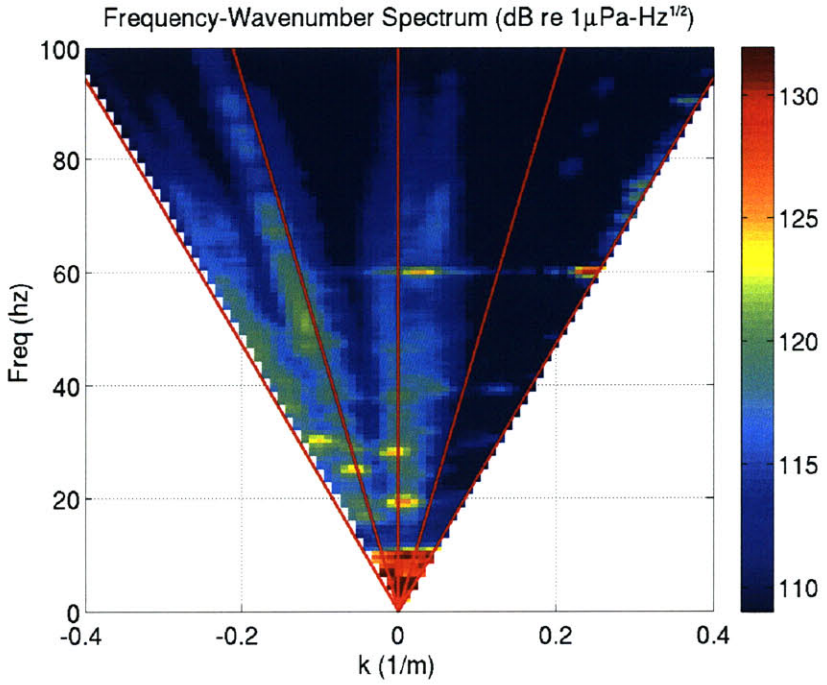

Figure 6-3: Estimated frequency-wavenumber spectrum of noise data in BASSEX record *jd268083141Spice*; zoomed view.

monics over time as the engine control system adapts to waves and varying wind and water current. Strong harmonics at 60 and 120 Hz are probably caused by electric power generation because they exist throughout the reception. A weak m-sequence signal is visible in the 200-300 Hz band, beginning at 210 sec.

The upper-right figure in Fig. 6-4 shows the power spectrum along the 62.2 deg beam. An m-sequence signal appears in the 200-300 Hz frequency band between 240-380 sec. Weak electrical noise is present in the frequency-power spectrum, as well as ambient noise in the lower frequencies below 100 Hz.

The lower-left figure in Fig. 6-4 shows the power spectrum along the 83.0 deg beam. The figure shows vibrational noise harmonics from the tow ship which appear throughout the reception in time without shifting frequency, and are consistent with vibrational noise harmonics seen in the 7.2 deg beam. Strong vibrational noise harmonics near broadside reduce SNR of LOAPEX transmissions received at broadside, which have a 68.2 Hz carrier frequency that is close to the 60 Hz vibrational noise harmonic.

The lower-right figure in Fig. 6-4 shows the power spectrum along the 125.8 deg beam; this beam is in the direction of the strongest shipping traffic noise. The wave pattern

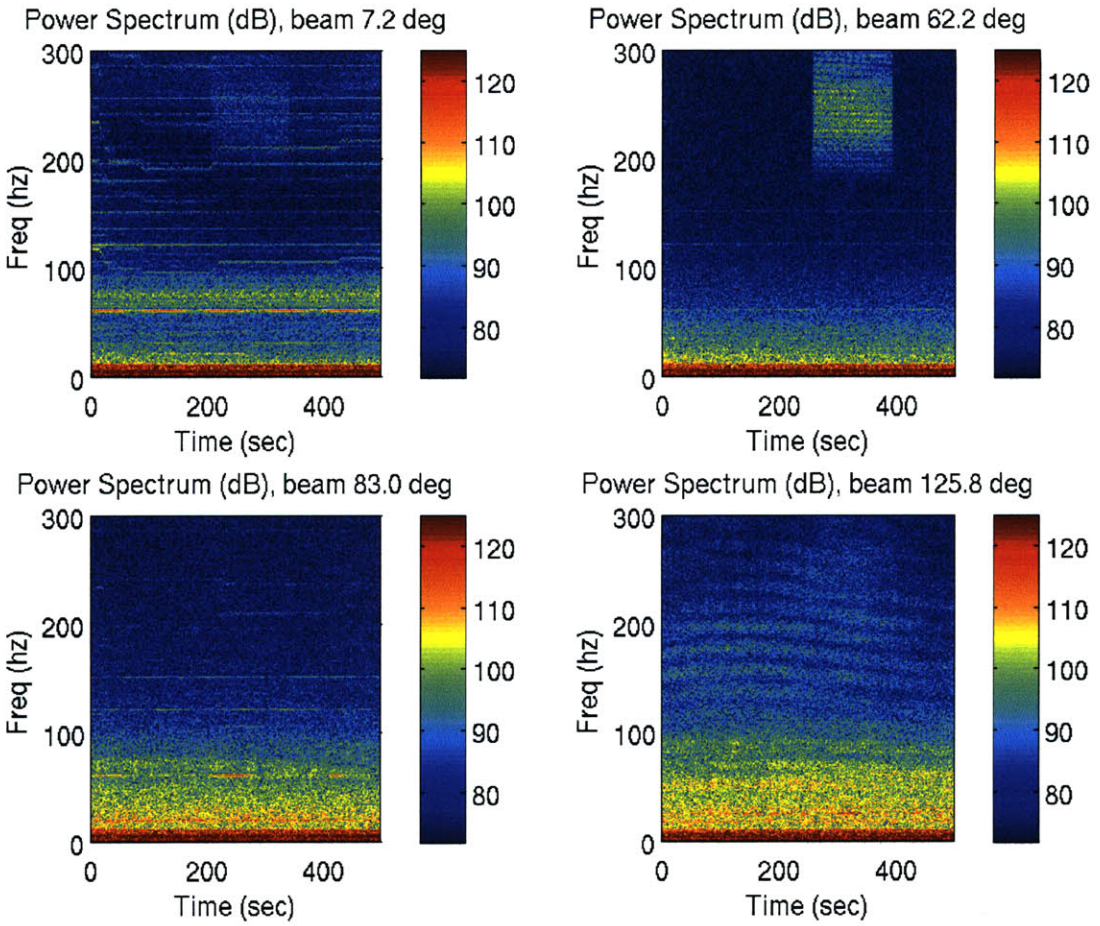

Figure 6-4: Power spectra of the ambient noise field using four discrete beams.

in frequency is caused by the change in the acoustic interference pattern at the receiver depth with frequency.[2] This phenomenon is referred to as the "bathtub" pattern. The pattern variation over time is attributed to changing array location and orientation relative to the source. Time-varying noise field statistics motivate MPDR time-varying adaptive beamforming.

Figure 6-5 shows the bearing-time response of ship-generated vibrational noise at 60 Hz. Strong responses are observed at 20 and 90 deg, and these responses appear correlated in time and multimodal near broadside. The non-stationarity and multimodal nature of the vibrational noise will increase the probability of false alarms and introduce unwanted sidelobes in the array beampattern.

[2]Heaney [61] presents shallow water noise field data from surface ships, with these same characteristics, as a means of determining geoacoustic sediment parameters.

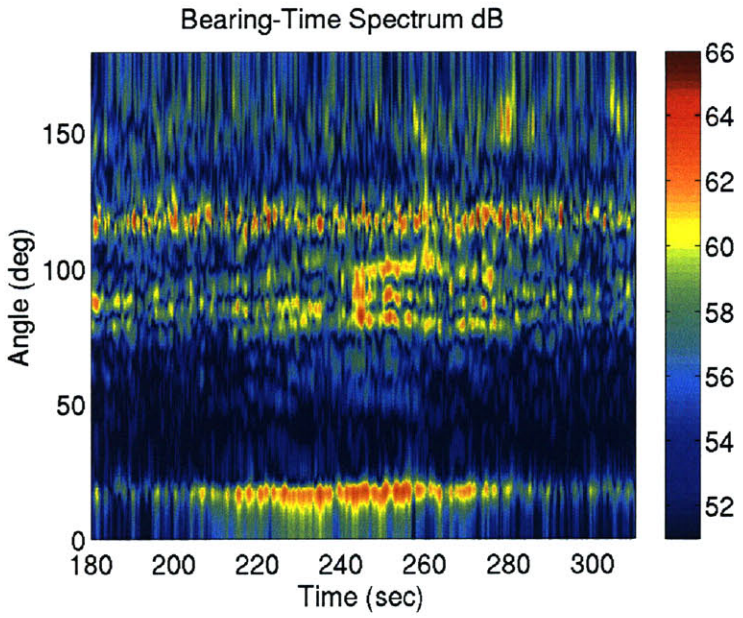

Figure 6-5: Bearing-time response at 60 Hz using MPDR beamforming shows a multimodal, non-stationary cable strum near broadside which is temporally correlated with the ship vibration noise visible at 20 deg.

6.1.2 NOAA Weather Buoy Data

Previous work [3] has shown a strong correlation between the amount of ambient noise in the ocean and wind speed. This section discusses the wind speed contribution to the ambient noise field measured in the ocean during the BASSEX experiment.

The 6-meter NOMAD weather buoy, Station 46006, was located 600 nm to the west of Eureka, CA at position 40.89° N, 137.45° W during the BASSEX experiment; the buoy is maintained by the National Data Buoy Center. The data from the weather station is obtained from the NOAA online database [62]. The buoy recorded wind speed, direction, temperature, wave height, and other important weather information. It is emphasized that the weather buoy was located approximately 400 miles from the Kermit-Roosevelt Seamount Complex, and while weather systems can be of this scale, the true weather conditions in the seamount complex may actually be significantly different.

Figure 6-6 shows the wind speed and measured acoustic noise level from the BASSEX experiment. The ambient noise level was lower during periods of slow and steady wind speed, and the ambient noise level was higher during periods of fast, erratic wind conditions. This figure suggests that the effects of wind speed introduce between 5 and 10 dB of acoustic noise during the BASSEX experiment, which is consistent with previous work; for example,

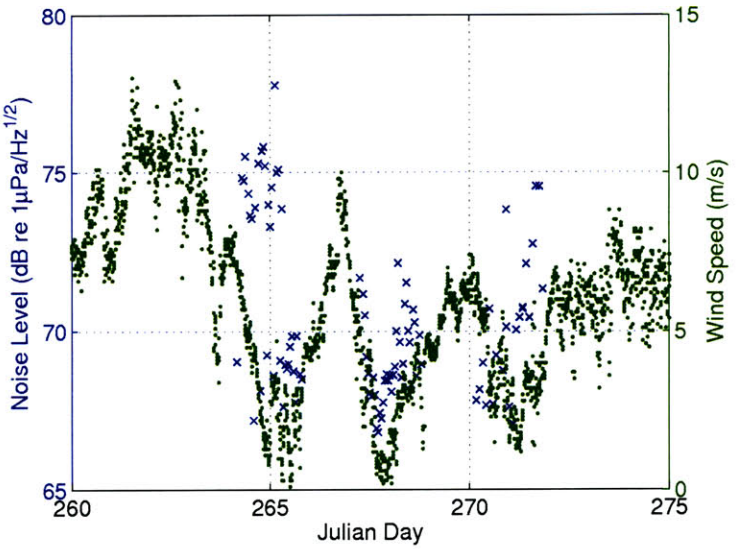

Figure 6-6: Wind speed and measured acoustic ambient noise level in the Central Pacific Ocean between Julian day 260 and 275.

on Julian days 267-268 the wind speed changed from 0 to 5 m/sec, during which time a well correlated change in ambient noise was observed from 65 to 70 dB.

6.2 Fresnel Zones and Ray Chaos

Measured data gathered inside the forward-scattered field of the Elvis Seamount revealed many refracted acoustic rays with amplitude significantly different than RAM simulated results; in some cases, these rays are highly correlated with refracted rays which are predicted by RAM to appear strongly at the receiver approximately 5-10 km closer or further in range. Rypina and Brown [63] show the Fresnel tube width is dependent on ray stability, brought on by environmental inhomogeneity, and micromultipaths consistent with ray chaos[3]; in particular, they showed that internal waves can increase the size of ray Fresnel tubes significantly. Larger Fresnel tube width can cause more energy to be cutoff by the seamount slopes, attenuating certain received refracted acoustic rays, and/or can cause more energy to diffract around the seamount peaks, strengthening certain received refracted acoustic rays.

Ray tracing is an acoustic modeling technique which accounts for propagation along a specific geometric path, solving the eikonal and first transport equations. A Fresnel tube specifies a region about an eigenray containing paths connecting the source and receiver, where the difference in path length is less than $\lambda/4$; this is based on Huygens's Principle which states that every point on an advancing wavefront acts as a source. Ray tracing neglects the Fresnel tube region of acoustic energy. If an obstacle, such as a seamount, blocks the eigenray but does not completely block the Fresnel tube, acoustic energy will still be received.

Assuming line-of-sight propagation, the radius of the Fresnel tube/zone is determined using

$$F_n = \sqrt{\frac{n\lambda D_1 D_2}{D_1 + D_2}}, \tag{6.2}$$

where n is the Fresnel zone number, D_1 is the range from the source, and D_2 is the range from the receiver. As an approximation, Eq. 6.2 suggests that the sound paths between SPICEX source S2 and the Elvis Seamount, for a receiver range of 500 km, have a Fresnel tube radius of about 634 m at the seamount peak; however, the BASSEX experimental results suggest a Fresnel zone of 5-10 km. Numeric results presented in Rypina and Brown [63], for a 100 Hz source and 500 km typical ocean environment, with Garrett-Munk internal waves, show the

[3]Ray chaos in range-dependent underwater acoustics was first reported by Palmer *et al.* [64], who suggested that acoustic ray paths in range-dependent deterministic ocean environments will have chaotic behavior with exponential sensitivity in range to initial conditions, such as launch angle.

Fresnel zone width to be approximately 10 km. The SPICEX source transmitted at 250 Hz, which should theoretically, using Eq. 6.2, reduce the size of the Fresnel tube by about 0.6; this implies a tube width of about 6 km, which is consistent with BASSEX results.

6.3 Analysis of the Kermit-Roosevelt Seamount Complex Forward-Scattered Fields

This section analyzes measured acoustic arrival patterns from data gathered inside the forward-scattered fields of the Kermit-Roosevelt and Elvis Seamounts. Measured results will be compared with numeric simulations using RAY and RAM acoustic model results generated by Hyun Joe Kim of MIT.

Figures 6-7(a) and 6-7(b) show the range-stacked normalized, beamformed, pulse compressed acoustic time series taken from 93 recordings measuring SPICEX m-sequence signals from SPICEX source S1 and S2, respectively. The figures also show ray trace results, for a flat-bottom ocean, generated by Edward Scheer of Woods Hole Oceanographic Institute; red dots indicate acoustic ray arrivals. The curved ray patterns indicate refracted rays, and the sparse, late arrival rays indicate bottom-reflected rays. Reduced time[4] is used for a 1500 m/s reference sound speed.

The measured data and ray-trace results show good agreement in terms of arrival time for open-ocean propagation; however, DAQ timing errors make a quantitative measure of arrival time agreement difficult to attain. Also, time series are difficult to compare with ray trace results behind the seamounts due to bathymetric scattering; acoustic arrival patterns in these regions will be rigorously investigated in Sections 6.4-6.6.

The acoustic rays appear to arrive earlier than expected for SPICEX source S1 receptions, and later for SPICEX source S2 receptions. Early arrival times for the SPICEX source S1 receptions are attributed to sound velocity profile uncertainty along the sound path. Late arrival times for the SPICEX source S2 receptions are attributed to a DAQ random start time error between 0-0.25 sec.

[4]Reduced time is useful for comparing arrival patterns at different ranges by removing the time shift associated with the difference in path length.

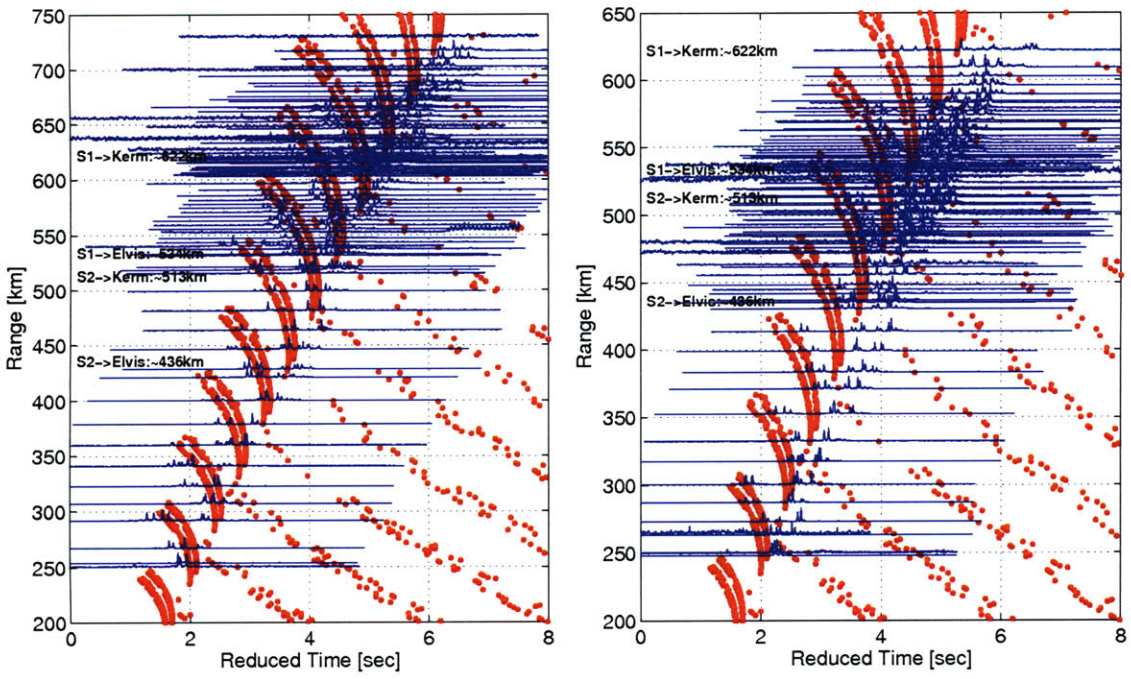

(a) SPICEX S1

(b) SPICEX S2

Figure 6-7: Range-stacked acoustic time series (blue) for 93 SPICEX receptions and ray trace results (red). Acoustic pressure is normalized and seamount ranges are given with respect to the source.

6.3.1 Acoustic Shadowing by the Kermit-Roosevelt Seamounts

This section demonstrates the formation of convergence zones and acoustic shadowing in the forward-scattered field of the Kermit-Roosevelt Seamounts. SPICEX sources transmitted 2.5 min m-sequences every hour during the experiment. The tow ship traveled throughout the Kermit-Roosevelt Seamout Complex during the experiment, providing a spatially-sparse sampling of the acoustic scatter field at a depth of about 280 m. Figure 6-8 shows the ship tracks during the experiment on top of a bathymetry contour map where acoustic data were gathered. Tracks 1, 2, 3, and 5 are used to measure the shadow zone regions of the Kermit-Roosevelt Seamounts, and Track 4 is used to measure the width of the perturbation zone behind the seamounts.

Acoustic shadowing and the formation of convergence zones in the forward-scattered fields of the Kermit-Roosevelt Seamount can be demonstrated using the measured peak acoustic pressure level of transmissions from the SPICEX sources. Figures 6-9 and 6-10 show the measured peak acoustic pressure in the Kermit-Roosevelt Seamount Complex, derived from beamformed, pulse compressed data. Test station locations are indicated using black

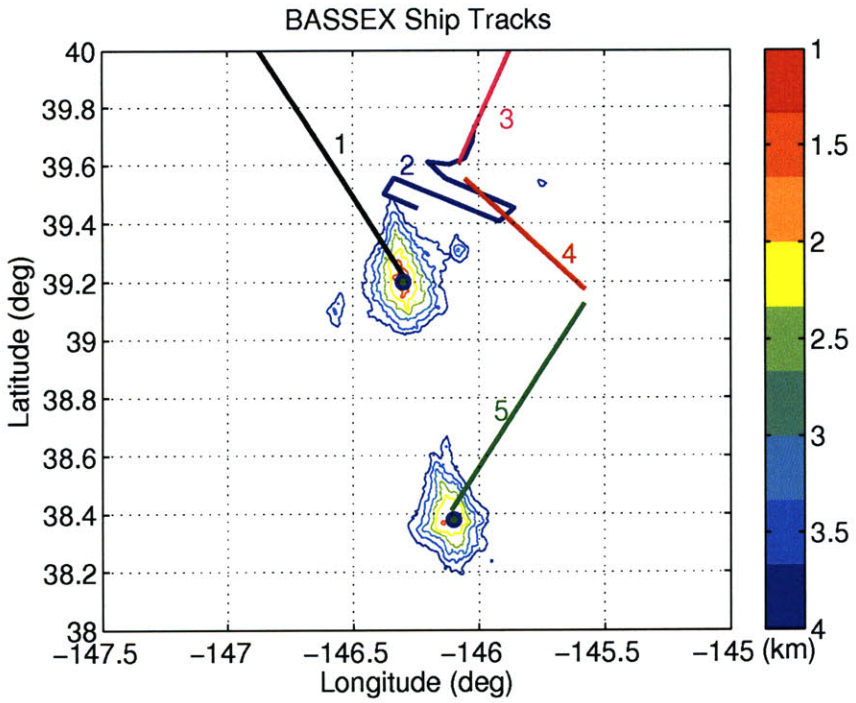

Figure 6-8: Ship Tracks inside the Kermit-Roosevelt Seamount Complex during the BASSEX experiment. Bathymetry is given in km.

crosses, the location of the two seamounts are indicated with green-blue circles, and the general direction of sound propagation from the source is indicated with arrows. Pressure levels are linearly interpolated where data is unavailable using the Delaunay triangulation algorithm, which is implemented by Matlab's *griddata* command.

Figure 6-9 shows the measured peak acoustic pressure from SPICEX source S1; very few samples of the Elvis Seamount forward-scattered field are available. This figure shows that convergence zones form in the forward-scattered field of the Kermit-Roosevelt Seamount, along Track 1, with acoustic pressure fluctuations of about 20 dB, relative to the ambient levels. There were no ship tracks perpendicular to the direct propagation path, and therefore the width of the acoustic shadow zone behind the seamount cannot be determined from this figure. Test stations behind the Elvis Seamount, located in the forward-scattered field, indicate acoustic shadowing of about 20 dB.

Figure 6-10 shows the measured peak acoustic pressure from SPICEX source S2. This figure shows that convergence zones form in the forward-scattered fields of both seamounts along Tracks 3 and 5, and acoustic pressure fluctuations are about 35 dB and 30 dB in the Kermit-Roosevelt and Elvis Seamount forward-scattered fields, respectively.

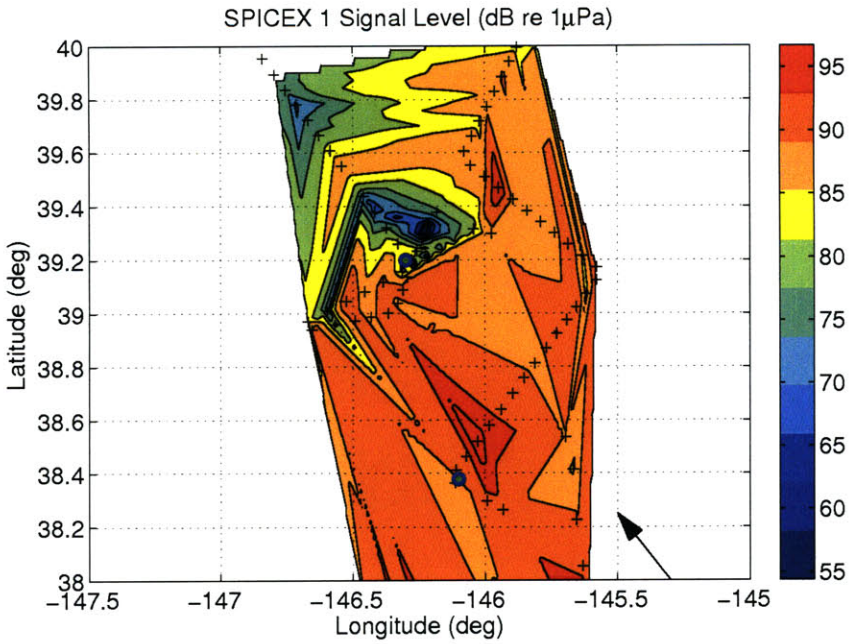

Figure 6-9: Measured peak sound level received from SPICEX source 1.

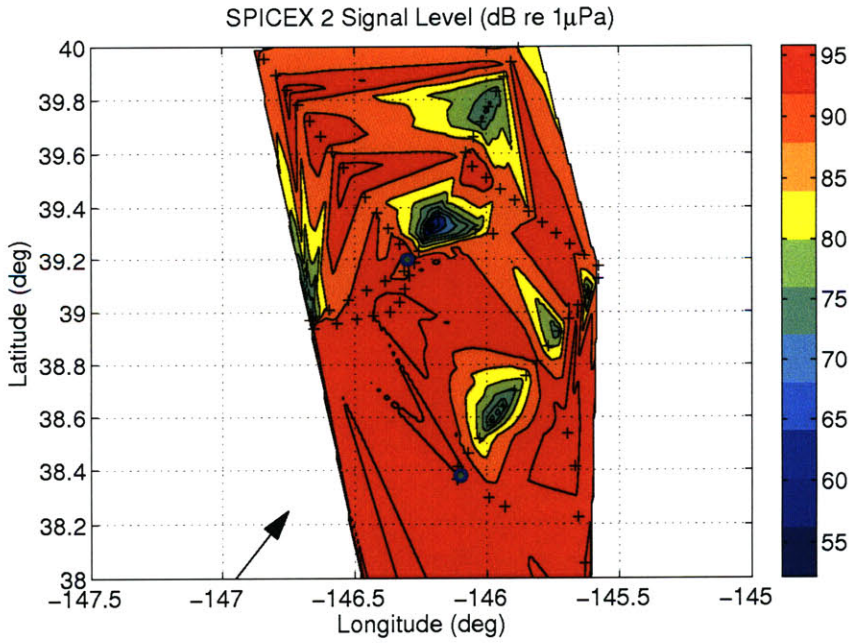

Figure 6-10: Measured peak sound level from SPICEX source 2.

6.3.2 The Width of the Forward-Scattered Fields

This section shows that the acoustic forward-scattered fields span the projected base width of the two seamounts, as was stated by Eskenazi [29] and Ebbeson and Turner [10]. Figure 6-11 shows the test station locations along Track 4 and the bathymetry contours of the seamounts between 0 and 4 km; these test stations are used to measure the width of the forward-scattered field.

Figure 6-12 shows the measured, normalized acoustic pressure for each test station along Track 4 overlayed on top of ray trace results (red dots). Complete acoustic shadowing of steep angle acoustic rays between 3.9-4.2 sec is observed in the forward-scattered field behind the Elvis Seamounts at test stations 26723-26801. The measured acoustic perturbation zone is bounded by the projected width of the Elvis Seamount at a depth of about 3 km. Partial acoustic shadowing of steep angle acoustic rays of about 15 dB is observed at test stations 26716-26718 behind the Kermit-Roosevelt Seamount, spanning the projected width of the seamount at a depth of about 4 km.

The ability to observe steep acoustic rays depends on the range of the receiver from the source. If the observable steep acoustic rays are those which dive below 3-4 km at the range of the seamount they will be completely cutoff; however, if the rays only graze the seamount they will appear attenuated (*i.e.*, Fresnel tube cutoff). The test stations behind the Kermit-Roosevelt Seamount are about 50 km from the peak; therefore, the steep acoustic rays at these test stations should be in the upper-water column at the range of the seamount slope, where they pass with little attenuation. On the contrary, the test stations behind the Elvis Seamount are about 80 km from the peak; the steep acoustic rays at these test stations should therefore be in the lower-water column at the range of the seamount, where they are cutoff.

6.3.3 Acoustic Ray Amplitude Variations

Every m-sequence SPICEX transmission contained 11 m-sequence signal periods, which can be averaged together at the receiver assuming adequate phase coherence; however, the phase of received m-sequence periods is highly sensitive to variations in array velocity and sensor position, as well as acoustic ray angle-of-arrival. The following example shows the phase variation of three acoustic rays in BASSEX record *jd268073141Spice*, gathered behind

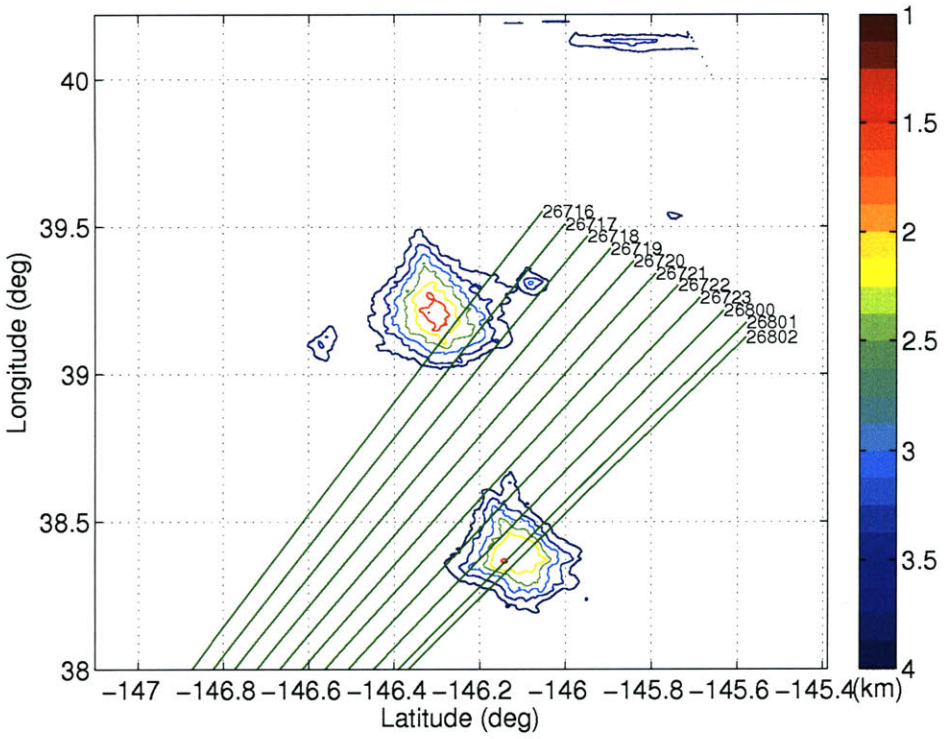

Figure 6-11: Test stations and sound paths along Track 4.

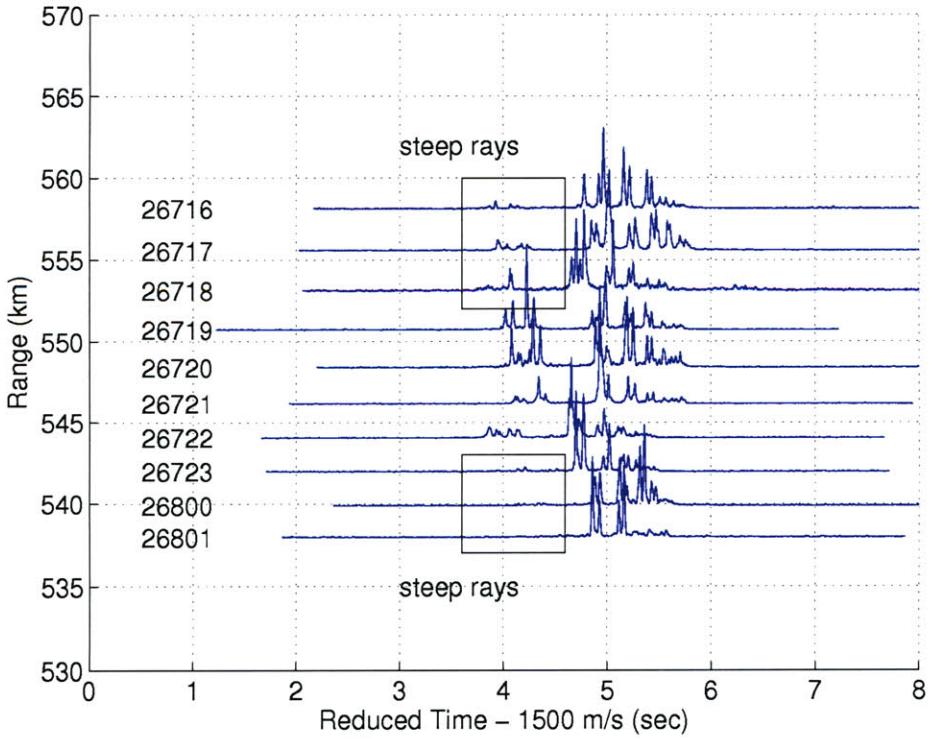

Figure 6-12: Measured, normalized acoustic pressure time series along Track 4.

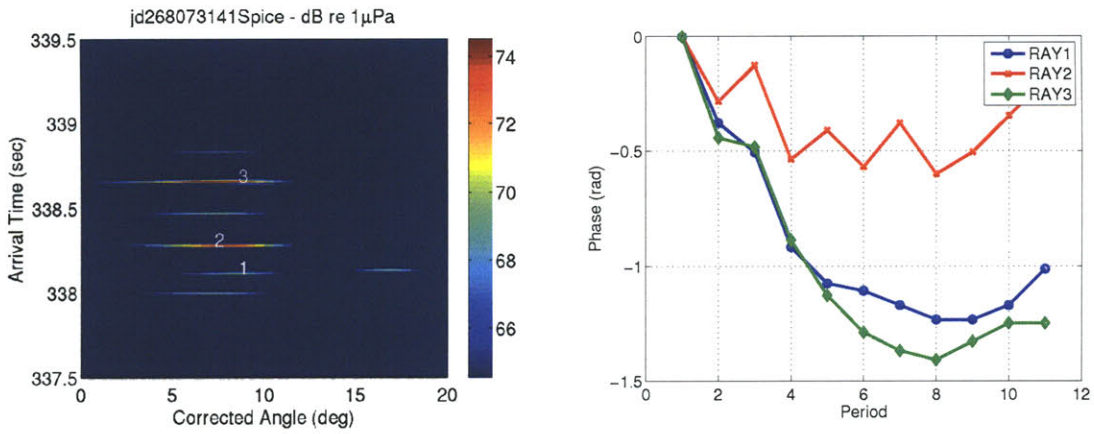

(a) Arrival Pattern

(b) Phase Variation

Figure 6-13: Phase variation of acoustic rays in BASSEX data record *jd268073141Spice*.

the Elvis Seamount inside a convergence zone; this data is processed using the algorithm presented in Fig. 4-3.

Figure 6-13(a) shows the measured acoustic arrival pattern for the first m-sequence period, which contains several reflected acoustic rays. Three acoustic rays with similar arrival angles are investigated, labeled RAY#. Figure 6-13(b) shows the phase of the acoustic ray amplitude at each period for the three acoustic rays; a linear 0.7 phase shift per period was removed to emphasize non-linear phase variations. The phase variations in the acoustic ray amplitudes are highly non-linear, and therefore difficult to remove without more accurate information about the array. An experiment with fixed receiver and/or precise receiver positioning capability is required to accurately measure acoustic ray amplitude temporal statistics.

A Matlab program was developed to incoherently average the acoustic arrival patterns for each SPICEX reception. Incoherent averaging is used to avoid errors caused by non-linear phase distortion between periods. The program identifies the strongest acoustic ray in the first period arrival pattern, and then searches for the same acoustic ray in subsequent arrival patterns. For most records, this approach is quite effective; however, human intervention is required in cases where ray amplitudes vary significantly between periods.[5]

[5]Ray amplitude variations between periods can be attributed to a number of factors: source amplitude variability, natural variability, changing path lengths, array flexing, bottom-reflection, etc..

6.4 The Elvis Seamount Forward-Scattered Field

The Elvis Seamount is a large, conical seamount in the Kermit-Roosevelt Seamount Complex which shoals at 1300 m and has a 50 km base. On Julian day 268, during the BASSEX experiment, measurements of SPICEX source S2 transmissions were taken with the FORA towed hydrophone array inside the seamount's forward-scattered field. The tow ship began the day approximately 100 km behind the seamount and traveled along the geodesic connecting the source and seamount peak. The speed of the array was approximately 4 knots and acoustic measurements were gathered every hour. This section presents the processed data recorded along Track 5 on day 268 and discusses the observed characteristics of the forward-scattered field in relation to numeric simulations and previous work.

6.4.1 Test Station Locations and Bathymetry

Figure 6-14 shows the locations of the test stations used to measure the Elvis Seamount shadow zone, the bathymetry of the seamounts, and the direct sound path between SPICEX source S2 and the Hour 2 test station; test stations are named by the hour in the day during which data was recorded. Figure 6-15 shows the three direct sound paths between the source and Hour 2, 8, and 14 test stations, and Fig. 6-16 shows the bathymetry under each of these sound paths. Clearly the tow ship did not follow the geodesic sound path connecting to the Hour 2 test station, and as a result the bathymetry of the seamount peak between the test stations and source changed significantly. Using RAM, simulated results did not show any significant difference in the acoustic field inside the shadow zone for any of the bathymetry profiles in Fig. 6-16. The sound path connecting the source and the Hour 2 test station are used to generate simulated results in Section 6.4.5.

6.4.2 RAM Simulated Results

Broadband acoustic arrival patterns were generated using the Fourier synthesis method and the RAM acoustic modeler to simulate measured acoustic data. Acoustic pressure is generated at 821 frequencies between 200-300 Hz to create 8.192 sec time series at 1000 Hz sample rate. There are numerous sound velocity profiles, measured with XBT's, available along the geodesic connecting SPICEX source S2 and the receiver locations behind the Elvis Seamount. A porous basalt homogeneous bottom profile is used to model the bottom

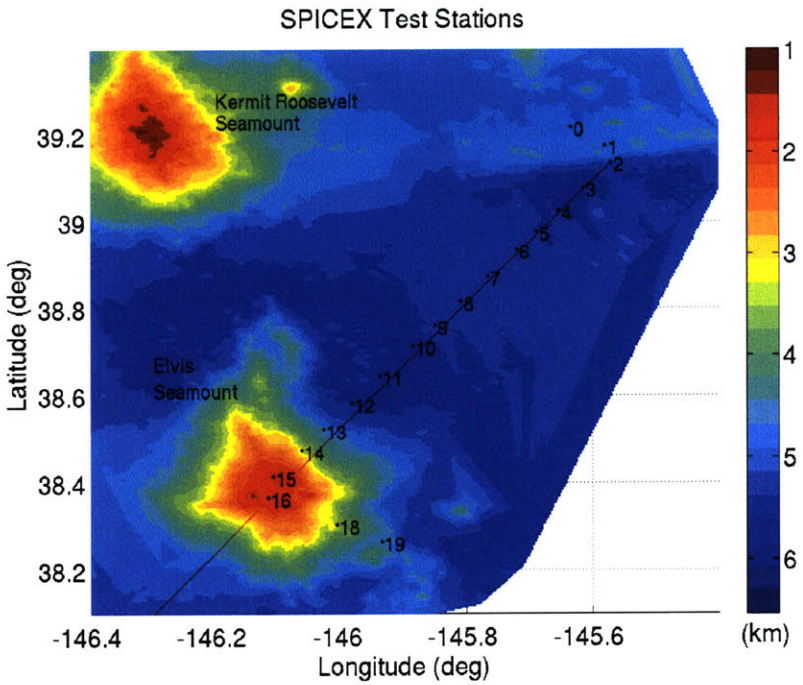

Figure 6-14: Test station locations during day 268.

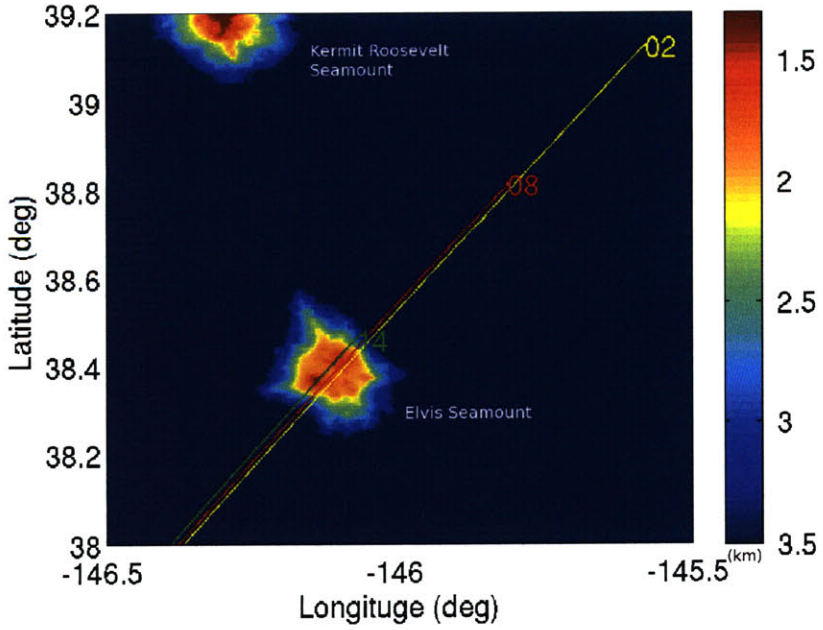

Figure 6-15: Direct sound paths for Hour 02, 08, and 14 during day 268.

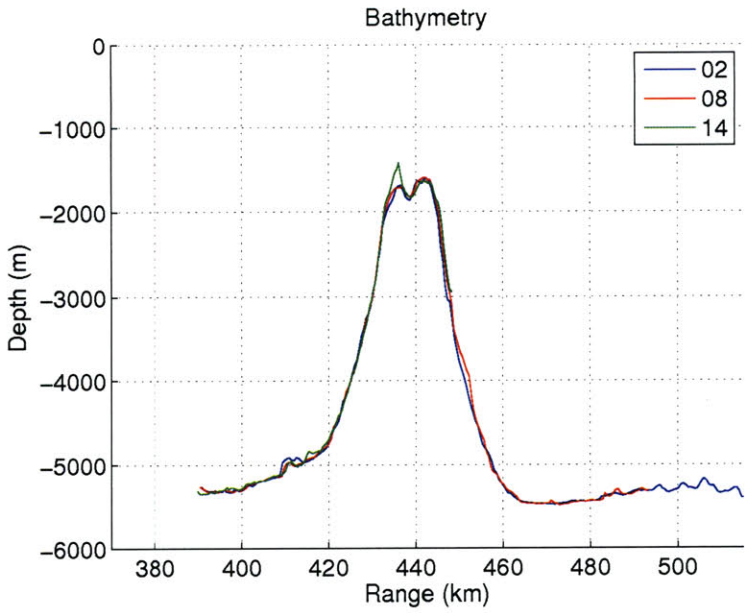

Figure 6-16: Bathymetry along the direct sound path for Hour 02, 08, and 14 during day 268.

sediment layer, with compressional speed of 2200 m/s, density of 2.1 kg/m^3, and attenuation of 0.1 dB/λ, and an absorptive sub-bottom. Simulated PE and ray trace results are provided by Hyun Joe Kim of MIT. [6]

Figure 6-17 shows the RAM generated acoustic pressure time series inside the Elvis Seamount shadow zone as a function of range from the source and reduced travel time. The seamount peak is located 440 km from the source. Strong signal spikes, which appear in groups of four, are ray groups that consist of refracted rays. Ray groups appear unaffected by the seamount in front of the seamount, as backscatter in this region is not modeled by the one-way RAM acoustic modeler. Figure 6-17 is a key tool for understanding and identifying acoustic energy in the forward-scattered field. This figure shows the changes in the forward-scattered field at many ranges, whereas the experimental results are only available every 5-10 km. These results give much more detail than ray trace results, which do not model diffraction. In particular, this figure helps identify acoustic rays in the convergence zone boundary regions where significant Fresnel tube cutoff/diffraction is observed.

Convergence zones appear as areas of strong acoustic energy inside the shadow zone. The strongest acoustic energy inside the convergence zones consists of refracted acoustic

[6]Internal waves are not modeled in these results; however, while investigating the BASSEX data set, RAM simulations which did model internal waves were used to understand and explain observed vertical broadening of the arrival pattern finale region.

energy, since there is no attenuation from bottom interaction. Reflected acoustic energy is present with ray group structure similar to that of refracted acoustic rays, but with time-delay, attenuation, and random perturbation. The time delay in the reflected rays, relative to nearby refracted rays, can be attributed to the additional time spent in shallow waters, which are slower, and the high variability in pressure level is attributed to the irregular bathymetry. In range, each major convergence zone is comprised of a region of strong refracted energy followed by a region of reflected energy. The refracted and reflected acoustic convergence zones appeared in the upper-water column with about 50 km periodicity. Strong reflected energy first appears in the shadow zone about 450 km behind the seamount peak, and strong refracted energy first appears at 475 km.

6.4.3 Measured Peak Acoustic Pressure

Figure 6-18 shows the measured and RAM simulated peak acoustic pressure levels at each test station in the Elvis Seamount shadow zone. The red line indicates the simulated pressure level, and the black indicates the measured pressure level; the errorbars indicate minimum and maximum peak signal level for each of the eleven periods in the m-sequence. The figure shows good agreement of acoustic pressure levels between experimental data and simulated results. The Hours 4, 5, 8, 9, and 10 test stations were located in convergence zones containing strong refracted acoustic energy, Hours 7, 13, and 14 test stations were located in convergence zones containing strong reflected acoustic energy, and Hours 6, 11, and 12 test stations were located in acoustic shadow zones. Experimental results are weaker than simulated results for Hour 10 because of significant Fresnel tube cutoff by the leeward slope of the seamount, and experimental results are stronger than simulated results for Hour 5 because of Fresnel tube diffraction around the seamount peak. In the RAM results, smooth regions are associated with strong refracted energy and "jittery" regions with reflected acoustic energy. Acoustic fluctuations of about 30 dB are observed in the experimental data between measurements taken at the Hour 12 and 15 test stations.

6.4.4 Ray Trace Results

The RAY ray trace modeling program is used to generate a set of observable eigenrays[7] at a given range and depth to identify and describe measured acoustic rays. Eigenrays are

[7]Eigenrays are the sound paths which connect the source and receiver.

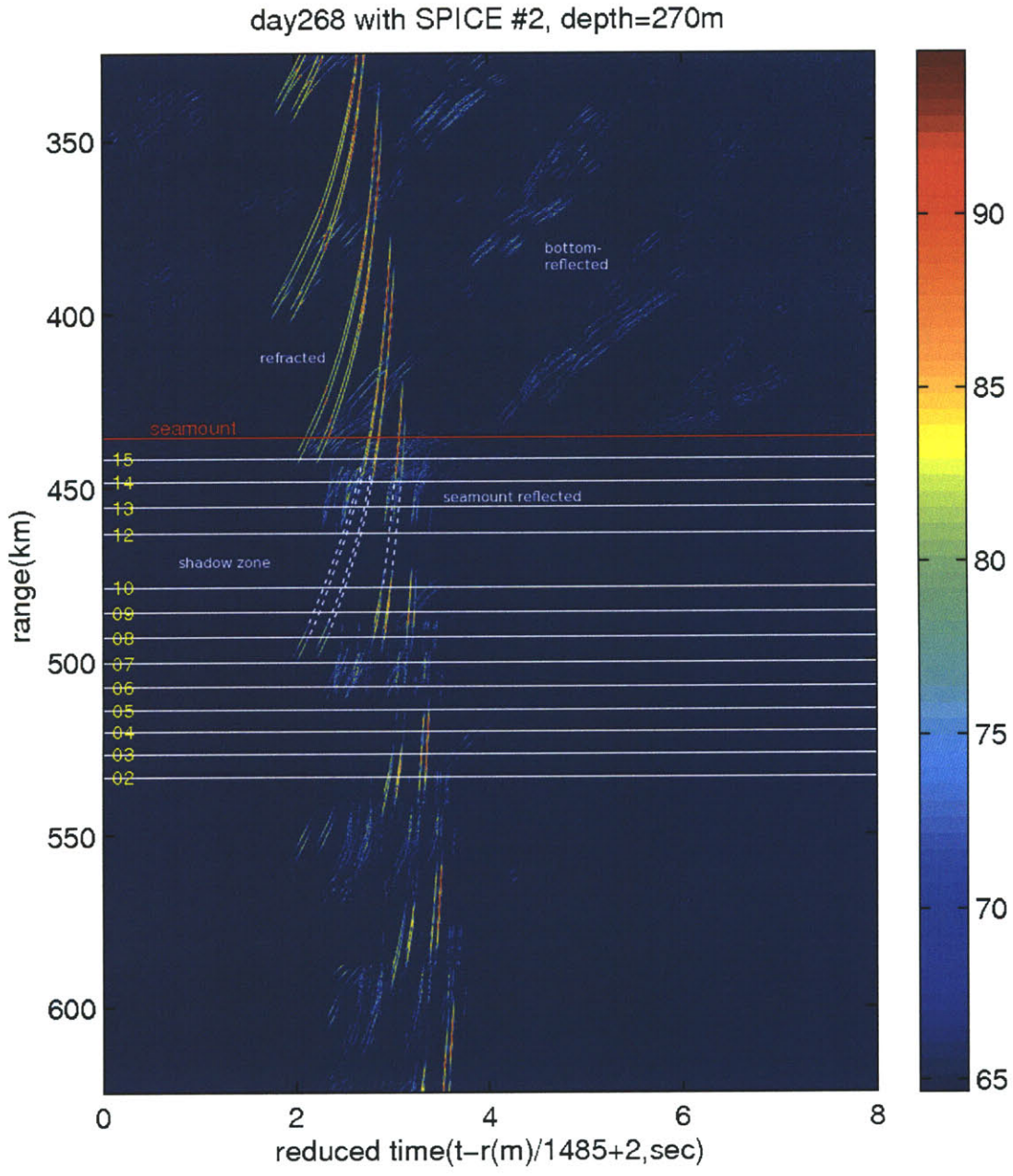

Figure 6-17: Acoustic pressure time series in the Elvis Seamount shadow zone. Test station and seamount peak ranges are indicated. Pressure is plotted in dB re 1μPa.

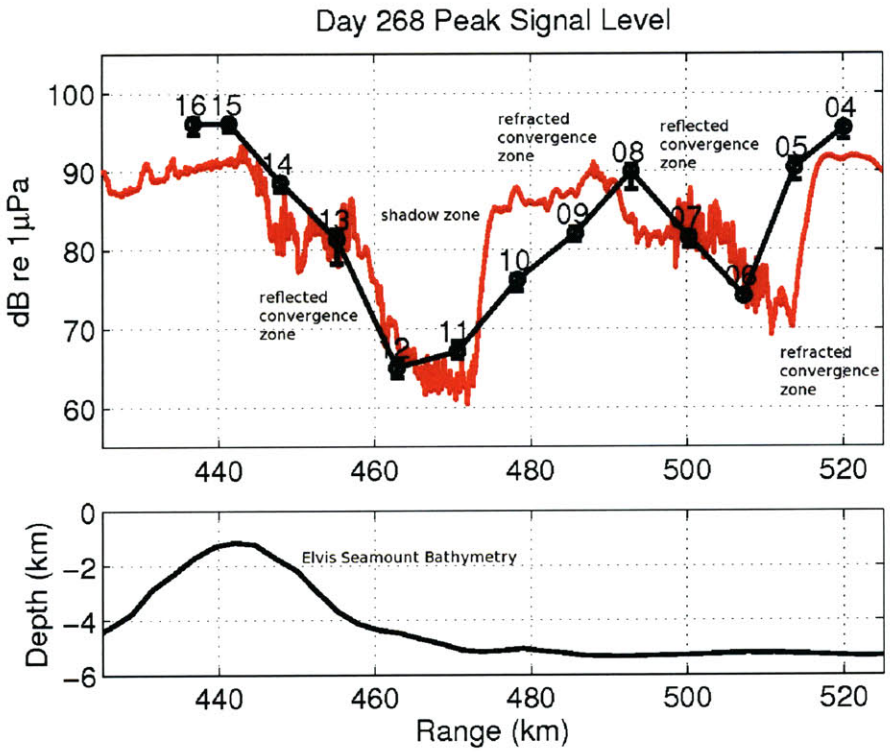

Figure 6-18: Peak signal level for Julian day 268 receptions for: (red) RAM simulated data, (black) MPDR beamformed BASSEX data. Errorbars indicate the maximum and minimum estimated peak power levels over all eleven m-sequence period receptions. Seamount bathymetry is included on the bottom for reference. The MPDR bias of -5.9 dB is removed.

designated with an identification number, followed by the number of turning points, and a +/- to indicate the upwards/downwards launch direction of the ray. The descriptors refracted (R), bottom-reflected (BR), or surface-reflected bottom-reflected (SRBR) are given to indicate any interaction with the surface and bottom bathymetry. A smoothed sound velocity profile was used to provide a bounded second derivative, and specular reflection is used to model bottom interaction.

Table 6.1 provides the refracted and reflected acoustic rays measured at each test station with the hydrophone array identified using RAY simulated results. The table shows that the forward-scattered field of the Elvis seamount is divided into refracted and BR-reflected convergence zones. SRBR energy is present throughout the shadow zone, and received results are difficult to reconcile with the ray trace simulations.

Table 6.1: Results of investigation of ray arrivals for Julian day 268.

Range (km)	arrival-angle (deg)	Refracted ray arrivals at receiver propagation path	arrival-angle (deg)	Reflected ray arrivals at receiver propagation path
520.2	2°-4°	23-R 24+R 25+R	8°-19°	
514.0				
507.4				
500.5			1°-12°	21-BR 23-BR 24+BR 22+BR 21+BR 20+BR
493.2	6°-13°	17-R 18+R 19+R 20-R 21+R	5°	
486.0	1°-8°	19-R 20-R 21-R 21+R 22-R 20+R		
478.6	5°	20+R		
463.2				
455.5			1°-9°	18-BR 19-BR 20+BR 21-BR 19+BR
448.3			1°-15°	18-BR 21-BR 22+BR 20+BR 18+BR 19+BR

6.4.5 Measured Acoustic Arrival Patterns

The following subsections will present the experimental data and simulated results for each test station along Track 5. Each subsection provides a description of the available data for each test station, labeled Hours 2-15. RAM, RAY, and BASSEX results are given as a function of angle-off-endfire and reduced travel time. RAM results are generated using the Bartlett beamformer, and BASSEX results are generated using the MPDR beamformer specified in Table 4.1. BASSEX data were processed using the algorithm given in Fig. 4-3, and an incoherent average was taken over the 11 m-sequence periods. The RAM and BASSEX results have a dynamic range of 30 dB.

Every subsection includes a table which describes each ray group identified in the experimental results. The acoustic ray groups are identified where possible, the identity and angle-of-arrival of individual rays inside the ray groups are given for measured and simulated data, and a comment is provided to describe the rays.

Hour 4

Data set *jd268043348Spice* was recorded in the second convergence zone in the Elvis Seamount's forward-scattered field. Figure 6-19(a) shows RAY results generated using measured bathymetry and sound velocity. Figure 6-19(b) shows the eigenrays, RAM simulated arrival pattern, and BASSEX measured arrival pattern. Table 6.2 gives a discription of the individual ray groups identified in Fig. 6-19(b).

Ray trace results show three refracted rays present in this arrival pattern and several late arriving, steeper SRBR rays. Both RAM and BASSEX results show two strong rays consistent with the arrival angle and time predictions for refracted rays in RAY results; the 2:25+ and 3:24+ rays are probably overlapped, and therefore not separable. Both RAM and BASSEX results are consistent in ray amplitude. Results show two faint, steep rays at 3.25 sec which are part of a refracted ray group believed to contain limiting rays which are partially cutoff by the seamount's leeward slope, due to a larger than expected Fresnel tube width.

Table 6.2: Hour 4 for Julian day 268.

Group	Ray #	sim-*RAY* (deg)	Measured (deg)	Comments
1	(1^{st} ray)	NA	7.0	refracted, weakened by Fresnel cutoff - leeward slope
	(2^{nd} ray)	NA	8.0	refracted, weakened by Fresnel cutoff - leeward slope
2	23-R	–3.0	7.0	
	24+R	–2.6	6.5	
	25+R	+2.0	7.0	
3	NA	NA	—	shallow, refracted

Hour 5

Data set *jd268053230Spice* was recorded in the shadow zone caustic of the second convergence zone in the Elvis Seamount's forward-scattered field. Figure 6-20(a) shows RAY results generated using measured bathymetry and sound velocity. Figure 6-20(b) shows the eigenrays, RAM simulated arrival pattern, and BASSEX measured arrival pattern. Table 6.3 gives a discription of the individual ray groups identified in Fig. 6-20(b).

RAY results show several SRBR rays present at this location. The RAM and BASSEX results both show what appear to be strong refracted limiting rays which are due to partial Fresnel tube diffraction around the seamount peak. The ray groups in the BASSEX results at 3.25 and 3.40 sec are well correlated with RAM in arrival angle and time; the observed amplitudes of these rays are higher than RAM results, possibly indicating significant environmental variability. BASSEX results show ray groups between 3.50-3.70 sec which are not clearly explained by simulated results, but are attributed to finale region broadening. SRBR rays at 4.00 and 4.20 sec in the RAM results are present in the BASSEX data at the correct arrival angle and time, but are very faint and difficult to discern in this figure.

Table 6.3: Hour 5 for Julian day 268.

Group	Ray #	sim-*RAM* (deg)	Measured (deg)	Comments
1	(1^{st} ray)	0.0	6.5	reflected off windward slope
	(2^{nd} ray)	0.0	5.5	reflected off windward slope
2	(1^{st} ray)	0.0	7.0	refracted, atributed to Fresnel tube diffraction
	(2^{nd} ray)	0.0	6.5	refracted, atributed to Fresnel tube diffraction
3	(1^{st} ray)	0.0	7.0	refracted, atributed to Fresnel tube diffraction
	(2^{nd} ray)	0.0	7.0	refracted, atributed to Fresnel tube diffraction
4	NA	NA	—	refracted, enhanced by Fresnel tube diffraction
5	NA	NA	—	shallow, refracted
6	NA	NA	—	SRBR

Hour 6

Data set *jd268062159KauaiSpice* was recorded in the shadow zone between the first and second convergence zone in the Elvis Seamount's forward-scattered field. Figure 6-21(a) shows RAY results generated using measured bathymetry and sound velocity. Figure 6-21(b) shows the eigenrays, RAM simulated arrival pattern, and BASSEX measured arrival pattern. Table 6.4 gives a discription of the individual ray groups identified in Fig. 6-21(b).

RAY results show one BR acoustic ray and several SRBR acoustic rays. Acoustic rays in the time range 2.30-2.50 sec are not accounted for by RAY because this test station contains mostly limiting reflected acoustic rays. Strong engine noise at 18 deg lowers the SNR of the acoustic rays above 10 deg. There are two reflected ray groups present in the time ranges 2.40-2.60 sec and 2.70-3.10 sec. The first ray group arrives at the highest angle, and is consistent with RAM results in arrival angle, time, and amplitude. The second ray group does not reconcile with RAM as well as the first ray group, and is attributed to environmental uncertainty and Fresnel tube cutoff. Several SRBR rays are observed between 4.00-5.00 sec, but are difficult to reconcile with RAM or RAY results.

Table 6.4: Hour 6 for Julian day 268.

Group	Ray #	sim-*RAM* (deg)	Measured (deg)	Comments
1	(1^{st} ray)	15.5	16.0	reflected off windward slope
	(2^{nd} ray)	10.0	6.0	reflected off windward slope
	(3^{rd} ray)	15.5	15.5	reflected off windward slope
	(4^{th} ray)	10.5	6.5	reflected off windward slope
2	NA	NA	—	b-r, attributed to Fresnel tube diffraction
3	NA	NA	—	reflected off windward slope
4	NA	NA	—	reflected off windward slope
5	NA	NA	—	SRBR

Hour 7

Data set *jd268073141Spicea* was recorded in the first convergence zone in the Elvis Seamount's forward-scattered field. Figure 6-22(a) shows RAY results generated using measured bathymetry and sound velocity. Figure 6-22(b) shows the eigenrays, RAM simulated arrival pattern, and BASSEX measured arrival pattern. Table 6.5 gives a discription of the individual ray groups identified in Fig. 6-22(b).

RAY results show several BR and SRBR acoustic rays at this location. BR acoustic rays

in the RAY results between 2.50-3.50 sec correlate well with RAM and BASSEX results. RAM and RAY results show three ray groups in the time ranges 2.40-2.80 sec, 3.00-3.20 sec, and 3.35-3.50 sec. Low SNR makes resolution at higher angles difficult because of the presence of engine noise at 18 deg, and there appears to be a delay in the BASSEX results of approximately 0.15 sec due to DAQ error. The ray group during time 3-3.2 sec in the RAM results is correlated with the ray group during time 3.25-3.35 sec in the BASSEX results. The ray group during time 3.35-3.40 sec in the RAM results is correlated with the ray group during time 3.40-3.50 sec in the BASSEX results. The first ray group is the steepest of the three, and the first ray [in the first ray group] appears to be missing from the observed arrival pattern. Acoustic ray amplitudes in the RAM results agree with those in the BASSEX results.

Table 6.5: Hour 7 for Julian day 268.

Group	Ray #	sim-*RAY* (deg)	Measured (deg)	Comments
1	20+BR	−7.5	10.5	reflected off windward slope
	21+BR	+3.5	8.5	reflected off windward slope
2	NA	NA	—	attributed to Fresnel tube diffraction
3	21-BR	−4.5	7.5	reflected off windward slope
	22+BR	−3.0	NA	reflected off seamount peak
4	NA	NA	—	
5	23-BR	−11.0	7.0	reflected off windward slope
	24+BR	−8.5	7.0	reflected off windward slope

Hour 8

Data set *jd268083141Spice* was recorded in the first convergence zone in the Elvis Seamount's forward-scattered field. Figure 6-23(a) shows RAY results generated using measured bathymetry and sound velocity. Figure 6-23(b) shows the eigenrays, RAM simulated arrival pattern, and BASSEX measured arrival pattern. Table 6.6 gives a discription of the individual ray groups identified in Fig. 6-23(b).

RAY results show five refracted, one BR, and two SRBR acoustic rays in the arrival pattern at this location. RAY, RAM, and BASSEX refracted ray results all show agreement with arrival angle, time, and amplitude. Acoustic rays are observed during 3.0-3.50 sec in the BASSEX results, which are probably caused by internal wave and ray chaos effects. Ray 20-BR does not appear in experimental results because of the bathmetry change between Hour 2 and 14. Reflected rays at 2.50 and 2.60 sec in the RAM results are not present in

the RAY or BASSEX results, and are attributed to environmental uncertainty.

Table 6.6: Hour 8 for Julian day 268.

Group	Ray #	sim-*RAY* (deg)	Measured (deg)	Comments
1	17–R	–13.5	13.5	
	18+R	–12.0	12.0	
	19+R	+12.0	11.0	
2	20–R	+7.5	7.5	
	21+R	+6.5	8.5	
3	NA	NA	—	shallow refracted rays

Hour 9

Data set *jd268093141Spice* was recorded in the first convergence zone in the Elvis Seamount's forward-scattered field. Figure 6-24(a) shows RAY results generated using measured bathymetry and sound velocity. Figure 6-24(b) shows the eigenrays, RAM simulated arrival pattern, and BASSEX measured arrival pattern. Table 6.7 gives a discription of the individual ray groups identified in Fig. 6-24(b).

RAY results show six refracted acoustic rays and several SRBR rays. The BASSEX results contain two refracted ray groups during 2.75-3.00 sec and 3.10-3.30 sec. The RAY, RAM, and BASSEX results all show good agreement in arrival angle and time, with respect to the refracted acoustic rays. Observed ray amplitudes appear lower than RAM results by about 6 dB; this is attributed to Fresnel tube cutoff by the leeward slope of the seamount. SRBR acoustic energy during 3.50-5.50 sec shows fair agreement in RAY, RAM, and BASSEX results in terms of relative steepness and arrival time of acoustic rays, but rays are difficult to conclusively resolve due to low SNR and environmental randomness. Both RAM and BASSEX results show a limiting ray at 2.40 sec and 10 deg, which RAY does not predict.

Hour 10

Data set *jd268102119KauaiSpice* was recorded in the caustic of the first convergence zone in the Elvis Seamount's forward-scattered field. Figure 6-25(a) shows RAY results generated using measured bathymetry and sound velocity. Figure 6-25(b) shows the eigenrays, RAM simulated arrival pattern, and BASSEX measured arrival pattern. Table 6.8 gives a discription of the individual ray groups identified in Fig. 6-25(b).

Table 6.7: Hour 9 for Julian day 268.

Group	Ray #	sim-*RAY* (deg)	Measured (deg)	Comments
1	NA	NA	—	enchanced by Fresnel tube diffraction
2	19-R	-7.5	8.0	weakened by Fresnel tube cutoff
	20-R	+7.0	6.5	weakened by Fresnel tube cutoff
	20+R	-6.0	8.0	weakened by Fresnel tube cutoff
	21+R	+6.0	7.0	weakened by Fresnel tube cutoff
3	22-R	+1.0	7.0	weakened by Fresnel tube cutoff
	21-R	-1.0	7.0	weakened by Fresnel tube cutoff
4	NA	NA	—	shallow refracted, bottom-reflected, SRBR

RAY results show one refracted ray in the arrival pattern and several SRBR rays. The refracted ray is visible in the RAY, RAM and BASSEX results and shows good agreement in arrival angle and time; the ray amplitude is about 10 dB weaker, suggesting Frenel tube cutoff by the leeward slope of the seamount. Limiting rays appear in the BASSEX and RAM results during 2.25-2.50 sec, which is not visible in the RAY results. Observed SRBR acoustic rays at 3.80 sec are well correlated with RAM in arrival angle and time.

Table 6.8: Hour 10 for Julian day 268.

Group	Ray #	sim-*RAY* (deg)	Measured (deg)	Comments
1	(1^{st} ray)	NA	9.5	attributed to Fresnel tube diffraction
	(2^{nd} ray)	NA	9.5	attributed to Fresnel tube diffraction
2	20+R	-5.0	9.0	weakened by Fresnel tube cutoff
3	NA	NA	—	shallow refracted, bottom-reflected, SRBR
4	NA	NA	—	shallow refracted, SRBR

Hour 11

Data set *jd268113141Spice* is not offered because no signal could be identified. This location is in the deepest part of the first shadow, and the lack of signal reception is not unexpected.

Hour 12

Data set *jd268123222Spice* was recorded in the first shadow zone in the Elvis Seamount's forward-scattered field. Figure 6-26(a) shows RAY results generated using measured bathymetry and sound velocity. Figure 6-26(b) shows the eigenrays, RAM simulated arrival pattern, and BASSEX measured arrival pattern. Table 6.9 gives a discription of the individual ray groups identified in Fig. 6-26(b).

RAY results show several SRBR acoustic rays at this test station. RAM and BASSEX show rays during 2.50-5.50 sec which steadily increase in arrival angle over time. The RAM and BASSEX results show agreement in arrival angle, time, and amplitude. Strong engine noise at 18 deg produces high sidelobes and reduces high angle arrival signal recognition. RAY fails to clearly identify any of the observed ray arrivals. The ability of RAM to model the observed rays is quite remarkable given the amount of seafloor interaction. Rays appear to steepen in time because steep rays spend more time over the peak of the seamount in slower sound speed waters. Steep, late arrival rays are less correlated with simulated results due to higher bottom interaction and time spent in the more variable upper water column.

Table 6.9: Hour 12 for Julian day 268.

Group	Ray #	sim-*RAM* (deg)	Measured (deg)	Comments
1	(1^{st} ray)	0.0	7.5	SRBR
	(2^{nd} ray)	0.0	8.0	SRBR
	(3^{rd} ray)	0.0	8.0	SRBR
	(4^{th} ray)	0.0	7.5	SRBR
2	(1^{st} ray)	0.0	8.0	SRBR
3	(1^{st} ray)	11.0	8.0	SRBR
	(2^{nd} ray)	11.0	8.0	SRBR
	(3^{rd} ray)	11.0	8.0	SRBR
	(4^{th} ray)	11.0	8.0	SRBR
4	(1^{st} ray)	13.0	8.0	SRBR/arrived late
	(2^{nd} ray)	13.5	8.0	SRBR/arrived late
5	NA	NA	—	SRBR
6	NA	NA	—	SRBR
7	NA	NA	—	SRBR

Hour 13

Data set *jd268133222Spice* was recorded in the first reflected convergence zone in the Elvis Seamount's forward-scattered field. Figure 6-27(a) shows RAY results generated using measured bathymetry and sound velocity. Figure 6-27(b) shows the eigenrays, RAM simulated arrival pattern, and BASSEX measured arrival pattern. Table 6.10 gives a discription of the individual ray groups identified in Fig. 6-27(b).

RAY results show several BR and SRBR acoustic rays in the arrival pattern. The BR acoustic rays in the RAY results are well correlated with RAM and BASSEX results in terms of arrival angle, time, and amplitude. Two BR ray groups are visible in the observed

and simulated results during 2.30-2.60 sec and 2.90-3.25 sec. The BASSEX data show a ray pair at 2.70 sec which does not appear in the RAM or RAY results, and is attributed to Fresnel tube diffraction over the seamount and environmental uncertainty.

Table 6.10: Hour 13 for Julian day 268.

Group	Ray #	sim-*RAY* (deg)	Measured (deg)	Comments
1	18-BR	+6.5	8.0	bottom-reflected off windward slope
	19+BR	+7.5	7.5	bottom-reflected off windward slope
2	NA	NA	—	refracted, due to Fresnel tube diffraction
3	19-BR	-1.0	8.0	bottom-reflected off windward slope
	20+BR	-3.0	8.0	bottom-reflected off windward slope
4	21-BR	-2.5	8.0	bottom-reflected off windward slope
5	NA	NA	—	shallow refracted

Hour 14

Data set *jd268142200KauaiSpiceb* was recorded in the caustic of the first shadow in the Elvis Seamount's forward-scattered field. Figure 6-28(a) shows RAY results generated using measured bathymetry and sound velocity. Figure 6-28(b) shows the eigenrays, RAM simulated arrival pattern, and BASSEX measured arrival pattern. Table 6.11 gives a discription of the individual ray groups identified in Fig. 6-28(b).

RAY results show several BR and SRBR acoustic rays in the arrival pattern. The reflected rays are initially shallow and become steeper with time. Ray groups visible at 3.00 and 2.25 sec in the observed results show good agreement with RAY and RAM results in arrival angle and time. There is a ray group at 2.75 sec which is not explained using RAM or RAY results; this ray group appears to be related to the unexplained ray group visible in Hour 13, which was attributed to Fresnel tube diffraction. Reflected energy which is present in the BASSEX data between 3.50 and 5.50 sec appears moderately correlated with RAY and RAM results in terms of arrival angle and time. Bathymetry inaccuracy, shown in Fig. 6-16, is the most likely cause of the discrepancy between simulated and experimental results at this test station.

6.4.6 Conclusion: The Elvis Seamount's Forward-Scattered Field

The results presented in Section 6.4.5 give a detailed description of the measured and simulated arrival patterns observed in the Elvis Seamount's forward-scattered field. RAY

Table 6.11: Hour 14 for Julian day 268.

Group	Ray #	sim-*RAY* (deg)	Measured (deg)	Comments
1	18-BR	+4.5	4.0	bottom-reflected/windward slope
	17+SRBR	−11.0	8.5	bottom-reflected/windward slope
	18+BR	−12.5	9.0	bottom-reflected/windward slope
	19+BR	+13.5	9.0	bottom-reflected/windward slope
	19+SRBR	+14.0	8.5	bottom-reflected/windward slope
2	NA	NA	—	refracted/Fresnel tube diffraction
3	NA	NA	—	refracted/Fresnel tube diffraction
4	20+BR	−11.5	4.0	bottom-reflected/windward slope
	21-BR	-8.5	8.0	bottom-reflected/windward slope
	22-BR	-10.0	9.0	bottom-reflected/windward slope
5	NA	NA	—	shallow refracted

and RAM results showed good agreement with BASSEX data for steep, refracted acoustic rays, and for BR acoustic rays in terms of arrival angle and time. Acoustic rays in the shadow zones consisted mostly of SRBR acoustic rays, and the results showed that acoustic rays steepened with arrival time. Ray trace modeling was completely ineffective in predicting SRBR acoustic ray arrivals due to the method's sensitivity to environmental uncertainty. RAM results showed good agreement with observed SRBR acoustic ray arrival angle, time, and amplitude in the deep shadow zones, especially for shallow, early arrival rays.

The measured location of shadow zone caustics varied significantly in range when compared with RAY predictions, by as much as 5 km; this was attributed to Fresnel tube broadening by natural variability in the ocean and partial Fresnel tube cutoff and/or diffraction around the seamount peak. Acoustic pressure levels appeared within 10 dB of the RAM predicted levels for all cases, except Hours 5 and 10 which were in boundary zones. The convergence zones were periodic by about 50 km, and consisted of regions of reflected and refracted acoustic energy.

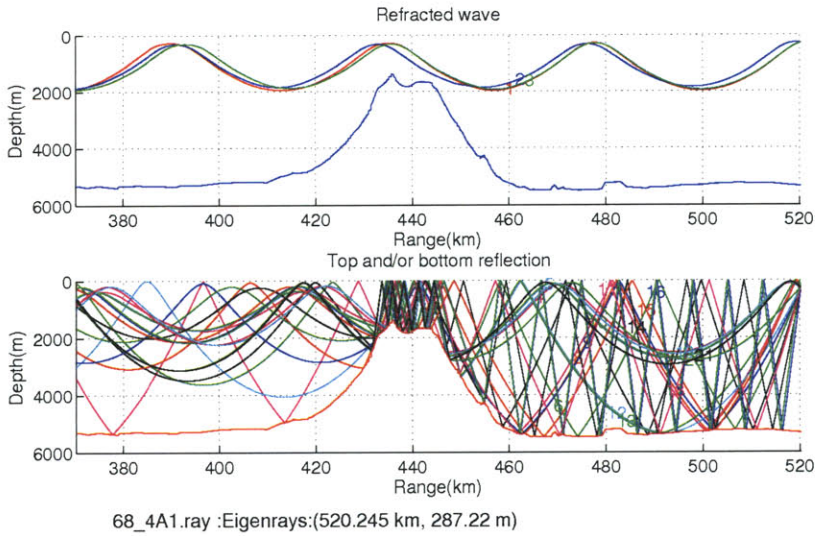

68_4A1.ray :Eigenrays:(520.245 km, 287.22 m)

1:23–R	8:24–SRBR	15:29+SRBR	16:42+SRBR
2:25+R	9:23–SRBR	16:42+SRBR	17:43+SRBR
3:24+R	10:26–SRBR	17:43+SRBR	18:32+SRBR
4:28–SRBR	11:28–SRBR	18:32+SRBR	19:31+SRBR
5:22–SRBR	12:29–SRBR	19:31+SRBR	20:30+SRBR
6:29–SRBR	13:30–SRBR	20:30+SRBR	21:31+SRBR
7:33–SRBR	14:34+SRBR	21:31+SRBR	

(a) RAY ray trace simulation

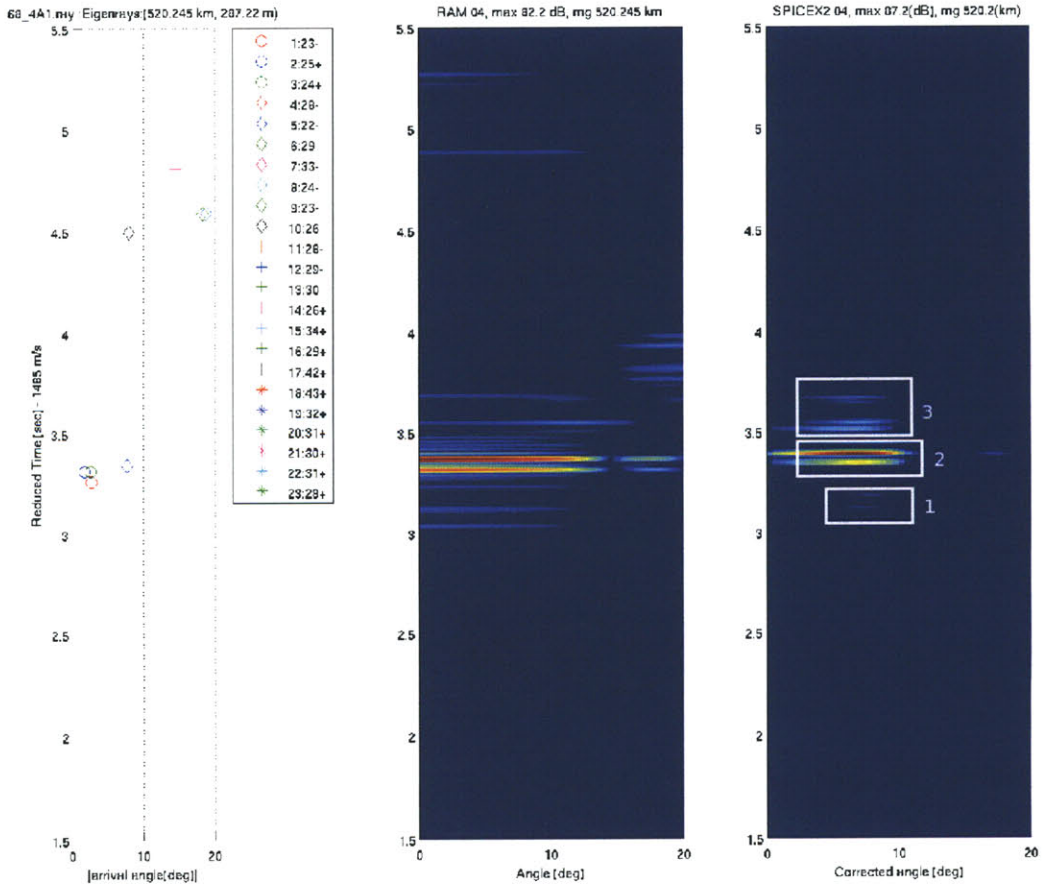

(b) (left) Ray trace, (middle) RAM, (right) BASSEX

Figure 6-19: Acoustic pressure data from hour 4 of Julian day 268.

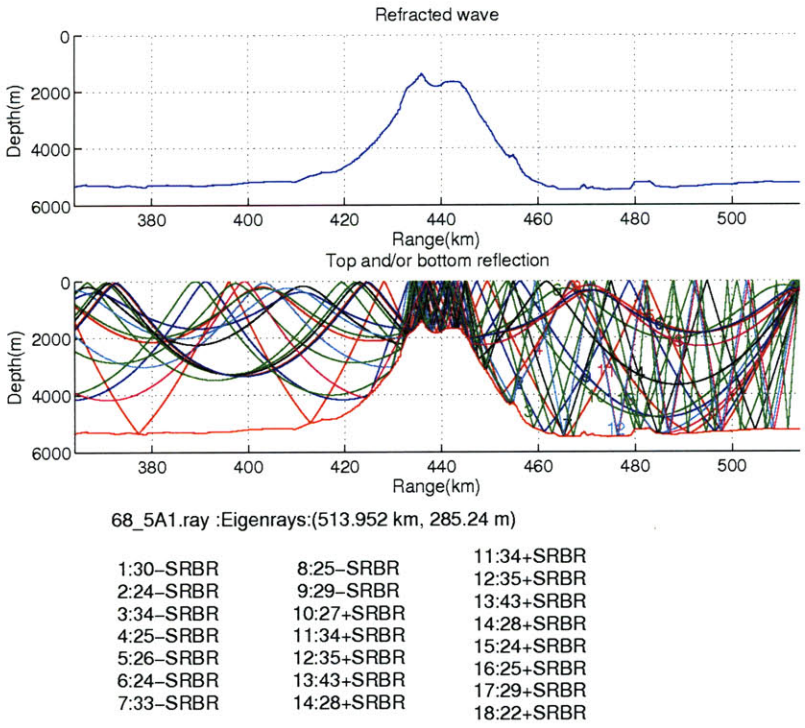

(a) RAY ray trace simulation

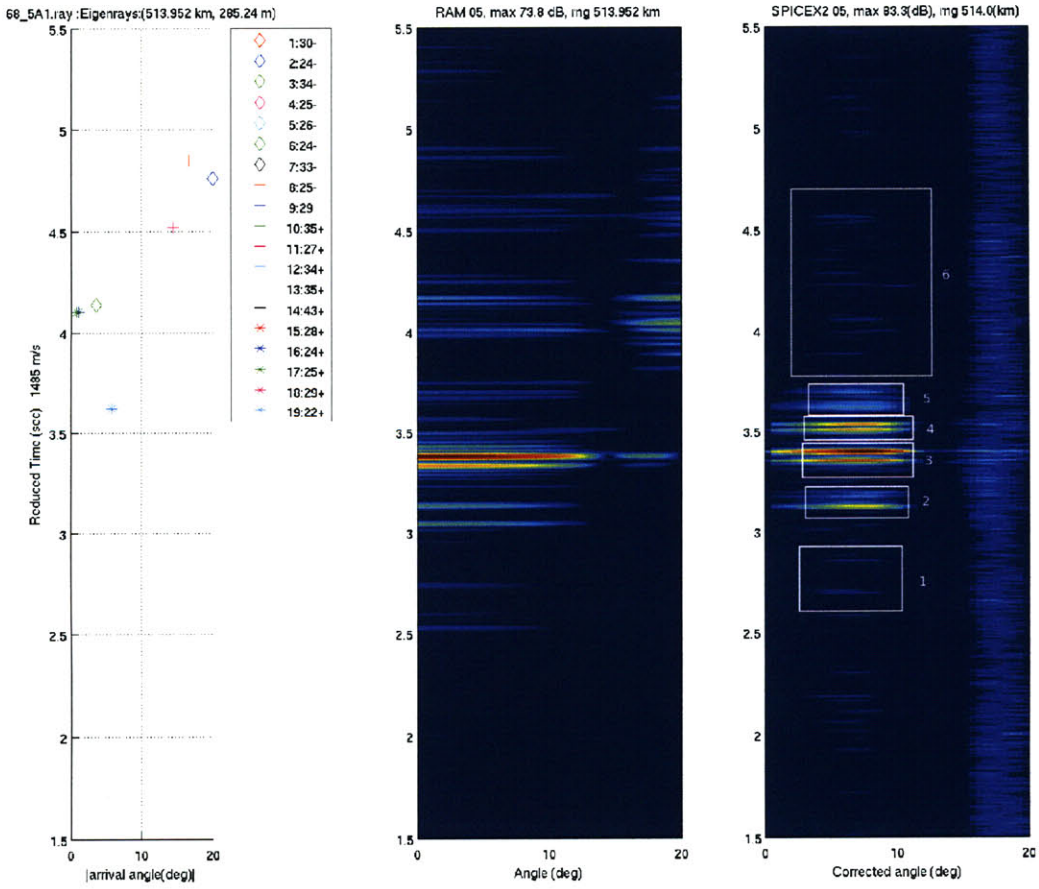

(b) (left) Ray trace, (middle) RAM, (right) BASSEX

Figure 6-20: Acoustic pressure data from hour 5 of Julian day 268.

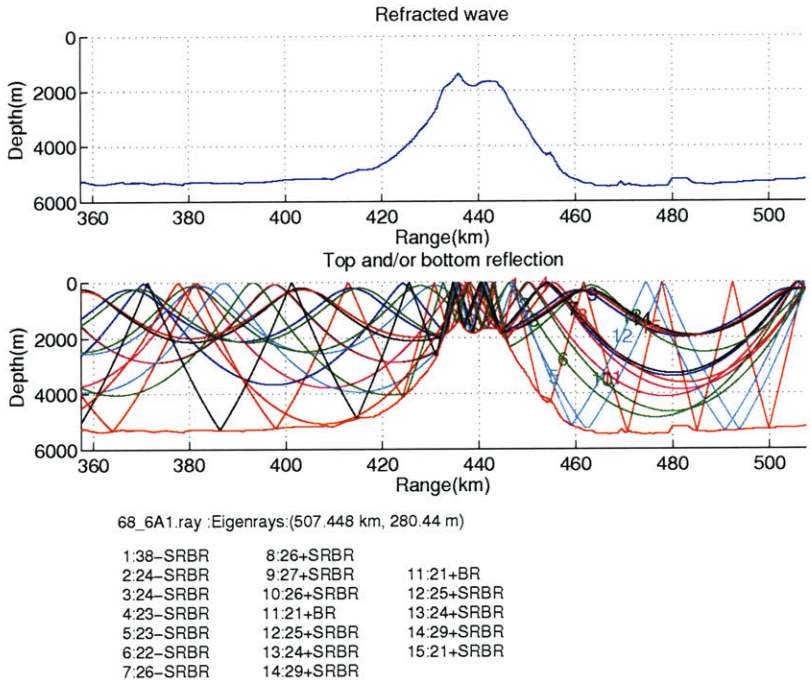

(a) RAY ray trace simulation

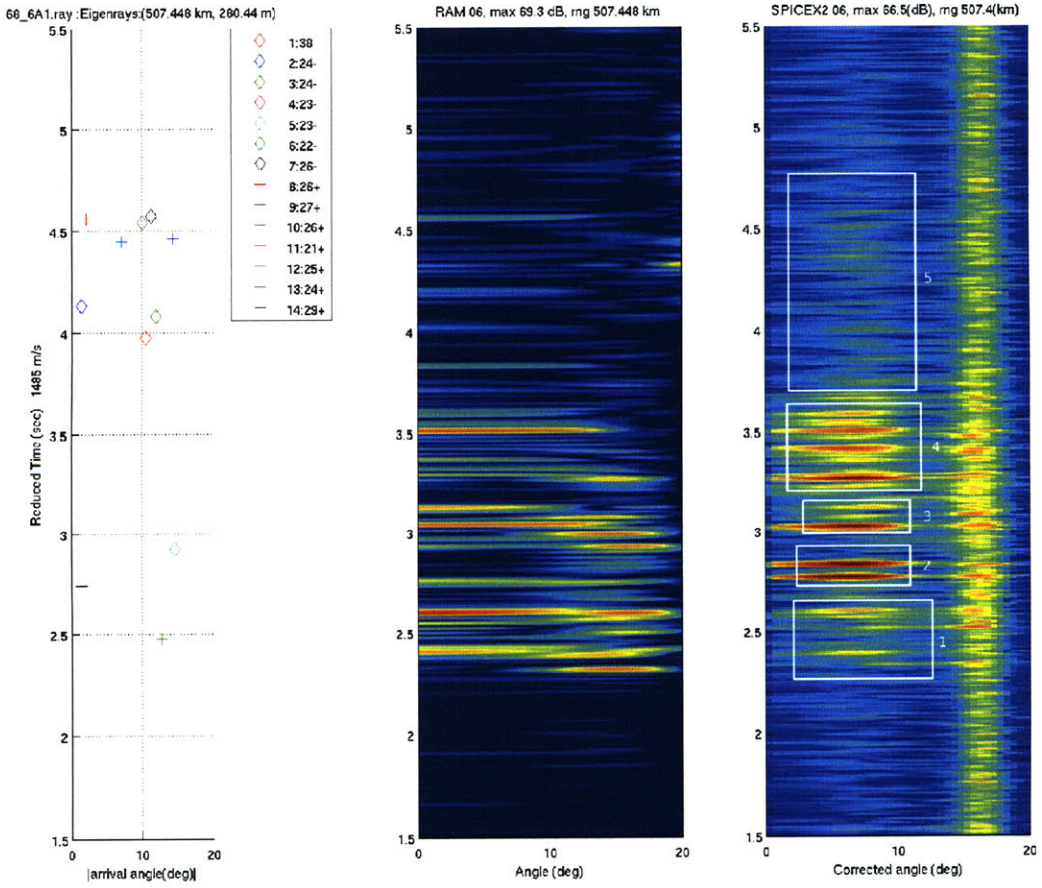

(b) (left) Ray trace, (middle) RAM, (right) BASSEX

Figure 6-21: Acoustic pressure data from hour 6 of Julian day 268.

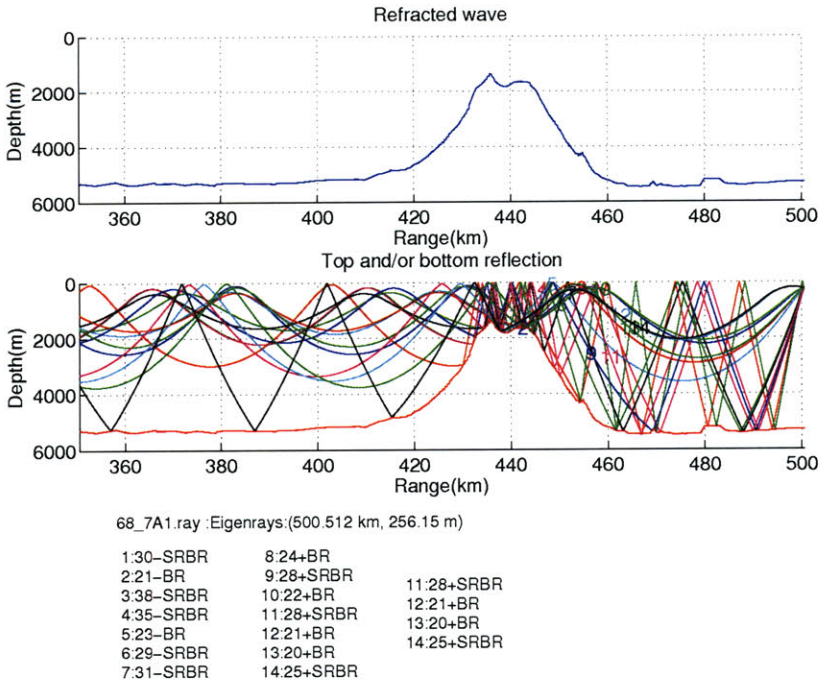

(a) RAY ray trace simulation

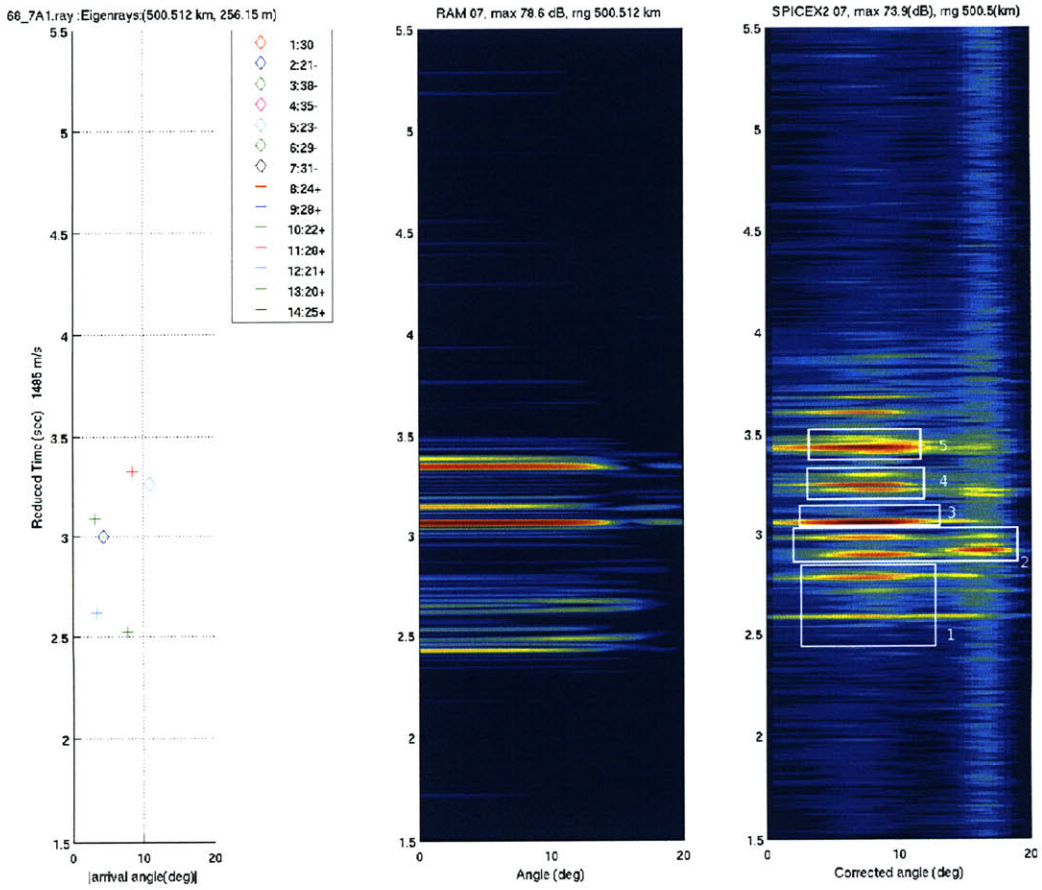

(b) (left) Ray trace, (middle) RAM, (right) BASSEX

Figure 6-22: Acoustic pressure data from hour 7 of Julian day 268.

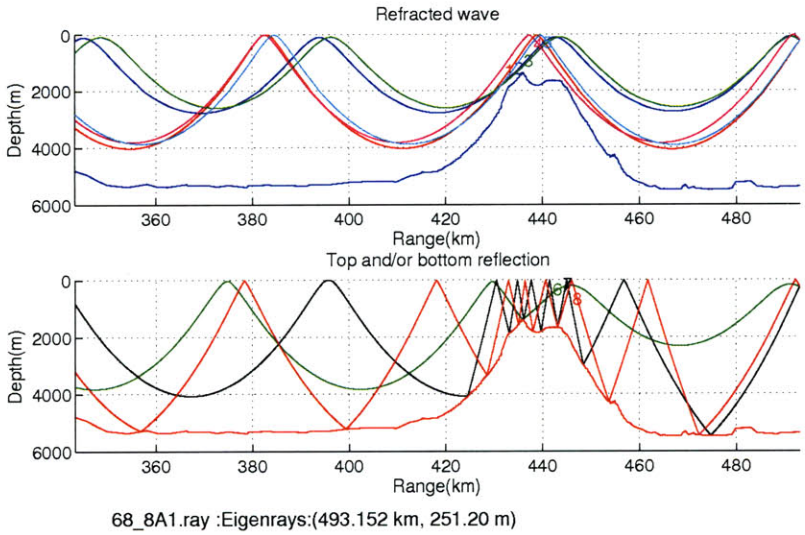

68_8A1.ray :Eigenrays:(493.152 km, 251.20 m)

1:17–R
2:20–R
3:21+R
4:19+R
5:18+R
6:20–BR
7:28+SRBR

6:20–BR
7:28+SRBR
8:29+SRBR

(a) RAY ray trace simulation

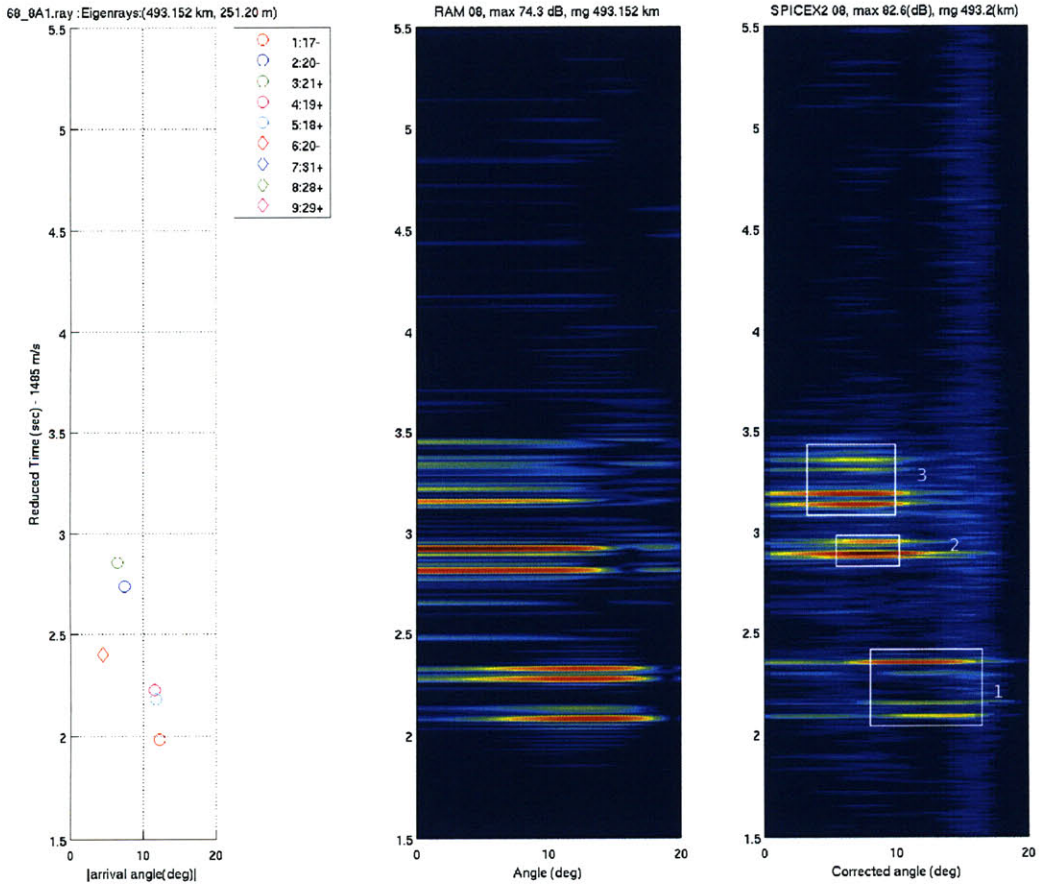

(b) (left) Ray trace, (middle) RAM, (right) BASSEX

Figure 6-23: Acoustic pressure data from hour 8 of Julian day 268.

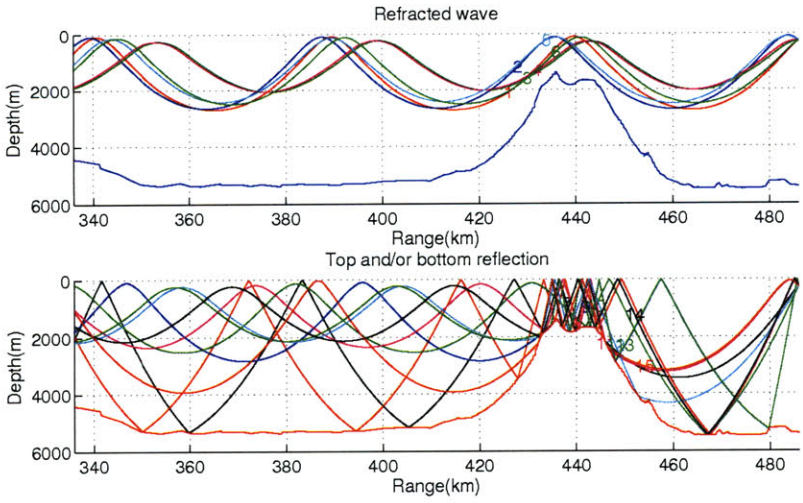

68_9A1.ray :Eigenrays:(486.001 km, 260.00 m)

1:19–R	8:26–SRBR	
2:20–R	9:26–SRBR	11:24–SRBR
3:21–R	10:21–SRBR	12:23–SRBR
4:22–R	11:24–SRBR	13:28–SRBR
5:21+R	12:23–SRBR	14:27+SRBR
6:20+R	13:28–SRBR	15:21+SRBR
7:23–SRBR	14:27+SRBR	

(a) RAY ray trace simulation

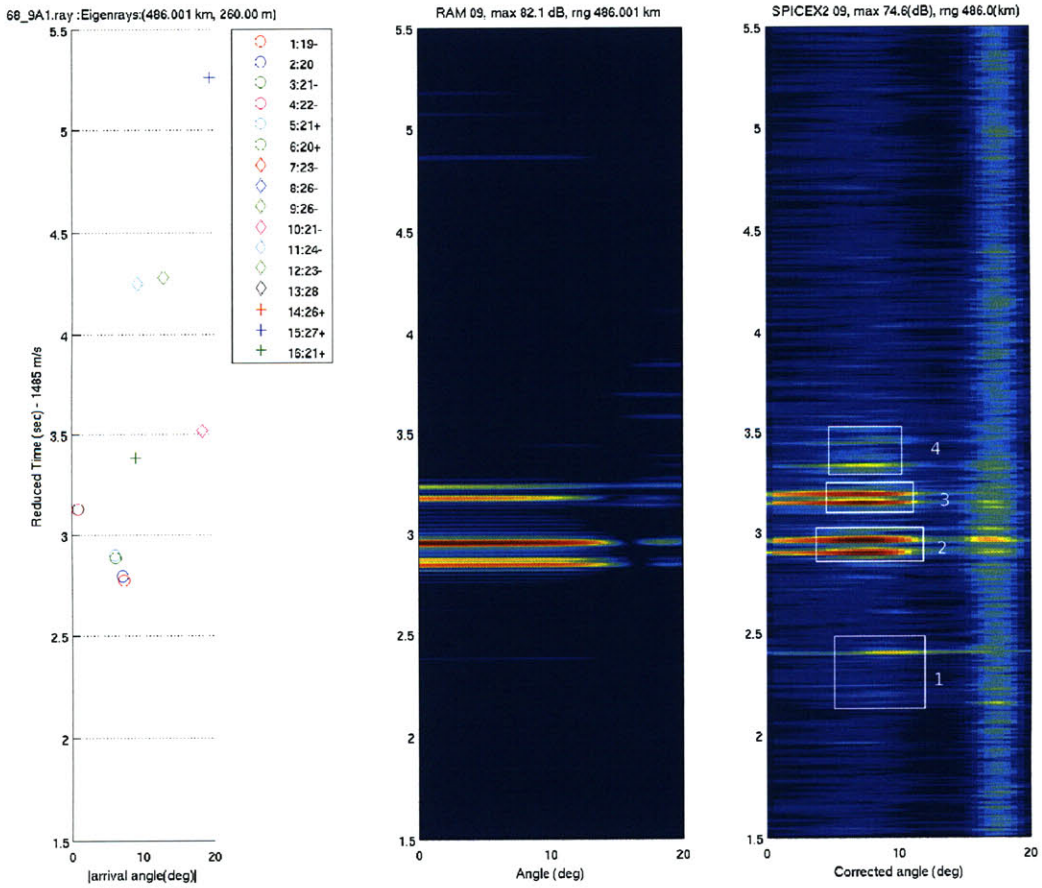

(b) (left) Ray trace, (middle) RAM, (right) BASSEX

Figure 6-24: Acoustic pressure data from hour 9 of Julian day 268.

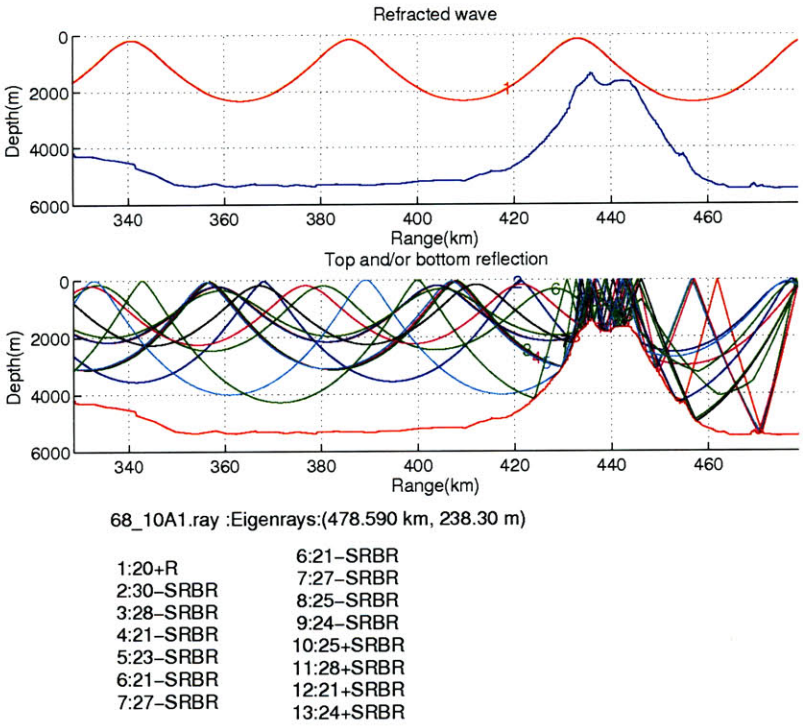

(a) RAY ray trace simulation

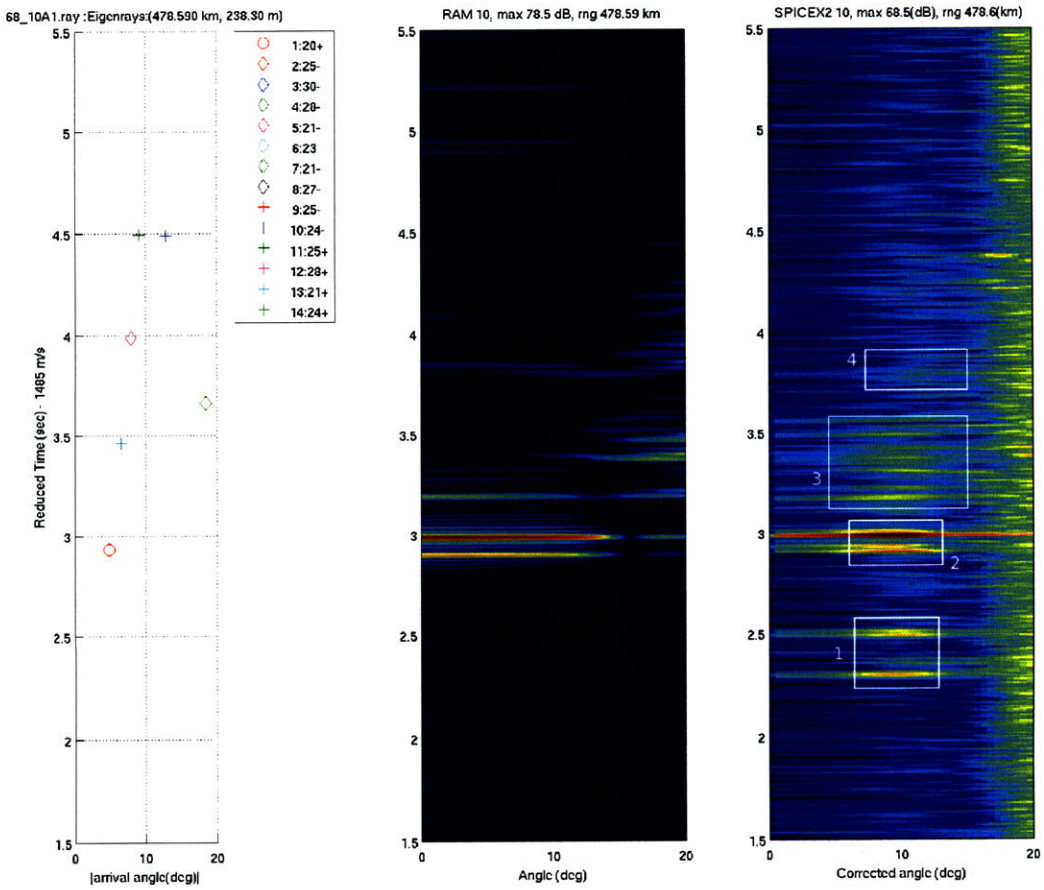

(b) (left) Ray trace, (middle) RAM, (right) BASSEX

Figure 6-25: Acoustic pressure data from hour 10 of Julian day 268.

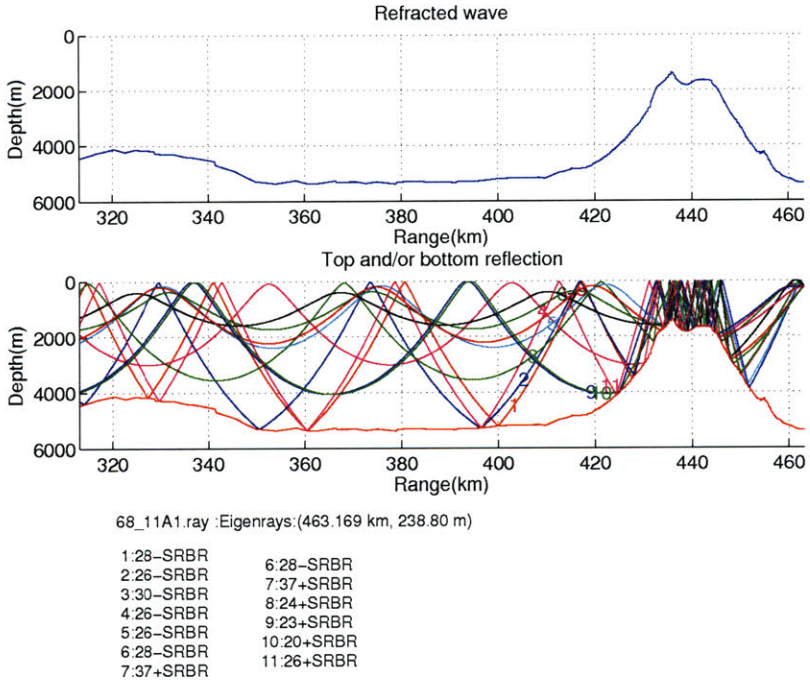

(a) RAY ray trace simulation

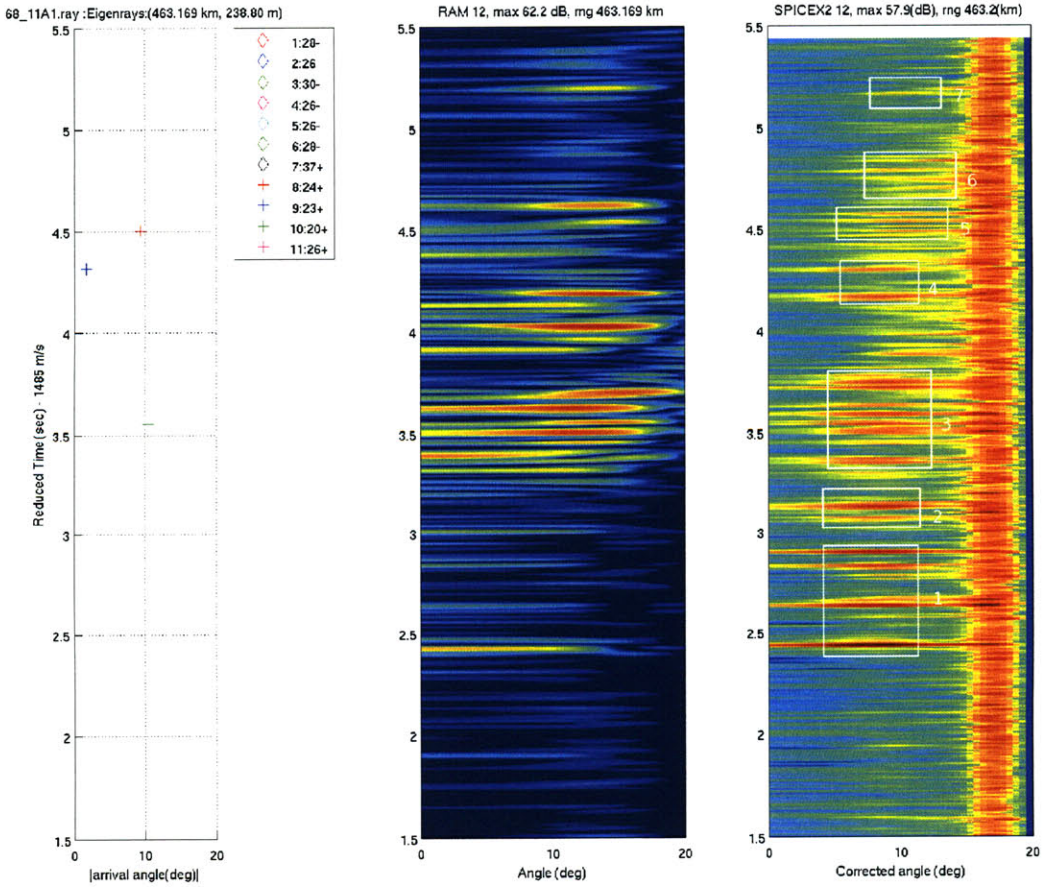

(b) (left) Ray trace, (middle) RAM, (right) BASSEX

Figure 6-26: Acoustic pressure data from hour 12 of Julian day 268.

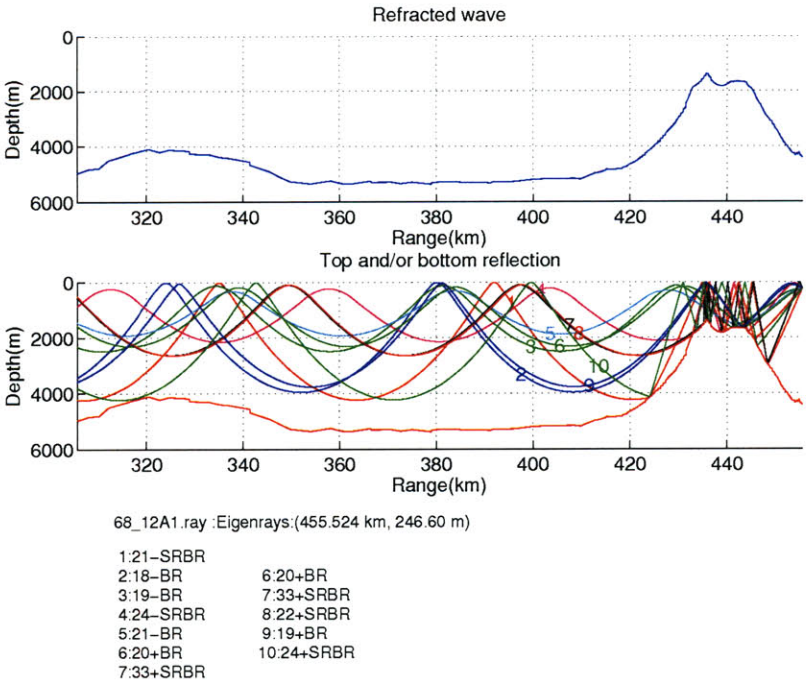

(a) RAY ray trace simulation

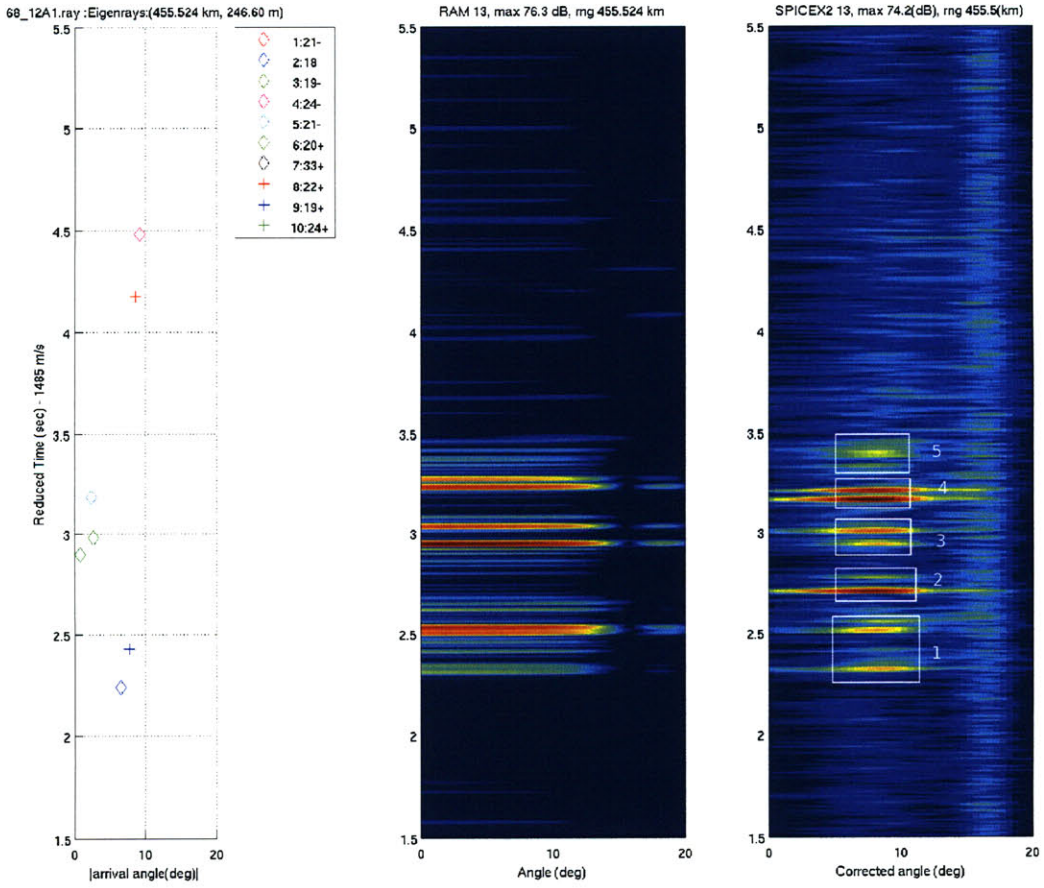

(b) (left) Ray trace, (middle) RAM, (right) BASSEX

Figure 6-27: Acoustic pressure data from hour 13 of Julian day 268.

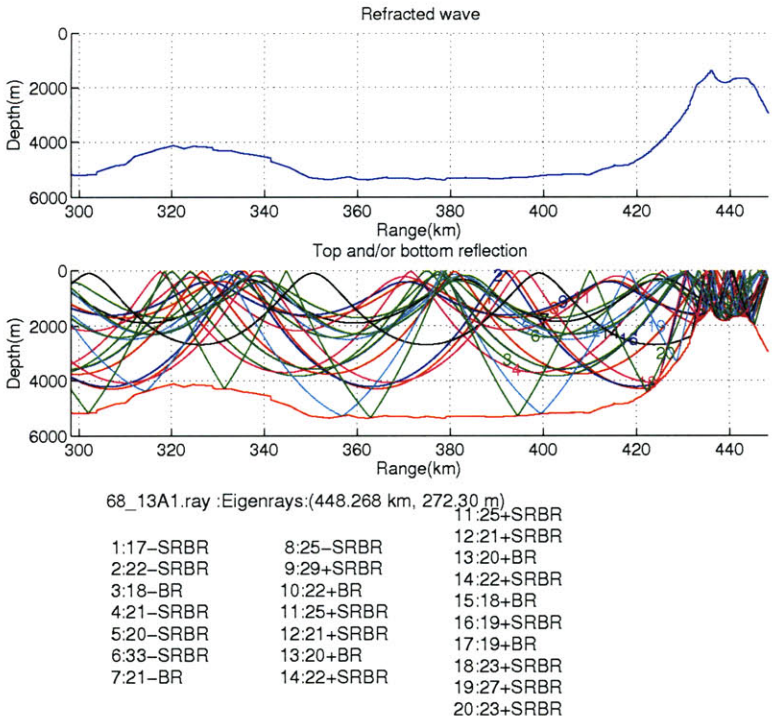

(a) RAY ray trace simulation

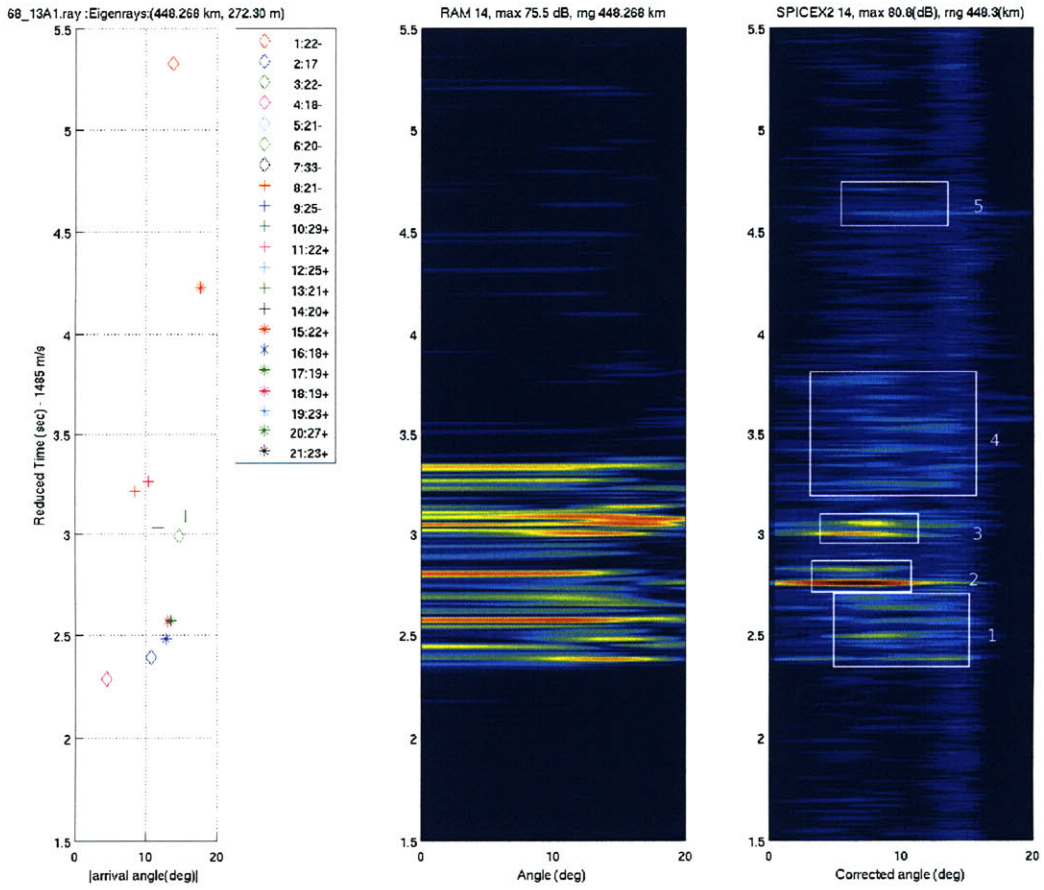

(b) (left) Ray trace, (middle) RAM, (right) BASSEX

Figure 6-28: Acoustic pressure data from hour 14 of Julian day 268.

6.5 The Kermit-Roosevelt Seamount's Forward-Scattered Field - Day 264

On Julian day 264 during the BASSEX experiment, acoustic data from the FORA hydrophone array was gathered in the forward-scattered field of the Kermit-Roosevelt Seamount for SPICEX source S1. This section will present the data gathered on day 264 and examine the results using available RAM and RAY simulations.

Figure 6-29 shows the bathymetry and location of the test stations in the Kermit-Roosevelt Seamount's forward-scattered field on Julian day 264. Figure 6-30 shows the measured and RAM simulated peak acoustic pressure levels at the test stations in the forward-scattered field. The black line is the measured peak pressure level and the red line is the RAM simulated pressure level. The seamount bathymetry is given on the bottom of the figure for reference. Sound velocity measurements were very sparse along the direct sound path to source S1 throughout the experiment. The figure shows that there is good agreement in the locations of the convergence zones between the observed and simulated data; however, without an accurate environmental model it is very difficult to interpret the results from the BASSEX experiment. Figures 6-31(a) and 6-31(b) are offered as typical examples of the available data for day 264; the simulated and measured arrival patterns show significant disagreement in terms of the number, travel time, and arrival angle of acoustic rays.

The results from Julian day 264 show that inaccuracy in the sound velocity profile model can cause simulated arrival patterns to deviate significantly from observed results. Even with inaccuracy in the sound velocity profile, the simulated and observed results show some agreement in the location of the convergence zones formed in the forward-scattered field of the seamount. Further study may be helpful in understanding the effect of environmental inaccuracy on the location of convergence zones, considering that a tomography or communication system operating at megameter ranges will most likely have inaccuracy in the sound velocity profile.

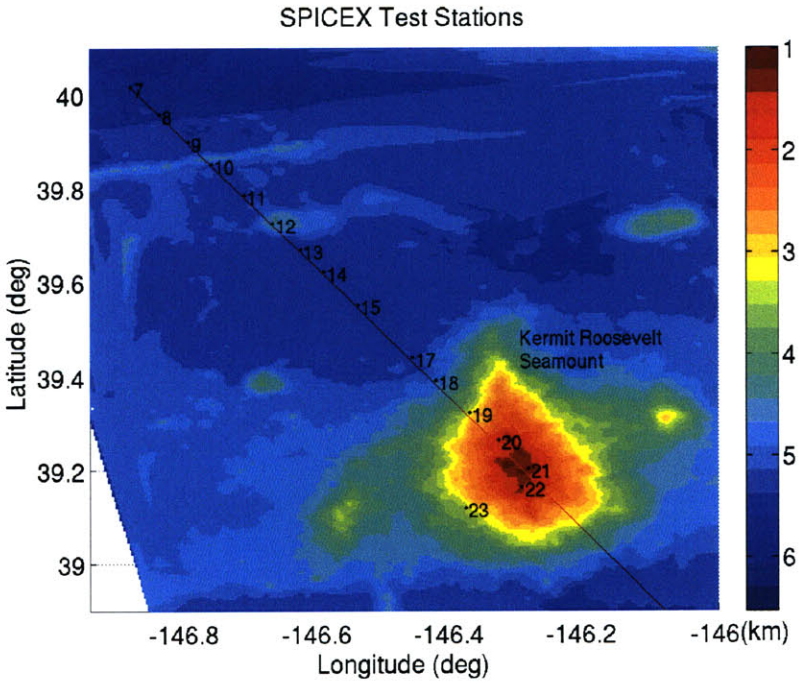

Figure 6-29: Test station locations during day 264.

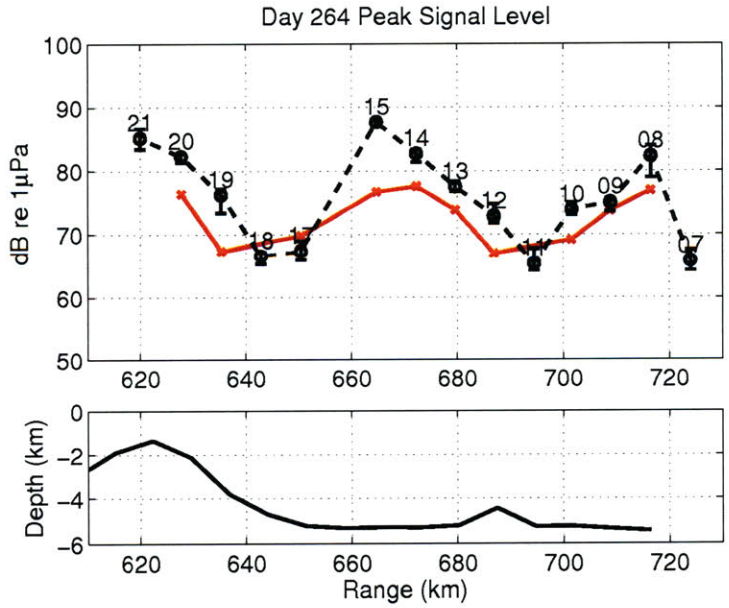

Figure 6-30: Peak signal level for Julian day 264 receptions: (black) BASSEX conventionally beamformed data, (red) RAM simulation.

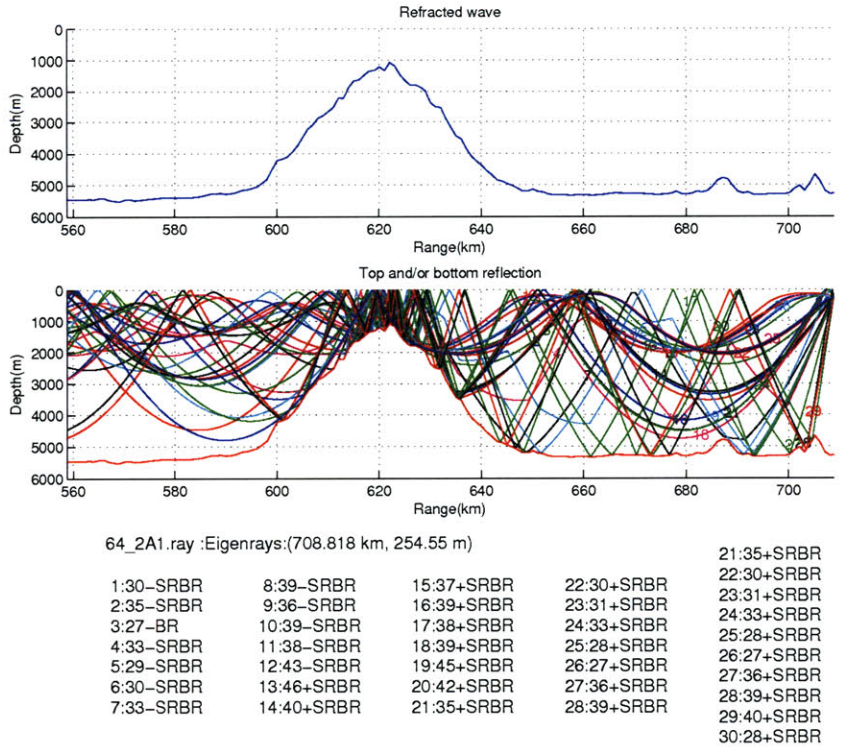

(a) RAY ray trace simulation

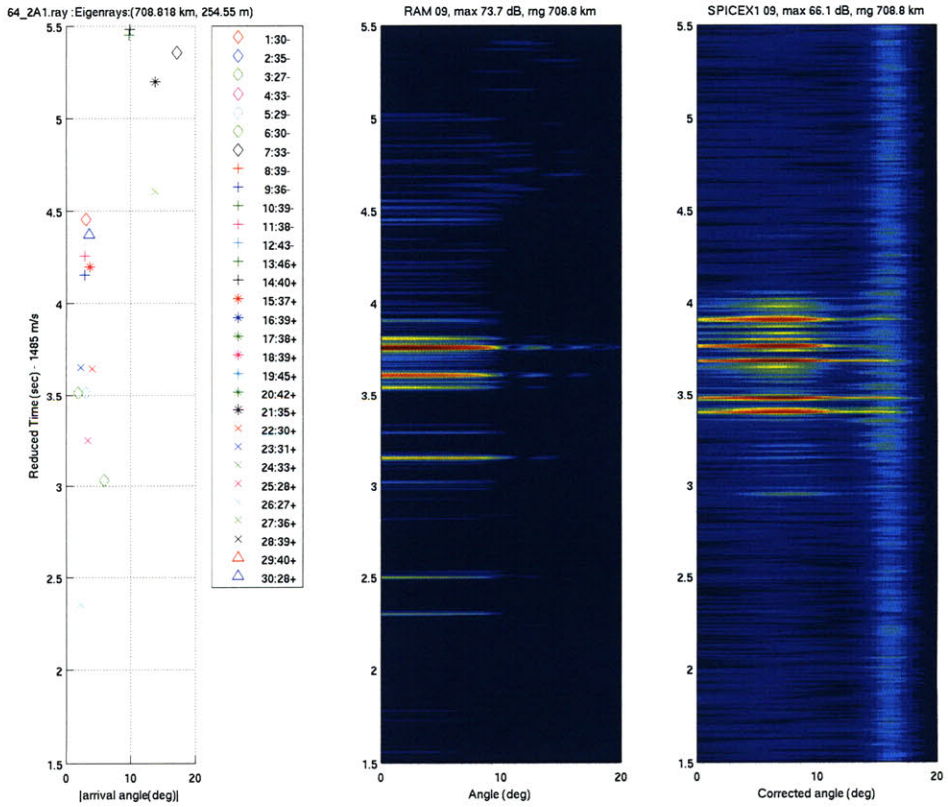

(b) (left) Ray trace, (middle) RAM, (right) BASSEX

Figure 6-31: Acoustic pressure data from hour 9 of Julian day 264.

6.6 The Kermit-Roosevelt Seamount's Forward Scattered Field - Day 267

On Julian day 267 during the BASSEX experiment, the forward-scattered field of the Kermit-Roosevelt Seamount was measured, with respect to SPICEX source S2. Figure 6-32 shows the locations of the test stations on days 265 and 267 of the experiment. From the figure it is clear that the data collected on day 265 does not lie along the geodesic sound path plotted from the location of *jd267083408Spice* to the source. Also, several data records from day 265 are very corrupt from DAQ error and array fluctuations. In this section only the data gathered on day 267 from Hours 2-15 will be analyzed. Several sound velocity measurements were taken along the direct sound path with XBT's.

Figure 6-33 shows the RAM simulated range stacked acoustic pressure time series for the Kermit-Roosevelt Seamount's forward-scattered field. The most notable differences between the Kermit-Roosevelt and Elvis shadow zones is the additional reflected energy convergence zone at 550 km.

Figure 6-34 shows the measured and RAM simulated peak acoustic source level inside the Kermit-Roosevelt Seamount's forward-scattered field on day 267. Experimental results show a good agreement with the simulated data; only a small discrepancy appears at range 575 km, where the RAM code apparently overestimates the amount of reflected energy by about 7 dB. Acoustic fluctuations were observed in the forward-scattered field of $O(18$ dB).

The following subsections will analyze the data from each test station and compare results with RAM simulated acoustic time series. The figures provide the (upper left) bathymetry and the location of each test station with the direct sound path between the source and receiver over the seamount, (upper middle) bearing-time response, (right) measured arrival pattern, (middle) measured acoustic time series[8], and (bottom) RAM simulated acoustic time series. It is noted that without RAY trace results or beamformed RAM results available, it is difficult to separate and identify the different ray arrivals observed in the data.

[8]The measured time series is determined by averaging the arrival pattern between 0-20 deg.

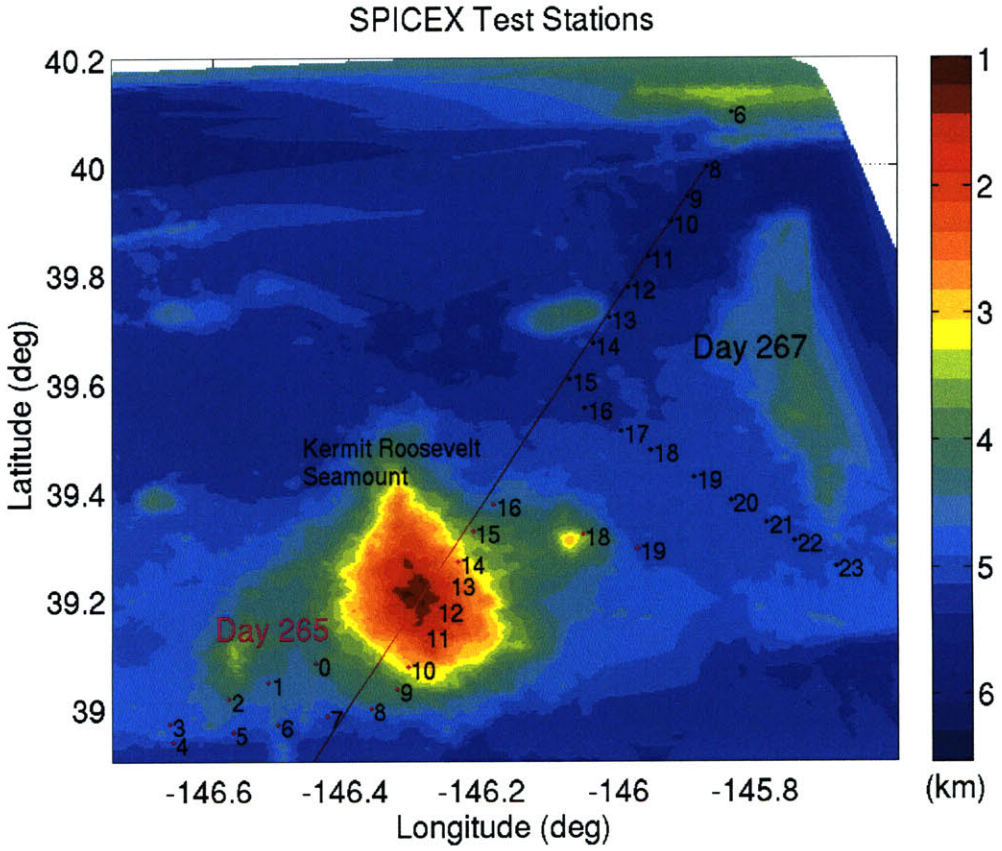

Figure 6-32: Test station locations during day 265 and day 267.

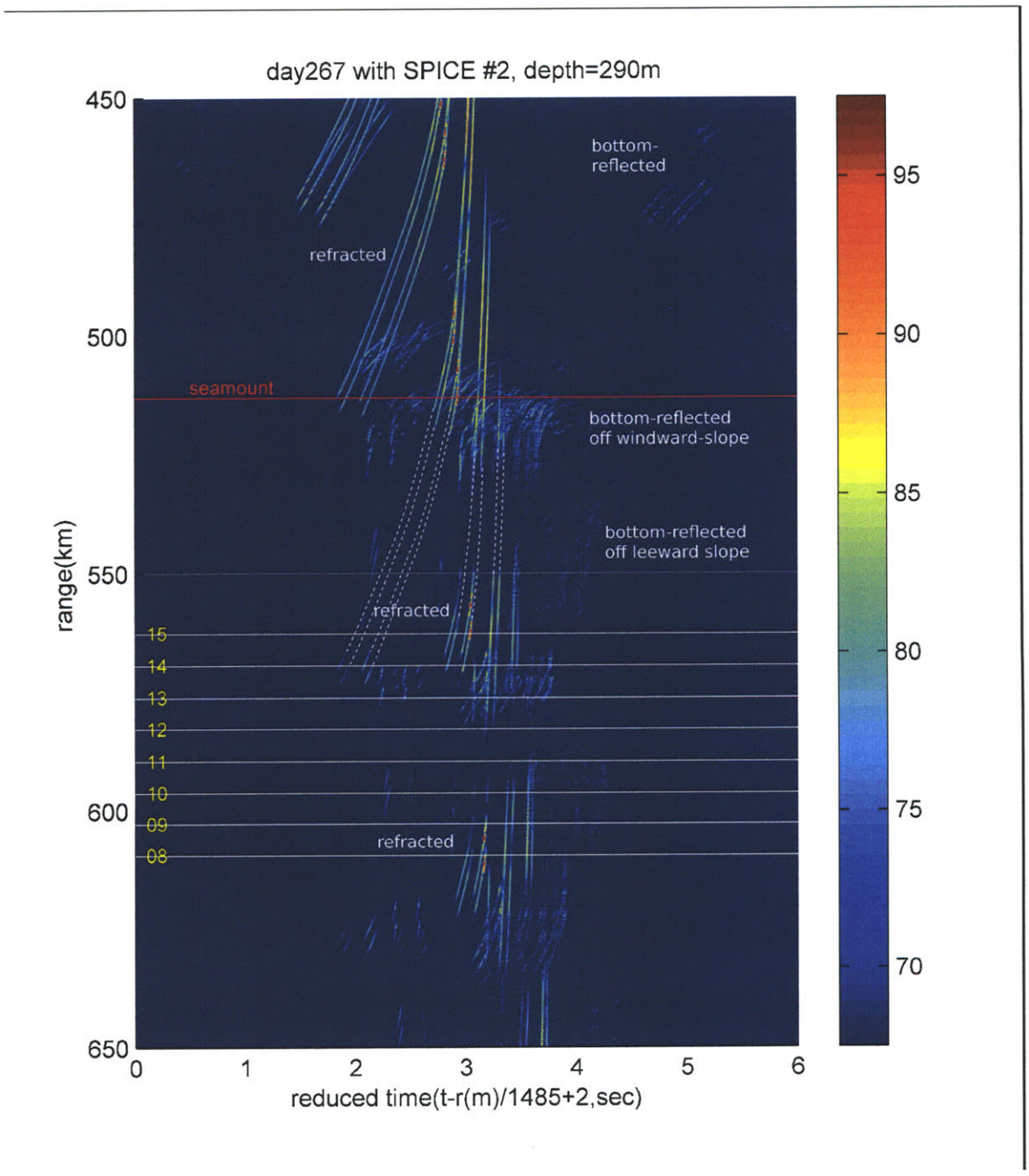

Figure 6-33: Acoustic pressure time series in the Kermit-Roosevelt Seamount's forward-scattered field. Test station and seamount ranges are indicated. Acoustic pressure is plotted in dB re 1μPa.

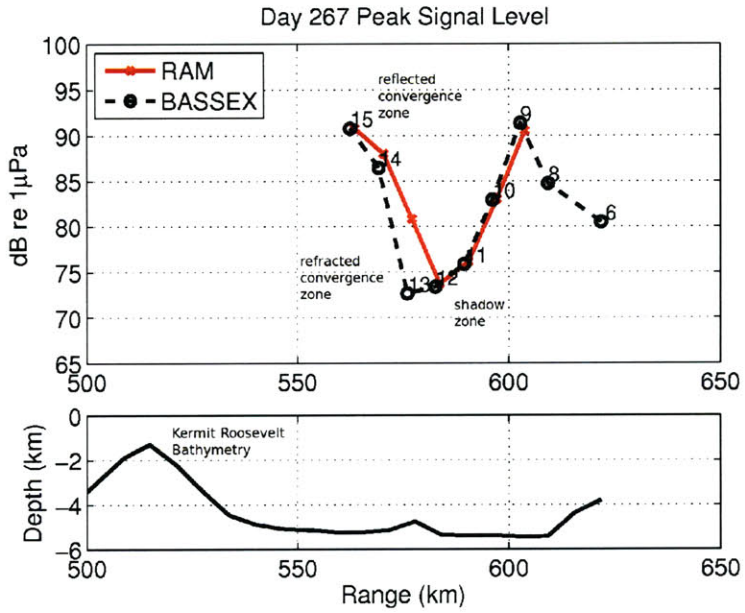

Figure 6-34: Peak signal level for Julian day 267 receptions: (black) BASSEX conventionally beamformed data, (red) RAM simulation.

Hour 08

Data set *jd267083408Spice* was recorded in the second refracted convergence zone behind the Kermit-Roosevelt Seamount and results are shown in Fig. 6-35. Both the RAM and BASSEX results show two distinct ray groups, starting at 3.00 sec [in the RAM time series]. The BASSEX results are delayed because of a DAQ randomly delayed start.

Acoustic rays with very low intensity are observed in the RAM and BASSEX results at 2.30 sec, and are associated with limiting rays. Acoustic rays during 3.60-4.00 sec consist of reflected acoustic energy.

Hour 09

Data set *jd267093408Spice* was recorded in the second refracted convergence zone behind the Kermit-Roosevelt Seamount and results are shown in Fig. 6-36. Both the RAM and BASSEX results show two distinct ray groups, starting at 3.00 sec [in the RAM time series]. The BASSEX results appear delayed because of a DAQ randomly delayed start.

The first and second rays in the first group appear partially cutoff by the seamount. Weak early arrival acoustic rays are visible in the RAM and BASSEX results at 2.25 sec and are associated with limiting rays. Acoustic rays during 3.60-4.00 sec consist of reflected acoustic energy.

Hour 10

Data set *jd267102333KauaiSpice* was recorded along the boundary between the second refracted convergence zone and the second shadow zone behind the Kermit-Roosevelt Seamount and results are shown in Fig. 6-37. The BASSEX results appear delayed because of a DAQ randomly delayed start.

Both the RAM and BASSEX results show a distinct ray group at 3.40 sec [in the RAM time series]. A weak ray group at 3.10 sec appears to have been partially cutoff by the seamount. Early arrival acoustic rays appear in the BASSEX and RAM results at 2.25 sec, and are associated with limiting rays. Engine noise is visible at 16 deg.

Hour 11

Data set *jd267113408Spice* was recorded in the second shadow region behind the Kermit-Roosevelt Seamount and results are shown in Fig. 6-38. In the RAM results, a ray group at 2.30 sec contains reflected rays. In the BASSEX results, ray groups at 3.20 and 3.70 sec contain limiting rays, based on their structure and location in time relative to refracted rays visible further out in range. The remainder of the rays in the observed pattern are mostly BR and/or SRBR. Engine noise is visible at 18 deg.

Hour 12

Data set *jd267123408Spice* was recorded in the second shadow zone behind the Kermit-Roosevelt Seamount and results are shown in Fig. 6-39. At 2.25 sec [in the RAM time series] a weak ray group is visible which is a reflected ray. In the BASSEX results, the ray groups at 3.20 and 3.80 sec contain limiting rays because of their structure and location in time relative to refracted rays visible further out in range. The remainder of the energy in the observed pattern contains BR and/or SRBR acoustic rays.

Hour 13

Data set *jd267133408Spice* was recorded in the second reflected convergence zone behind the Kermit-Roosevelt Seamount and results are shown in Fig. 6-40. The arrival pattern consists only of BR and SRBR acoustic rays, given the low intensity of the rays. Ray group stucture is visible, and the early arrival rays are well correlated with RAM.

Hour 14

Data set *jd267142333KauaiSpice* was recorded along the boundary between the first refracted convergence zone and shadow zone behind the Kermit-Roosevelt Seamount and results are shown in Fig. 6-41. The RAM and BASSEX results show agreement between ray groups at 1.8, 2.7, and 3.2 sec in terms of arrival time. The ray groups which arrive between 1.8 and 2.5 sec are limiting rays, and the rest are refracted rays. Several BR and SRBR acoustic rays are present betwee 3.5 and 4 sec. The butterfly pattern visible in the steeper arrivals is an artifact of MPDR beamforming.

Hour 15

Data set *jd267153408Spice* was recorded in the first refracted convergence zone behind the Kermit-Roosevelt Seamount and results are shown in Fig. 6-42. The BASSEX and RAM results show good agreement between two refracted ray groups at 2.80 and 3.40 sec in terms of arrival time. The faint ray group visible in the RAM results at 1.95 sec is not observed in the BASSEX data, which suggests inaccurate environmental modeling. Also, the BASSEX results appear expanded in time compared with the RAM results, which again could be attributed to minor environmental mismatch. There are some additional ray groups observed at 2.90 sec and 3.60-3.85 sec which are BR acoustic rays, and are not visible in the RAM results.

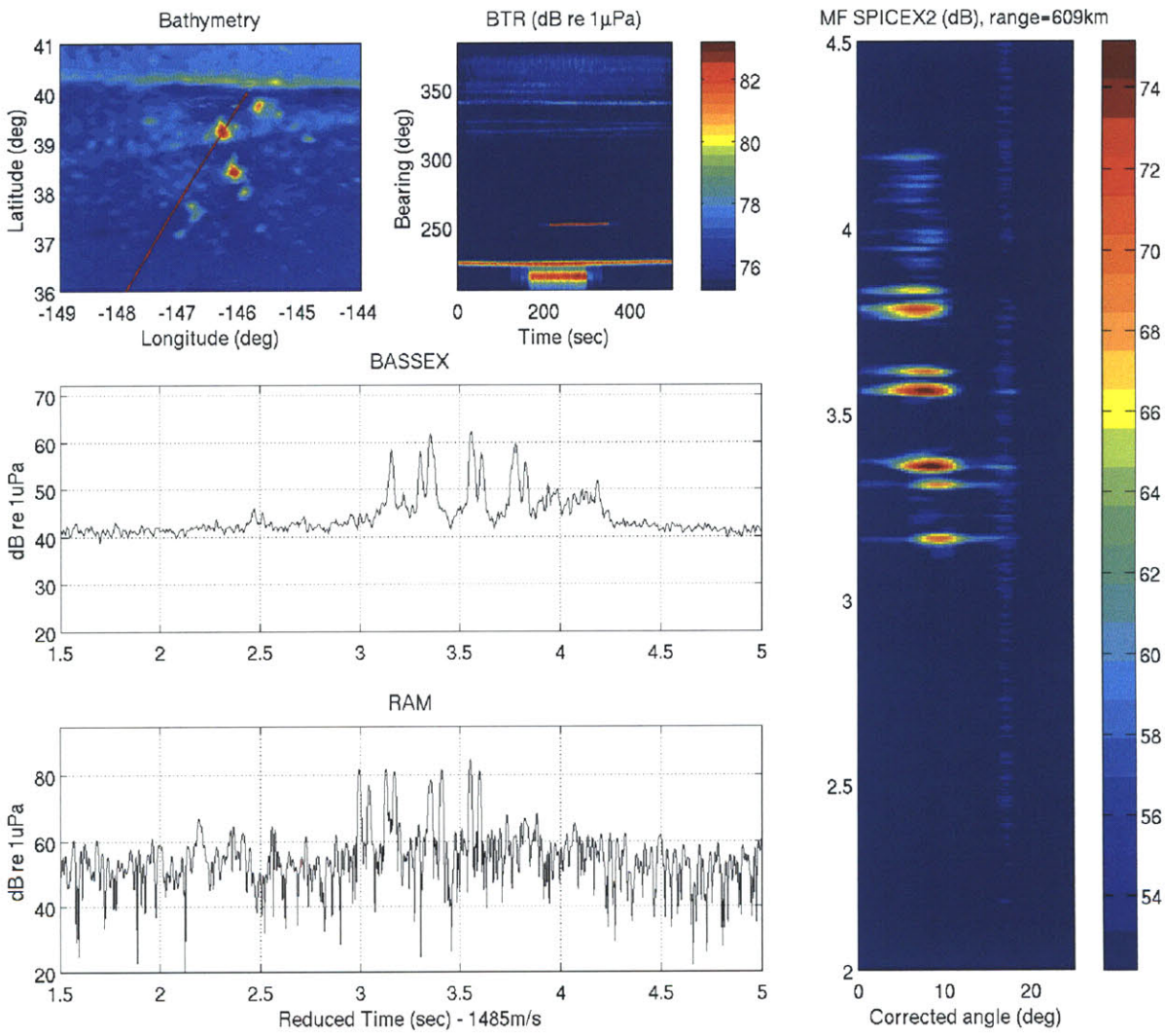

Figure 6-35: BASSEX data from hour 8 of Julian day 267.

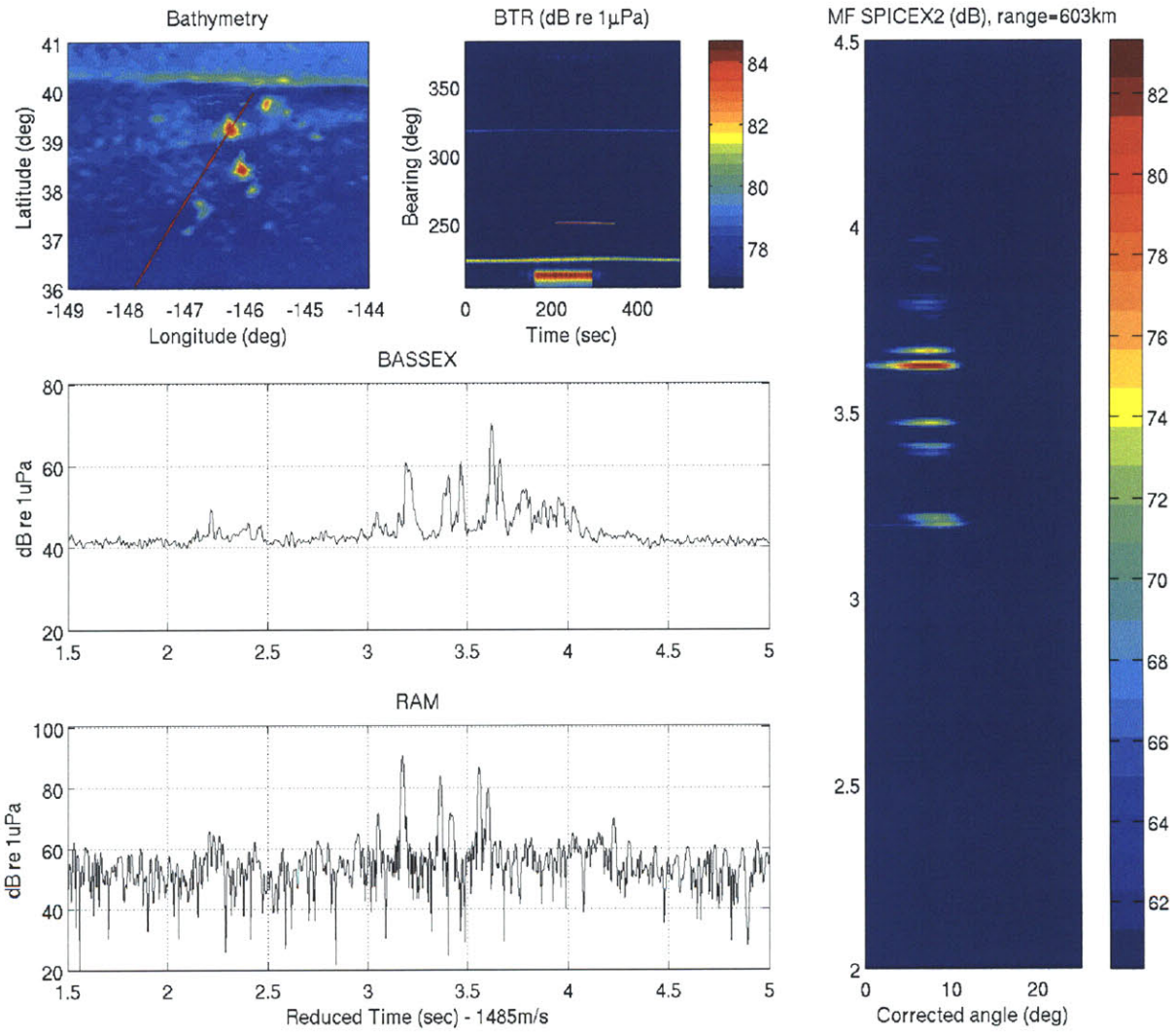

Figure 6-36: BASSEX data from hour 9 of Julian day 267.

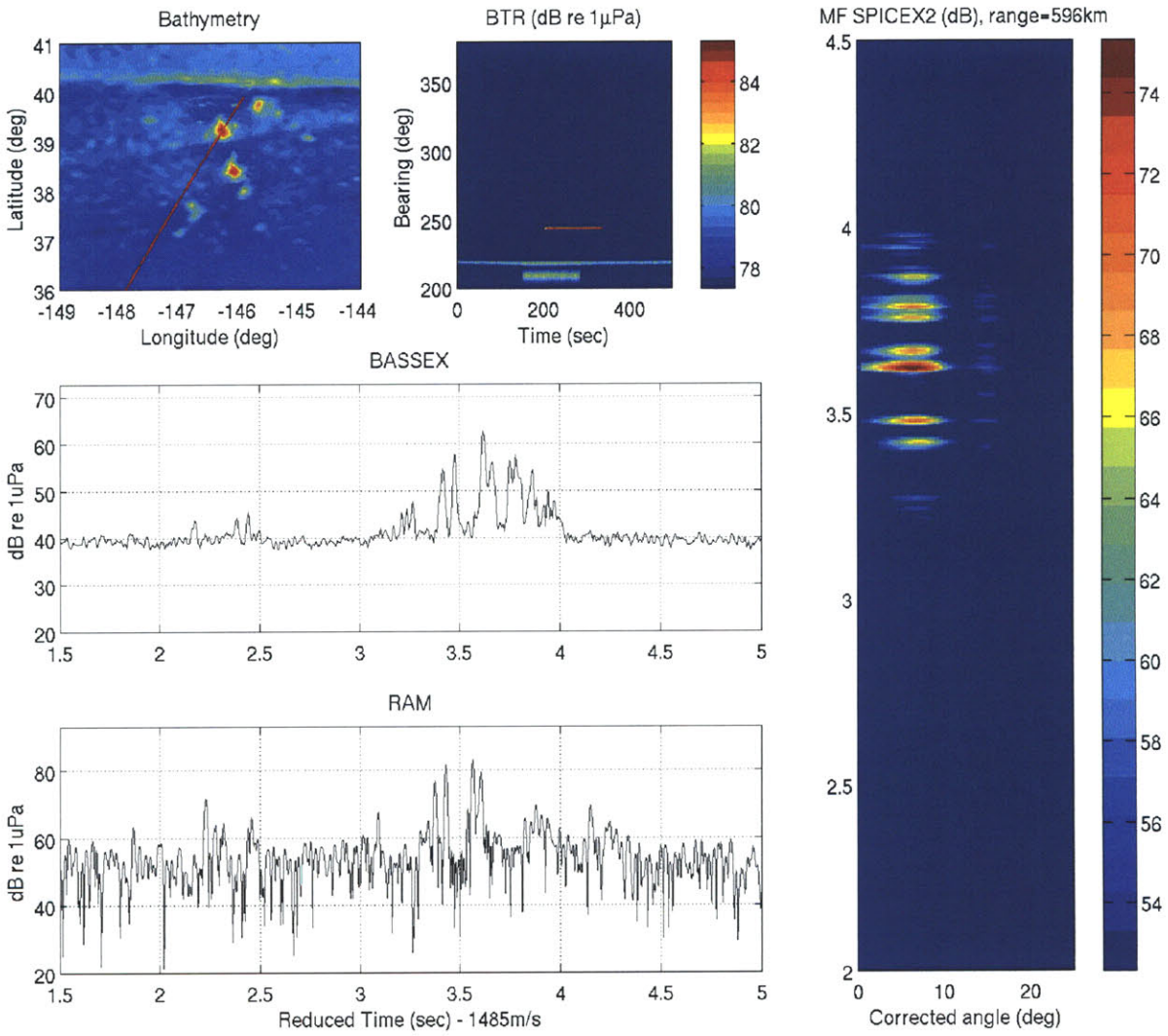

Figure 6-37: BASSEX data from hour 10 of Julian day 267.

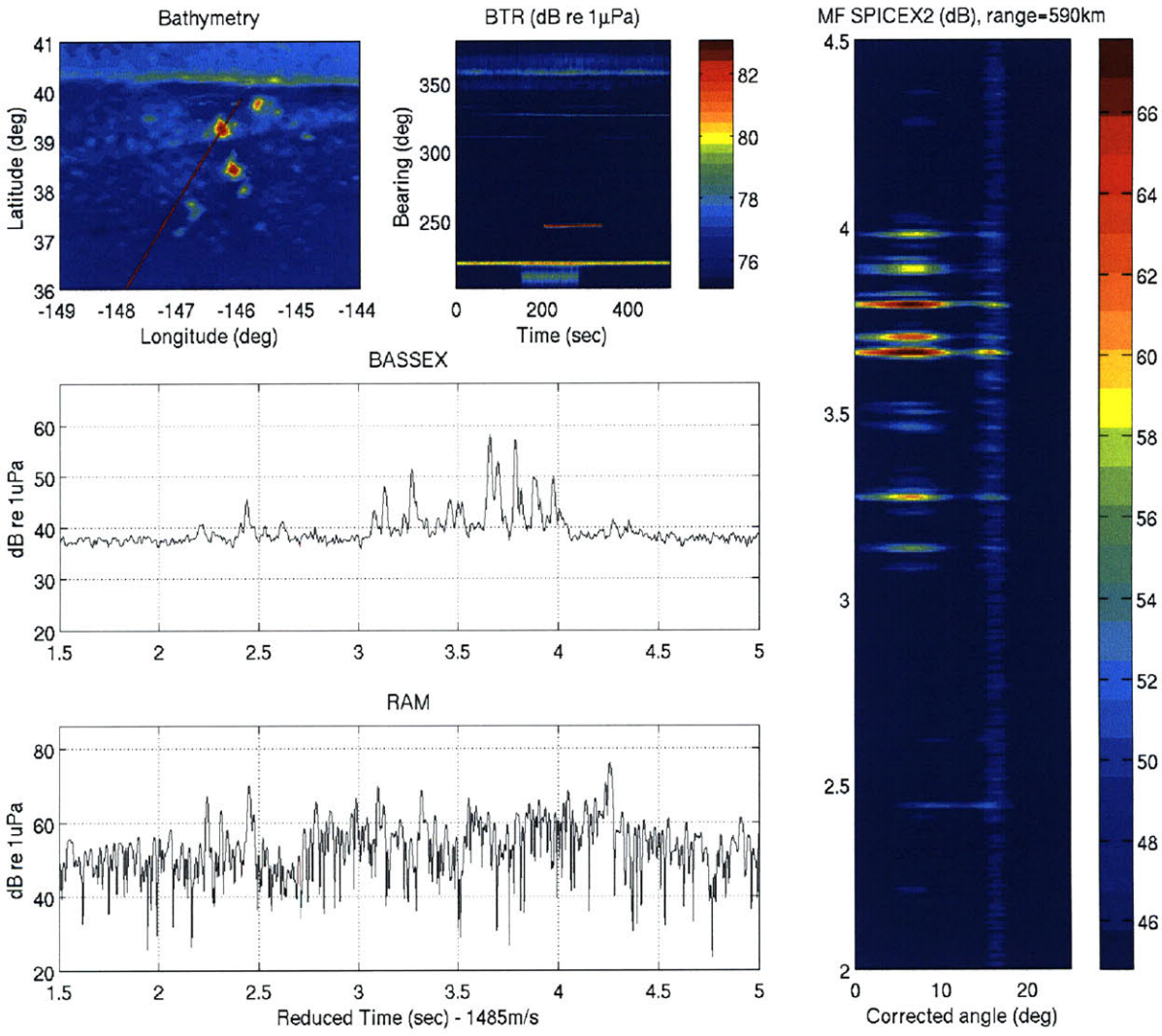

Figure 6-38: BASSEX data from hour 11 of Julian day 267.

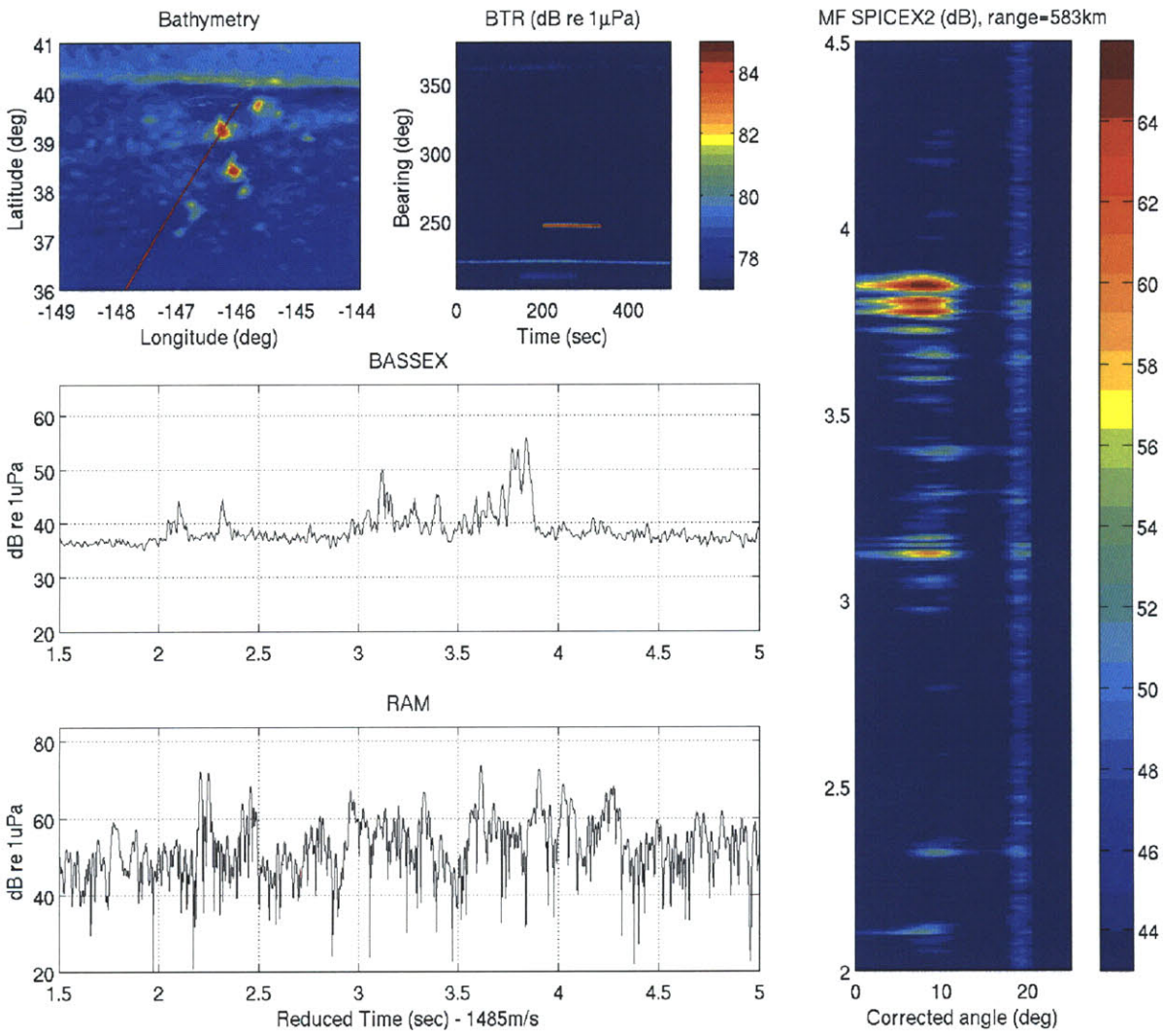

Figure 6-39: BASSEX data from hour 12 of Julian day 267.

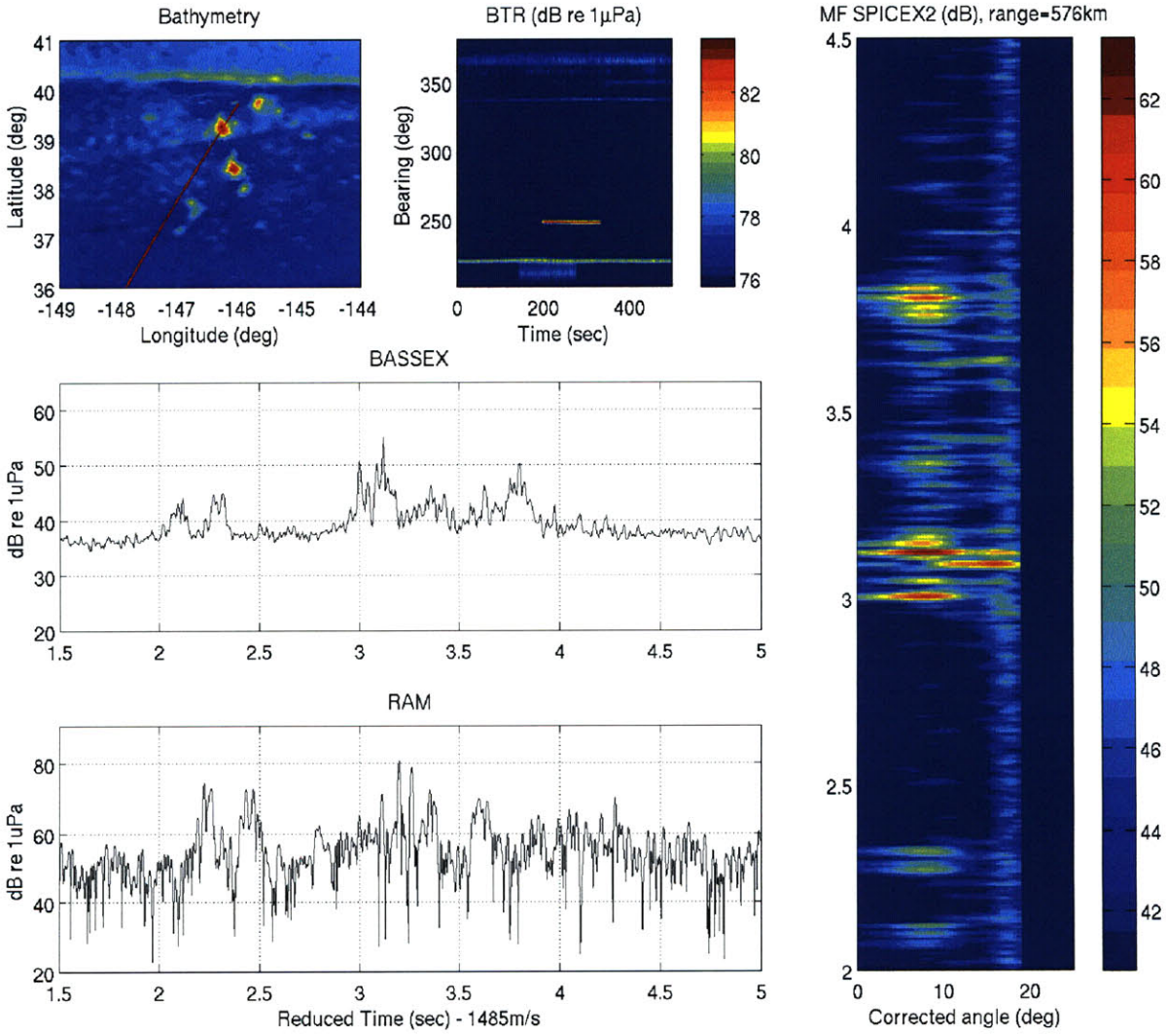

Figure 6-40: BASSEX data from hour 13 of Julian day 267.

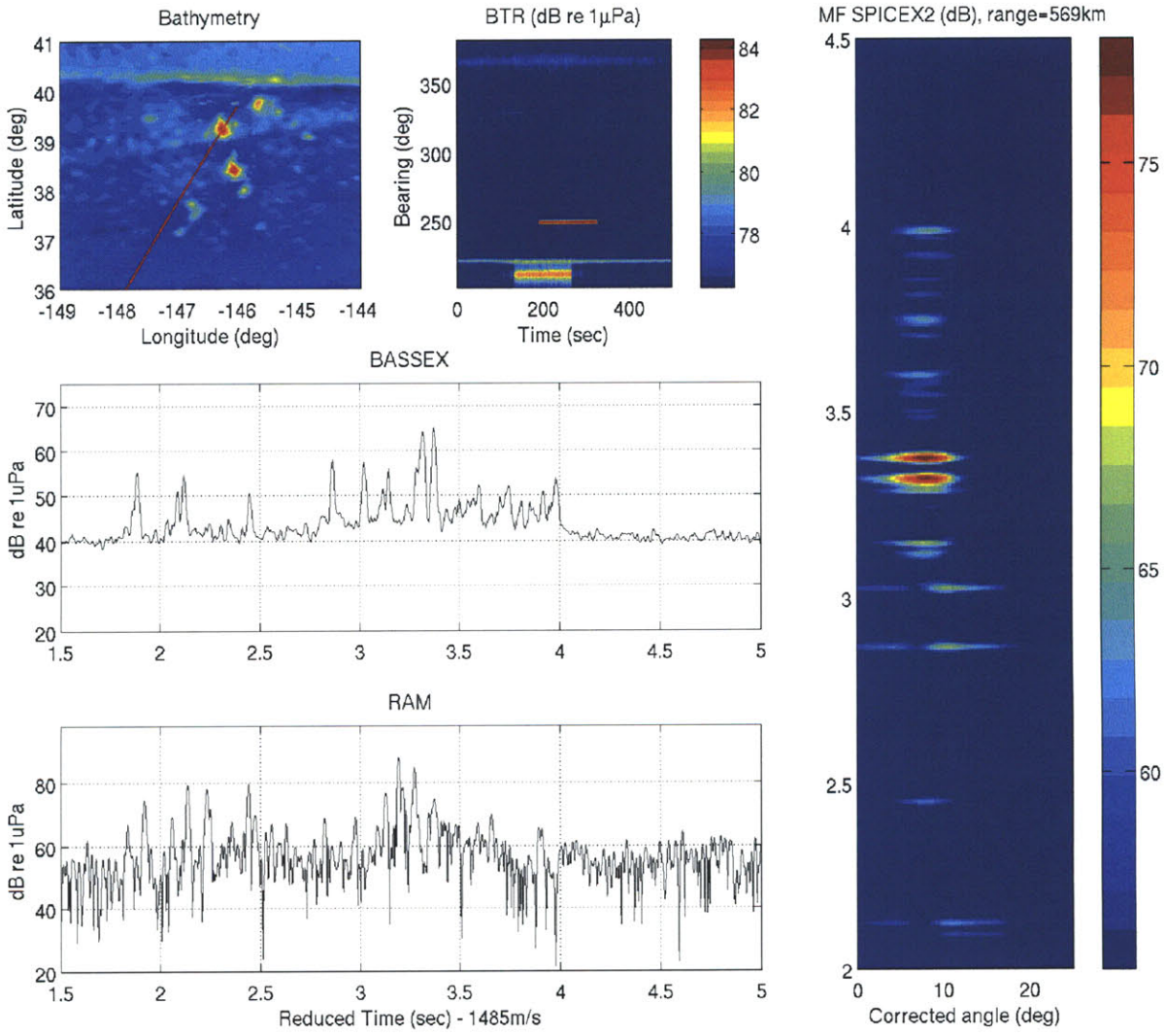

Figure 6-41: BASSEX data from hour 14 of Julian day 267.

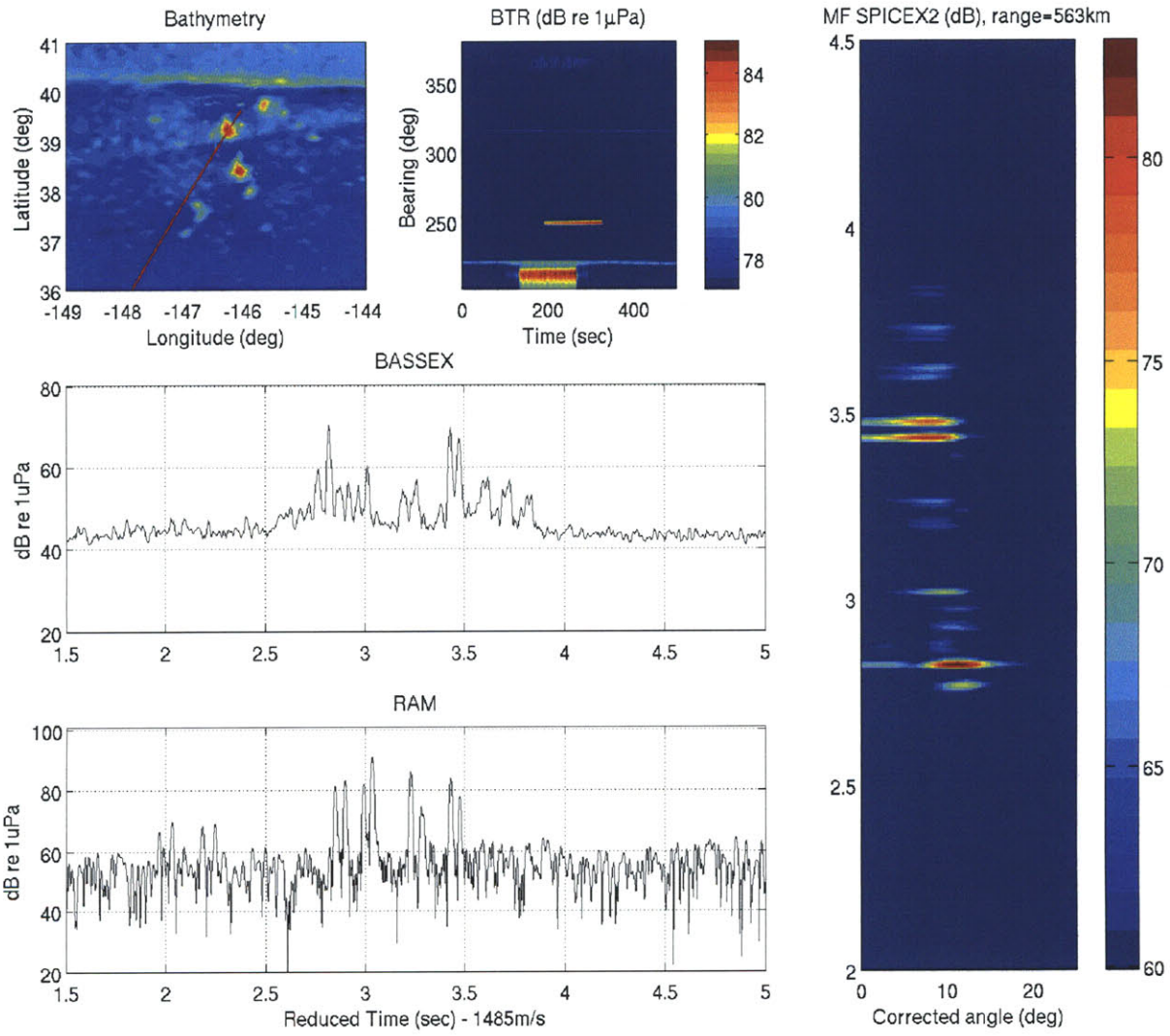

Figure 6-42: BASSEX data from hour 15 of Julian day 267.

6.6.1 Conclusion: The Kermit-Roosevelt Seamount Forward-Scattered Field - Day 267

This section investigated the data gathered in the shadow zone of the Kermit-Roosevelt Seamount on Julian day 267 during the BASSEX experiment. RAM simulated time series were used to determine the accuracy of observed results and environmental modeling issues. Reflected convergence zones were observed at lower acoustic amplitudes than RAM results predicted, which could be the result of environmental uncertainty; *i.e.*, the sound velocity profile was measured along the geodesic connecting the source with test stations behind the Elvis, not Kermit-Roosevelt, Seamount. Acoustic rays in the shadow zones behind the Kermit-Roosevelt Seamount could not be identified due to a lack of beamformed RAM data and ray trace results. BASSEX and RAM results showed good agreement in peak pressure levels inside the refracted convergence zones and shadow zones. An assessment of the accuracy of the RAM acoustic modeler is not offered here because simulated array data and eigenrays were unavailable.

6.7 Kermit-Roosevelt Seamount Side Scatter LOAPEX Data

This section examines the available side-scattered acoustic data gathered during the BASSEX experiment using the LOAPEX ship deployed source, which was located nearby the SPICEX source S2. On Julian day 266, the FORA array was towed northeast of the Kermit-Roosevelt Seamount on ship tracks perpendicular to the direct sound path. The LOAPEX signals were approximately 1300 sec in duration with 44 periods. Significant data drop-outs and low SNR in the seamount shadow zone motivated the use of the PS-PCML beamformer. Data were processed using the process shown in Fig. 4-3.

Figure 6-43 shows the measured peak acoustic pressure, superimposed over bathymetry contours of the seamount for reference, and test station locations and sound paths are indicated. The bi-harmonic spline interpolation algorithm, presented by Sandwell [65], is applied to interpolate the sparse data set. The figure shows three distinct acoustic shadow regions. The Hour 0 and 6 test stations showed the strongest acoustic shadow at a level of about 20 dB.

Currently there are no 3-D PE or coupled mode acoustic modelers available which can efficiently simulate the broadband acoustic scatter field of the Kermit-Roosevelt Seamount of $O(600\text{ km})$. Arrival patterns from test station recordings *jd266005147L1000* and *jd266015147L1000*, which show the most significant side-scattered acoustic energy, are presented to aid future work; other LOAPEX data sets do not reveal any discernable side-scatter, and will therefore not be presented in this thesis.

Hour 00

As the DAQ recorded *jd266005147L1000*, the array moved from deep shadow to a penumbra region where direct[9] acoustic arrivals were observed. Figures 6-44(a), 6-44(b), and 6-44(c) show the PS-PCML beamformed, pulse compressed time series from periods 5, 12, and 20 of the recorded LOAPEX transmission, and the location of the array over the seamount, with angle off-endfire plotted for reference.

The observed arrival pattern changes significantly over the course of this reception because of the relatively short distance between the array and the seamount, and the long duration of the source transmission. The SNR increased steadily between periods 5-20,

[9]Direct acoustic arrivals travel without reflecting off any surfaces.

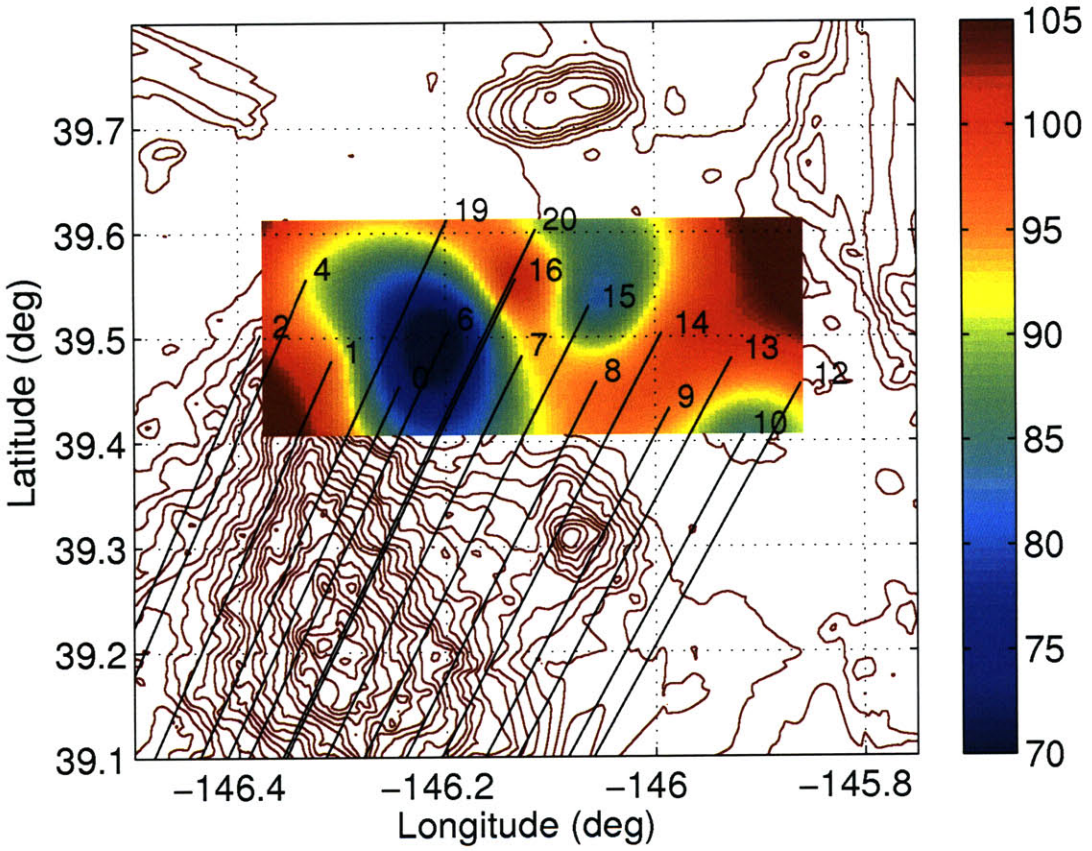

Figure 6-43: Peak acoustic pressure level in the Kermit-Roosevelt Seamount forward-scattered field, measured on Julian day 266 from the LOAPEX source. Pressure is given in dB re 1μPa.

and the arrival pattern began to show characteristics of open-ocean direct acoustic arrival patterns at this range, indicating a possible boundary between the deep shadow zone and penumbra regions of the forward-scattered field.

Period 5 shows ray arrivals between 90 and 95 deg, which could either be direct or side-scattered acoustic rays given their amplitude and angle of arrival.[10] The acoustic rays which arrive above 95 deg are not realizable with direct path arrivals, and are therefore associated with side-scattered acoustic energy. The location on the seamount surface where the energy was reflected could not be discerned because of the conical ambiguity of the array.

Hour 01

Figures 6-45(a), 6-45(b), and 6-45(c) show the PS-PCML beamformed, pulse compressed time series from periods 5, 23, and 41 of the m-sequence for test station *jd266015147L1000*. The results were gathered outside the "deep shadow region" and appear stronger than hour 00 results.

The observed data show three strong, direct arrival acoustic rays at 95 deg. There are significant acoustic rays above 95 deg at about 85 dB which are associated with side-scattered acoustic energy. It is suggested that the curved northwest face of the seamount "funnels" acoustic energy to the receiver array at this location.

6.7.1 Conclusion: Kermit-Roosevelt Side-Scattered Field

The available LOAPEX data from the BASSEX experiment shows that side-scattered acoustic rays can emanate from the seamount with audible and significant signal strength, within 10 dB of the direct arrival signals. Results suggest that the shape of the seamount has some effect on the amount of side-scattered acoustic data, and that to accurately determine the origin of the reflected energy, a different array geometry needs to be employed in subsequent experiments, or a 3-D acoustic modeler must be used to corroborate these experimental results.

This data set is the first presented which is processed with the modified PS-PCML beamformer. The PS-PCML beamformer was chosen for improved resolution, low-biased

[10]The array was broadside to the direct sound path; therefore, rays will appear closer to 90 deg, with increasing steepness for increasing acoustic ray arrival angle.

power estimation, and robustness to snap-shot deficiency and data drop-outs. The most significant disadvantage of using the PS-PCML beamformer is the height of the first side-lobes, observed to be about -20 dB from the main lobe height, which can cause false alarms when using a high dynamic range.

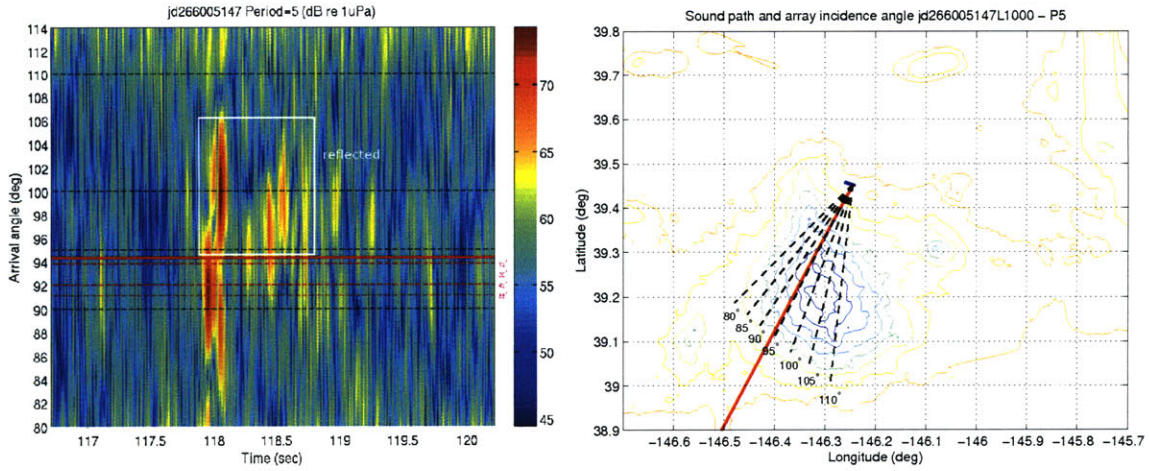

(a) jd266005147L1000 - Period 5

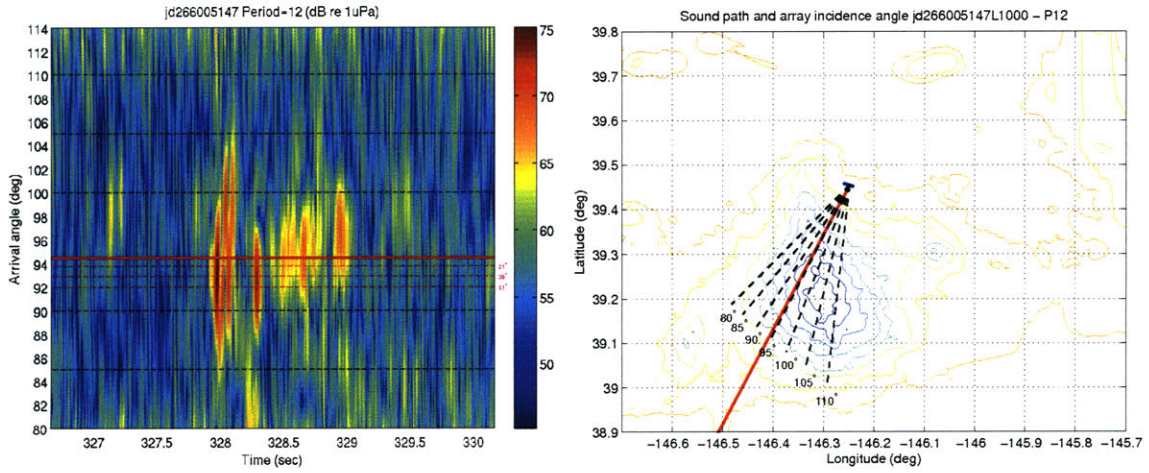

(b) jd266005147L1000 - Period 12

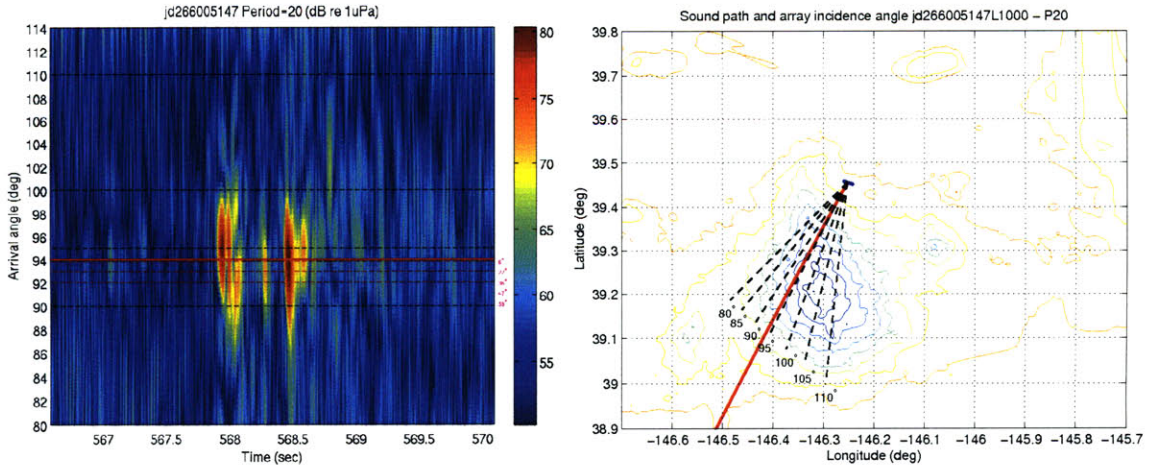

(c) jd266005147L1000 - Period 20

Figure 6-44: Measured arrival pattern and sound path for BASSEX data record *jd266005147L1000*.

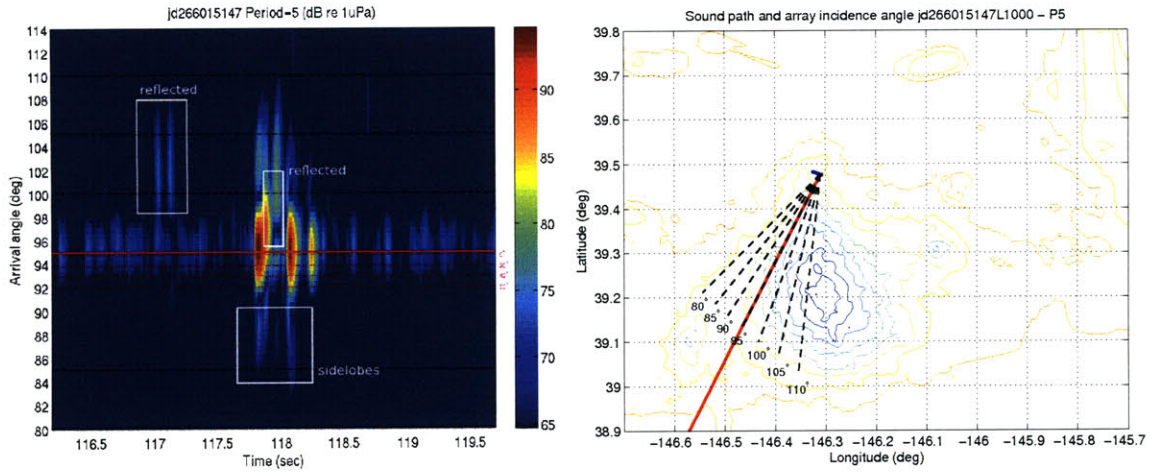

(a) jd266015147L1000 - Period 5

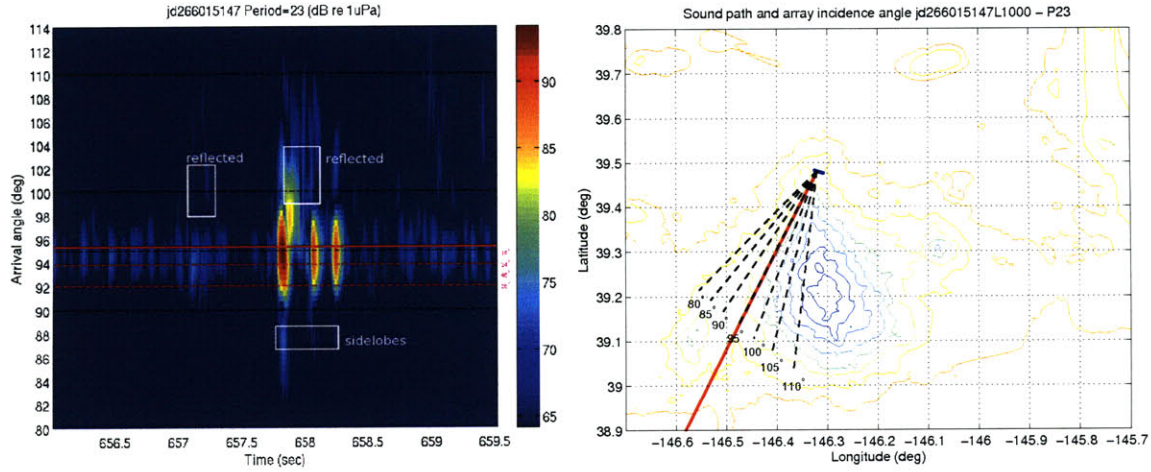

(b) jd266015147L1000 - Period 23

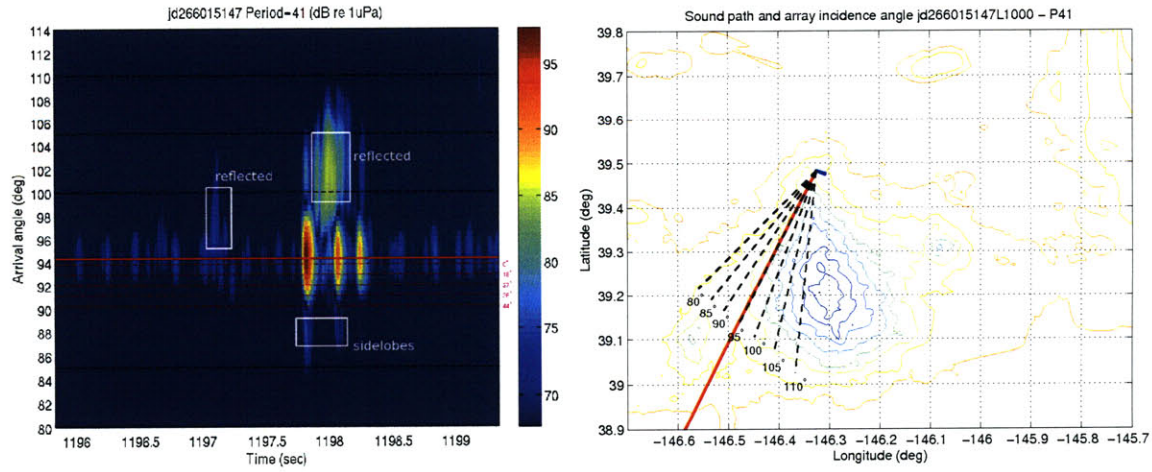

(c) jd266015147L1000 - Period 41

Figure 6-45: Measured arrival pattern and sound path for BASSEX data record *jd266015147L1000*.

Chapter 7

Conclusions and Future Work

This thesis described methods for measuring acoustic arrival patterns in the presence of strong interference, and the use of those methods to investigate low frequency modal coupling by the Kermit-Roosevelt Seamounts with data from the BASSEX experiment. This chapter summarizes the specific contributions made by the research performed in support of this thesis and the challenges encountered, and also motivates future work.

It was the underlying goal of this thesis to show that seamounts which shoal in the SOFAR channel do not severely attenuate acoustic energy in long-range ocean waveguides, which was answered in the affirmative. This thesis investigated two ocean seamounts which shoal just below the minimum sound channel axis of the ocean and showed that a significant amount of acoustic energy is able to pass over the seamount forming strong convergence zones which eventually widen and fill-in the forward-scattered field. These results can be generalized to seamounts with different characteristics – *e.g.*, height, base radius, geoacoustic properties – which affect the structure of the scattered field. For example, taller seamounts should create wider shadow zones in the forward-scattered field and have higher modal coupling, and thus wider reflected convergence zones. Seamounts with wider base radii should show less 3-D scattering in the forward-scattered field. More absorptive sediment in the sea floor should have weaker reflected convergence zones.

7.1 Forward-Scattered Field Investigation

A significant contribution of the work described in this thesis is a detailed investigation of the forward-scattered fields of the Kermit-Roosevelt and Elvis Seamounts in the Pacific

Ocean. Previous work has focused on flat-bottom acoustic propagation, and the transmission loss caused by seamounts. The data analysis presented in this thesis is the first to specifically measure acoustic arrival patterns in the forward-scattered fields of seamounts at long-range, using broadband pseudorandom sequence transmissions and a towed hydrophone array. An investigation of the forward-scattered field revealed that refracted and reflected acoustic energy convergence zones exist in the upper-water column behind the seamounts, and that environmental variability and diffraction strongly affect the location of shadow zone boundaries.

7.1.1 Acoustic Shadowing

Acoustic shadowing in the forward-scattered field of the seamounts was measured in the upper-water column of about 20 dB, relative to flat-bottom acoustic propagation, and showed good agreement with RAM simulated results. High order mode blockage by the seamount created strong convergence zones in the forward-scattered field consisting of refracted acoustic rays which skipped over the seamount peak. Modal coupling, caused by the seamount bathymetry, created convergence zones in the forward-scattered field which were approximately 10 dB weaker than refracted convergence zones, and in some cases fill the acoustic shadow zones.

7.1.2 Range-dependent Acoustic Modeling

Ray trace model results generated with RAY showed agreement with steep, refracted and bottom-reflected acoustic rays in terms of arrival angle and travel time; however, simulated results did not agree with observed surface-reflected-bottom-reflected acoustic rays in the forward-scattered field due to environmental uncertainty and ray chaos [34]. Missing shallow angle acoustic rays in simulated results are attributed to low acoustic ray code precision.

Parabolic equation approximation model simulated results, generated using RAM, showed good agreement with most of the observed refracted and reflected acoustic rays in terms of amplitude, travel time, and arrival angle, with the exception of steep SRBR and limiting acoustic rays. Signal fluctuations of 30 dB were observed inside a seamount forward-scattered field which agreed with simulated results.

7.1.3 Measured Acoustic Noise

Acoustic noise was measured in the Kermit-Roosevelt Seamount Complex from distant shipping traffic, natural phenomena, propeller blade rate, and vibrations from shipboard motors and compressors. The measured ambient noise field was correlated with wind measurements gathered by a nearby weather buoy to show that wind contributed between 5-10 dB re $1\mu\text{Pa}/\sqrt{\text{Hz}}$ acoustic noise throughout the experiment. Significant directional noise sources in BASSEX hydrophone array data motivated analysis using adaptive beamformers.

7.1.4 Three-dimensional Scatter Field Investigation

This thesis also investigated the 3-D scatter field of the Kermit-Roosevelt Seamount. Acoustic arrival patterns measured behind the seamounts along Track 4, which was perpendicular to the direct sound propagation path, showed high-angle acoustic ray attenuation of about 15 dB for regions spanning the projected width of the seamounts at base depths between 3-4 km.

Two data records gathered over the top of the seamount were investigated and revealed significant side-scattered acoustic energy; in one record, the towed array was observed traveling out of the shadow zone of the seamount into the penumbra region during the time of one 20 minute transmission. Observed side-scattered acoustic energy was approximately 10 dB weaker than flat-bottom propagation acoustic rays. The location from which the observed side-scattered acoustic energy reflected off the seamount could not be determined because of the conical ambiguity of the array.

In terms of future research, 3-D range-dependent acoustic models should be used to verify these results. Currently, coupled mode and parabolic equation acoustic codes are not sufficiently computationally efficient to handle complex bathymetry at the range scale and acoustic frequencies used in the BASSEX experiment.

7.2 Physically Constrained Maximum Likelihood Beamforming using Trigonometric Basis Functions

This thesis developed and implements an efficient PCML beamformer, which has low-bias and is robust to snap-shot deficiency. The new PS-PCML beamforming approach mod-

els the array spectral covariance matrix with orthonormal trigonometric basis functions which mimic the array response to plane wave interference spanning visible wavenumber space; using orthonormal basis vectors leads to an analytic formula for propagating power terms, improving computational efficiency. Physical constraints are applied to form a maximum-likelihood covariance matrix which is well conditioned and invertible. The PS-PCML approach forms a Toeplitz covariance matrix, and differs from previous methods by determining the maximum-likelihood sensor noise diagonal loading term, and by smoothing the power spectrum which improves computational efficiency and equally weights all plane wave interference across visible wavenumber space.

Simulated data reveals the following about PS-PCML performance: the estimated wavenumber-power along the main-response axis has low sensitivity to sensor position perturbation than the Capon beamformer, the HPBW is about 50% the size of the Bartlett beamformer, the method produces broad nulls in the beampattern, the array gain is 2 dB higher than the Capon beamformer (0 dB diagonal loading) in the sidelobe region for a spectral covariance matrix estimated with only two snap-shots, on average. When the number of snap-shots is less than $2N$ the PS-PCML beamformer has higher output SNR than the Capon and Bartlett beamformers.

The PS-PCML beamformer was applied to real acoustic towed array data from the BASSEX data set to determine its performance in complicated noise field environments. The ultra-low frequency section of the FORA array was used, which consisted of 62 hydrophones with 3 m spacing. The measured resolution from the PS-PCML beamformer was approximately 3.5 deg, which was approximately half that of the Bartlett beamformer. The measured peak signal strength from the PS-PCML and Bartlett beamformers were approximately equal throughout the reception; this demonstrated that the PS-PCML beamformer has very low bias.

7.3 Challenges

The most challenging aspects of attaining the experimental results presented in this thesis were array stability, DAQ malfunctions, and vibrational noise from the tow ship; these issues should be addressed before a similar experiment is executed. In analyzing the data, the conical ambiguity of the array made it difficult to separate upward and downward

propagating plane waves, as well as horizontally separated rays. In the future, vector sensors will likely be available which can separate plane waves in the horizontal and vertical directions, but currently do not operate at low frequencies.

7.4 Future Work

One issue which was not addressed by this thesis is the temporal coherence of acoustic modes in the scattered-field of a seamount. The temporal coherence of low order acoustic mode amplitudes was determined to be about 5.5 min at 5 Mm ranges for relatively flat-bottom propagation, as part of the ATOC experiment [8]. As part of future work, it would be of interest to measure the temporal coherence of reflected acoustic energy inside the forward-scattered field of a seamount at long-range; this work would likely require a fixed receiver array with accurate sensor positioning capability. In particular, this thesis showed the most significant deviation between experimental and simulated results occurs along shadow zone caustics, and therefore these regions should be the focus of any future study of long-range bathymetric modal coupling.

The investigation of the effects of the Kermit-Roosevelt Seamounts presented in this thesis focused on 2-D acoustic propagation in the upper water column and showed good agreement between experimental and simulated results in the near forward-scattered fields. The effects of horizontal diffracted acoustic energy in the forward-scattered field of seamounts at long-range has still not been carefully investigated in the forward-scattered field and should be the focus of future research; *e.g.*, interference between horizontal and axial modes could affect the location and intensity of convergence zones.

A test with an array which changes orientation fairly rapidly in time – *e.g.*, a sensor array on an autonomous underwater vehicle – would be useful to validate the PS-PCML beamformer. Also, the PCML method could potentially be applied to vector sensor arrays, which have much larger spectral covariance matrices and require more snap-shots, to improve spatial resolution.

Appendix A

Computing Technical Details

The research supporting this thesis was performed on an IBM-PC compatible computer running the Fedora Linux operating system (http://fedoraproject.org/). The computer uses a quad-core 2.2 GHz AMD Phenom central processor and 4 GB DDR2 system memory.

The computer programming language Matlab is used to process data and generate the figures presented in this thesis. Matlab is a technical computing language used for numeric computations and 2-D and 3-D visualization of data, and is produced by The MathWorks (http://www.mathworks.com).

The Ocean Acoustical Ray-Tracing Software, or RAY, program, written in 1992 by James Bowlin *et al.* [17] for the Woods Hole Oceanographic Institution, is used to reconcile data from the BASSEX experiment. The RAY program is a ray tracer code that can handle range-varying sound velocity profiles and bathymetry. Most notably, the RAY code smooths sound velocity and bathymetry data between samples to eliminate false caustics.

The Range-dependent Acoustic Modeler, or RAM, is also used to simulate acoustic propagation, and uses the parabolic equation and split-step Padé approximation method; see Collins *et al.* [18], [19]. RAM was written by Michael Collins, of the Office of Naval Research, for use by the Navy.

Appendix B

Matched Filtering

Analysis of the experimental data assumes that sound propagation along ray paths is linear, non-dispersive, and contains added white Gaussian noise. The optimal method for detecting time of arrival is to use matched filters. Matched filters provide the best signal to noise ratio (SNR) and highest probability of detection. The following algebraic analysis shows that the matched filter is optimal in this circumstance.

The observed signal is the sum of the desired signal, $s[m]$, and noise, $n[m]$,

$$x = s + n. \tag{B.1}$$

To determine the time of arrival in the presence of noise, the data must be passed through a filter, yet to be determined. The output of the filter is

$$y = \sum_{k=-\infty}^{\infty} h^* x = h^H x = h^H s + h^H n. \tag{B.2}$$

The signal to noise ratio of the filter output is

$$SNR = \frac{|h^H s|^2}{E\{|h^H n|^2\}} = \frac{|h^H s|^2}{h^H R_n h}, \tag{B.3}$$

where $R_n = E\{nn^H\}$. Applying the Cauchy-Schwartz inequality reveals that

$$SNR = \frac{|(R_n^{1/2}h)^H(R_n^{-1/2}s)|^2}{(R_n^{1/2}h)^H(R_n^{1/2}h)} \leq s^H R_n^{-1} s. \tag{B.4}$$

To achieve the upper bound h must be chosen such that $R_n^{1/2}h = \alpha R_n^{-1/2}s$. Therefore, the optimal filter is

$$h = \alpha R_n^{-1}s, \tag{B.5}$$

where

$$\alpha = \frac{1}{\sqrt{s^H R_n^{-1}s}}. \tag{B.6}$$

The additive white Gaussian noise assumption implies that R_n is diagonal and α is a simple scale factor. Since the amplitude of the Gaussian noise is unknown, the best matched filter is simply the time reversed reference signal, $h[m] = s[-m]$.

Appendix C

Angle Correction Algorithm

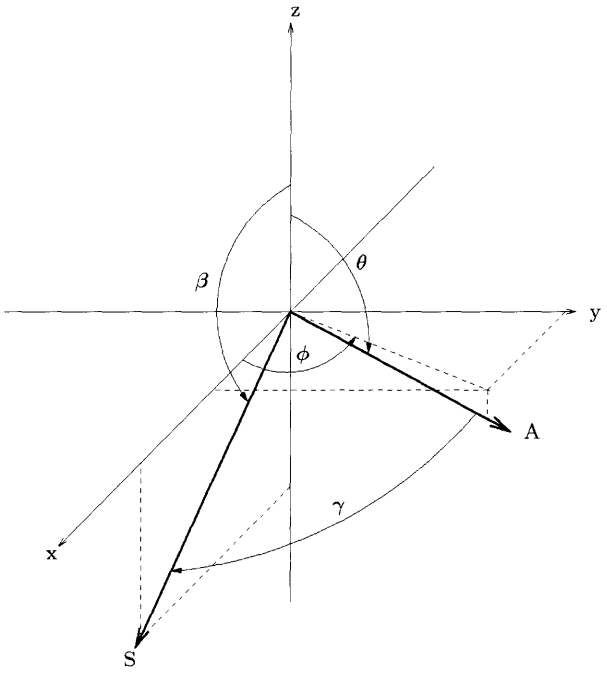

Figure C-1: Array orientation

$$
\begin{aligned}
\mathbf{S} &= \text{orientation vector of incoming ray path, unit length} \\
\mathbf{A} &= \text{orientation vector of hydrophone array, unit length} \\
\mathbf{x} &= \text{the direction to the source} \\
\gamma &= \text{measured angle} \\
\beta &= \text{desired ray path angle} \\
\phi &= \text{array heading deviation from x-axis} \\
\theta &= \text{array pitch}
\end{aligned}
\tag{C.1}
$$

$$
\begin{aligned}
x &= \sin\theta\cos\phi \\
y &= \sin\theta\sin\phi \\
z &= \cos\theta
\end{aligned}
$$

$$
\mathbf{S} = \begin{bmatrix} \sin\beta & 0 & \cos\beta \end{bmatrix}^T
$$

$$
\mathbf{A} = \begin{bmatrix} \sin\theta\cos\phi & \sin\theta\sin\phi & \cos\theta \end{bmatrix}^T
$$

$$
\mathbf{A}^T\mathbf{S} = \sin\theta\cos\phi\sin\beta + \cos\theta\cos\beta = |\mathbf{A}||\mathbf{S}|\cos\gamma = \cos\gamma \tag{C.2}
$$

$$
J = \sin\theta\cos\phi\sin\beta + \cos\theta\cos\beta - \cos\gamma \tag{C.3}
$$

C.1 Processing Real World Data

Measured angles are determined using beamforming and matched filtering algorithms. The heading to the source is determined using the GPS location of the ship and source, and the WGS 1984 ellipsoid model of the Earth. The heading of the array is averaged between the two magnetic sensors inside the array, bow and stern. Magnetic deviation is corrected given the time and ship location, and the heading measurement is averaged over 11 samples. The pitch of the array is measured using depth sensors in the bow and stern of the array. The arc tangent of the difference in sensor depths divided by the length yields the pitch of the array.

C.2 Method for Finding Zero-crossings

In order to determine β, the zero-crossings of J must be found. A simple version of the bi-section technique can be applied here – finely sample β from 90° to 180° degrees and search for any sign flips.

Often there will be two zero-crossings. β_{min} is the value of $\beta > 90°$ which produces the minimum possible value of γ. Values of $\beta < \beta_{min}$ can give the same γ as values of $\beta > \beta_{min}$, leading to multiple zero-crossings. The software developer must decide which zero-crossing is appropriate to choose. (In this thesis, the greater of the two is chosen since most rays arrive at angles higher than β_{min}.)

C.3 Handling "Impossible" Angles

If the array is oriented along the x-axis, directly towards the source, $\gamma = \beta - 90°$ for $0° < \beta < 360°$. If the array's heading is different than the source heading it is easy to see that there are some values of γ which cannot be achieved for any value of β. For example, if the array's heading were off from the source heading by 5°, and there were no pitch, $\min \gamma = 5°$. Adding pitch or having a heading difference greater than 90° complicate the matter further.

These angles which cannot be achieved, these "impossible" angles, need to be accounted for in the code used to correct for array position and orientation. Ideally the "impossible" angles should be removed from the final output or pushed off to 0° degrees. The analytic approach of determining the minimum possible value of γ is to apply equation (C.2), and then solve for γ. This leads to the expression

$$\gamma_{min} = \arccos(\sin^2\theta\cos\phi + \cos^2\theta). \tag{C.4}$$

Figure C-2 shows simulated values of β, given γ, and corrected values of β given γ using the same Matlab code that was used in the thesis. The results show that the code handles the measured angles as described above.

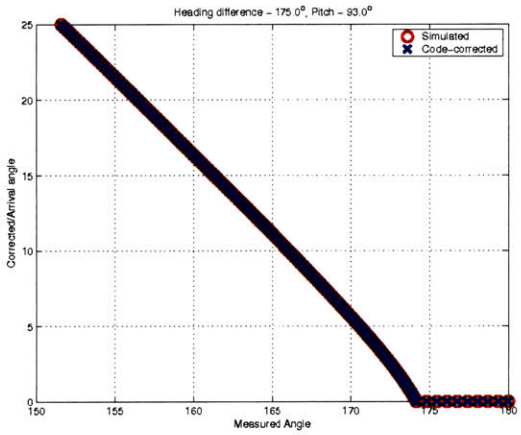

(a) Angle correction example 1

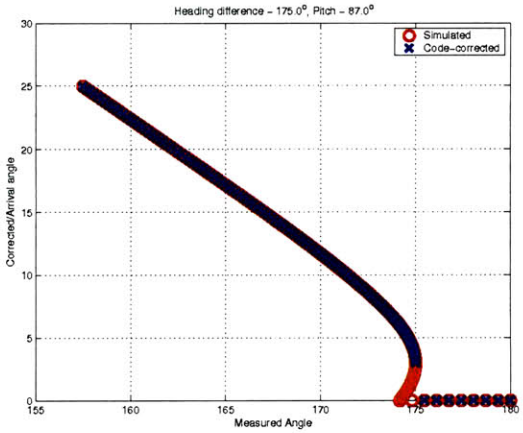

(b) Angle correction example 2

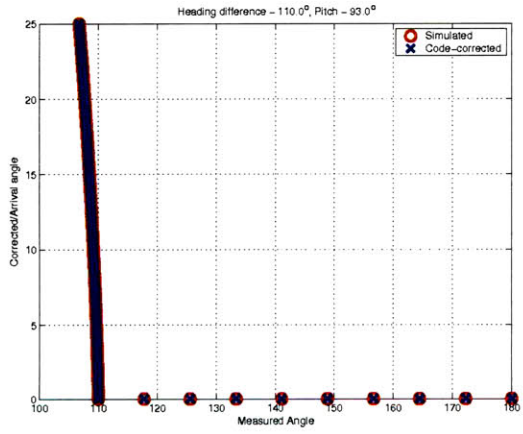

(c) Angle correction example 3

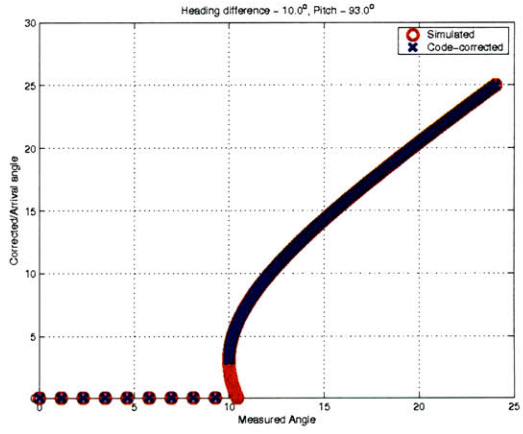

(d) Angle correction example 4

Figure C-2: Angle correction simulation results.

Appendix D

Spectral Covariance Matrix Estimation

First, the array snap-shot is represented by the sequence $x_l[m]$. The autocorrelation, or autocovariance function since the sequence is zero mean, is given by

$$c_{xx}[m] = E_l\left\{x[m] * x^*[-m]\right\}. \tag{D.1}$$

The autocorrelation can be represented as the sum of a set of trigonometric functions, determined using the discrete Fourier transform; *i.e.*,

$$c_{xx}[m] = \sum_{n=1}^{2N} p_n e^{jm\psi_n} = \sum_{n=1}^{2N} p_n \Phi_n[m]. \tag{D.2}$$

The maximum-likelihood spectral covariance matrix, without using physical constraints, is given by

$$\hat{\mathbf{S}}_{DATA} = E_l[\mathbf{x}\mathbf{x}^H]; \tag{D.3}$$

this matrix can be represented in terms of the cross-correlation of sensor outputs; *i.e.*,

$$\hat{\mathbf{S}}_{DATA} = \begin{bmatrix} E_l(x[1]x[1]^*) & E_l(x[1]x[2]^*) & \dots & E_l(x[1]x[N]^*) \\ E_l(x[2]x[1]^*) & E_l(x[2]x[2]^*) & \ddots & \vdots \\ \vdots & \ddots & \ddots & E_l(x[N-1]x[N]^*) \\ E_l(x[N]x[1]^*) & \dots & E_l(x[N]x[N-1]^*) & E_l(x[N]x[N]^*) \end{bmatrix}_{N\times N}; \tag{D.4}$$

this matrix is centrohermitian, but not necessarily Toeplitz structured. The sampled covariance matrix becomes Hermitian Toeplitz as the number of snap-shots, L, goes to infinity, and can be expressed in terms of the autocorrelation sequence; *i.e.*,

$$\lim_{L\to\infty} \hat{\mathbf{S}}_{DATA} = \begin{bmatrix} \frac{1}{N}c_{xx}[0] & \frac{1}{N-1}c_{xx}[1] & \cdots & c_{xx}[N-1] \\ \frac{1}{N-1}c_{xx}[-1] & \frac{1}{N}c_{xx}[0] & \ddots & \vdots \\ \vdots & \ddots & \ddots & \frac{1}{N-1}c_{xx}[1] \\ c_{xx}[-N+1] & \cdots & \frac{1}{N-1}c_{xx}[-1] & \frac{1}{N}c_{xx}[0] \end{bmatrix}_{N\times N} \tag{D.5}$$

The physical model for the covariance matrix is chosen to be the sum of a sensor noise and propagating plane wave noise covariance matrix; *i.e.*,

$$\hat{\mathbf{S}} = \sigma^2\mathbf{I} + \hat{\mathbf{S}}_{prop}. \tag{D.6}$$

To eliminate aliasing of the autocorrelation sequence terms in the covariance matrix, the propagating power covariance matrix is defined by a $2N$ set of basis vectors as follows:

$$\hat{\mathbf{S}}_{p2} = \sum_{n=1}^{2N} p_n\Phi_n\Phi_n^H, \tag{D.7}$$

$$\hat{\mathbf{S}}_{p2} = \sum_{n=1}^{2N} p_n \begin{bmatrix} \Phi_n[1]\Phi_n^*[1] & \Phi_n[1]\Phi_n^*[2] & \cdots & \Phi_n[1]\Phi_n^*[2N-1] \\ \Phi_n[2]\Phi_n^*[1] & \Phi_n[2]\Phi_n^*[2] & & \vdots \\ \vdots & & \ddots & \\ \Phi_n[2N-1]\Phi_n^*[1] & \cdots & & \Phi_n[2N-1]\Phi_n^*[2N-1] \end{bmatrix}_{2N\times 2N}, \tag{D.8}$$

$$\hat{\mathbf{S}}_{p2} = \begin{bmatrix} c_{xx}[0] & c_{xx}[1] & \cdots & c_{xx}[2N-1] \\ c_{xx}[-1] & c_{xx}[0] & & \vdots \\ \vdots & & \ddots & \\ c_{xx}[-2N+1] & \cdots & & c_{xx}[0] \end{bmatrix}_{2N\times 2N}, \tag{D.9}$$

$$\hat{\mathbf{S}}_{prop} = \begin{bmatrix} c_{xx}[0] & c_{xx}[1] & \cdots & c_{xx}[N-1] \\ c_{xx}[-1] & c_{xx}[0] & & \vdots \\ \vdots & & \ddots & \\ c_{xx}[-N+1] & \cdots & & c_{xx}[0] \end{bmatrix}_{N\times N}. \tag{D.10}$$

The propagating covariance matrix can be represented in terms of the sampled covariance matrix in the limit as L goes to infinity; *i.e.*,

$$\lim_{L\to\infty} \hat{\mathbf{S}}_{prop} = \hat{\mathbf{S}}_{DATA} \odot \begin{bmatrix} N & N-1 & \cdots & 1 \\ N-1 & N & & \vdots \\ \vdots & & \ddots & N-1 \\ 1 & \cdots & N-1 & 2N \end{bmatrix}_{N\times N} . \tag{D.11}$$

This is rather interesting in that the physically constrained covariance matrix estimation approach results in the tapered ensemble spectral covariance matrix. Figure D-1 shows the wavenumber-power spectrum of the taper matrix in Eq. D.11. The PCML covariance matrix can never achieve the SNR performance of the Capon beamformer in the limit because of the covariance matrix taper inherent to the method; however, when snap-shot support is poor, the PCML approach results in a Hermitian Toeplitz matrix formed from physically realizable propagating plane wave and sensor noise, and in many cases will have higher SNR and less sensitivity.

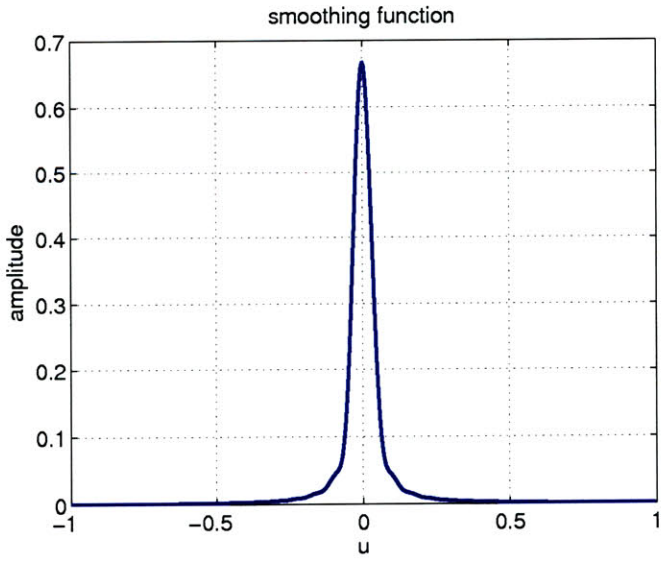

Figure D-1: Smoothing in wavenumber domain from taper matrix; *i.e.* the second term in Eq. D.11.

Bibliography

[1] D. L Sengupta, J. J. Bowman, T.B.A. Senior, and P. L. E. Usenghi. *Electromagnetic and Acoustic Scattering by Simple Shapes.* Hemisphere Publishing Corp., New York, 1987.

[2] W. H. Munk and F. Zachariasen. Refraction of sound by islands and seamounts. *Journal of Atmospheric and Oceanic technology*, 8:554–574, 1991.

[3] G.M. Wenz. Acoustic ambient noise in the ocean: spectra and sources. *J. Acoust. Soc. Am.*, 34:1936, 1962.

[4] John A. Colosi and Michael G. Brown. Efficient numerical simulation of stochastic internal-wave induced sound-speed perturbation fields. *J. Acoust. Soc. Am.*, 103(4), April 1998.

[5] John A. Colosi, Stanley M. Flatté, and Charles Bracher. Internal-wave effects on 1000-km oceanic acoustic pulse propagation: Simulation and comparison with experiment. *J. Acoust. Soc. Am.*, 96(1), July 1994.

[6] Walter H. Munk, Robert C. Spindel, Arthur B. Baggeroer, and Theodore G. Birdsall. The Heard Island Feasibility Test. *J. Acoust. Soc. Am.*, 96(4), Oct. 1994.

[7] B.D. Dushaw, B.M. Howe, J.A. Mercer, R.C. Spindel, A.B. Baggeroer, D. Menemenlis, C. Wunsch, T.G. Birdsall, K. Metzger, C. Clark, J.A. Colosi, B.D. Comuelle, M. Dzieciuch, W. Munk, P.F. Worcester, D. Costa, and A.M.G. Forbes. Multimegameter-range acoustic data obtained by bottom-mounted hydrophone arrays for measurement of ocean temperature. *Oceanic Engineering, IEEE Journal of*, 24(2):202–214, Apr 1999.

[8] Kathleen E. Wage. *Broadband modal coherence and beamforming at megameter ranges.* PhD thesis, Massachusetts Institute of Technology, 2000.

[9] John A. Colosi, Arthur B. Baggeroer, Bruce D. Cornuelle, Matthew A. Dzieciuch, Walter H. Munk, Peter F. Worcester, Brian D. Dushaw, Bruce M. Howe, James A. Mercer, Robert C. Spindel, Theodore G. Birdsall, Kurt Metzger, and Andrew M. G. Forbes. Analysis of multipath acoustic field variability and coherence in the finale of broadband basin-scale transmissions in the north pacific ocean. *The Journal of the Acoustical Society of America*, 117(3):1538–1564, 2005.

[10] Gordon R. Ebbeson and R. Glenn Turner. Sound propagation over Dickins Seamount in the Northeast Pacific Ocean. *J. Acoust. Soc. Am.*, 73(1):143–152, 1983.

[11] N. R. Chapman and Gordon R. Ebbeson. Acoustic shadowing by an isolated seamount. *J. Acoust. Soc. Am.*, 73(6):1979–1984, 1983.

[12] F. E. Hale. Long-range propagation in the deep ocean. *J. Acoust. Soc. Am.*, 33(4), 1961.

[13] Andrea L. Kraay and Arthur Baggeroer. Physically constrained maximum-likelihood method for snapshot-deficient adaptive array processing. *IEEE Transactions on Signal Processing*, 5:4048–4063, 2007.

[14] K.M. Becker and J.R. Preston. The ONR Five Octave Research Array (FORA) at Penn State. *OCEANS 2003. Proceedings*, 5:2607–2610 Vol.5, Sept. 2003.

[15] F.D.Tappert and Xin Tang. Ray chaos and eigenrays. *J. Acoust. Soc. Am.*, 99(1), Jan. 1996.

[16] Finn B. Jensen, William A. Kuperman, Michael B. Porter, and Henrik Schmidt. *Computational Ocean Acoustics*. Springer-Verlag New York, Inc., 2000.

[17] Timothy F. Duda James B. Bowlin, John L. Speisberger and Lee F. Freitag. Ocean Acoustical ray-Tracing Software RAY. Technical report, Woods Hole Oceanographic Institution, 1992.

[18] Michael D. Collins. A split-step Padé solution for the parabolic equation method. *Journal of Computational Acoustics*, 93:1736–1742, 1996.

[19] Michael D. Collins and R. J. Cederberg. Comparison of algorithms for solving parabolic wave equations. *Journal of Computational Acoustics*, 100:178–182, 1996.

[20] Elisabeth Larsson and Leif Abrahamsson. Helmholtz and parabolic equation solutions to a benchmark problem in ocean acoustics. *J. Acoust. Soc. Am.*, 37(1):19–27, 1965.

[21] John Northrop. Underwater sound propagation across the Hawaiian Arch. *J. Acoust. Soc. Am.*, 48(1):417–418, 1970.

[22] David A. Nutile and Albert N. Guthrie. Acoustic shadowing by seamounts. *J. Acoust. Soc. Am.*, 66(6):1813–1817, 1979.

[23] H. Medwin and R. Spaulding. The seamount as a diffracting body. *Bottom-Interacting Ocean Acoustics*, pages 421–438, 1980.

[24] Allan D. Pierce. Extension of the method of normal modes to sound propagation in an almost-stratified medium. *J. Acoust. Soc. Am.*, 37(1):19–27, 1965.

[25] Richard B. Evans. Stepwise coupled mode scattering of ambient noise by a cylindrical symmetric seamount. *J. Acoust. Soc. Am.*, 119(1):161–167, 2006.

[26] C. H. Harrison. Acoustic shadow zones in the horizontal plane. *J. Acoust. Soc. Am.*, 65(1):56–61, 1979.

[27] C. H. Harrison. Three-dimensional ray paths in basins, troughs, and near seamounts by use of ray invariants. *J. Acoust. Soc. Am.*, 62(6), Dec. 1977.

[28] M.I. Taroudakis. A coupled-mode formulation for the solution of the Helmholtz equation in water in the presence of a conical seamount. *Journal of Computational Acoustics*, 4:101–121, 1996.

[29] Jérémie Eskenazi. A computer model for sound propagation around conical seamounts. Master's thesis, Massachusetts Institute of Technology, 2001.

[30] H. Schmidt and G. Tango. Efficient global matrix approach to the computation of synthetic seismograms. *Geophys. J. R. Astr. Soc.*, 84:331–359, 1986.

[31] Wenyu Luo. *Three-dimensional propagation and scattering around a conical seamount.* PhD thesis, Massachusetts Institute of Technology, 2007.

[32] Clarence S. Clay and Herman Medwin. *Acoustical Oceanography: Principles and Applications.* John Wiley & Sons, Inc. New York, 1977.

[33] Xavier Lurton. *An introduction to underwater acoustics.* Praxs Publishing, Chichester, UK, 2002.

[34] Walter Munk, Peter Worcester, and Carl Wunsch. *Ocean Acoustic Tomography.* Cambridge University Press, New York, 1995.

[35] James Mercer, Rex Andrew, Bruce Howe, and John Colosi. Cruise Report: Long-range Ocean Propagation Experiment. Technical report, Applied Physics Laboratory, University of Washington, Woods Hole Oceanographic Institute, 2005.

[36] W.H.F. Smith and D.T. Sandwell. Global sea floor topography from satellite altimetry. *Science*, 277(5334):1956–1962, 1997.

[37] GEBCO Bathymetric Grid. <http://www.ngdc.noaa.gov/mgg/gebco/grid/1mingrid.html>, Mar 2004.

[38] H. Medwin. *Fundamentals of Acoustical Oceanography.* Academic Press, Sandiego, 1997.

[39] Walter H. Munk. Sound channel in an exponentially stratified ocean, with application to SOFAR. *J. Acoust. Soc. Am.*, 55(2), Feb. 1974.

[40] S. T. Daniel. Propagation of normal mode in the parabolic approximation. *Journal of Computational Acoustics*, 57:307–311, 1975.

[41] R.J. Urick. *Principles of Underwater Sound*, volume 3. McGraw-Hill, New York, 1983.

[42] National Geophysical Data Center (NGDC). NGDC - Geomagnetic Data, June 2008. http://www.ngdc.noaa.gov/geomagmodels/Declination.jsp.

[43] P.D. Welch. The Use of Fast Fourier Transform for the Estimation of Power Spectra: A Method Based on Time Averaging Over Short, Modified Periodograms. *IEEE Trans. Audio Electroacoustics*, AU-15, June 1967.

[44] Fredric J. Harris. On the Use of Windows for Harmonic Analysis with the Discrete Fourier Transform. *Proceedings of the IEEE*, 66(1), Jan. 1978.

[45] Harry L. Van Trees. *Optimum Array Processing*, volume IV of *Detection, Estimation, and Modulation Theory.* John Wiley & Sons, Inc., New York, 2002.

[46] J. Capon and N.R. Goodman. Probability distributions for estimators of the frequency-wavenumber spectrum. *Proceedings of the IEEE*, 58(10):1785–1786, Oct. 1970.

[47] Raj Rao Nadakuditi and Alan Edelman. *Applied stochastic eigen-analysis.* PhD thesis, Massachussets Institute of Technology, 2007.

[48] B.D. Carlson. Covariance matrix estimation errors and diagonal loading in adaptive arrays. *IEEE Trans. Aerosp. Electron. Syst.*, 24:397–401, July 1988.

[49] Henry Cox. Robust Adaptive Beamforming. *IEEE Transactions on Acoustics, Speech, and Signal processing*, ASSP-35(10), Oct. 1987.

[50] A.V. Oppenheim and R.W. Schafer. *Discrete-Time Signal Processing.* Prentice-Hall, 1989.

[51] A. Baggeroer and H. Cox. Passive sonar limits upon nulling multiple moving ships with large aperture arrays. *Proceedings of the 33rd Aslomar Conference on Signals, Systems & Computers (Pacific Grove, CA)*, pages 103–108, Nov. 1999.

[52] M. Herdin and E. Bonek. A MIMO correlation matrix based metric for characterizing non-stationarity. In *Proceedings of the 13th IST Mobile & Wireless Communications Summit 2004*, Lyon, France, June 2004.

[53] N.R. Goodman. Statistical analysis based on a certain multivariate complex Gaussian distribution. *Ann. Math. Stat.*, 34:152–177, March 1963.

[54] M. Miller and D. Snyder. The role of likelihood and entropy in incomplete-data problems: applications to estimating point-process intensities and toeplitz constrained covariances. *Proc. IEEE*, vol. 75:892–907, 1987.

[55] John Parker Burg, David G. Leunberger, and Daniel L. Wenger. Estimation of structured covariance matricies. *Proceedings of the IEEE*, 70(9), Sept. 1982.

[56] T.A. Barton and D.R. Fuhrmann. Covariance structures for multidimensional data. *Signals, Systems and Computers, 1991. 1991 Conference Record of the Twenty-Fifth Asilomar Conference on*, pages 297–301 vol.1, Nov 1991.

[57] Joseph R. Guerci. Theroy and Application of Covariance Matrix Tapers for Robust Adaptive Beamforming. *IEEE Trans. on Signal Processing*, 47(4), April 1999.

[58] J. Capon. High-resolution frequency-wavenumber spectrum analysis. *Proceedings of the IEEE*, 57:1408–1418, 1969.

[59] I.S. Reed, J.D. Mallett, and L.E. Brennan. Rapid convergence rate in adaptive arrays. *Aerospace and Electronic Systems, IEEE Transactions on*, AES-10(6):853–863, Nov. 1974.

[60] Victor Wowk. *Machinery Vibration: Measurement and Analysis.* McGraw-Hill, Inc., 1991.

[61] K.D. Heaney. Rapid geoacoustic characterization using a surface ship of opportunity. *Oceanic Engineering, IEEE Journal of*, 29(1):88–99, Jan. 2004.

[62] National Data Buoy Center. NDBC - Station 46006, June 2008. http://www.ndbc.noaa.gov/.

[63] I. I. Rypina and M. G. Brown. On the width of a ray. *Acoustical Society of America Journal*, 122:1440–+, 2007.

[64] David Palmer, Michael Brown, Fredrick Tappert, and Hugo Bezdek. Classical chaos in nonseparable wave propagation problems. *Geophysical Research Letters*, 15(6):569–572, June 1988.

[65] David T. Sandwell. Biharmonic spline interpolation of GEOS-3 and SEASAT altimeter sata. *Geophysical Research Letters*, 14(2):139–142, 1987.